

Synthesis, Characterization and Application of Pesticide-Encapsulated Silica Nanoparticles in Agriculture

Vinicius Bueno

Department of Civil Engineering
McGill University, Montreal, Canada

October 2021

A thesis submitted to McGill University in partial fulfillment of the requirements of the degree of Doctor of Philosophy

© Vinicius Bueno, 2021

Table of Contents

List of Figures	VIII
List of Supporting Figures	XIII
List of Tables	XVI
List of Supporting Tables.....	XVII
Abstract	XVIII
Résumé.....	XX
Acknowledgments.....	XXII
Preface and Contribution to Original Knowledge	XXIII
Preface.....	XXIII
Contribution to knowledge	XXIII
Contribution of Authors and Publications	XXVI
Abbreviations	XXIX
Chapter 1. Introduction	1
1.1. Nano-enabled agriculture	1
1.2. Nanoencapsulation for sustainable agricultural practices.....	2
1.3. Plant uptake of engineered nanoparticles	5
1.4. Environmental fate of nanoencapsulated pesticides	7
1.5. Impacts of nanoencapsulated pesticide on the microbial community	9
1.6. Knowledge gaps.....	11
1.7. Research objectives.....	12
1.8. Thesis organization	13
1.9. References.....	14
Connecting Text to Chapter 2	23
Chapter 2. Literature Review: Inorganic porous nanoparticles as pesticide or nutrient carriers ..	24

2.1. Abstract	24
2.2. Introduction.....	24
2.3. Nanoparticles as active ingredients and carriers of active ingredients	25
2.3.1. Silica Nanoparticles	26
2.3.2. Hydroxyapatite Nanoparticles	27
2.3.3. Iron Oxide Nanoparticles.....	28
2.3.4. Zinc Oxide Nanoparticles	29
2.3.5. Copper Oxide Nanoparticles.....	31
2.3.6. Clay Nanoparticles.....	31
2.4. Impact of size and surface properties for efficient uptake in foliar and root systems	32
2.5. Surface functionalization to facilitate uptake and to target delivery	34
2.6. Stimuli responsive porous nanocarriers	36
2.7. Conclusions.....	42
2.8. References.....	43
Connecting Text to Chapter 3	66
Chapter 3. Self-assembled surfactant-templated synthesis of porous hollow silica nanoparticles: mechanism of formation and feasibility of post-synthesis nanoencapsulation.....	67
3.1. Abstract	67
3.2. Introduction.....	67
3.3. Experimental Section.....	70
3.3.1. Materials	70
3.3.2. Synthesis of PHSN.....	71
3.3.3. Characterization of PHSN.....	71
3.3.4. Understanding the synthesis mechanism of formation with SS-NMR and FTIR.....	71
3.3.5. Assessment of encapsulation in PHSN post-synthesis and calcination	72

3.4. Results and Discussions	72
3.4.1. PHSN Characterization	72
3.4.2. Interactions and bonds between Pluronic P123, CTAB and SiO ₂ with SS-NMR spectra	74
3.4.3. Using FTIR to complement the information obtained with SS-NMR	78
3.4.4. Mechanisms of formation and structure of PHSN	81
3.4.5. Internalization of FeCl ₃ /NaBH ₄ and formation of iron nanoparticles inside the PHSN	81
3.5. Conclusions	85
3.6. Supporting Information	86
3.7. References	88
Connecting Text to Chapter 4	93
Chapter 4. Mobility of Solid and Porous Hollow SiO ₂ Nanoparticles in Saturated Porous Media: Impacts of Surface and Particle Structure	94
4.1. Abstract	94
4.2. Introduction	94
4.3. Materials and Methods	96
4.3.1. Porous Media	96
4.3.2. SiO ₂ Nanoparticles	98
4.3.3. Solution Chemistry	98
4.3.4. Column Experiments	99
4.3.5. Interaction Energies and Collector Efficiency	100
4.4. Results and Discussion	100
4.4.1. SiO ₂ NPs Characterization	100
4.4.2. pH Effect of the Transport Behavior	102

4.4.3. IS Effect on the Transport Behavior	106
4.4.4. Single Collector Contact Efficiencies (η_0) and Particle-Collector Attachment Efficiencies (α_{pc})	109
4.4.5. Surface Roughness and the DLVO Theory	109
4.5. Conclusions.....	113
4.6. Supporting Information.....	114
4.6.1. Equations Used for the DLVO Energy Profile Computations.....	115
4.7. References.....	120
Connecting Text to Chapter 5	130
Chapter 5. Impacts of Porous Silica-Nanoencapsulated Pesticide Applied on Soils on Plant Growth and Soil Microbial Community	131
5.1. Abstract	131
5.2. Environmental Significance.....	131
5.3. Introduction.....	132
5.4. Experimental Section	133
5.4.1. Materials	133
5.4.2. SiO ₂ NPs Synthesis.....	134
5.4.3. Azoxystrobin loading and release rates	135
5.4.4. Plant growth conditions and soil amendment	135
5.4.5. Plant health data.....	136
5.4.6. Azoxystrobin uptake measurements in plants.....	136
5.4.7. DNA extraction and sequencing	137
5.4.8. Sequencing analysis	137
5.4.9. Quantitative polymerase chain reaction (qPCR).....	138
5.5. Results and discussion	138

5.5.1. PHSN encapsulation provides controlled release properties	138
5.5.2. Azoxystrobin uptake profiles differed significantly among the treatments	140
5.5.3. Azoxystrobin when loaded in a SiO ₂ porous nanocarrier minimized its inhibitory effects on plants	143
5.5.4. Nanopesticides had limited impact on the soil microbial community structures	145
5.6. Conclusions.....	150
5.7. Supporting Information.....	151
5.7.1. Matrix Effects on the Azoxystrobin Detection	151
5.7.2. Pielou's evenness index (<i>J'</i>) and Faith's Phylogenetic Diversity (PD)	155
5.8. References.....	158
Connecting Text to Chapter 6.....	167
Chapter 6. Uptake and Translocation of a Silica Nanocarrier and an Encapsulated Organic Pesticide Following Foliar Application in Tomato Plants.....	168
6.1. Abstract	168
6.2. Introduction.....	168
6.3. Experimental Section.....	171
6.3.1. Chemicals.....	171
6.3.2. Nanocarrier synthesis.....	171
6.3.3. Azoxystrobin nanoencapsulation	172
6.3.4. Seed germination and hydroponic system	172
6.3.5. Azoxystrobin uptake quantification.....	173
6.3.6. Total Si uptake quantification.....	173
6.3.7. spICP-MS measurements of PHSN uptake.....	174
6.4. Results and Discussion	174
6.4.1. Azoxystrobin loading in PHSN	174

6.4.2. Uptake and translocation of azoxystrobin in different plant parts	175
6.4.3. Uptake and translocation of Si in different plant parts	177
6.4.4. Characterization of particulate SiO ₂ uptake and translocation in different plant parts	179
6.4.5. Uptake and Translocation Mechanisms of Azoxystrobin and SiO ₂	181
6.5. Environmental Implications.....	183
6.6. Supporting Information.....	184
6.6.1. List of Chemicals	184
6.6.2. Pesticide Extraction	185
6.7. References.....	190
Chapter 7. Conclusions, Implications and Future Work.....	197
7.1. Conclusions.....	197
7.2. Implications.....	199
7.3. Future work.....	202

List of Figures

Figure 2-1. Commonly studied nanomaterials, morphologies, encapsulated active ingredients and application methods for nano-enabled agriculture.....	25
Figure 2-2. Schematic representation of possible nanocarrier pathways for uptake through the roots or the leaves followed by translocation through the vascular systems (xylem and phloem).....	33
Figure 2-3. Conceptual schematic of a (A) pH-responsive nanocarrier suggested by Mattos et al. ¹⁹⁸ : at neutral pH there is a strong interaction between the negatively charged hydroxyl group in thymol and the positively charged amino group in the functionalized biogenic nano-SiO ₂ and when the pH becomes more acidic, this interaction is weakened due to the protonation of the hydroxyl group in thymol; (B) light-responsive nanocarrier suggested by Chen et al. ¹⁸³ : under UV-Vis light radiation at 435 nm, azobenzene undergoes isomerization releasing the encapsulated glyphosate from the porous biochar-attapulgite framework; (C) general stimulus-responsive nanocarrier: the AI is trapped within the nanocarrier until a stimulus disrupts the structure of the gatekeeper compound, thus liberating the pores and allowing the AI to be released.	39
Figure 3-1. The upper images represent (a) the particle size distribution of calcined PHSN obtained from DLS and (b) the particle size distribution (N=100) of calcined PHSN from TEM. The lower figures represent (c) the TEM image of calcined PHSN, (d) the nitrogen sorption/desorption isotherm type IV profile and (d, inset) the pore size distribution of calcined PHSN obtained from BET and BJH respectively.....	74
Figure 3-2. The upper images are SS-NMR spectra of (a) as-synthesized PHSN and (b) calcined PHSN. The lower images are schematic representations of (c) Q ³ and (d) Q ⁴ Si.....	75
Figure 3-3. The upper image illustrates Pluronic P123 and CTAB structures with protons labeled from a to h. The lower images represent the pcal-PHSN SS-NMR spectra of (a) 1-D CP-MAS ¹ H, (b) 1-D CP-MAS ¹³ C, (c) 2-D ¹ H- ²⁹ Si HETCOR and (d) 2-D ¹ H- ¹³ C HETCOR.....	77
Figure 3-4. PHSN SS-NMR spectra of 2-D 1H-1H exchange MAS with (a) mixing time = 20 ms and (b) mixing time = 100 ms.....	78

Figure 3-5. FTIR spectra of the (a) 400-200 cm^{-1} region, (b) 1300-1800 cm^{-1} region and (c) 2750-3050 cm^{-1} region.	80
Figure 3-6. Schematic representation of the formation of CTAB-Pluronic emulsion, followed by its silanization with TEOS and calcination to make the PHSN ready for downstream applications.	82
Figure 3-7. FeNP@PHSN (a-f) TEM images and (g) EDX spectrum of the marked site (*) in Figure 3-7a.	84
Figure 4-1. TEM images of (a and b) SSNs and (c and d) PHSNs. The images on the right exhibit more magnified images of singular (b) SSN and (d) PHSN to show the different features between both structures. Although both structures are spherically shaped, PHSNs feature a hollow core and pores. The latter is directly responsible for the increased surface area and roughness of PHSNs when compared to SSNs.	101
Figure 4-2. Particle size distribution at pH 9.5 and IS 1 mM of (a) SSNs and (b) PHSNs. The width of the PHSN size distribution is broader than that for SSN, indicating a higher PDI as confirmed in Table 4-1.	103
Figure 4-3 BTCs at fixed IS 1 mM and varying pH for (a) SSNs and (b) PHSNs. The shaded zones represent the standard deviation of the particle concentration run in triplicates. Wider shaded areas represent greater standard deviation among replicates. The conditions with no visible shaded areas represent runs with not relevant difference among replicates.	104
Figure 4-4. DLVO energy profiles at fixed IS 1 mM and varying pH for (a) SSN particle-particle interactions, (b) PHSN particle-particle interactions, (c) SSN particle-collector interactions, and (d) PHSN particle-collector interactions.	105
Figure 4-5. BTCs at fixed pH 9.5 and varying IS for (a) SSNs and (b) PHSNs. The shaded zones represent the standard deviation of the particle concentration run in triplicates. Wider shaded areas represent greater standard deviation among replicates. The conditions with no visible shaded areas represent runs with not relevant difference among replicates.	108

Figure 4-6. DLVO energy profiles at fixed pH 9.5 and varying IS for (a) SSN particle-particle interactions, (b) PHSN particle-particle interactions, (c) SSN particle-collector interactions, and (d) PHSN particle-collector interactions..... 110

Figure 4-7. Estimates of η_0 for (a) SSNs and (b) PHSNs, and (c) the SSN-PHSN η_0 ratio. 111

Figure 4-8. Schematic representation of the distance between sites in the SSN (a) and PHSN (b), and a hypothetical surface. For SSNs, the distance from point *a* to the surface, h_a , and the distance from a relatively distant point *a'* to the same surface, $h_{a'}$, are approximately the same. Meanwhile, in PHSNs, the distances h_b , h_c and h_d may vary significantly, even if they are at the same distance as points *a* and *a'* in scheme (a). Effectively, the overall separation distance between rough spherical surfaces and a hypothetical surface is larger than the distance between smooth spherical surfaces and a hypothetical surface..... 113

Figure 5-1. (a) Relative concentration (C/C_0) of azoxystrobin in solution (20% v/v methanol) phase over time and (b) Concentration of azoxystrobin over time in solution (20% v/v methanol) released from pure (Azo) and encapsulated azoxystrobin (Azo@PHSN)..... 140

Figure 5-2. (A) Azoxystrobin concentration per unit of dry plant biomass at days 10 and 20 for Azo and Azo@PHSN treatments. The dry biomass was derived from plants after thorough rinse of the roots. (B) Azoxystrobin absolute uptake at days 10 and 20. Different letters (*A*, *B*, *C* and *D*) indicate significant statistical differences among samples (ANOVA one-way test followed by Tukey's test, $p < 0.05$ threshold). (B) Photos of the plants harvested at day 10. (C) Photos of the plants harvested at day 20. 142

Figure 5-3. The measures of five phenotypic traits (dry mass, root length, shoot length, number of leaflets and length of the longest leaflet) as indicators of the impacts of each treatment in the plant growth. Different letters (*a*, *b* and *c* for samples at day 10, *A*, *B* and *C* for samples at day 20) indicate significant statistical differences among samples (ANOVA one-way test followed by Tukey's test, $p < 0.05$ threshold). 143

Figure 5-4. Relative taxonomic abundance of fungi communities at a class level. The communities obtained from loosely attached soil to the roots have the prefix *R-* in front of the treatment ID. The communities obtained from bulk soil have no prefix in front of the treatment ID. 146

Figure 5-5. Relative taxonomic abundance of bacterial and archaea communities at a phylum level. The communities obtained from loosely attached soil to the roots have the prefix *R-* in front of the treatment ID. The communities obtained from bulk soil have no prefix in front of the treatment ID. 147

Figure 5-6. PCoAs for (a) bacterial and archaea communities and (b) fungi community. The communities obtained from loosely attached soil to the roots have the prefix *R-* in front of the treatment ID. The communities obtained from bulk soil have no prefix in front of the treatment ID. 149

Figure 6-1. Characterization of (A) particle size and shape using TEM and (B) azoxystrobin loading and release profiles within the PHSN based on the data of a previous work.⁴² The black data points (●) represent the amount of azoxystrobin being loaded in the PHSN over time after introducing the nanocarriers in a methanolic solution of azoxystrobin. The red data points (●) represent the amount of azoxystrobin remaining in the PHSNs over time after separating the azoxystrobin-loaded PHSN and introducing them into an aqueous release medium containing methanol (20% v/v)..... 175

Figure 6-2. Azoxystrobin distribution in different plant parts 2 and 4 days after dosing with Azo and Azo@PHSN treatments. (A) Mass of azoxystrobin in different plant parts. Error bars represent the standard deviation of the samples ($N = 3$). Different letters (*A* and *B*) indicate significant statistical differences among samples, while same letters indicate no significant statistical differences among samples (ANOVA one-way test followed by Tukey's test, $p < 0.05$). (B) Mass of azoxystrobin in different plant parts normalized by the total amount of azoxystrobin. 177

Figure 6-3. Si distribution in different plant parts 2 and 4 days after dosing Azo@PHSN treatment. (A) Mass of Si in different plant parts. Error bars represent the standard deviation of the samples ($N = 3$). Different letters (*A* and *B*) indicate significant statistical differences among samples, while same letters indicate no significant statistical differences among samples (ANOVA one-way test followed by Tukey's test, $p < 0.05$). (B) Mass of Si in different plant parts normalized by the total amount of Si measured by ICP-OES. 179

Figure 6-4. PHSN size distribution in different plant parts at different harvesting periods measured by spICP-MS. No PHSN signal was measured in mature leaflets at days 2 and 4 of harvesting. These experiments were performed in triplicates ($N = 3$)..... 181

List of Supporting Figures

Figure S3-1. TEM image on the left (a) shows the nanoparticles synthesized with a high CTAB:Pluronic P123 ratio 0.75:1 wt% and on the right (b) nanoparticles synthesized with a low CTAB:Pluronic P123 ratio 0.1:1 wt%. When the amount of the pore-shell directing agent is exceeding (CTAB), the resulting nanoparticle that is porous without a hollow core. When the amount of core directing agent is exceeding, the resulting nanoparticle has a large hollow core and thin SiO ₂ shell (Pluronic P123).....	86
Figure S3-2. Schematic representation of the internalization of FeCl ₃ and NaBH ₄ in an oxygen-deprived environment and the formation of iron nanoparticles (FeNP) inside the PHSSN. First, the calcined PHSN was immersed in a concentrated FeCl ₃ solution. Some of the dissolved Fe and Cl ions permeated through pores and filled the hollow-core. The suspension was centrifugated, followed by having the supernatant decanted and rinsed with DI water to remove the non-internalized ions. It was observed Fe(0) formation on the PHSN shell, therefore, either some of the ions inside the shell possibly diffused out of the PHSN or some Fe ³⁺ remained attached to the surface of PHSN after rinsing with DI water. Later, NaBH ₄ solution was dripped over the FeCl ₃ @PHSN pellet. NaBH ₄ reacted to form Fe(0).....	87
Figure S4-1. Scanning electronic microscopy (SEM) image of white quartz sand.....	114
Figure S4-2. TEM size distribution ($N = 100$) of (a) SSNs and (b) PHSNs.....	117
Figure S4-3. Nitrogen sorption/desorption isotherms with inset representation of the structure and specific surface area for (a) SSNs and (b) PHSNs, ³⁶ and (c) FTIR spectra of the 4000-400 cm ⁻¹ region for SSNs and PHSN previously reported.....	119
Figure S5-1. Relative concentration (C/C_0) of azoxystrobin in solution (20% v/v methanol) phase over time using solid SiO ₂ NPs (SSN) and porous hollow SiO ₂ NPs (PHSN) as nanocarriers..	152
Figure S5-2. Percentage of day 0 soil microbial community following qPCR targeting the gene 16S rRNA for total bacterial and archaea communities using (A) bulk soil and (B) soil loosely attached to the roots. Different letters (<i>A</i> and <i>B</i>) indicate significant statistical differences among samples (ANOVA one-way test followed by Tukey's test, $p < 0.05$ threshold).	153

Figure S5-3. Percentage of day 0 soil microbial community following qPCR targeting the gene 18S rRNA for total fungi communities using (A) bulk soil and (B) soil loosely attached to the roots. Different letters (A and B) indicate significant statistical differences among samples (ANOVA one-way test followed by Tukey’s test, $p < 0.05$ threshold). 154

Figure S5-4. α -diversity boxplots representing (a) Pielou’s evenness index for samples at day 10, (b) Pielou’s evenness index for samples at day 20, (c) Faith’s PD for samples at day 10, and (d) Faith’s PD for samples at day 20 for the bacterial and archaea communities. α -diversity boxplots representing (e) Pielou’s evenness index for samples at day 10, (f) Pielou’s evenness index for samples at day 20, (g) Faith’s PD for samples at day 10, and (h) Faith’s PD for samples at day 20 for the fungi communities. The black dots above and below the error bars in some instances indicate outliers. 156

Figure S6-1. Total amount of (A) azoxystrobin and (B) Si that were translocated to different plant parts measured in LC-QToF-MS and ICP-OES, respectively. These values excluded the amount of azoxystrobin and SiO₂ measured in the dosed leaflet because some amounts may remain non-internalized on the surface of the leaflet. Error bars represent the standard deviation of the replicates ($N = 3$). Asterisk symbol (*) indicates significant statistical differences among samples with $p < 0.05$ (ANOVA one-way test followed by Tukey’s test). 186

Figure S6-2. Images of the dosed leaflet ($N = 3$) upon harvesting at day 2 for the Azo@PHSN treatment (top) and Azo treatment (bottom). The red arrows indicate the PHSN powder residue remaining on the surface of the leaflet. No leaflet burn or other adverse effects were observed for either treatment. 187

Figure S6-3. Images of the dosed leaflet ($N = 3$) upon harvesting at day 4 for the Azo@PHSN treatment (top) and Azo treatment (bottom). The red arrows indicate the PHSN powder residue remaining on the surface of the leaflet. No leaflet burn or other adverse effects were observed for either treatment. 188

Figure S6-4. Dry biomass (mg) of different plant parts in different treatments upon harvesting at day 2. The error bars correspond to the standard deviation of the triplicates. The letter A above the error bars indicate that there were no statistical differences among treatments (ANOVA one-way test followed by Tukey’s test, $p < 0.05$ threshold). 189

Figure S6-5. Dry biomass (mg) of different plant parts in different treatments upon harvesting at day 4. The error bars correspond to the standard deviation of the triplicates. The letter *A* above the error bars indicate that there were no statistical differences among treatments (ANOVA one-way test followed by Tukey's test, $p < 0.05$ threshold)..... 189

List of Tables

Table 2-1. List of stimuli responsive nanocarriers with their respective gatekeepers and active ingredients.....	41
Table 4-1. Particle characterization data and calculated DLVO interaction energies by nanoparticle type, pH, IS (mM, electrolyte NaCl). Measurements of zeta potential (mV), Z-average diameter (nm), Polydispersity Index (PdI), depths of primary minima (Φ_{\min}), heights of energy barriers (Φ_{\max}) and depths of secondary wells (Φ_{sec}) for the DLVO energy profiles. Errors denote standard deviations corresponding to measurement of 3 samples.....	97
Table 6-1. Si to azoxystrobin ratio in different systems.	183

List of Supporting Tables

Table S3-1. List of chemicals used for the synthesis of a standard batch of PHSN.....	86
Table S3-2. Relaxation times (T_1 and $T_{1\rho}$) assigned to the peaks in the 1-D CP-MAS ^1H . The relaxation times were obtained with recycle delays of 120s. The standard deviation for both T_1 and $T_{1\rho}$ were obtained to analyze whether the differences among different peaks are representative. Note that T_1 was considered to be constant because the average was 0.51 s with a standard deviation of 0.04 s (9% of the average). Several $T_{1\rho}$ were found ranging from 0.004 to 0.044 s. According to Apperley et al., ³⁵ when T_1 is constant with multiple $T_{1\rho}$ the average domain sizes are in between 5 and 50 nm distant.....	87
Table S4-1. White quartz sand zeta potential values at various conditions.....	115
Table S4-2. Physical properties of SiO_2 , water and white quartz sand at 100 nm.....	116
Table S4-3. Expressions used for the prediction of single collector contact efficiencies.....	118
Table S4-4. Parameters used for calculations of single collector contact efficiency.....	120
Table S4-5. Particle-Collector Attachment Efficiencies (α_{pc}) for the varying experimental conditions.....	120
Table S5-1. List of the soil properties.....	151
Table S5-2. Azoxystrobin recoveries in homogenized biomass for low- and high-range concentrations.	152
Table S5-3. List of suspected metabolites derived from azoxystrobin in tomato plants for different treatments and data points. The peaks were categorized by low, medium and high based on the comparison among them and do not have quantification purposes.	157
Table S6-1. Key parameters obtained from PHSN characterization.	185

Abstract

Agriculture is under heavy pressure to innovate due to the needs of feeding a rapidly growing global population while agricultural productivity has largely plateaued in recent decades. It is estimated that the world population will reach 9.1 billion by 2050 and the yearly demand for cereals, for instance, will increase by 43%, from 2.1 to 3 billion tonnes. Optimizing crop productivity and addressing current process inefficiencies are critical to meeting the increased demand without creating excessive energy and materials resource demands. Pesticide application, for example, is a highly inefficient process and it is estimated 2.45 billion kg of pesticides are wasted every year because of current application practices. That corresponds to 90% of the total pesticide applied, which end up contaminating the soil, water bodies, and impacting a range of living organisms, including humans. Nanotechnology is viewed as a promising technology to improve pesticide application. Nanocarriers, a class of nanomaterials, can be used as delivery agents for pesticides to provide slow and targeted release in the plant, and protect them against premature degradation and uptake in plants. Therefore, the use encapsulated pesticides within nanocarriers, have the potential to reduce wastage during application. The objective of the thesis is to explore the feasibility and efficacy of deploying silica nanoparticles as pesticide nanocarriers for agriculture. The scope includes the synthesis, characterization, and application of silica nanocarriers and assessing their mobility in the subsurface. The first objective was to develop a reproducible method to synthesize porous hollow silica nanoparticles (PHSN) through soft templating. In summary, when combined in the right ratio, two surfactants, cetyltrimethylammonium bromide and Pluronic P123, self-assemble forming the template onto which the SiO_2 precursor can anchor to grow the SiO_2 shell. The resulting PHSN population was monodisperse with diameter of 258 nm, specific surface area of $287 \text{ m}^2 \text{ g}^{-1}$ and pore size ranging from 1.5 to 2 nm. The characterization was performed using a suite of techniques, including solid-state nuclear magnetic resonance, Fourier-transform infrared spectroscopy, transmission electronic microscopy and light scattering. It was also the first imaging demonstration of nanoencapsulation where iron (Fe) and borohydride ions diffused in the pores to reach the hollow cavity and reacted forming entrapped Fe nanoparticles. The second objective was to investigate the impacts of particle architecture and surface properties on transport in saturated porous media. Solid SiO_2 nanoparticles and PHSN were tested under varying experimental conditions of pH and ionic

strength. Retention of PHSN was significantly higher across the board, which was not captured by modeling. This suggests that particle architecture and surface properties play a role in the transport profile. The third objective was to investigate the impacts of nanoencapsulated azoxystrobin added to soils on plant growth and soil microbial community and how these compare with non-encapsulated formulations. Not only did the nanocarriers mitigate the toxicity of the pesticide, they also did not interfere with the soil and plant health. The fourth objective was to explore the uptake and translocation of the nanoencapsulated azoxystrobin in tomato plants following foliar application. It was demonstrated that both the nanocarrier and the pesticide were taken up and distributed throughout the plant, even though the particle size exceeded the size excluding limits discussed in the literature.

Résumé

L'agriculture est soumise à une forte pression pour innover en raison des besoins de nourrir une population mondiale en croissance rapide, tandis que la productivité agricole a largement plafonné au cours des dernières décennies. Il est estimé que la population mondiale atteindra 9,1 milliards d'ici 2050 et que la demande annuelle de céréales, par exemple, augmentera de 43%. L'optimisation de la productivité des cultures et la résolution des inefficacités actuelles des processus sont essentielles pour répondre à la demande accrue sans créer de demandes excessives en matière d'énergie et de ressources matérielles. L'application de pesticides, par exemple, est un processus très inefficace et il est estimé que 2,45 milliards de kg de pesticides sont gaspillés chaque année en raison des pratiques d'application actuelles. Cela correspond à 90% du total des pesticides appliqués, qui finissent par contaminer le sol, les plans d'eau et impacter une gamme d'organismes vivants, y compris les humains. La nanotechnologie est considérée comme une technologie prometteuse pour améliorer l'application des pesticides. Les nanotransporteurs, une classe de nanomatériaux, peuvent être utilisés comme agents de libération des pesticides pour assurer une libération lente et ciblée dans la plante et les protéger contre la dégradation et l'absorption prématurées par les plantes. Par conséquent, l'utilisation de pesticides encapsulés dans des nanotransporteurs a le potentiel de réduire le gaspillage lors de l'application. L'objectif de la thèse est d'explorer la faisabilité et l'efficacité du déploiement de nanoparticules de silice comme nanotransporteurs de pesticides pour l'agriculture. La portée de la thèse comprend la synthèse, la caractérisation et l'application de nanotransporteurs de silice et l'évaluation de leur mobilité dans le sous-sol. Le premier objectif était de développer une méthode pour synthétiser des nanoparticules de silice creuses poreuses (PHSN). En résumé, lorsque deux tensioactifs, le bromure de cétyltriméthylammonium et le Pluronic P123, sont combinés dans le bon rapport, ils s'auto-assemblent pour former le gabarit sur lequel le précurseur de SiO_2 peut s'ancrer pour faire croître la coque de SiO_2 . La population de PHSN résultante était monodisperse avec un diamètre de 258 nm, une surface spécifique de $287 \text{ m}^2 \text{ g}^{-1}$ et une taille de pores allant de 1,5 à 2 nm. La caractérisation a été effectuée à l'aide d'une suite de techniques, notamment la résonance magnétique nucléaire à l'état solide, la spectroscopie infrarouge à transformée de Fourier, la microscopie électronique à transmission et la diffusion de la lumière. Il s'agit également de la première démonstration d'imagerie de nanoencapsulation des nanoparticules de Fe dans des PHSN.

Le deuxième objectif était d'étudier les impacts de l'architecture des particules et des propriétés de surface sur le transport dans des milieux poreux saturés. Des nanoparticules de SiO₂ solides et les PHSN ont été testés dans diverses conditions expérimentales de pH et de force ionique. La rétention de PHSN était significativement plus élevée dans l'ensemble, ce qui n'a pas été capturé par la modélisation. Cela suggère que l'architecture des particules et les propriétés de surface jouent un rôle dans le profil de transport. Le troisième objectif était d'étudier les impacts de l'azoxystrobine nanoencapsulée ajoutée aux sols sur la croissance des plantes et la communauté microbienne du sol. Non seulement les nanotransporteurs ont atténué la toxicité du pesticide, mais ils n'ont pas non plus interféré avec la santé du sol et des plantes. Le quatrième objectif était d'explorer l'absorption et la translocation de l'azoxystrobine nanoencapsulée dans les plants de tomates après application foliaire. Il a été démontré que le nanotransporteur et le pesticide étaient absorbés et distribués dans toute la plante, même si la taille des particules dépassait la taille hors limites discutée dans la littérature.

Acknowledgments

Throughout the writing of this thesis, I have received an appreciable deal of support and assistance.

Firstly, I would like to dedicate this thesis to my parents and sister, who supported me emotionally and financially throughout my studies and adventures in France, United States, United Arab Emirates and Canada. You were always there for me. I will always remember your wise counsel and sympathetic ear.

Secondly, I would like to thank my favorite person in this world, Karen Nadur, for the crucial support throughout my graduate studies. You offered a shoulder for me to cry on during difficult times, kept me focused, helped me enjoy life outside of the lab and made the frigid winters in Montreal bearable. I would not have completed this thesis without your support, and I will be forever in debt.

Thirdly, I would like to thank my supervisor, Professor Subhasis Ghoshal, whose expertise was invaluable in formulating the research questions and methodology. Your insightful feedback pushed me to sharpen my thinking and brought my work to a higher level.

Finally, I would like to acknowledge my colleagues scattered all around the globe and my peers from McGill University, particularly from the Environmental Engineering Benedek Laboratory. You gave me the support necessary to go through this crazy journey that is a Ph.D. and for that I will be forever grateful.

Thank you for this amazing ride!



Vinicius Bueno

Montreal, Canada

Preface and Contribution to Original Knowledge

Preface

In accordance with the *McGill Guidelines of Thesis Preparation*, this thesis was prepared in the manuscript-based format. Chapter 1 presents the introduction to the field, knowledge gaps, thesis objectives and structure. Chapter 2 presents a literature review focusing in the nano-enabled agriculture field and was prepared as a book chapter. Chapters 3 to 6 were prepared as research articles and include the experimental methods, results of the experimental work and discussions. Chapter 7 presents the conclusions, major implications of the findings and potential future work. The author of this thesis is the primary author for all the manuscripts stated above. A detailed description of the contributions to new knowledge is presented below.

Contribution to knowledge

- 1) **Development of a novel method to synthesize hollow porous silica (SiO₂) nanoparticles (PHSN).** Previously reported synthesis of such particles can be separated in hard template and soft template methods. While hard template methods require the use of a hard sphere, such as polystyrene, and functionalization of its surface to allow for the SiO₂ precursor to attach and grow, soft template methods use a combination of surfactants and a swelling agent, usually an oil phase, and further functionalize the water-oil interface of the nano-emulsion to allow for the SiO₂ precursor to attach and grow. Here, a protocol was presented using two surfactants, cetyltrimethylammonium bromide and Pluronic P123, that self-assemble forming the template for the PHSN without the need for a hard or soft template and their functionalization. The resulting PHSN was determined to be hollow and porous, an ideal structure for nanocarriers. Furthermore, the size distribution was monodispersed, and batch-to-batch reproducibility was achieved.
- 2) **First imaging demonstration of active ingredient (AI) post-synthesis nanoencapsulation within PHSN.** Previous studies claimed that AI nanoencapsulation within nanoparticles was successful by comparing the release profile of AI in the encapsulated form and how that compared with the non-encapsulated form. Then, these results were combined with measurement of the decrease of the concentration of the AI in

the bulk solution during the loading experiments to show proof that the AI was being loaded into the nanocarrier. Nonetheless, no images could be provided to show proof of encapsulation post-synthesis. The main obstacles were that post-synthesis encapsulation are usually done with organic molecules, which cannot be imaged, e.g., using transmission electron microscopy (TEM). TEM images were provided of the post-synthesis encapsulation of iron (Fe) and borohydride ions, that subsequently reacted forming Fe nanoparticles within the PHSN, indicating the successful nanoencapsulation of the AI.

- 3) **Experimental demonstration of how particles surface roughness can influence the transport of nanoparticles in saturated porous media.** Previous studies on how nanoparticle characteristics influence the transport of a nanoparticles in porous media have largely focused on attributes such as particle size, aggregation extent, charge, and presence/absence of polymer coatings. Here, the transport profile of solid SiO₂ nanoparticles was compared to PHSN of the same size in varying experimental conditions of pH and ionic strength. Although they had the same size and were comprised of the same material, the retention of PHSN was 3-fold higher than that of solid SiO₂. Detailed characterization and analysis showed that surface roughness and porosity of PHSN play an important role in the transport profile of nanoparticles and cause deviations in the particle-collector interactions from that predicted by the Derjaguin-Landau-Verwey-Overbeek theory.
- 4) **Demonstration of the impacts of an inorganic nanocarrier-encapsulated pesticide on plant growth and soil microbial community.** In this study, the effects of nanoencapsulated pesticides on plant and soil health was demonstrated and compared to non-encapsulated pesticide. It is the first study to assess uptake of pesticide encapsulated in a silica nanocarrier in soil system. Furthermore, it was unclear whether the nanopesticide, or the encapsulating nanoparticle alone, would have any detrimental impact on agricultural practices. Overall, the experiments showed that not only the nanoformulation did not negatively impacted the plant and soil health, but it also mitigated the toxic effects of the pesticide towards tomato plants evidenced with the non-encapsulated pesticide. Moreover, it was demonstrated that the pesticide uptake was higher for the nanoencapsulated pesticide when compared to the non-encapsulated pesticide.

- 5) **First evaluation of the uptake and translocation of PHSN-encapsulated pesticide by tracking both the nanocarrier as well as the pesticide.** Previous studies have tracked uptake and translocation of nanopesticides by tracking the pesticide alone. Therefore, it was unclear whether the pesticide was being taken up and translocated while encapsulated in the nanocarrier particle. It was also unclear whether the nanoparticles played a role in the uptake and translocation of the pesticide, or they depended solely on the physiochemical properties of the pesticide. This knowledge gap was addressed by tracking the uptake and translocation of the nanoparticle and pesticide simultaneously and provided important insights of the mechanisms of distribution of a nanoencapsulated pesticide in tomato plants and how it compared with the distribution of the non-encapsulated pesticide.
- 6) **First analytical quantification of Si in plant matrices without the use of hydrofluoric acid (HF).** Previous studies employing SiO₂ nanoparticles either did not quantify Si uptake in plant matrices or utilized HF as part of the process to dissolve SiO₂ before the measurements. The HF-protocol, however, is highly hazardous because it involves the handling of HF, an extremely toxic and corrosive chemical, which requires specialized laboratories and training for handling. Here, a modified version of a protocol without the use of HF described in the literature was implemented and was able to quantify Si translocation in plants using Inductively Coupled Plasma Optical Emission Spectroscopy (ICP-OES).

Contribution of Authors and Publications

The main body of this thesis consists of five chapters (Chapter 2 to Chapter 6) that have been prepared in a manuscript-based format.

Chapter 2

The literature review in Chapter 2 was prepared as a *book chapter* and submitted to **Springer Nature**.

Bueno, V; Ghoshal, S. Porous Inorganic Nanoparticles as Pesticide or Nutrient Carriers. In *Inorganic Nanopesticides and Fertilizers: A View from Mechanism of Action*. Springer Nature 2021.

- Bueno, V: Conceptualization, design and writing of the original draft of the manuscript.
- Ghoshal, S: Conceptualization, design, review and editing of the manuscript, and supervision.

Chapter 3

Chapter 3 was prepared for submission as a *research article* and published in **Langmuir**.

Bueno, V; Ghoshal, S. Self-Assembled Surfactant-Templated Synthesis of Porous Hollow Silica Nanoparticles: Mechanism of Formation and Feasibility of Post-Synthesis Nanoencapsulation. *Langmuir* 2020, 36, 48, 14633–14643. <https://doi.org/10.1021/acs.langmuir.0c02501>.

- Bueno, V: Designed and conducted experiments, analysed data and wrote the original draft of the manuscript.
- Ghoshal, S: Experimental design, research supervision, discussion of experimental results, revision of manuscript.

Chapter 4

Chapter 4 was prepared for submission as a *research article* and published in **Journal of Colloid and Interface Science**.

Bueno, V; Bosi, A; Tosco, T; Ghoshal, S. Mobility of Solid and Porous Hollow SiO₂ Nanoparticles in Saturated Porous Media: Impacts of Surface and Particle Structure. *Journal of Colloid and Interface Science* 2022, 606, 480–490. <https://doi.org/10.1016/j.jcis.2021.07.142>.

- Bueno, V: Designed and conducted experiments, analysed data and wrote the original draft of the manuscript.
- Bosi, A: Designed and conducted the preliminary experiments, performed the modeling, and revised the manuscript.
- Tosco, T: Discussion of experimental results and revision of manuscript.
- Ghoshal, S: Experimental design, research supervision, discussion of experimental results, revision of manuscript.

Chapter 5

Chapter 5 was prepared as a *research article* and submitted to **Environmental Science: Nano**.

Bueno, V; Wang, P; Harrison, O; Bayen, S; Ghoshal, S. Impacts of Porous Silica-Nanoencapsulated Pesticide Applied on Soils on Plant Growth and Soil Microbial Community. *Environmental Science: Nano* 2021.

- Bueno, V: Designed and conducted experiments, analysed data and wrote the original draft of the manuscript.
- Wang, P: Performed the quantification of azoxystrobin in the LC-MS and revised the manuscript.
- Harrison, O: Performed the qPCR and revised the manuscript.

- Bayen, S: Experimental design, research supervision, discussion of experimental results, revision of manuscript.

- Ghoshal, S: Experimental design, research supervision, discussion of experimental results, revision of manuscript.

Chapter 6

Chapter 6 was prepared as a *research article* and submitted to **Environmental Science and Technology**.

Bueno, V; Gao, X; Rahim, A. A; Wang, P; Bayen, S; Ghoshal, S. Uptake and Translocation of a Silica Nanocarrier and an Encapsulated Organic Pesticide Following Foliar Application in Tomato Plants. *Environmental Science and Technology* 2021.

- Bueno, V: Designed and conducted experiments, analysed data and wrote the original draft of the manuscript.

- Gao, X: Provided help to maintain the hydroponic system, performed the measurements in ICP-OES and revised the manuscript.

- Rahim, A. A: Performed the measurements in spICP-MS and revised the manuscript.

- Wang, P: Performed the quantification of azoxystrobin in the LC-MS and revised the manuscript.

- Bayen, S: Experimental design, research supervision, discussion of experimental results, revision of manuscript.

- Ghoshal, S: Experimental design, research supervision, discussion of experimental results, revision of manuscript.

Abbreviations

AI	Active ingredient
Azo	Azoxystrobin
Azo@PHSN	Azoxystrobin encapsulated in hollow porous silica nanoparticle
BET	Brenauer-Emmet-Teller
BTC	Breakthrough curve
BJH	Barrett-Jyner-Halenda
CMC	Carboxymethyl cellulose
CP	Cross-polarization
CTAB	Cetyltrimethylammonium bromide
DI	Deionized
DLS	Dynamic light scattering
DLVO	Derjaguin-Landau-Verwey-Overbeek
EDX	Energy-dispersive X-ray
EPA	The United States Environmental Protection Agency
FTIR	Fourier-transform infrared spectroscopy
GFP	Green fluorescent protein
HAP	Hydroxyapatite
HETCOR	Heteronuclear correlation
HPLC	High-performance liquid chromatography
ICP-OES	Inductively coupled plasma optical emission spectrometry
IRP	Iron-Regulated Transporters

IS	Ionic strength
ITS	Internal transcribed spacer
LC	Liquid chromatograph
MSN	Mesoporous silica nanoparticles
nCuO	Copper oxide nanoparticle
nHAP	Hydroxyapatite nanoparticle
MA	Mugineic acid
MAS	Magic angle spinning
NP	Nanoparticle
NZVI	Nano zerovalent iron
Pcal-PHSN	Pre-calcined porous hollow silica nanoparticles
PCoA	Principal Coordinate Analysis
PdI	Polydispersity index
PHSN	Porous hollow silica nanoparticles
PTFE	Polytetrafluoroethylene
PV	Pore volume
QD	Quantum dot
qPCR	Quantitative Polymerase Chain Reaction
QToF-MS	Quadrupole time-of-flight mass spectrometer
QuEChERS	Quick, easy, cheap, effective, rugged, and safe
rRNA	Ribosomal RNA
SEL	Size exclusion limit

spICP-MS	Single particle mode inductively coupled plasma mass spectrometry
SR	Surface roughness
SSN	Solid silica nanoparticle
SS-NMR	Solid-state nuclear magnetic resonance
TEM	Transmission electron microscopy
TEOS	Tetraethyl orthosilicate
UV	Ultraviolet
UV-vis	Ultraviolet-visible
YSL	Yellow Stripe-Like
ZIP	Zinc- and Iron-Regulated Transporter-Like Proteins
1-D	One-dimensional
2-D	Two-dimensional

Chapter 1. Introduction

1.1. Nano-enabled agriculture

A recent report on the global market of pesticides, published in 2017 by the United States Environmental Protection Agency (EPA), estimated that approximately 2.7 billion kilograms of pesticides are used annually.¹ This study, however, analyzed the market between 2008 and 2012, and therefore the current number may be even greater. It is estimated that only 10% reach their final destination,² i.e., 2.45 billion kilograms of unused pesticides are discharged into the environment as a result of losses during application. Hence, contaminating the soil, water bodies and affecting a range of living organisms, including humans. Several pathways contribute for these losses. Approximately, 20 to 50% of the pesticides can be lost due to emissions into the air, which are controlled by factors such as wind speed, humidity, and temperature.^{3,4} The rest is lost to runoff by leaching from soil to groundwater, and by chemical and biological degradation.⁵ Agricultural practices rely on pesticides to protect the crops against pests. Pesticides are essential to help supply the ever-growing food demand worldwide. Studies estimate that the projected world's population will reach 9.1 billion by 2050.⁶ As a result, the demand for cereals will increase from 2.1 billion tones yearly to 3 billion tones⁶ for both food and animal feed.⁷ Reducing the use of these agrochemicals would have a severe impact in the food availability around the world. For this reason, the major challenge is to maintain the efficacy of pesticides, while reducing the quantity applied. Encapsulation of pesticides in carrier media does not only protect the pesticide against degradation and volatilization but can also provide targeted controlled release.

Nanotechnology is increasingly viewed as a promising tool to increase crop productivity and reduce the environmental footprint of the agriculture industry.⁸⁻¹⁰ Interestingly, while the nano-market is still in its early stages in agriculture,¹¹ nanotechnology research in the biomedical field increased tremendously over the past few years, particularly in targeted drug delivery for cancer and autoimmune disease treatments.¹²⁻¹⁵ Some of the knowledge from biomedicine may establish the grounds to develop technologies for targeted delivery of active ingredients (AI) for agriculture, such as pesticides,¹⁶ nutrients,¹⁷ genetic material¹⁸ and growth hormones. Targeted delivery could ensure that the right amount of the AI is delivered in the specific target, thus

reducing the quantity of chemicals wasted during application. Furthermore, the nanocarriers also function as a protective barrier against premature degradation of the AI.^{19, 20}

Most of the research on nanoencapsulation of pesticides has focused on loading the AI within polymeric structures.²¹ However, their lack of thermal and chemical stability has led to the investigation of other nanomaterials such as silica. Polymeric structures can be easily degraded by enzymes in the soil or inside the plants, which may not be desirable when prolonged release is required. Moreover, the monomers generated from the structure breakdown may be toxic or acidic, thus adversely impacting plant growth.²¹ Inorganic compounds such as silica are earth-abundant, a micronutrient for plants and have low toxicity potential. Thus, silica nanoparticles are deemed to be a promising encapsulation alternative to polymeric nanoparticles.²² Concomitantly, it is important to mention that other compounds are also being studied as alternatives for nanocarrier materials, such as lipid nanoparticles, nanoemulsions, liposomes, dendrimers, carbon nanotubes, nanocomposites and wax-based nanoparticles.^{23, 24}

The overall objective of this thesis was to develop silica nanoparticle capsules for organic pesticides, such that they are effective pesticide delivery agents and lead to substantially reduced environmental impacts. This will be achieved by optimizing different methodologies to synthesize distinct nanosilica structures loaded with pesticides, particularly hollow shell particles. Then, the most promising nanoformulation, in terms of size range, polydispersity index (PDI) and colloidal stability, will be tested for their respective pesticide loading, release rates and uptake in plants. The environmental impact of nanoencapsulated pesticides and their non-encapsulated formulations will be compared through assessment of the effective mobility of pesticides in saturated porous medium, as well as the pesticide biodegradation and effects on the microbial community in soil.

1.2. Nanoencapsulation for sustainable agricultural practices

The applications of engineered nanoparticles are already mature and well-developed in the food industry where synthetic amorphous silica has been used as anti-caking agent in food processing for many years²⁵ and are deemed safe for the human health by the World Health Organization.²⁶ Also in medicine, liposomes, silicon and metal oxide nanoparticles have been used for drug

delivery, bio-sensing and cancer treatments.²⁷ Given the growing knowledge and examples of the safe use of nanomaterials, there exists considerable room for new applications and contributions in the rapidly growing agrochemical industry. A literature review carried out by Peters et al.¹¹ underscored that research on nanomaterials in the biomedicine far exceeds that in agriculture. A major challenge in agriculture is to reduce the extensive use of pesticides and fertilizers while maintaining their efficiency. In line with this rationale, nanomaterials can potentially be used for targeted and effective delivery of these agrochemicals to plants through drug delivery. One strategy is to encapsulate these agrochemicals within nanocarriers, which provides two distinct advantages: (1) the nanostructure protects the AI from chemical and biological degradation, (2) while providing slow and controlled release of the AI for extended protection against pests. Nanoencapsulation also reduces the dosage of the AI applied, hence the exposure to the environment and ultimately the exposure to humans.¹¹

A diverse range of materials have been used to fabricate nanocarriers for delivery of pesticides. Organic nanoshell structures can be synthesized using polypeptides and polysaccharides as blocs for the polymeric matrix. Alternatively, inorganic materials for nanocarriers comprise metals (silver, titanium, iron, and gold) and metalloids (silicon). Most of the research has focused on polymer-based structures.²¹ Polymer-based nanocarriers present some limitations such as limited thermal stability, limited internalization of the nanostructures in plants, potential risk for their (bio)degradation before pesticide release, and accumulation in the environment as byproducts from incomplete degradation reactions.^{21,28} Based on these limitations, inorganic porous materials have emerged as an option to encapsulate agrochemical compounds.²¹ Metal and metalloid nanomaterials are resistant to degradation and are stable over a large range of pH and ionic strength. Some inorganic compounds are often taken up as nutrients for plants, such as silica, iron, magnesium, among others, thus taking advantage of natural transportation pathways to internalize the nanoparticulate formulations. In particular, mesoporous silica nanoparticles (MSN) and porous hollow silica nanoparticles (PHSN) have structural properties and surface chemistry that facilitate surface functionalization with organic compounds and high loading rates. Furthermore, their meso-structures and pores are essential for the sustained controlled release of the AI.²⁹

The simplest method to synthesize silica nanoparticles is through the Stöber method,³⁰ which consists in utilizing tetraethyl orthosilicate (TEOS) as the silica precursor, ammonium hydroxide as the catalyst and short alkyl chain alcohols as solvent. Stöber et al.³⁰ showed it is possible to obtain solid monodispersed silica spheres with diameter ranging from 50 to 2,000 nm by varying the concentration of the reactants and the conditions of the solution (pH, temperature, ionic strength). More recent methods have synthesized structures as small as 5 nm.³¹ Several studies have suggested different modifications for the synthesis of monodisperse spherical silica. For MSN synthesis, surfactants are added to the solution to provide the basic porous structure, which are further removed by calcination or washing in order to form the pore cavities.²¹ Popat et al.²² showed that the loading rate of the pesticide imidacloprid varied amongst different structures of MSN. In this study, the loading method consisted in suspending the particles in the pesticide solution overnight; hence, the phenomenon that dictated the loading was diffusion and deposition of the pesticide within the spherical silica. The most popular MSN structures are MCM-41 (named after Mobil Corporation as Mobil Composition Matter), MCM-48, SBA-15 (named after the University of California, Santa Barbara), TUD-1, HMM-33, FSM-16 among many others. The main differences between each structure are the chemicals used for synthesis, and its physical characteristics, such as pore size, pore distribution, pore shape and surface area. Wanyika³² incorporated the fungicide metalaxyl by the same method as Popat et al.,²² with the exception that the solution was slowly evaporated using a rotary evaporator rather than centrifuged.

The hollow structure of PHSN allows a higher AI loading rate, and its synthesis follow a different approach than for MSN and solid spherical particles.³³ Generally, the silica shell is grown around a solid spherical template that is further removed by calcination or chemical dissolution. Chen et al.³⁴ synthesized PHSN with the aid of CaCO₃ nano-spheres as template. The authors obtained PHSN of around 100 nm which were loaded with avermectin and validamycin pesticides by immersion method aforementioned. Using a similar approach for the synthesis, Liu et al.³⁵ loaded PHSN with a water-soluble pesticide using supercritical carbon dioxide and improved loading while reducing the adsorption saturation period. Sasidharan et al.³⁶ showed adsorption of ibuprofen in PHSN improved with the functionalization of the silica particles with 3-aminopropyl. The greatest potential for nanoencapsulation, however, relies on the synthesis on nanoemulsion templates. Qian et al.³⁷ solubilized the fungicide tebuconazole within an organic non-aqueous

liquid phase, which was further suspended in aqueous solution resulting in a micro-emulsion. This oil-in-water emulsion served as template for the oil-core PHSN synthesis.

A number of studies have confirmed that the release of the AI can be controlled by the conditions of the medium such as pH, temperature and ionic strength. Wen et al.³⁸ showed that the release rate of avermectin increased substantially with increasing pH and temperature. Popat et al.²² demonstrated that the release rate of the same pesticide reduces dramatically after some minutes of the application. The nanoshell also provided UV protection to the photosensitive avermectin as shown in other studies.^{19, 20} Ultimately, the encapsulation of avermectin within PHSN resulted in an improved stability of the pesticide from 6 hours to 30 days.³⁹

One of the major gaps in this field is the lack of reproducibility of synthesis protocols, particularly during the pesticide encapsulation phase. Furthermore, no study so far compared the loading and release rate of chemicals within mesoporous and porous hollow silica. Although, porous silica offers a greater volume for loading, mesoporous have orders of magnitude higher surface area, which can play a role in loading and release rates if the AI sorbs on silica.

1.3. Plant uptake of engineered nanoparticles

Research into synthesizing the ideal nanostructures for encapsulating AI would be meaningless if the plant is not able to internalize the AI in the aftermath. Ideally, the goal is to have the uptake of the nanocarrier-AI system to avoid premature degradation and losses of the active material. When plants are transplanted to media spiked with metallic nanoparticles, it is possible to measure an increase in the respective metal concentration inside the plants. One phenomenon to explain the uptake of these metals from nanoparticles is through its dissolution and further uptake of ions⁴⁰. However, plants can also take up metal nanoparticles directly. This is derived from the following observation: when plants are exposed to metal nanoparticles, the total concentration of the respective metal inside the plant does not match the amount of dissolved metal generated from the nanoparticles alone,⁴¹ and thus another source of this metal is required. In conclusion, the plant is likely able to internalize whole nanoparticles as well. Moreover, Yang et al.⁴² showed that the concentration of cerium inside *Arabidopsis* was greater when exposed to CeO₂ nanoparticles (NPs) than when it was exposed to the same concentration of bulk CeO₂. Wang et al.⁴³ demonstrated that

silver nanoparticles of sizes varying from 30 nm to 120 nm were directly internalized by wheat and cucumber in their intact form, without any substantial modification. This is rather surprising because the plant root size exclusion limits (SEL) are smaller than 20 nm, suggesting there must exist a mechanism to uptake whole nanoparticles. Coincidentally, here lies a major knowledge gap in the field, the uptake mechanism of whole nanoparticles into plants is still unclear.⁴¹

Mazumdar and Ahmed⁴⁴ showed that nanosilver taken up by the root was later found in the aerial parts including stem and leaves. Although this transport is probably regulated by the xylem, little is known on how such relatively large and dense particles move upward from the roots to aerial parts.⁴⁵ Keller et al.⁴⁶ demonstrated what few studies before have: the uptake of nanoparticles by edible plants. Lettuce, kale, and collard were exposed to nano-copper (nCuO). Although most of the nCuO were washed away, a small fraction of nCuO were identified within the plants' tissue through Single Particle Inductively Coupled Plasma Mass Spectrometry techniques. Furthermore, Roche et al.,⁴⁷ simultaneously exposed imidacloprid, silver and CeO₂ in bulk and in nanoparticle form to zucchini plants. Although the phytotoxicity remained unaltered in all cases, the uptake of imidacloprid decreased when the drug was co-exposed to the Ag and Ce, both as NP and bulk forms. In its turn, bioaccumulation of Ag and Ce in aerial parts of the plant decreased 80% when exposed to NPs compared to when exposed to the bulk elements. In conclusion, the uptake of the drug follows the following order: free drug > drug-bulk Ag and Ce > drug-NP Ag and Ce, and the uptake of Ag and Ce was higher when exposed to the bulk material rather than the NPs. Differences in DNA suppression and toxicity between NP and bulk elements were not representative. Nevertheless, it is important to understand why the uptake of Ce and Ag decreased so steeply when the elements were co-exposed with pesticides. A recent study⁴⁸ showed that titanium and iron nanoparticles were deployed to suppress viral infection in tobacco. Both elements accumulated in chloroplasts and increased production of phytohormones by 40%, which stimulated the plant growth and boosted defense mechanisms. Sun et al.⁴⁹ evaluated the internalization of MSN marked with fluorescent proteins inside lupin, wheat, and maize plants. The authors observed that nanosilica spheres with diameter as small as 20 nm were internalized by all three species of plants through the roots and transported to their stems and leaves. Nanoparticles distribution in the tissues were identified by transmission electron microscopy, and confocal microscopy techniques were used to quantify the amount of NP in these tissues by

evaluating the intensity of the fluorescence. Rui et al.⁵⁰ assessed the uptake, transport, distribution, and toxicity of different concentrations of nanosilica in cotton. They observed that nanosilica uptake in cotton had significant positive effects on the root and shoot biomass size as well as in the height of the plants. Moreover, the increase in the concentration of Si NPs led to increased uptake of other micronutrients such as iron, manganese, potassium, zinc, magnesium, and copper. TEM images confirmed the existence of intact Si NPs in the roots, xylem, and shoots, suggesting that the transport of such nanoparticles occur through the plant vascular systems, the xylem and possibly phloem. Pyrimethanil-loaded MSN ranging from 200 and 300 nm was also observed to be assimilated in various compartments of the plant.

The capacity of plants to assimilate nanoencapsulated pesticides is critical to their efficacy. However, limited research has been conducted about the extent to which plants can assimilate nanostructures, in terms of size, mass, as well as the mobility of more complex nanostructures (such as nanopesticides) within the plant vascular system. There are also knowledge gaps on how the size, surface charge and surface composition influence the uptake of the nanoparticles, and what the effects of functionalizing the surface with bioactive compounds are.

1.4. Environmental fate of nanoencapsulated pesticides

A handful of studies have briefly characterized nano-enabled agrochemicals in terms of their efficiency in hindering pest proliferation while promoting plant growth.⁵¹⁻⁵³ Nonetheless, one of the major gaps in these studies was not comparing the environmental fate of AIs in nano-formulations with conventional, non-encapsulated AI. Environmental fate is a very general term, but four direct measurements can give a better picture in how these nanopesticides behave in the ecosystem. They include the rate to which these materials sorb to soil, the rate to which these materials are degraded in soil, the photolysis kinetics, and the efficacy (pest inhibition rates). Studies on nanopesticides tend to analyze the nanocarrier synthesis, AI loading, AI release and formulation efficacy solely, leaving the environmental fate analysis unaddressed. The lack of information concerning the plant uptake of these nanopesticides and their subsequent effect in the ecosystem hinders the commercial deployment of the technology, because policy makers have no basis to decide whether these particles pose a risk to the ecosystem and to the human health. One

of the major gaps in this area is the lack of understanding on how nanoparticles affect the microbial community, which co-exist in symbiosis with the plants being exposed to such chemicals.

Ideally, the AI-nanocarrier formulations should demonstrate a great potential to improve efficiency of the AI while reducing the environmental impacts resulted from its application. The efficiency of pesticides, for instance, is determined by assessing the rate of mortality and specificity towards the pest that threatens the crops. It is also important to demonstrate prolonged pest inhibition and decrease in the pesticide concentration applied. A number of studies identified that certain nanostructures are able to sustain prolonged and controlled AI release for days^{19,54} and improved mortality compared to conventional pesticide formulations.⁵⁵ According to Kah et al.,⁵⁶ nanopesticides are in average twice as effective to the target organisms when compared to the conventional pesticide formulation. These studies, however, tend to be limited to assessments of mortality and whether the AI release rates are more efficient in the nanoform, whereas experiments assessing the environmental fate of the nanoformulations are not addressed.

Encapsulating the AI will likely change the way it behaves in the environment. Desirable environmental fate behavior of nanoencapsulants will protect the AI against premature degradation, improve its mobility in soil and ensure to reach its predetermined destination without leaching into areas beyond the target and water bodies. The transport of colloids (nanoencapsulants) is influenced by its physicochemical properties such as size, surface charge and composition^{57,58} as well as soil properties, groundwater flow and chemistry.⁵⁹ AI transport on the other hand is a function of the charge and hydrophobicity of the molecule, which will have different interactions with soil surfaces and groundwater constituents.^{60,61} Transport of colloids are largely dependent on deposition/attachment to soil particle surfaces whereas the transport of the non-encapsulated AI is regulated by sorption of the AI to soils – and thus their transport will be fundamentally different. Firdaus et al.⁶² demonstrated that nanoencapsulated bifenthrin, when compared to its conventional formulation, decreased the sorption rate to soil, increased the persistence of the pesticide after the application, and altered the uptake and distribution of bifenthrin in earthworms. Hence, it is urgently recommended that new research on this field include a comprehensive study comparing the mortality, concentration efficiency, prolonged release and environmental fate of nano-enabled products and their respective conventional

formulation. It is important to understand that encapsulation, on one hand, renders the AI protection against premature degradation, reduces losses during application and, in some cases, facilitates the mobility in complex media. On the other hand, the same protection envisaged during the application can result in rendering the AI more persistent and recalcitrant than the conventional formulation in the aftermath. After the crops have grown and been harvested, the residual nanoparticle-AI conjugate that remains in the soil become a liability/contaminant if it cannot be recovered. When this happens, the so-desired protective properties become an issue because the natural degradation of the AI is hindered. Understanding how the fate differs between non-encapsulated and nanoencapsulated pesticide is fundamental to guarantee the safe deployment of this technology in large scale.

Another major knowledge gap in this area is the lack of field work studies. Kah et al.⁵⁶ published a critical literature review stressing that no single field study comparing nano-enabled agrochemicals and their respective commercial formulation has been developed. Field studies are of extreme importance especially after the work of Graham et al.⁶³ demonstrated that the efficiency of nanopesticides in the field were different from the results obtained in laboratory experiments. Moreover, Takeshita et al.⁶⁴ reported that nanoencapsulated atrazine had greater and higher leaf uptake than the conventional formulation, and as well, positive impacts of the nanoformulation in the field was greater than that in greenhouse conditions. In summary, having a better understanding on how the nanopesticides differentiate from the non-encapsulated formulation in terms of their behavior and fate in the environment are necessary to estimate the risks they impose to human health and the ecosystem.

1.5. Impacts of nanoencapsulated pesticide on the microbial community

If nanopesticides are to be deployed in agricultural practices, this may involve intentional (application to soil) or unintentional (runoff from foliar application) introduction of engineered nanostructures to agricultural soils. These engineered nanoparticles will thus interact with the soil microbes, including rhizosphere microbes, which are involved in very significant elemental cycling processes. A very important example of plant-microbe symbiosis is the pathway for nitrogen fixation in plants.⁶⁵ If the population of nitrogen-fixing bacteria abruptly shifts, it will directly affect the health of the plant. For instance, if a nanomaterial is toxic towards this

population of microbes, less symbiotic interaction will take place, diminishing the quantity of ammonia available for the plant. On the other hand, if the nanomaterial promotes the growth of these bacteria, there might be enhanced plant growth and other negative environmental consequences such as increased carbon dioxide, methane, and nitrous oxide, which are known greenhouse gases contributing to global warming.

Advancements in genetics, DNA amplification through PCR and high throughput sequencing techniques allow identifying a great number of microorganisms that was once constrained by cultivation limitations. Most recently, utilizing amplified gene markers, 16S ribosomal RNA for instance, has been the preferred technique to evaluate microbial community phylogenetic diversity.^{66, 67} Muturi et al.⁶⁸ assessed the effects of pesticides in aquatic microbial communities by evaluating how the community shifted before and after the pesticide applications. The study demonstrated that pesticides reduce the diversity of the microbial population and induces shifts in the taxonomic characteristics of the aquatic environment. For example, they observed that some bacteria taxa benefited from the pesticide exposure, using the chemical as carbon and nitrogen source, whereas others were completely eradicated after the exposure. Furthermore, the new classes of pesticides are synthetic and in most cases not easily biodegradable⁶⁹. Thus, these agrochemicals persist in the environment after application and end up leaching to groundwater reservoirs or even more remote locations. Thus, endangering the indigenous organisms of that region.

A major question to be explored is how the microbial diversity will be impacted by the presence of nanocarriers. Some heavy metals, such as zinc, are often necessary for adequate enzyme activity, as they play an important role in the enzyme structure, catalytic properties, and thus, in the microorganism metabolism.⁷⁰ Nonetheless, in high concentrations, these metals can be toxic. Asadishad et al.⁷¹ observed shifts in microbial community and impairment in certain enzymes' activity. Such enzymes could potentially be associated with nitrogen and phosphorous cycling – or simply put, the health of the soil. On the same line, Wu et al.⁷² assessed the toxicity of zinc towards the soil microbiota as nanoparticle as well as its ionic form. The results revealed that the impacts of zinc in the nitrification rate are not only associated with the ionic species – dissociated from the NP – but the NP itself also caused disruption in the N-cycling and triggered

the death of certain taxonomic units. Among SiO₂, Al₂O₃, CeO₂ and TiO₂, silica impacted anaerobic ammonium oxidation the most, which are associated to N-cycling.⁷³ Whether the nanocarriers will cause a shift in the microbial community needs to be determined. Any disturbance in the soil media – in this case the addition of a foreign compound (the AI-nanocarrier conjugate) – can trigger changes in the community. The focus should be in whether these alterations are causing any representative impact in terms of soil fertility, nutrients cycling and crops yield.

In terms of degradation and environmental fate of these pesticides, azoxystrobin have its own trends. Azoxystrobin is a synthetic broad-spectrum fungicide and accounted for more than 415 million dollars within the first four years of sale.⁷⁴ Adetutu et al.⁷⁵ studied the impact of azoxystrobin in soil microbial community in both dark and light conditioned microcosms. Less than 1% of the compound mineralized and over 60% was degraded within 21 days of incubation. The genomic analysis comprised the sequencing of 16S and 18S rRNA up to 84 days of incubation. The results revealed that for microcosms exposed to light, fungal diversity increased, but for microcosms without light, fungal diversity decreased, while bacterial diversity remained unaltered in both scenarios.

1.6. Knowledge gaps

Based on the literature review in this chapter and the scope of this thesis, the knowledge gaps that must be prioritized to assess the feasibility of deploying nano-enabled agriculture are summarized below:

- 1) Lack of reproducible and uncomplicated protocols to synthesize porous hollow nanocarriers capable of carrying a high-density load of AI in a restricted space. Current methodologies are based on hard templating, where surface modifications must be performed on hard templates to allow the anchorage and growth of the porous nanoshell, and on soft templating, where the use of surfactants and an oil phase as the swelling agents are necessary. In both cases, surface functionalization for hard templates or in the water-oil interface of nano-emulsions increases the degree of complexity of the synthesis.

- 2) Lack of evidence of the encapsulation of AI within porous nanocarriers. Based on the publications in the literature, authors claimed that slow, controlled release of the AI is proof of encapsulation, while no imaging is available. Because porous nanocarriers possess enhanced surface area, instead of encapsulation, AIs could be depositing onto the nanocarrier outer surface.
- 3) Lack of data to understand whether structure properties, such as particle architecture and surface characteristics, play a role in the transport profile of nanoparticles through saturated porous media. This is the initial steps towards understanding the fate of nanoparticles in more complex matrices such as unsaturated agricultural soil.
- 4) Little is known about the impacts of nanoformulations on plant and soil health. It is unclear whether the nanoparticles alone may have malign effects on the plant development and soil microbial community, or the nanoencapsulated pesticides will behave differently from their non-encapsulated counterparts. It is important to assess whether the potential benefits of deploying nanotechnology in agriculture will outweigh the shortcomings, that is, creating a new emerging contaminant.
- 5) Lack of data in understanding the uptake and translocation of nanoparticles and nanoencapsulated pesticides in plants, particularly when their diameter surpasses the size exclusion limits reported in the literature. Furthermore, more sophisticated methodologies are necessary to efficiently quantify nanoparticles extracted from plant matrix.

1.7. Research objectives

The overall objective of this work was to develop SiO₂-based nanocarrier capable of encapsulating pesticide and further delivering it to plants as well as to compare the environmental fate of the pesticides in soil when they are applied in the encapsulated and non-encapsulated forms. The pesticide selected for the entirety of the work was azoxystrobin because it is the top-selling broad-spectrum fungicide (1.2 billion dollar market in 2014) extensively used in agricultural settings.⁷⁶

The specific objectives of this thesis were:

- 1) Synthesize of hollow porous SiO₂ NPs through soft-template methods, that is, using surfactants to create the template for the pores and hollow cavity in the SiO₂ nanoshell.

- 2) Understand the formation mechanisms dictating the surfactant self-assembly followed by the SiO₂ precursor anchorage in the surfactant template and growth of the SiO₂ shell using Fourier-transform infrared spectroscopy and solid-state nuclear magnetic resonance techniques.
- 3) Demonstrate proof of encapsulation of ions and organic molecules (azoxystrobin) within the SiO₂ NPs and further quantifying the loading and release rates of the latter.
- 4) Investigate the impacts of particle surface architecture on the transport profile of two different SiO₂ NPs.
- 5) Investigate the impacts of nanoencapsulated azoxystrobin in the plant growth and soil microbial community and how these compare with the non-encapsulated formulations.
- 6) Investigate the uptake of nanoencapsulated azoxystrobin and this compare with non-encapsulated formulations.

1.8. Thesis organization

- **Chapter 1** introduces the thesis scope, objectives and structure.
- **Chapter 2** provides a detailed literature review on the research topics explored in this thesis, including the discussion of promising nanomaterials and their potential to be explored in nano-enabled agriculture, the impact of size and surface properties for efficient uptake in foliar and root systems, the role of surface functionalization to facilitate uptake and to target delivery, and a summary of stimuli responsive porous nanocarriers.
- **Chapter 3** presents a novel method to synthesize porous hollow SiO₂ NPs using a combination of two surfactants, cetrimonium bromide and Pluronic P123, that self-assembled forming the template for the nanoparticle's hollow porous structure. The chapter also investigates the mechanism of formation of the self-assembled surfactant structure and the further SiO₂ growth. Finally, it shows proof of the encapsulation of Fe and borohydride ions that reacted forming Fe NPs.
- **Chapter 4** investigates the effects of particle architecture and particle surface properties on the transport profiles through saturated porous medium. Solid spherical SiO₂ and porous hollow SiO₂ NPs were studied in this study and acid-washed white sand was the model saturated porous medium.

- **Chapter 5** investigates the impacts of SiO₂-nanoencapsulated azoxystrobin on plant growth and soil microbial community and how these compare with the non-encapsulated formulation. The impacts on plant growth were evaluated by observing five observable traits including plant dry biomass, root length, shoot length, number of leaves, and the length of the longest leaf. The impacts on soil microbial community were evaluated by extracting genomic DNA from soil, sequencing them targeting three genes, 16S rRNA, 18S rRNA and ITS rRNA, processing and analyzing the sequences based on relative abundance, absolute abundance, α diversity, and β diversity for bacteria, archaea and fungi communities.
- **Chapter 6** investigates the uptake profiles of SiO₂-nanoencapsulated azoxystrobin following foliar application and how these compare with the non-encapsulated formulation. In this chapter, SiO₂ NPs were extracted and quantified from plant matrix using a non-hydrofluoric acid method, which involves the safer handling of chemicals and will facilitate the tracking of the uptake of SiO₂ in future works.
- **Chapter 7** summarizes the major findings in this thesis, highlights the importance of the results and how they contribute to fill current knowledge gaps, and indicates the future work necessary to advance research on the field.

1.9. References

1. Atwood, D.; Paisley-Jones, C., Pesticides Industry Sales and Usage: 2008–2012 Market Estimates. *United States Environmental Protection Agency: Washington, DC, USA* **2017**.
2. Perlatti, B.; de Souza Bergo, P. L.; Fernandes, J. B.; Forim, M. R., Polymeric nanoparticle-based insecticides: a controlled release purpose for agrochemicals. In *Insecticides-Development of Safer and More Effective Technologies*, InTech: 2013.
3. Van den Berg, F.; Kubiak, R.; Benjey, W.; Majewski, M.; Yates, S.; Reeves, G.; Smelt, J.; Van der Linden, A., Emission of pesticides into the air. In *Fate of Pesticides in the Atmosphere: Implications for Environmental Risk Assessment*, Springer: 1999; pp 195-218.
4. Bedos, C.; Cellier, P.; Calvet, R.; Barriuso, E., Occurrence of pesticides in the atmosphere in France. *Agronomie* **2002**, 22 (1), 35-49.

5. Mogul, M. G.; Akin, H.; Hasirci, N.; Trantolo, D. J.; Gresser, J. D.; Wise, D. L., Controlled release of biologically active agents for purposes of agricultural crop management. *Resources, Conservation and Recycling* **1996**, *16* (1-4), 289-320.
6. FAO, F., Global agriculture towards 2050. FAO Rome: 2009.
7. Alexandratos, N.; Bruinsma, J. *World agriculture towards 2030/2050: the 2012 revision*; ESA Working paper FAO, Rome: 2012.
8. Nair, R.; Varghese, S. H.; Nair, B. G.; Maekawa, T.; Yoshida, Y.; Kumar, D. S., Nanoparticulate material delivery to plants. *Plant Science* **2010**, *179* (3), 154-163.
9. Scott, N.; Chen, H., Nanoscale science and engineering for agriculture and food systems. *Industrial Biotechnology* **2013**, *9* (1), 17-18.
10. Iavicoli, I.; Leso, V.; Beezhold, D. H.; Shvedova, A. A., Nanotechnology in agriculture: Opportunities, toxicological implications, and occupational risks. *Toxicology and Applied Pharmacology* **2017**, *329*, 96-111.
11. Peters, R. J.; Bouwmeester, H.; Gottardo, S.; Amenta, V.; Arena, M.; Brandhoff, P.; Marvin, H. J.; Mech, A.; Moniz, F. B.; Pseudo, L. Q., Nanomaterials for products and application in agriculture, feed and food. *Trends in Food Science and Technology* **2016**, *54*, 155-164.
12. Karimi, M.; Sahandi Zangabad, P.; Baghaee-Ravari, S.; Ghazadeh, M.; Mirshekari, H.; Hamblin, M. R., Smart nanostructures for cargo delivery: uncaging and activating by light. *Journal of the American Chemical Society* **2017**, *139* (13), 4584-4610.
13. Song, Y.; Li, Y.; Xu, Q.; Liu, Z., Mesoporous silica nanoparticles for stimuli-responsive controlled drug delivery: advances, challenges, and outlook. *International Journal of Nanomedicine* **2017**, *12*, 87.
14. Peer, D.; Karp, J. M.; Hong, S.; Farokhzad, O. C.; Margalit, R.; Langer, R., Nanocarriers as an emerging platform for cancer therapy. *Nature Nanotechnology* **2007**, *2* (12), 751.

15. Fontana, F.; Figueiredo, P.; Bauleth-Ramos, T.; Correia, A.; Santos, H. A., Immunostimulation and Immunosuppression: Nanotechnology on the Brink. *Small Methods* **2018**, 2 (5), 1700347.
16. Zhao, P.; Cao, L.; Ma, D.; Zhou, Z.; Huang, Q.; Pan, C., Synthesis of pyrimethanil-loaded mesoporous silica nanoparticles and its distribution and dissipation in cucumber plants. *Molecules* **2017**, 22 (5), 817.
17. Karny, A.; Zinger, A.; Kajal, A.; Shainsky-Roitman, J.; Schroeder, A., Therapeutic nanoparticles penetrate leaves and deliver nutrients to agricultural crops. *Scientific Reports* **2018**, 8 (1), 7589.
18. Kashyap, P. L.; Xiang, X.; Heiden, P., Chitosan nanoparticle based delivery systems for sustainable agriculture. *International Journal of Biological Macromolecules* **2015**, 77, 36-51.
19. Li, Z.-Z.; Xu, S.-A.; Wen, L.-X.; Liu, F.; Liu, A.-Q.; Wang, Q.; Sun, H.-Y.; Yu, W.; Chen, J.-F., Controlled release of avermectin from porous hollow silica nanoparticles: Influence of shell thickness on loading efficiency, UV-shielding property and release. *Journal of Controlled Release* **2006**, 111 (1), 81-88.
20. Li, Z. Z.; Chen, J. F.; Liu, F.; Liu, A. Q.; Wang, Q.; Sun, H. Y.; Wen, L. X., Study of UV-shielding properties of novel porous hollow silica nanoparticle carriers for avermectin. *Pest Management Science* **2007**, 63 (3), 241-246.
21. Nuruzzaman, M.; Rahman, M. M.; Liu, Y.; Naidu, R., Nanoencapsulation, nano-guard for pesticides: a new window for safe application. *Journal of Agricultural and Food Chemistry* **2016**, 64 (7), 1447-1483.
22. Popat, A.; Liu, J.; Hu, Q.; Kennedy, M.; Peters, B.; Lu, G. Q. M.; Qiao, S. Z., Adsorption and release of biocides with mesoporous silica nanoparticles. *Nanoscale* **2012**, 4 (3), 970-975.
23. ud Din, F.; Aman, W.; Ullah, I.; Qureshi, O. S.; Mustapha, O.; Shafique, S.; Zeb, A., Effective use of nanocarriers as drug delivery systems for the treatment of selected tumors. *International Journal of Nanomedicine* **2017**, 12, 7291.

24. Arias, M. A.; Loxley, A.; Eatmon, C.; Van Roey, G.; Fairhurst, D.; Mitchnick, M.; Dash, P.; Cole, T.; Wegmann, F.; Sattentau, Q., Carnauba wax nanoparticles enhance strong systemic and mucosal cellular and humoral immune responses to HIV-gp140 antigen. *Vaccine* **2011**, *29* (6), 1258-1269.
25. Peters, R.; Kramer, E.; Oomen, A. G.; Herrera Rivera, Z. E.; Oegema, G.; Tromp, P. C.; Fokkink, R.; Rietveld, A.; Marvin, H. J.; Weigel, S., Presence of nano-sized silica during in vitro digestion of foods containing silica as a food additive. *ACS Nano* **2012**, *6* (3), 2441-2451.
26. Athanassiou, C.; Kavallieratos, N.; Benelli, G.; Losic, D.; Rani, P. U.; Desneux, N., Nanoparticles for pest control: current status and future perspectives. *Journal of Pest Science* **2018**, 1-15.
27. Gulati, S.; Sachdeva, M.; Bhasin, K. In *Emerging applications of nanoparticles: Biomedical and environmental*, AIP Conference Proceedings, AIP Publishing: 2018; p 030213.
28. Wen, J.; Kim, G. J.; Leong, K. W., Poly (d, llactide-co-ethyl ethylene phosphate) s as new drug carriers. *Journal of Controlled Release* **2003**, *92* (1-2), 39-48.
29. Tang, F.; Li, L.; Chen, D., Mesoporous silica nanoparticles: synthesis, biocompatibility and drug delivery. *Advanced Materials* **2012**, *24* (12), 1504-1534.
30. Stöber, W.; Fink, A.; Bohn, E., Controlled growth of monodisperse silica spheres in the micron size range. *Journal of Colloid and Interface Science* **1968**, *26* (1), 62-69.
31. Feifel, S. C.; Lisdat, F., Silica nanoparticles for the layer-by-layer assembly of fully electro-active cytochrome c multilayers. *Journal of Nanobiotechnology* **2011**, *9* (1), 59.
32. Wanyika, H., Sustained release of fungicide metalaxyl by mesoporous silica nanospheres. In *Nanotechnology for Sustainable Development*, Springer: 2013; pp 321-329.
33. He, D.; Wang, S.; Lei, L.; Hou, Z.; Shang, P.; He, X.; Nie, H., Core-shell particles for controllable release of drug. *Chemical Engineering Science* **2015**, *125*, 108-120.

34. Chen, J.-F.; Wang, J.-X.; Liu, R.-J.; Shao, L.; Wen, L.-X., Synthesis of porous silica structures with hollow interiors by templating nanosized calcium carbonate. *Inorganic Chemistry Communications* **2004**, *7* (3), 447-449.
35. Liu, F.; Wen, L.-X.; Li, Z.-Z.; Yu, W.; Sun, H.-Y.; Chen, J.-F., Porous hollow silica nanoparticles as controlled delivery system for water-soluble pesticide. *Materials Research Bulletin* **2006**, *41* (12), 2268-2275.
36. Sasidharan, M.; Zenibana, H.; Nandi, M.; Bhaumik, A.; Nakashima, K., Synthesis of mesoporous hollow silica nanospheres using polymeric micelles as template and their application as a drug-delivery carrier. *Dalton Transactions* **2013**, *42* (37), 13381-13389.
37. Qian, K.; Shi, T.; He, S.; Luo, L.; Cao, Y., Release kinetics of tebuconazole from porous hollow silica nanospheres prepared by miniemulsion method. *Microporous and Mesoporous Materials* **2013**, *169*, 1-6.
38. Wen, L. X.; Li, Z. Z.; Zou, H. K.; Liu, A. Q.; Chen, J. F., Controlled release of avermectin from porous hollow silica nanoparticles. *Pest Management Science* **2005**, *61* (6), 583-590.
39. Auffan, M.; Rose, J.; Bottero, J.-Y.; Lowry, G. V.; Jolivet, J.-P.; Wiesner, M. R., Towards a definition of inorganic nanoparticles from an environmental, health and safety perspective. *Nature Nanotechnology* **2009**, *4* (10), 634.
40. Schwabe, F.; Tanner, S.; Schulin, R.; Rotzetter, A.; Stark, W.; Von Quadt, A.; Nowack, B., Dissolved cerium contributes to uptake of Ce in the presence of differently sized CeO₂ nanoparticles by three crop plants. *Metallomics* **2015**, *7* (3), 466-477.
41. Ma, X.; Yan, J., Plant Uptake and Accumulation of Engineered Metallic Nanoparticles from Lab to Field Conditions. *Current Opinion in Environmental Science and Health* **2018**.
42. Yang, X.; Pan, H.; Wang, P.; Zhao, F.-J., Particle-specific toxicity and bioavailability of cerium oxide (CeO₂) nanoparticles to *Arabidopsis thaliana*. *Journal of Hazardous Materials* **2017**, *322*, 292-300.

43. Wang, P.; Lombi, E.; Sun, S.; Scheckel, K. G.; Malysheva, A.; McKenna, B. A.; Menzies, N. W.; Zhao, F.-J.; Kopittke, P. M., Characterizing the uptake, accumulation and toxicity of silver sulfide nanoparticles in plants. *Environmental Science: Nano* **2017**, *4* (2), 448-460.
44. Mazumdar, H.; Ahmed, G., Phytotoxicity effect of silver nanoparticles on *Oryza sativa*. *International Journal ChemTech Research* **2011**, *3* (3), 1494-1500.
45. Núñez, E. V.; de la Rosa-Álvarez, G., Environmental behavior of engineered nanomaterials in terrestrial ecosystems: Uptake, transformation and trophic transfer. *Current Opinion in Environmental Science and Health* **2018**.
46. Keller, A. A.; Huang, Y.; Nelson, J., Detection of nanoparticles in edible plant tissues exposed to nano-copper using single-particle ICP-MS. *Journal of Nanoparticle Research* **2018**, *20* (4), 101.
47. Roche, R. D. L. T.; Pagano, L.; Majumdar, S.; Eitzer, B. D.; Zuverza-Mena, N.; Ma, C.; Servin, A. D.; Marmioli, N.; Dhankher, O. P.; White, J. C., Co-exposure of imidacloprid and nanoparticle Ag or CeO₂ to *Cucurbita pepo* (zucchini): Contaminant bioaccumulation and translocation. *NanoImpact* **2018**, *11*, 136-145.
48. Hao, Y.; Yuan, W.; Ma, C.; White, J.; Zhang, Z.; Adeel, M.; Zhou, T.; Yukui, R.; Xing, B., Engineered nanomaterials suppress Turnip mosaic virus infection in tobacco (*Nicotiana benthamiana*). *Environmental Science: Nano* **2018**.
49. Sun, D.; Hussain, H. I.; Yi, Z.; Siegele, R.; Cresswell, T.; Kong, L.; Cahill, D. M., Uptake and cellular distribution, in four plant species, of fluorescently labeled mesoporous silica nanoparticles. *Plant Cell Reports* **2014**, *33* (8), 1389-1402.
50. Rui, Y.; Gui, X.; Li, X.; Liu, S.; Han, Y., Uptake, transport, distribution and bio-effects of SiO₂ nanoparticles in Bt-transgenic cotton. *Journal of Nanobiotechnology* **2014**, *12* (1), 50.
51. Kah, M.; Beulke, S.; Tiede, K.; Hofmann, T., Nanopesticides: state of knowledge, environmental fate, and exposure modeling. *Critical Reviews in Environmental Science and Technology* **2013**, *43* (16), 1823-1867.

52. Gogos, A.; Knauer, K.; Bucheli, T. D., Nanomaterials in plant protection and fertilization: current state, foreseen applications, and research priorities. *Journal of Agricultural and Food Chemistry* **2012**, *60* (39), 9781-9792.
53. Kah, M.; Hofmann, T., Nanopesticide research: current trends and future priorities. *Environment International* **2014**, *63*, 224-235.
54. Chen, J.; Wang, W.; Xu, Y.; Zhang, X., Slow-release formulation of a new biological pesticide, pyoluteorin, with mesoporous silica. *Journal of Agricultural and Food Chemistry* **2010**, *59* (1), 307-311.
55. Wibowo, D.; Zhao, C.-X.; Peters, B. C.; Middelberg, A. P., Sustained release of fipronil insecticide in vitro and in vivo from biocompatible silica nanocapsules. *Journal of Agricultural and Food Chemistry* **2014**, *62* (52), 12504-12511.
56. Kah, M.; Kookana, R. S.; Gogos, A.; Bucheli, T. D., A critical evaluation of nanopesticides and nanofertilizers against their conventional analogues. *Nature Nanotechnology* **2018**, *1*.
57. Tan, W.; Peralta-Videa, J. R.; Gardea-Torresdey, J. L., Interaction of titanium dioxide nanoparticles with soil components and plants: current knowledge and future research needs—a critical review. *Environmental Science: Nano* **2018**, *5* (2), 257-278.
58. Demangeat, E.; Pédrot, M.; Dia, A.; Bouhnik-Le-Coz, M.; Grasset, F.; Hanna, K.; Kamagate, M.; Cabello-Hurtado, F., Colloidal and chemical stabilities of iron oxide nanoparticles in aqueous solutions: the interplay of structural, chemical and environmental drivers. *Environmental Science: Nano* **2018**, *5* (4), 992-1001.
59. Reith, F.; Cornelis, G., Effect of soil properties on gold- and platinum nanoparticle mobility. *Chemical Geology* **2017**, *466*, 446-453.
60. Dollinger, J.; Schacht, V. J.; Gaus, C.; Grant, S., Effect of surfactant application practices on the vertical transport potential of hydrophobic pesticides in agrosystems. *Chemosphere* **2018**.

61. Tian, B. B.; Zhou, J. H.; Xie, F.; Guo, Q. N.; Zhang, A. P.; Wang, X. Q.; Yu, Q. Q.; Li, N.; Yang, H., Impact of surfactant and dissolved organic matter on uptake of atrazine in maize and its mobility in soil. *Journal of Soils and Sediments* **2018**, 1-10.
62. Mohd Firdaus, M. A.; Agatz, A.; Hodson, M. E.; Al-Khazrajy, O. S.; Boxall, A. B., Fate, uptake, and distribution of nanoencapsulated pesticides in soil–earthworm systems and implications for environmental risk assessment. *Environmental Toxicology and Chemistry* **2018**, 37 (5), 1420-1429.
63. Graham, J.; Johnson, E.; Myers, M.; Young, M.; Rajasekaran, P.; Das, S.; Santra, S., Potential of nano-formulated zinc oxide for control of citrus canker on grapefruit trees. *Plant disease* **2016**, 100 (12), 2442-2447.
64. Takeshita, V.; de Sousa, B. T.; Preisler, A. C.; Carvalho, L. B.; Santo Pereira, A. d. E.; Tornisielo, V. L.; Dalazen, G.; Oliveira, H. C.; Fraceto, L. F., Foliar absorption and field herbicidal studies of atrazine-loaded polymeric nanoparticles. *Journal of Hazardous Materials* **2021**, 126350.
65. Sprent, J. I.; Ardley, J.; James, E. K., Biogeography of nodulated legumes and their nitrogen-fixing symbionts. *New Phytologist* **2017**, 215 (1), 40-56.
66. Gloor, G. B.; Hummelen, R.; Macklaim, J. M.; Dickson, R. J.; Fernandes, A. D.; MacPhee, R.; Reid, G., Microbiome profiling by illumina sequencing of combinatorial sequence-tagged PCR products. *PLoS One* **2010**, 5 (10), e15406.
67. e Silva, M. C. P.; Schloter-Hai, B.; Schloter, M.; van Elsas, J. D.; Salles, J. F., Temporal dynamics of abundance and composition of nitrogen-fixing communities across agricultural soils. *PLoS One* **2013**, 8 (9), e74500.
68. Muturi, E. J.; Donthu, R. K.; Fields, C. J.; Moise, I. K.; Kim, C.-H., Effect of pesticides on microbial communities in container aquatic habitats. *Scientific Reports* **2017**, 7, 44565.
69. Doolotkeldieva, T.; Konurbaeva, M.; Bobusheva, S., Microbial communities in pesticide-contaminated soils in Kyrgyzstan and bioremediation possibilities. *Environmental Science and Pollution Research* **2017**, 1-15.

70. Wyszowska, J.; Borowik, A.; Kucharski, M. a.; Kucharski, J., Effect of cadmium, copper and zinc on plants, soil microorganisms and soil enzymes. *Journal of Elementology* **2013**, *18* (4).
71. Asadishad, B.; Chahal, S.; Akbari, A.; Cianciarelli, V.; Azodi, M.; Ghoshal, S.; Tufenkji, N., Amendment of Agricultural Soil with Metal Nanoparticles: Effects on Soil Enzyme Activity and Microbial Community Composition. *Environmental Science and Technology* **2018**, *52* (4), 1908-1918.
72. Wu, Q.; Huang, K.; Sun, H.; Ren, H.; Zhang, X.-x.; Ye, L., Comparison of the impacts of zinc ions and zinc nanoparticles on nitrifying microbial community. *Journal of Hazardous Materials* **2018**, *343*, 166-175.
73. Zhang, Z.-Z.; Cheng, Y.-F.; Bai, Y.-H.; Xu, J.-J.; Shi, Z.-J.; Shen, Y.-Y.; Jin, R.-C., Evaluating the effects of metal oxide nanoparticles (TiO₂, Al₂O₃, SiO₂ and CeO₂) on anammox process: Performance, microflora and sludge properties. *Bioresource Technology* **2018**, *266*, 11-18.
74. Bartlett, D. W.; Clough, J. M.; Godwin, J. R.; Hall, A. A.; Hamer, M.; Parr-Dobrzanski, B., The strobilurin fungicides. *Pest Management Science* **2002**, *58* (7), 649-662.
75. Adetutu, E.; Ball, A.; Osborn, A., Azoxystrobin and soil interactions: degradation and impact on soil bacterial and fungal communities. *Journal of Applied Microbiology* **2008**, *105* (6), 1777-1790.
76. Lu, T.; Zhu, Y.; Xu, J.; Ke, M.; Zhang, M.; Tan, C.; Fu, Z.; Qian, H., Evaluation of the toxic response induced by azoxystrobin in the non-target green alga *Chlorella pyrenoidosa*. *Environmental Pollution* **2018**, *234*, 379-388.

Connecting Text to Chapter 2

Chapter 1 introduced the specific literature review, knowledge gaps, thesis structure and objectives that are relevant to the scope of Chapters 3 to 6. Chapter 2, however, presents a broader review of the use of inorganic porous nanoparticles as carriers for agrochemicals, such as pesticides and fertilizers. While the scope of the research performed in this dissertation involved the use of silica nanoparticles for the encapsulation and transport of azoxystrobin (a commonly used pesticide), Chapter 2 reviews the use of different inorganic nanomaterials as promising nanocarriers in nano-enabled agriculture, including silica, hydroxyapatite, iron, zinc, copper, and clay. Some of other topics also reviewed in this chapter includes the impacts of size and surface properties for efficient uptake in foliar and roots systems, the benefits of surface functionalization to facilitate uptake and target delivery, and finally, the promising use of stimuli responsive porous nanocarriers.

Chapter 2. Literature Review: Inorganic porous nanoparticles as pesticide or nutrient carriers

2.1. Abstract

Nano-enabled agriculture has been gaining interest recently as a pathway to improve crop yield and protection while reducing fertilizer and pesticide application rates compared to traditional agricultural practices. Inorganic, porous nanoparticles can have a pivotal role in the successful deployment of nanotechnology. Inorganic porous nanoparticles can provide a structurally stable framework to encapsulate and transport active ingredients, such as pesticides and fertilizers. Herein, we provide a review of promising features that these porous nanocarriers possess that may be of interest in agriculture. For instance, porous nanocarriers can increase the apparent solubility and mobility of poorly soluble pesticides and control the release of these over time. Commonly studied inorganic nanomaterials include silica, iron oxide, zinc oxide, copper oxide, clays, and hydroxyapatites, each of which have their own attributes and characteristics that can be relevant to crop growth and protection in the field. This chapter also includes explanations of the uptake of these nanocarriers through roots and leaves, and their further translocation within the plants. The important role of particle physicochemical characteristics, e.g., zeta potential and size in uptake and translocation are reviewed along with emerging approaches for rational design of nanoparticles to provide them with stimuli-responsive characteristics that can be triggered by changes in pH, temperature, ionic strength, light, enzymes, and redox agents.

2.2. Introduction

Inorganic porous nanoparticles (NPs) are versatile, because of their wide range of mechanical and physicochemical properties. They can be chemically stable over long periods of time and are promising candidates for nanocarriers for pesticide agriculture. As a nanocarrier, they can provide the matrix to carry the active ingredient (AI), which includes a vast spectrum of organic and inorganic molecules,^{1,2} and/or they can be used as an AI itself. Several metallic NPs have been reported to have antimicrobial properties,³⁻⁵ thus can act as a nanopesticide. Furthermore, some metals are essential micronutrients to plants, such as zinc (Zn),⁶ and therefore, the respective metallic NPs can be directly used as a nanofertilizer. Inorganic NPs are in general more easily

manufactured with consistent properties when it comes to size distribution, shape, and batch-to-batch reproducibility, compared to organic NPs.⁷ Furthermore, inorganic NPs are currently easier to analytically track in plant matrices and are more chemically stable in the field with respect to temperature, photo- and biodegradation over time.^{8,9}

A wide range of inorganic porous nanomaterials have potential applications in agriculture, such as those composed of SiO₂,¹⁰ Zn,¹¹ Fe,¹² hydroxyapatite,¹³ Cu,¹⁴ and clay.¹⁵ These inorganic nanoparticles can be tailored to specific sizes,¹⁶ porosity,¹⁷ intraparticle pore sizes,¹⁸ and functionalized with molecules to manipulate surface charge or functional groups.^{19,20} Generally, surface modifications of nanocarriers are made to facilitate uptake and translocation, target the delivery and to provide controlled stimuli-responsive to the NPs.

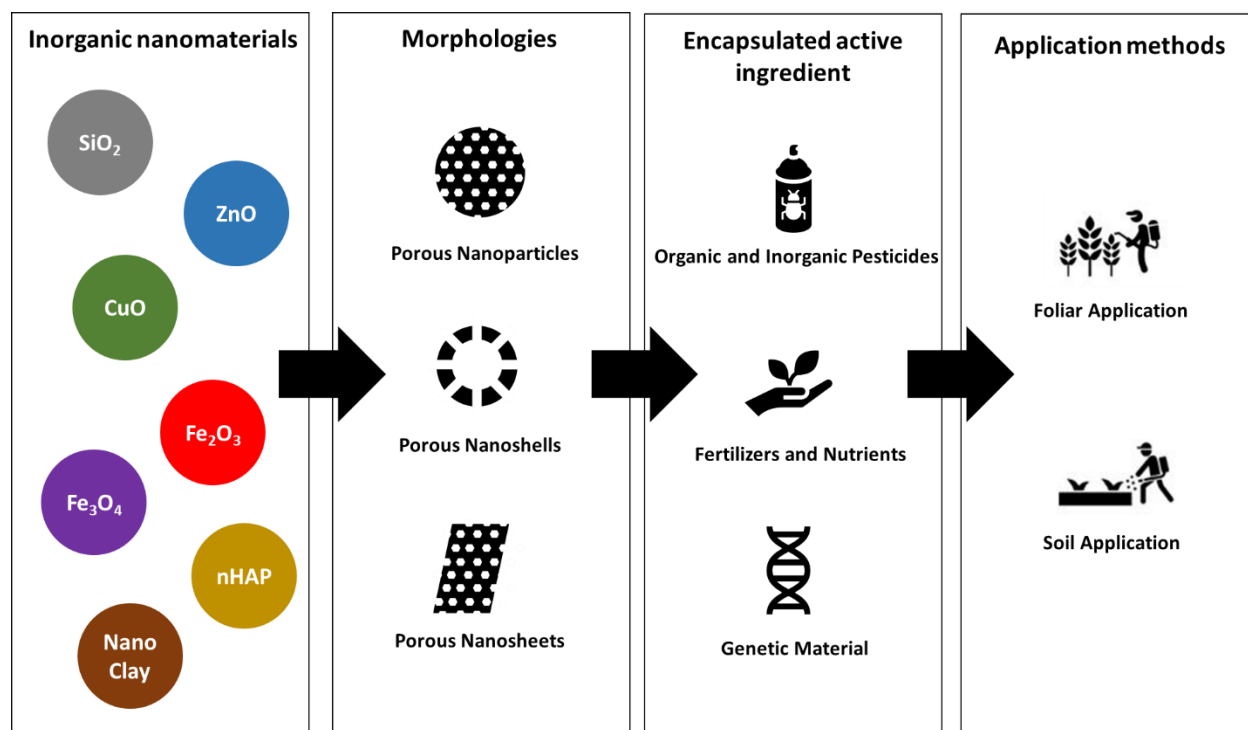


Figure 2-1. Commonly studied nanomaterials, morphologies, encapsulated active ingredients and application methods for nano-enabled agriculture.

2.3. Nanoparticles as active ingredients and carriers of active ingredients

Typically, metal oxides NPs (ZnO, Fe₂O₃, Fe₃O₄, CuO) and nHAP are themselves molecules of interest to be taken up by plants, because they are essential elements for plant development and

nutrition. Thus, these NPs are nanocarriers delivering the essential nutrients in their structural matrix, and a different AI embedded in the matrix. These NPs can be applied bare and as synthesized, without further modifications to the NP surface. This is generally the case when plants have dedicated internalization pathways for the elements delivered by the nanocarrier, e.g., Si, and thus no modifications are required to facilitate the internalization of the NPs.

2.3.1. Silica Nanoparticles

The use of silica NPs have been proposed for nano-enabled agriculture, primarily for two reasons: (1) Si is considered a *quasi*-essential nutrient for plants²¹ and the use of SiO₂ NPs as a source of Si, has been shown to result in beneficial effects on plant health.²²⁻²⁵ (2) Synthesis and functionalization of SiO₂ NPs of varied forms with a wide range of pore structures and particle characteristics are feasible. Currently, there are established procedures for synthesis of SiO₂ NPs of various structures, such as solid spherical nanoparticles,²⁶ mesoporous nanoparticles,²⁷ and porous hollow nanoparticles.²⁸ Furthermore, certain characteristics can be controlled during synthesis, including particle size distribution,^{29, 30} pore size,^{31, 32} shell thickness,³³ and even functionalization of the surfaces with bioactive molecules.³⁴ Potential applications of SiO₂ NPs in agriculture include acting as nanocarriers for pesticides and fertilizers^{35, 36} as well as the AI itself, delivering Si to plants.³⁷

Si is considered a *quasi*-essential nutrient, that is Si is not essential for plant development, but it is beneficial to plants when present.³⁸ For this reason, Si also has dedicated transport pathways for uptake in plants. Si is generally internalized as Si(OH)₄ through aquaporin-like channels.²² Foliar application of SiO₂ NPs has demonstrated to be beneficial for plant growth.^{37, 39} Porous hollow SiO₂ NPs are promising candidates to carry a wide spectrum of organic and inorganic molecules. SiO₂ NP structure is highly malleable during the synthesis, as one can tune characteristics such as the particle size, the size of the pores, the overall porosity, and the presence and size of a hollow core. The facile synthesis of different SiO₂ NP structures and biocompatibility makes them exceptional candidates as nanocarriers. Although most research have been done on solid spherical nanoparticles first synthesized by Stöber et al.,²⁶ most agricultural applications involve the use of mesoporous nanoparticles, such as the MCM-41, and porous hollow SiO₂ NPs (PHSNs). MCM-41 is a popular choice for medical and agricultural applications because of the

enhanced surface area providing the potential for the high-density loading of molecules of interest through sorption. The synthesis procedure is a modification of the Stöber method with the addition of a surfactant called cetyltrimonium bromide (CTAB), which provides a highly uniform distribution of pores etched in the SiO₂ matrix and an enhanced specific surface area that could reach over 1000 m² g⁻¹.⁴⁰ Several studies have reported having encapsulated pesticides such as prochloraz,⁴² abamectin,⁴³ and herbicides in general⁴⁴ within mesoporous SiO₂ NPs for targeted delivery. PHSNs have a more complex structure because of the presence of a hollow core within a porous SiO₂ shell. This structure can be achieved either through hard templating using materials such as polystyrene⁴⁵ or soft-templating using surfactants.^{28, 46} While hard-templating methods require the functionalization of the hard template to allow for the anchoring of the soon-to-be nanoshell and the post-synthesis removal of the template by either calcination or solvent extraction, soft-templating methods involve the use of surfactants and/or oil phase as template, which could be part of the final nanoformulation or removed through means of heating or acid wash.^{28, 47} The hollow core of PHSNs provide a cargo space for the high-density loading of biomolecules or even other nanoparticles. Bueno and Ghoshal²⁸ used the hollow core as a nanoreactor to synthesize Fe NPs within the porous SiO₂ shell through the successive addition of Fe ions and sodium borohydride. Some studies reported the encapsulation of biomolecules, such as avermectin,⁴¹ fipronil⁴⁸ and even DNA strands.⁴⁹ The PHSN shell also provides physical protection to the cargo molecules and avoid premature degradation.⁵⁰

2.3.2. Hydroxyapatite Nanoparticles

Hydroxyapatite (HAP) is one of the most commonly occurring forms of calcium phosphate in nature, with well-defined crystalline structures.¹³ Most P-based fertilizers in current use are derived from phosphoric acid, such as triple super phosphate and ammonium dihydrogen phosphate, which rapidly chelate with Al³⁺, Fe²⁺/Fe³⁺ and Ca²⁺ in soil thus becoming unavailable for plants.⁵¹ Therefore, there is increasing interest in HAP as a fertilizer because it is a highly stable, naturally occurring material, which will not chelate with earth-abundant metal ions nor precipitate as easily as phosphoric acid-based fertilizers. Moreover, it is a naturally occurring compound in the environment instead of emerging contaminants from the transformation of phosphoric acid-based fertilizers, which carry in their commercial formulation, particularly triple superphosphate, a certain amount of heavy metals, such as As, Cd, Cr, Pb, Hg, Ni and V that are

released into the environment once the phosphorous fertilizer is metabolized.^{52, 53} HAP is biocompatible, naturally porous, and can be found in bones and teeth of vertebrates, and for this reason, it has been the target of study for biomedical applications.⁵⁴⁻⁵⁶ Due to the reduced size when compared to the bulk counterpart, nanosized HAP (nHAP) can be internalized through the roots and leaves. To date, although promising, few studies used nHAP as nanofertilizer to provide P to plants. However, Szameitat et al.⁵¹ recently reported the foliar and root application of nHAP in phosphorous deficient barley restored the plant metabolism and functionalities that were previously limited due to the lack of the element. These promising results may pave the way to more research on nHAP applications in nanoenabled agriculture in the near future.

Conventional phosphorous fertilizers, consisting mostly of soluble phosphates, are estimated to have an overall efficiency of 20% because of their high mobility in soil and susceptibility to being transported with runoff.⁵⁷ In this context, nHAP can be a promising candidate to replace conventional phosphorous fertilizers due to its properties of slow but pH-dependent dissolution, and hindered mobility in soil when compared to soluble phosphates.^{57, 58} Generally, nHAP surfaces are functionalized to maintain their colloidal stability in suspension, and enhance uptake, for instance with carboxymethyl cellulose (CMC) as reported by Liu and Lau⁵⁹ and with urea as reported by Kottegoda et al.⁶⁰

2.3.3. Iron Oxide Nanoparticles

Fe is among the essential nutrients for plant health because it participates in several metabolic processes such as photosynthesis, nitrogen cycling, and biomolecules synthesis, as it is involved in the reaction mechanisms of the formation of chlorophyll, chloroplasts and cytochromes.⁶¹ The lack of Fe in plant nutrition hinders plant chlorophyll production and respiration, thus leading to chlorosis.⁶² In fact, the impacts of Fe deficiency go beyond the agriculture, as over 25% of the human population suffer from anemia,⁶³ a condition directly correlated with the insufficient amount of Fe in the blood. Some studies have reported that increasing the amount of Fe in food crops, particularly rice, has a direct positive impact on human health.^{64, 65} Current methods for Fe fertilization have very low efficiencies, because Fe rapidly complexes with organic matter and becomes biologically unavailable to plants and microorganisms.⁶⁶ The nano-sized forms of Fe minerals, however, is more stable and takes longer to release Fe ions compared to the salt-based

formulations. The synthesis of porous and hollow-porous Fe NPs can involve different synthesis mechanisms, such as sol-gel,^{67, 68} micelle-assisted,⁶⁹ co-precipitation method,^{70, 71} radiation-assisted method,^{72, 73} and hydrothermal-assisted method.^{74, 75} There are conflicting results in the agriculture about the use of Fe NPs in nano-enabled agriculture. Depending on the oxidation state of Fe and concentration of these NPs, they can lead to positive and negative impacts on the plant growth. Rui et al.⁷⁶ reported that ppm levels of Fe₂O₃ NPs had a positive impact in the production of chlorophyll and increased the Fe stock in the *Arachis hypogaea*. Nonetheless, a higher concentration of Fe₂O₃ NPs (50 mg L⁻¹) led to decreased photosynthesis activity in another study.⁷⁷ At 30 mg L⁻¹, Fe₃O₄ NPs have been reported to cause oxidative stress to ryegrass and pumpkin grown hydroponically.⁷⁸ However, in another study, at 50 mg L⁻¹, the treatment with Fe₃O₄ NPs resulted in higher chlorophyll activity and attenuated oxidative stress.⁷⁹

There are two pathways for uptake of Fe in plants, particularly rice. The first pathway is through the adsorption of insoluble Fe(III) on the roots, followed by its chelation and reduction to Fe²⁺ ions catalyzed by the ferric-chelate reductase, and lastly the transport of the ions from the cell wall to cytosol mediated by iron-regulated transporters (IRT).^{80, 81} Liu et al.⁸² recently reported that nZVI promoted the formation of an iron plate on rice root surface which resulted in further increase in biomass, chlorophyll content and grain yield up to 55%, while it simultaneously induced the removal of pentachlorophenol (PCP) from contaminated soil used for rice cultivation. The second pathway consists in excreting mugineic acid (MA) that complexes with insoluble Fe(III), forming MA-Fe(III) that are internalized to the cytosol mediated by YSL transporters.⁸³ Fe translocation from the cytosol to the other parts of the plants are then mostly mediated by protein members of the YSL family.⁸⁴

2.3.4. Zinc Oxide Nanoparticles

Zn is an essential micronutrient for plant health that plays a critical role in maintaining key metabolic activities.⁸⁵ It is also a cofactor for several metalloenzymes involved in antioxidant reactions as well as in the synthesis of biomolecules such as nucleic acids, proteins, carbohydrates, and lipids.⁸⁶ Furthermore, it participates in the control of cell proliferation, and chloroplast formation, thus being directly involved in the photosynthesis activity.⁸⁷ In terms of uptake and translocation within plants, Zn is internalized mostly by the roots in the form of Zn²⁺ or complexed

with organic chelators⁸⁸ and is distributed through the xylem by transporters known as zinc regulatory transporters.⁸⁹ Zn uptake could take place through the leaf surface or the roots. The latter is aided by dedicated protein transporters referred to as Zinc-Regulated, Iron-Regulated Transporter-Like Proteins, as known as ZIP protein family.⁹⁰ These proteins are located in the cell wall and mediate the internalization of Zn to the cell plasma and vacuoles.⁸⁹ The internalized Zn is then transferred to the xylem with the aid of another group of transport proteins called Heavy Metal ATPase, particularly HMA2 and HMA4.⁹¹ Then, from the xylem, the Zn is distributed throughout the plant. There are reports of translocation of Zn through the phloem with the aid of Yellow Stripe-Like (YSL) proteins, but the mechanism is not yet well elucidated.⁹² Foliar uptake of ZnO NPs has been reported to take place through the stomata, which then migrate to the apoplast to be dissolved into Zn²⁺.⁹³ The cations and some undissolved ZnO NPs are then transferred to mesophyll cells before they finally reach the xylem, leading to the further translocation of Zn inside the plant.⁹³ Porous Zn NPs can be synthesized by a variety of different methodologies, including microemulsion-based synthesis,⁹⁴ co-precipitation,⁹⁵ hydrothermal synthesis,⁹⁶ sol-gel,⁹⁷ and self-assembly synthesis.⁹⁸

ZnO NPs have been suggested as a fertilizer alternative to increase the availability of Zn ions to plants. In practice, both positive and negative effects have been reported followed by application of ZnO NPs to plants. Khan and Siddiqui⁹⁹ reported that ZnO NP application promoted pathogen resistant of beetroot crops against *Pectobacterium betavasculorum*, *Meloidogyne incognita* and *Rhizoctonia solani*. Semida et al.¹⁰⁰ reported that ZnO NPs promoted drought stress resistance in eggplants. Dutta et al.¹⁰¹ synthesized ZnO NPs functionalized with humic acid and citrate, which promoted smart, sustained release of Zn when photoinduced, and enhanced the growth of wheat. In contrast, other studies listed toxic effects from the application of ZnO NPs such as inhibition of root and shoot growth, cell wall damage, and chlorophyll synthesis impairment.^{85, 102, 103} In summary, the factors influencing whether the application will result in positive or negative effects were mostly nanoparticle concentration, method of application, and plant species.

2.3.5. Copper Oxide Nanoparticles

Cu is not only an essential nutrient for plant health, but also has antimicrobial properties. This allows the use of Cu-based products for both fertilization and pesticidal activity. Cu NPs have been tested to a variety of food crops leading to contrasting results depending on the dose concentration. At low doses (up to 20 mg per plant), CuO NPs have been reported to increase Cu accumulation inside the plant leading to beneficial metabolic activities, such as the oxidative stress tolerance and increased sulfur metabolization, due to the ROS generation from the internalized Cu.^{104, 105} Further increases in dosage, however, leads to increased ROS generation and damaging oxidative stress, which have been reported to impact seed germination,¹⁰⁶ promote phytotoxicity,¹⁰⁷ and inhibit photosynthesis.¹⁰⁸ The synthesis of porous Cu NPs has been systematically reported in the literature.¹⁰⁹⁻¹¹³

Both excess Cu and a deficiency in Cu can lead to an increase in the formation of ROS leading to oxidative stress that can harm the plant.¹¹⁴ Therefore, plants have developed a mechanism that closely control the level of Cu inside the cells. Cu uptake takes place mostly through the rhizosphere with the aid of Cu-specific high-affinity protein transporters, as known as the COPT family, which mediate the internalization from the external media to the cell cytoplasm and further facilitate the transfer from the root cells to the xylem.^{115, 116}

2.3.6. Clay Nanoparticles

Clays are naturally occurring minerals with varying shapes, sizes, and chemical compositions. When at least one the dimensions of these minerals are in the nano-sized range, they are generally referred to as nanoclays. These nanoclays are usually formed by stratified sheets of aluminosilicates, such as silicon tetrahedra and aluminum octahedra, stacked above one another.^{117, 118} Due to the porosity, elevated surface area, and ionic charge, nanoclays have been suggested as a promising nanocarrier for the delivery of AIs, such as fertilizers and pesticides.^{119, 120} For instance, aluminosilicate nanoclays are generally negatively charged, allowing the complexation with charged or polar organic and inorganic chemicals that are essential for plant nutrition, such as zinc,^{121, 122} copper,¹²³ ammonium,¹²⁴ nitrate,¹²⁵ urea,¹²⁶ and potassium.¹²⁷ The elevated surface area and ionic charge of nanoclays facilitates the loading of molecules of interest through sorption and ionic interactions. Some examples include diammonium phosphate (DAP),¹²⁸

Zn²⁺,¹²⁹ urea,¹³⁰ potassium phosphate,¹³¹ and potassium nitrate.¹³² The high porosity of nanoclays allow for the loading of these AI through extended surface area of the structure followed by their subsequent slow and/or controlled release, which is one of the advantages of using porous inorganic nanocarriers to deliver AI. Although most studies with nanoclays involved the loading of small molecules and ions, these nanocomposites have also been tested, at a lesser extent, to analyze the sorption efficiency of larger molecule pesticides, such as atrazine, imidacloprid and thiamethoxam, on nano-montmorillonite and its potential to be used as a delivery system for larger agrochemical molecules.¹³³ A more sophisticated application involved the topical delivery of RNA interference, loaded on layered double hydroxide clay nanosheets, to *Arabidopsis thaliana*, providing these plants with sustained protection against viruses.¹³⁴

Nanoclays, however, are not as tunable and controlled during synthesis as SiO₂ NPs. The size distribution is less uniform, and one can have population of nanoclay with different size and morphology, and thus unpredictable loading capacity. On the other hand, MCM-41 and PHSN are engineered NPs whereas most nanoclays occur naturally, reducing the energy and materials footprint of chemicals applied in the agriculture and in the environment as a whole.

2.4. Impact of size and surface properties for efficient uptake in foliar and root systems

Nanocarriers must possess very specific properties to overcome several chemical and physical barriers in plants. The NPs are primarily taken up through plant tissues in the roots and in the foliar region, particularly through cuticles, stomata, trichomes and specialized pores, such as lenticels and hydathodes.^{135, 136} To achieve significant uptake, NPs are required to have the right size and surface properties to cross cellular membranes until they successfully reach the vascular systems and translocate within the plant. The first barriers for foliar entry are the size exclusion limits (SELs) of each pore structure. The stomata are minute orifices on foliar surface to control gas exchange, with sizes ranging from 10 to 100 μm.^{137, 138} However, there is evidence that NPs can be internalized through stomatal uptake for particles up to 50 nm in diameter.¹³⁹ A second route for foliar uptake would be through the cuticles, which is a protective waxy and porous layer for the leaves and stem. There are significantly more cuticular area than stomatal areas on leaves, however, the SELs for cuticles are remarkably smaller, ranging from 0.1 to 10 nm.¹³⁵ However,

Larue et al.¹⁴⁰ estimated that NPs up to 100 nm can traverse the cuticle region under certain conditions, such as a temporary disruption of the waxy layer.

Once the NPs cross the first barrier, they must navigate across cellular membranes and organelles before reaching the vascular systems. One important route to cross from one cell to another is the apoplastic transport, which is a channel where materials can diffuse freely between adjacent cells. The apoplastic pathway is restricted by the opening of the space which can vary from 5 to 20 nm.^{137, 141, 142} The apoplast, however, can be interrupted by Casparian strips which have a SEL below 1 nm limiting the diffusion of compounds.¹⁴³ Following the apoplastic pathway, the symplastic pathway plays a crucial role in transporting low-density molecules through an interconnected network of protoplast plasmodesmata, which opening size vary from 3 to 50 nm and limit the transport of larger particles.^{144, 145}

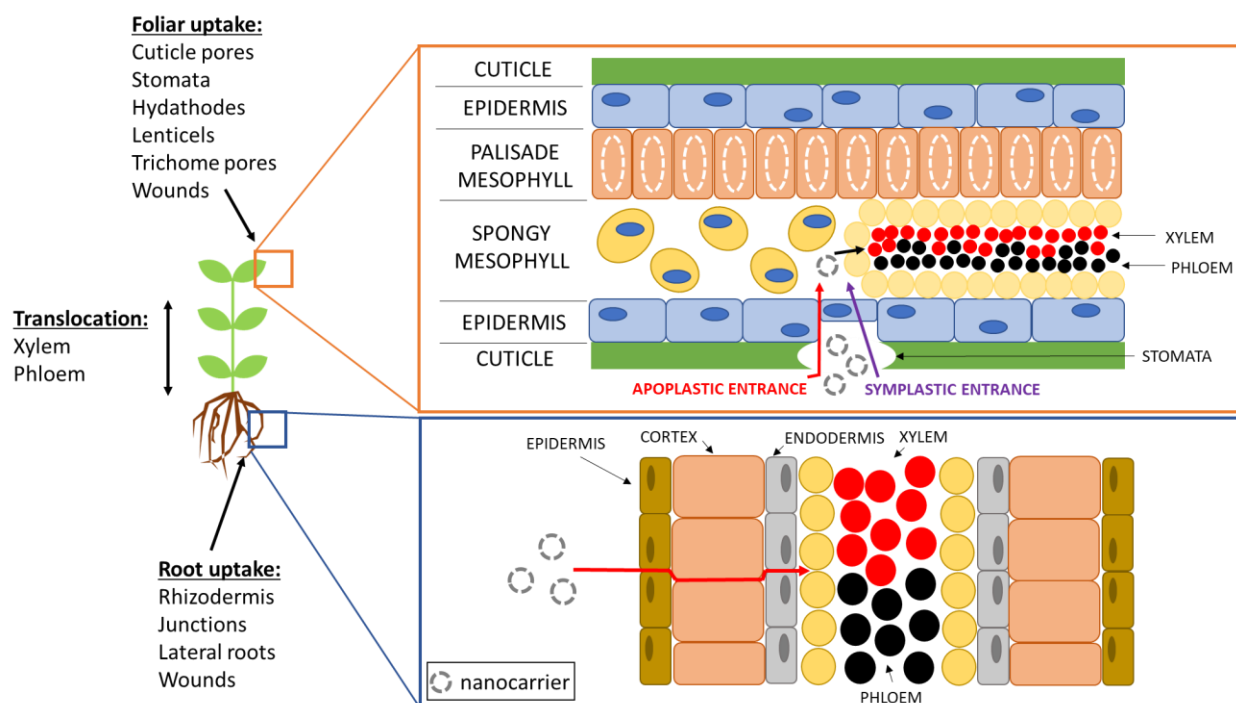


Figure 2-2. Schematic representation of possible nanocarrier pathways for uptake through the roots or the leaves followed by translocation through the vascular systems (xylem and phloem).

A priori, one would not expect uptake of NPs exceeding the upper size limit of the SELs. However, some studies reported the uptake and translocation of larger particles, such as gold NPs

of 50 nm¹³⁹ and polymeric NPs of 258 nm,¹⁴⁶ which clearly exceed the size barrier for apoplastic and Casparian strip transport. It is speculated that the SEL can be influenced by the particle's surface charge, the presence of some elements such as Ca and Si, (a)biotic stress, which can induce structural changes in these openings.^{140, 142, 147, 148}

Surface characteristics also play a crucial role in the uptake and translocation of NPs. Surface charge, for instance, can enhance adsorption to rhizodermis, facilitate the chelation process of specialized protein transporters within the cells and vascular systems that further distribute the NPs across the organism, and allow the passage of molecules through cellular ionic channels in plants. It has been reported that positively charged NPs easily attach to the commonly negatively charged rhizodermis of wheat and tomato roots,^{149, 150} whereas negatively charged particles have enhanced translocation to aerial parts.¹⁵¹⁻¹⁵³ Both positively and negatively charged NPs are more likely to be internalized when their absolute surface charge surpass 30 mV, while NPs with surface charge close to zero have difficulties in crossing the cellular lipidic bilayer.^{154, 155} Furthermore, the combination of size and surface properties may facilitate or exclude the uptake of NPs. It has been suggested that smaller-sized NPs requires a greater absolute surface charge than larger particles of comparable chemical composition and surface structure.¹⁵⁴⁻¹⁵⁶

Overall, it is known that surface charge plays a crucial role in the interaction of the NPs with different biological structures and the subsequent capability to cross the cuticular, stomatal, or rhizodermis barriers, diffuse between adjacent cells and be carried in the vascular system to distant organelles,^{154, 157} therefore it is important to produce a nanocarrier with specific size and surface properties that has the ability to enter the plant and target the delivery to the specific regions of interest.

2.5. Surface functionalization to facilitate uptake and to target delivery

Surface properties play an important role in the uptake of NPs in plants. Surface charge and charge intensity influences the ability of NP to be internalized and its further translocation.¹⁵¹⁻¹⁵⁴ Therefore, although the size is an important factor when designing nanocarriers, surface properties may dictate whether the NP will indeed be internalized and distributed to the organelles of interest. As synthesized NPs might not always fit in all the criteria and thus, surface modifications are a

popular pathway to transform bare NPs into a versatile nanocarrier. Santana et al.¹⁵⁸ functionalized quantum dots (QD) with peptide recognition motifs to target the delivery of these NPs to chloroplasts in *Arabidopsis thaliana*. In this study, the authors used specific guiding peptides on the surface of the QD to mimic chloroplast-biorecognition mechanisms and to target its delivery to the organelle. Although QD are not relevant to plant growth or protection, this approach has the potential to be used for different porous materials as peptide-functionalization has been reported in MSN.¹⁵⁹

Future applications might rely on this mechanism to target the delivery of an AI-encapsulated nanocarrier to specific organelles and tissues. Different plant compartments require specific molecules to ensure proper functioning. To obtain these molecules of interest, the cells forming the outer surfaces of these organelles and tissues developed mechanisms to selectively identify the essential biomolecules and facilitate their uptake. In the case of chloroplasts, the redox status controls the diffusion of molecules in and out of the organelle. Santana et al.¹⁵⁸ took advantage of this mechanism to introduce a chain of polypeptides capable of imitating the redox conditions specific to this organelle and thus being identified by the chloroplast-biorecognition system in the cell membrane leading to the nanocarrier internalization. Another example was the use of citrate to enhance the adhesion of Au NPs to the leaf and the α -1,5-arabinan antibody to target stomata on the leaf surfaces, thus guiding and facilitating the internalization of the NPs.¹⁶⁰ Similar rationale can be used to design nanoformulations to target other organelles and tissues. These rationally designed surface modifications are crucial to further nano-enabled agriculture applications and thus are necessary for the next-generation porous inorganic nanopesticides and nanofertilizers. Nano-enabled agriculture can also benefit from the advances in nanomedicine, where a vast spectrum of molecules have been tested to target the delivery, including antibodies, peptides, aptamers, saccharides and proteins¹⁶¹ and porous SiO₂ nanocarriers, in particular, are promising candidates because they can transport and deliver AI in plants and can be easily functionalized their surfaces.¹⁶²

Functionalization can also enhance NP stability and improve the apparent solubility of hydrophobic compounds in aqueous media. For example, reported that functionalizing nHAP with citric acid^{163, 164} and CMC⁵⁹ improved overall NP stability in suspension and thus increased P

delivery to plants. Carboxylic acid ligands have been reported to enhance the apparent solubility of carbon nanotubes in water by providing a hydrophilic surface coverage.^{165, 166} Other advantages of surface modifications include aiding the loading and release of AI in porous nanocarriers and provide different functionalities to the nanoformulation. MSN surfaces were functionalized with nontoxic trimethylammonium to enhance loading and promote the slow-release of 2,4-dichlorophenoxy acetic acid¹⁶⁷ and pyraclostrobin¹⁶⁸. Functionalizing CuO NPs with biocompatible polymers provided fungicidal properties to the nanoformulation.¹⁶⁹

More sophisticated surface modifications can use the surface ligands to trigger a reaction involving a second molecule of interest loaded within the NP. Torney et al.¹⁷⁰ loaded mesoporous SiO₂ NPs (MSN) with β -oestradiol, capped the pores with small gold NPs to prevent the cargo from leaching out, and functionalized the MSN surface with a double-stranded DNA plasmid containing a green fluorescent protein (GFP) gene. Then, immature maize embryos were bombarded with the transformed MSN to assess whether these NPs could deliver not only the genetic material but also the β -oestradiol, which is responsible to trigger the GFP gene expression. This work successfully reported that the MSN system simultaneously delivered the plasmid as well as β -oestradiol, the chemical responsible to trigger the gene expression to targeted plant cells. Porous nanocarriers are particularly ideal to carry two or more biomolecules that complement each other activities because they can be stored in different areas of the nanoparticle, for example inside the pores, hollow core or on the surface of PHSN. Ultimately, these particles can be designed in a way that the multiple molecules of interest loaded in them will only interact with one another at the destination site, usually controlled by gatekeeper molecules, which control the release of AIs after chemical or physical stimuli.

2.6. Stimuli responsive porous nanocarriers

Porous nanoparticles are not only able to carry a wide variety of organic and inorganic compounds, protect them from premature degradation, and target their delivery, but they can also provide controlled release of molecules of interest upon triggered on-demand responses. That is, the AIs are loaded into the nanocarrier pores, which are further capped with another type of compound, referred to as gatekeepers, that prevent the AI from leaching out prematurely. These gatekeepers are designed to block the AIs from leaving the pores and unwanted molecules from entering the

pores, and to enable release of the cargo when triggered by a stimulus. Triggering factors include pH change,¹⁷¹⁻¹⁷⁸ light stimulus,¹⁷⁹⁻¹⁸⁴ ionic strength,^{167, 185, 186} redox agents,¹⁸⁷⁻¹⁹¹ enzymes,¹⁹²⁻¹⁹⁴ and temperature¹⁹⁵⁻¹⁹⁷ as summarized in Table 2-1.

For pH-triggered nanocarriers, the gatekeeper compound capping the pores is sensitive to pH. Compounds containing amines, hydroxyl and carboxylic acid functional groups are susceptible to protonation and deprotonation depending on the pH of the medium. This can affect the charge of the gatekeeper compound, and thus the interactions with the nanocarrier and AI. Mattos et al.¹⁹⁸ functionalized thymol-loaded SiO₂ NPs with amino functional group (-NH₂), which at neutral pH is protonated (-NH₃⁺), thus strongly interacting with the electronegative group O⁻ in thymol and preventing the AI from being released. At acidic pH, however, thymol undergoes protonation, weakening the interaction with the gatekeeper, which then leads to a greater release of the AI. Complex structures, such as polymers (i.e., hydrogels), denature and undergo structural changes depending on the pH of the medium. Sarkar and Singh¹⁹⁹ reported that at alkaline pH, a hydrogel coating comprised of CMC and citric acid undergo hydrolysis, liberating the release of chlorpyrifos pesticide from a nanoclay matrix.

Photo-responsive gatekeepers can undergo structural change when exposed to light of a certain wavelength. Some structural changes include oxidation, isomerization, and fragmentation of the interaction with the carrier.²⁰⁰ Chen et al.¹⁸³ functionalized a glyphosate-loaded porous nano-sized biochar with amino-silicon oil, which undergoes isomerization when exposed to light at 420 nm wavelength. This process, then, releases the loaded glyphosate. Interestingly, when this nanoformulation ceases to be exposed to the specific wavelength of light, the gatekeeper returns to cap the pores of the nanocarrier and block the AI to be released. That is, one can turn on and off the release of the molecule of interest by simply exposing or not the nanoformulation to light.

Ionic strength-responsive gatekeepers generally rely in the electrostatic interactions among the medium, nanocarrier, AI and the gatekeeper itself. Cao et al.¹⁶⁷ functionalized 2,4-dichlorophenoxy acetic acid (2,4-D)-loaded MSNs with trimethylammonium (TA) to avoid premature release of the pesticide. Because 2,4-D is extremely soluble in aqueous media, leaching is generally a threat when it is applied in agricultural soils. The TA acts as a binding agent for the 2,4-D, increasing the loading by 21.7% and as a capping agent to avoid leaching. The change in

ionic strength, however, can affect the interaction between TA and 2,4-D, leading to either more release of the AI, or a stronger interaction thus preventing the discharge of the pesticide in the soil.

An example of redox-responsive release is when disulfide bonds between the nanocarriers and the capping agent are undone, liberating the loaded molecules to be released. The most common gatekeepers for redox-sensitive response are β -cyclodextrins, sulfidated polyethylene glycol (S-PEG), and cadmium sulfide. Yi et al.¹⁹¹ designed MSN functionalized with decanethiol, through disulfide conjugation. The disulfide bonds between the MSN and decanethiol could be easily cleaved by glutathione (GSH). In this study, the release of salicylic acid was directly controlled by the concentration of GSH in the medium.

Enzyme-triggered response involves using enzymes to degrade the gatekeepers associated with the loaded nanocarrier. Kaziem et al.¹⁹² synthesized PHSN, loaded these nanocarriers with chlorantraniliprole, and functionalized their surface with α -cyclodextrin. The α -cyclodextrin-PHSN successfully retained the AI under thermal stress and UV radiation, however, the release was triggered when α -amylase was introduced, leading to the degradation of the capping agent, and unblocking the pathway for the AI to be discharged.

AI release can also be triggered by thermal stress. This happens when the gatekeepers are thermosensitive, particularly compounds that are sensitive to temperatures in the environmental range. Because high temperatures can lead to the degradation of the AI and nanocarrier as well, the gatekeeper must be able to undergo transformation with light variations of ambient temperatures. Ye et al.¹⁹⁵ used a thermosensitive polymer, poly(N-isopropylacrylamide-co-acrylamide), to cover MSN-coated Fe₃O₄ NPs. The subtle difference in temperature from 34 to 42°C led to changes in structure and magnetic properties of the nanocarrier, that can be used in conjunction with molecules of interest to modulate their release.

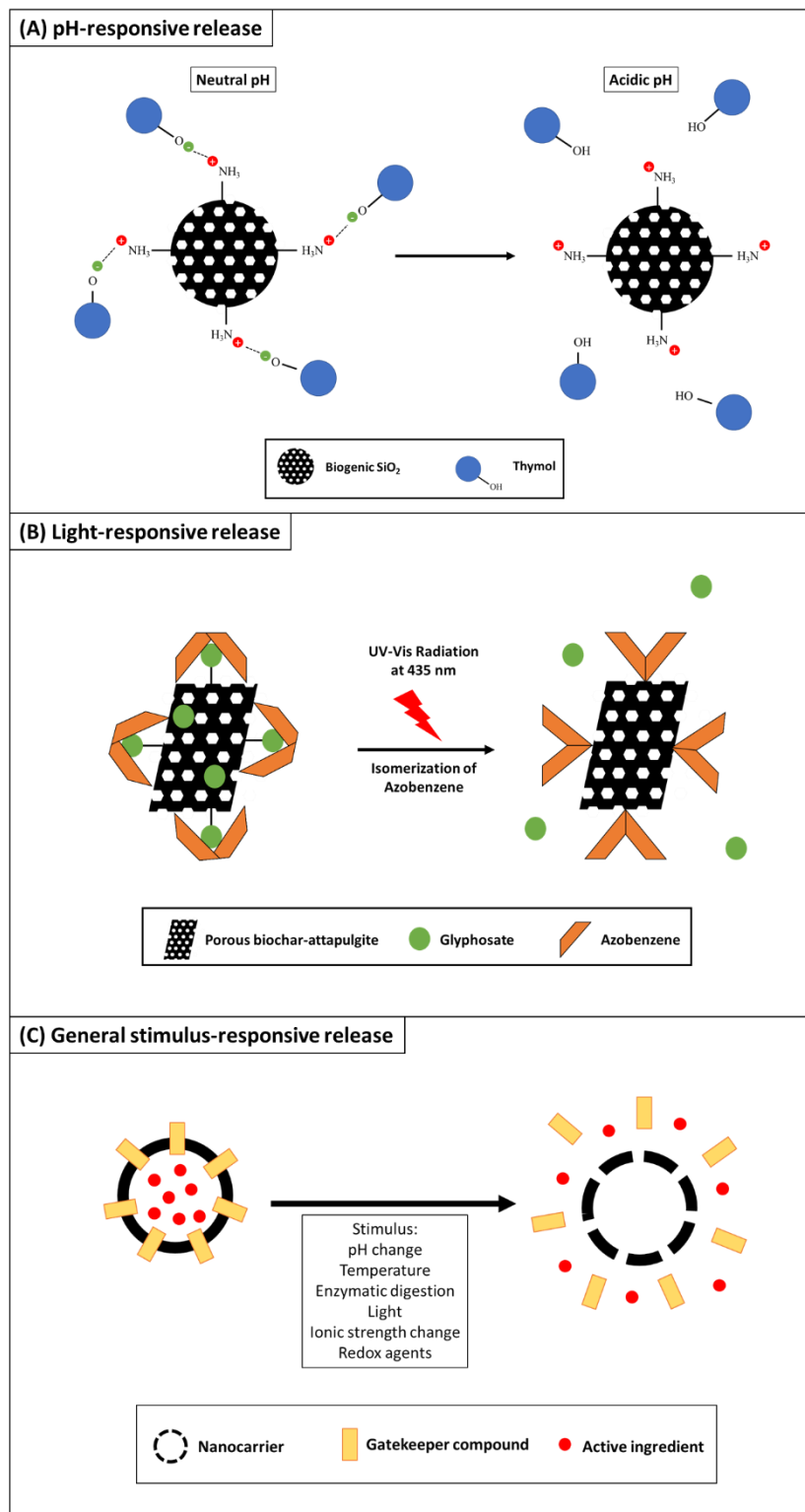


Figure 2-3. Conceptual schematic of a (A) pH-responsive nanocarrier suggested by Mattos et al.¹⁹⁸: at neutral pH there is a strong interaction between the negatively charged hydroxyl group in thymol

and the positively charged amino group in the functionalized biogenic nano-SiO₂ and when the pH becomes more acidic, this interaction is weakened due to the protonation of the hydroxyl group in thymol; (B) light-responsive nanocarrier suggested by Chen et al.¹⁸³: under UV-Vis light radiation at 435 nm, azobenzene undergoes isomerization releasing the encapsulated glyphosate from the porous biochar-attapulgite framework; (C) general stimulus-responsive nanocarrier: the AI is trapped within the nanocarrier until a stimulus disrupts the structure of the gatekeeper compound, thus liberating the pores and allowing the AI to be released.

In the future, sophisticated applications of nanotechnology in agriculture will take advantage of the ability to functionalize porous nanocarriers, particularly SiO₂ and clay NPs, to target the delivery of the formulation to specific plant organelles and tissues, and to promote stimuli responsive release of molecules of interest, all at once while carrying several molecules of interest that will only interact with one another at the destination. Two or more compounds will play a role in capping the pores to prevent AI premature release, mimicking biorecognition mechanisms in the different parts of the plants, and in some cases, activating the AI. More research should be focused on the functionalization of porous nanocarriers with biomolecules and how their interaction can modulate the uptake and release of pesticides, fertilizers, and genetic material to plants.

Table 2-1. List of stimuli responsive nanocarriers with their respective gatekeepers and active ingredients.

Stimulus	Nanocarrier material	Gatekeeper(s)	Active Ingredient	Reference
pH	Mesoporous silica	Poly(allylamine hydrochloride)	Doxorubicin	Yang et al. ¹⁷¹
	Mesoporous silica	Gold NPs and acid-labile acetal linker	2,2'-bipyridine	Liu et al. ¹⁷²
	Mesoporous silica	ZnO QDs	Doxorubicin	Muhammad et al. ¹⁷³
	Mesoporous silica	Poly(acrylic acid)	Doxorubicin	Yuan et al. ¹⁷⁴
	Mesoporous silica	Calcium carbonate	Prochloraz	Gao et al. ¹⁷⁵
	Mesoporous silica	Pluronic F127	Chlorpyrifos	Chen et al. ¹⁷⁷
	Clay	Hydrogel	Chlorpyrifos	Sarkar and Singh ¹⁹⁹
	Biogenic silica	Functionalized amino group	Thymol	Mattos et al. ¹⁹⁸
Light	Mesoporous silica	Gold NPs	Doxorubicin	Niu et al. ¹⁷⁹
	Mesoporous silica	Sulfonatocalix(4)arene	Gold nanorods	Li et al. ¹⁸⁰
	Mesoporous silica	Gold NPs	Doxorubicin	Zhang et al. ¹⁸¹
	Porous biochar-attapulgit	Azobenzene	Glyphosate	Chen et al. ¹⁸³
Ionic Strength	Porous hollow carbon	Cationic polymer PEI	Selenate	Zhang et al. ¹⁸⁵
	Hydrotalcite	Mg and Al	Phosphate	Bernardo et al. ¹⁸⁶
	Mesoporous silica	Trimethylammonium	2,4-dichlorophenoxy acetic acid	Cao et al. ¹⁶⁷
Redox Agents	Mesoporous silica	Glutathione	N-acetyl-L-cysteine	Koo et al. ¹⁸⁷
	Mesoporous silica	Glutathione	Fluorescein	Cui et al. ¹⁸⁸
	Mesoporous silica	Glutathione	Cyclodextrin	Kim et al. ¹⁸⁹
	Mesoporous silica	Glutathione	Salicylic acid	Yi et al. ¹⁹¹
Enzymes	Hollow porous silica	α -cyclodextrin	Chlorantraniliprole	Kaziem et al. ¹⁹²
	Mesoporous silica	Isocyanate and poly(ethylenimine)	Pendimethalin	Liang et al. ¹⁹³
	Mesoporous silica	Carboxymethylcellulose	Emamectin benzoate	Guo et al. ¹⁹⁴
Temperature	Hollow porous silica	Poly(N-isopropylacrylamide)	Fe ₃ O ₄	Ye et al. ¹⁹⁵

2.7. Conclusions

Inorganic porous nanoparticles play a pivotal role in nano-enabled agriculture and towards making agricultural practices more sustainable. A variety of methodologies for synthesis and structure modifications of inorganic nanomaterials have been extensively studied, providing us with the expertise to fabricate nanocarriers with specific features to encapsulate, transport and release agrochemicals in a way that avoids wastage by targeting specific sites in the plant. For instance, the shape, diameter and porosity can be tuned to optimize the loading of AI but keep it in the range for uptake through roots or leaves, and translocation through the xylem and phloem. Further modifications can be done to improve uptake and translocation as well as target specific organelles, such as changing the zeta potential or functionalizing the nanocarrier surfaces with biomolecules to mimic biorecognition mechanisms.

Given the immense possibilities for inorganic porous nanomaterials to increase crop yields and to offer crop protection many new nanotechnology solutions will be proposed in the near future, with the objective to make agricultural practices more efficient. However, to ensure these developments are sustainable, nanomaterials should be formulated with safe and/or earth-abundant chemicals and using green chemistry principles. However, given that in some instances materials at the nano-range may be toxic compared to their bulk counterparts, the environmental and human health exposures and risks of new nanomaterials used in agriculture need to be evaluated. Although the goal of use of nanomaterials and nanocarriers is to ensure that AI delivered is utilized efficiently, without wastage, some losses to the environment are expected. For example, the nanomaterials can be washed off leaves and deposit on the ground during precipitation events, and along with nanomaterials applied in soils, may be mobilized in the soil and groundwater. As well nanomaterials dosed in plants may lead to exposures to insects, including those involved in pollination, as well as birds. Thus, their ecological safety needs to be verified. Various silica and other inorganic porous nanomaterials are being used in medicine, which suggest that their safety to human health may already be verified.^{201, 202}

It is also important to assess the scalability of production of inorganic porous NPs for field applications, and as well field studies need to perform to verify if the efficacy determined in lab studies are translated adequately to the field. In a recent assessment of technology efficacy and readiness level for commercial applications, nanocarriers for fertilization and pesticide delivery

ranked high on both counts, suggesting that their commercial applications are likely to grow rapidly.²⁰³

2.8. References

1. Fernandez-Fernandez, A.; Manchanda, R.; McGoron, A. J., Theranostic applications of nanomaterials in cancer: drug delivery, image-guided therapy, and multifunctional platforms. *Applied Biochemistry and Biotechnology* **2011**, *165* (7), 1628-1651.
2. Pérez-de-Luque, A.; Rubiales, D., Nanotechnology for parasitic plant control. *Pest Management Science* **2009**, *65* (5), 540-545.
3. Rai, M.; Yadav, A.; Gade, A., Silver nanoparticles as a new generation of antimicrobials. *Biotechnology Advances* **2009**, *27* (1), 76-83.
4. Zhang, H.; Chen, G., Potent antibacterial activities of Ag/TiO₂ nanocomposite powders synthesized by a one-pot sol–gel method. *Environmental Science and Technology* **2009**, *43* (8), 2905-2910.
5. Richter, A. P.; Brown, J. S.; Bharti, B.; Wang, A.; Gangwal, S.; Houck, K.; Hubal, E. A. C.; Paunov, V. N.; Stoyanov, S. D.; Velev, O. D., An environmentally benign antimicrobial nanoparticle based on a silver-infused lignin core. *Nature Nanotechnology* **2015**, *10* (9), 817-823.
6. Tarafdar, J.; Raliya, R.; Mahawar, H.; Rathore, I., Development of zinc nanofertilizer to enhance crop production in pearl millet (*Pennisetum americanum*). *Agricultural Research* **2014**, *3* (3), 257-262.
7. Mostafa, M.; Ahmed, F. K.; Alghuthaymi, M.; Abd-Elsalam, K. A., Inorganic smart nanoparticles: a new tool to deliver CRISPR systems into plant cells. In *CRISPR and RNAi Systems*, Elsevier: 2021; pp 661-686.
8. Lino, C. A.; Harper, J. C.; Carney, J. P.; Timlin, J. A., Delivering CRISPR: a review of the challenges and approaches. *Drug Delivery* **2018**, *25* (1), 1234-1257.
9. Jesus, M.; Grazu, V., *Nanobiotechnology: Inorganic Nanoparticles vs Organic Nanoparticles*. Elsevier: 2012.

10. Rastogi, A.; Tripathi, D. K.; Yadav, S.; Chauhan, D. K.; Živčák, M.; Ghorbanpour, M.; El-Sheery, N. I.; Brestic, M., Application of silicon nanoparticles in agriculture. *3 Biotech* **2019**, *9* (3), 1-11.
11. Sabir, S.; Arshad, M.; Chaudhari, S. K., Zinc oxide nanoparticles for revolutionizing agriculture: synthesis and applications. *The Scientific World Journal* **2014**, *2014*.
12. Shan, Y.; Cao, L.; Muhammad, B.; Xu, B.; Zhao, P.; Cao, C.; Huang, Q., Iron-based porous metal–organic frameworks with crop nutritional function as carriers for controlled fungicide release. *Journal of Colloid and Interface Science* **2020**, *566*, 383-393.
13. Marchiol, L.; Filippi, A.; Adamiano, A.; Degli Esposti, L.; Iafisco, M.; Mattiello, A.; Petrusa, E.; Braidot, E., Influence of hydroxyapatite nanoparticles on germination and plant metabolism of tomato (*Solanum lycopersicum* L.): Preliminary evidence. *Agronomy* **2019**, *9* (4), 161.
14. Kasana, R. C.; Panwar, N. R.; Kaul, R. K.; Kumar, P., Copper nanoparticles in agriculture: biological synthesis and antimicrobial activity. In *Nanoscience in Food and Agriculture 3*, Springer: 2016; pp 129-143.
15. Manjunatha, S.; Biradar, D.; Aladakatti, Y. R., Nanotechnology and its applications in agriculture: A review. *Journal of Farm Sciences* **2016**, *29* (1), 1-13.
16. Lin, Y.-S.; Haynes, C. L., Synthesis and characterization of biocompatible and size-tunable multifunctional porous silica nanoparticles. *Chemistry of Materials* **2009**, *21* (17), 3979-3986.
17. Parra-Nieto, J.; Del Cid, M. A. G.; de Cárcer, I. A.; Baeza, A., Inorganic Porous Nanoparticles for Drug Delivery in Antitumoral Therapy. *Biotechnology Journal* **2021**, *16* (2), 2000150.
18. Zhang, J.; Li, X.; Rosenholm, J. M.; Gu, H.-c., Synthesis and characterization of pore size-tunable magnetic mesoporous silica nanoparticles. *Journal of Colloid and Interface Science* **2011**, *361* (1), 16-24.

19. Mishra, V.; Mishra, R. K.; Dikshit, A.; Pandey, A. C., Interactions of nanoparticles with plants: an emerging prospective in the agriculture industry. In *Emerging Technologies and Management of Crop Stress Tolerance*, Elsevier: 2014; pp 159-180.
20. Subbiah, R.; Veerapandian, M.; S Yun, K., Nanoparticles: functionalization and multifunctional applications in biomedical sciences. *Current Medicinal Chemistry* **2010**, *17* (36), 4559-4577.
21. Epstein, E., *Mineral Nutrition of Plants: Principles and Perspectives*. 1972.
22. Luyckx, M.; Hausman, J.-F.; Lutts, S.; Guerriero, G., Silicon and plants: current knowledge and technological perspectives. *Frontiers in Plant Science* **2017**, *8*, 411.
23. Abdel-Haliem, M. E.; Hegazy, H. S.; Hassan, N. S.; Naguib, D. M., Effect of silica ions and nano silica on rice plants under salinity stress. *Ecological Engineering* **2017**, *99*, 282-289.
24. Abdelrahman, T. M.; Qin, X.; Li, D.; Senosy, I. A.; Mmby, M.; Wan, H.; Li, J.; He, S., Pectinase-responsive carriers based on mesoporous silica nanoparticles for improving the translocation and fungicidal activity of prochloraz in rice plants. *Chemical Engineering Journal* **2021**, *404*, 126440.
25. El-Shetehy, M.; Moradi, A.; Maceroni, M.; Reinhardt, D.; Petri-Fink, A.; Rothen-Rutishauser, B.; Mauch, F.; Schwab, F., Silica nanoparticles enhance disease resistance in Arabidopsis plants. *Nature Nanotechnology* **2020**, 1-10.
26. Stöber, W.; Fink, A.; Bohn, E., Controlled growth of monodisperse silica spheres in the micron size range. *Journal of Colloid and Interface Science* **1968**, *26* (1), 62-69.
27. Slowing, I.; Trewyn, B. G.; Lin, V. S.-Y., Effect of surface functionalization of MCM-41-type mesoporous silica nanoparticles on the endocytosis by human cancer cells. *Journal of the American Chemical Society* **2006**, *128* (46), 14792-14793.
28. Bueno, V.; Ghoshal, S., Self-Assembled Surfactant-Templated Synthesis of Porous Hollow Silica Nanoparticles: Mechanism of Formation and Feasibility of Post-Synthesis Nanoencapsulation. *Langmuir* **2020**, *36* (48), 14633-14643.

29. Fernandes, R. S.; Raimundo Jr, I. M.; Pimentel, M. F., Revising the synthesis of Stöber silica nanoparticles: A multivariate assessment study on the effects of reaction parameters on the particle size. *Colloids and Surfaces A: Physicochemical and Engineering Aspects* **2019**, *577*, 1-7.
30. Pack, C.-G.; Paulson, B.; Shin, Y.; Jung, M. K.; Kim, J. S.; Kim, J. K., Variably Sized and Multi-Colored Silica-Nanoparticles Characterized by Fluorescence Correlation Methods for Cellular Dynamics. *Materials* **2021**, *14* (1), 19.
31. Nandiyanto, A. B. D.; Kim, S.-G.; Iskandar, F.; Okuyama, K., Synthesis of spherical mesoporous silica nanoparticles with nanometer-size controllable pores and outer diameters. *Microporous and Mesoporous Materials* **2009**, *120* (3), 447-453.
32. Ren, D.; Xu, J.; Chen, N.; Ye, Z.; Li, X.; Chen, Q.; Ma, S., Controlled synthesis of mesoporous silica nanoparticles with tunable architectures via oil-water microemulsion assembly process. *Colloids and Surfaces A: Physicochemical and Engineering Aspects* **2021**, *611*, 125773.
33. Tsou, C.-J.; Hung, Y.; Mou, C.-Y., Hollow mesoporous silica nanoparticles with tunable shell thickness and pore size distribution for application as broad-ranging pH nanosensor. *Microporous and Mesoporous Materials* **2014**, *190*, 181-188.
34. Wang, X. D.; Rabe, K. S.; Ahmed, I.; Niemeyer, C. M., Multifunctional silica nanoparticles for covalent immobilization of highly sensitive proteins. *Advanced Materials* **2015**, *27* (48), 7945-7950.
35. Plohl, O.; Gyergyek, S.; Zemljič, L. F., Mesoporous silica nanoparticles modified with N-rich polymer as a potentially environmentally-friendly delivery system for pesticides. *Microporous and Mesoporous Materials* **2021**, *310*, 110663.
36. Gao, X.; Kundu, A.; Bueno, V.; Rahim, A. A.; Ghoshal, S., Uptake and Translocation of Mesoporous SiO₂-Coated ZnO Nanoparticles to Solanum lycopersicum Following Foliar Application. *Environmental Science and Technology* **2021**, *55*, 20, 13551-13560.
37. Attia, E. A.; Elhawat, N., Combined foliar and soil application of silica nanoparticles enhances the growth, flowering period and flower characteristics of marigold (*Tagetes erecta* L.). *Scientia Horticulturae* **2021**, *282*, 110015.

38. Siddiqui, H.; Ahmed, K. B. M.; Sami, F.; Hayat, S., Silicon nanoparticles and plants: current knowledge and future perspectives. *Sustainable Agriculture Reviews 41* **2020**, 129-142.
39. Suriyaprabha, R.; Karunakaran, G.; Yuvakkumar, R.; Rajendran, V.; Kannan, N., Foliar application of silica nanoparticles on the phytochemical responses of maize (*Zea mays* L.) and its toxicological behavior. *Synthesis and Reactivity in Inorganic, Metal-Organic, and Nano-Metal Chemistry* **2014**, *44* (8), 1128-1131.
40. Chen, C.-Y.; Li, H.-X.; Davis, M. E., Studies on mesoporous materials: I. Synthesis and characterization of MCM-41. *Microporous Materials* **1993**, *2* (1), 17-26.
41. Li, Z.-Z.; Xu, S.-A.; Wen, L.-X.; Liu, F.; Liu, A.-Q.; Wang, Q.; Sun, H.-Y.; Yu, W.; Chen, J.-F., Controlled release of avermectin from porous hollow silica nanoparticles: Influence of shell thickness on loading efficiency, UV-shielding property and release. *Journal of Controlled Release* **2006**, *111* (1-2), 81-88.
42. Zhao, P.; Cao, L.; Ma, D.; Zhou, Z.; Huang, Q.; Pan, C., Translocation, distribution and degradation of prochloraz-loaded mesoporous silica nanoparticles in cucumber plants. *Nanoscale* **2018**, *10* (4), 1798-1806.
43. Feng, J.; Yang, J.; Shen, Y.; Deng, W.; Chen, W.; Ma, Y.; Chen, Z.; Dong, S., Mesoporous silica nanoparticles prepared via a one-pot method for controlled release of abamectin: Properties and applications. *Microporous and Mesoporous Materials* **2021**, *311*, 110688.
44. Shan, Y.; Cao, L.; Xu, C.; Zhao, P.; Cao, C.; Li, F.; Xu, B.; Huang, Q., Sulfonate-functionalized mesoporous silica nanoparticles as carriers for controlled herbicide diquat dibromide release through electrostatic interaction. *International Journal of Molecular Sciences* **2019**, *20* (6), 1330.
45. Vu, K. B.; Phung, T. K.; Tran, T. T.; Mugemana, C.; Giang, H. N.; Nhi, T. L. P., Polystyrene nanoparticles prepared by nanoprecipitation: A recyclable template for fabricating hollow silica. *Journal of Industrial and Engineering Chemistry* **2021**.

46. Bueno, V.; Bosi, A.; Tosco, T.; Ghoshal, S., Mobility of Solid and Porous Hollow SiO₂ Nanoparticles in Saturated Porous Media: Impacts of Surface and Particle Structure. *Journal of Colloid and Interface Science* **2022**, *606*, 480-490.
47. Yang, J.; Gao, Y.; Zhou, Z.; Tang, J.; Tang, G.; Niu, J.; Chen, X.; Tian, Y.; Li, Y.; Cao, Y., A simple and green preparation process for PRO@PIL-PHS-PEC microcapsules by using phosphonium ionic liquid as a multifunctional additive. *Chemical Engineering Journal* **2021**, *424*, 130371.
48. Wibowo, D.; Zhao, C.-X.; Peters, B. C.; Middelberg, A. P., Sustained release of fipronil insecticide in vitro and in vivo from biocompatible silica nanocapsules. *Journal of Agricultural and Food Chemistry* **2014**, *62* (52), 12504-12511.
49. Hai, L.; Jia, X.; He, D.; Zhang, A.; Wang, T.; Cheng, H.; He, X.; Wang, K., DNA-functionalized hollow mesoporous silica nanoparticles with dual cargo loading for near-infrared-responsive synergistic chemo-photothermal treatment of cancer cells. *ACS Applied Nano Materials* **2018**, *1* (7), 3486-3497.
50. Li, Z. Z.; Chen, J. F.; Liu, F.; Liu, A. Q.; Wang, Q.; Sun, H. Y.; Wen, L. X., Study of UV-shielding properties of novel porous hollow silica nanoparticle carriers for avermectin. *Pest Management Science* **2007**, *63* (3), 241-246.
51. Szameitat, A. E.; Sharma, A.; Minutello, F.; Pinna, A.; Er-Rafik, M.; Hansen, T. H.; Persson, D. P.; Andersen, B.; Husted, S., Unravelling the interactions between nano-hydroxyapatite and the roots of phosphorus deficient barley plants. *Environmental Science: Nano* **2021**, *8* (2), 444-459.
52. Mortvedt, J., Heavy metal contaminants in inorganic and organic fertilizers. In *Fertilizers and Environment*, Springer: 1996; pp 5-11.
53. Molina, M.; Aburto, F.; Calderón, R.; Cazanga, M.; Escudey, M., Trace element composition of selected fertilizers used in Chile: phosphorus fertilizers as a source of long-term soil contamination. *Soil and Sediment Contamination* **2009**, *18* (4), 497-511.

54. Sadat-Shojai, M.; Khorasani, M.-T.; Dinpanah-Khoshdargi, E.; Jamshidi, A., Synthesis methods for nanosized hydroxyapatite with diverse structures. *Acta Biomaterialia* **2013**, *9* (8), 7591-7621.
55. Verma, G.; Barick, K.; Manoj, N.; Sahu, A.; Hassan, P., Rod-like micelle templated synthesis of porous hydroxyapatite. *Ceramics International* **2013**, *39* (8), 8995-9002.
56. Ansari, L.; Derakhshi, M.; Bagheri, E.; Shahtahmassebi, N.; Malaekheh-Nikouei, B., Folate conjugation improved uptake and targeting of porous hydroxyapatite nanoparticles containing epirubicin to cancer cells. *Pharmaceutical Development and Technology* **2020**, *25* (5), 601-609.
57. Taşkın, M. B.; Şahin, Ö.; Taskin, H.; Atakol, O.; Inal, A.; Gunes, A., Effect of synthetic nano-hydroxyapatite as an alternative phosphorus source on growth and phosphorus nutrition of lettuce (*Lactuca sativa* L.) plant. *Journal of Plant Nutrition* **2018**, *41* (9), 1148-1154.
58. Maghsoodi, M. R.; Ghodszad, L.; Lajayer, B. A., Dilemma of hydroxyapatite nanoparticles as phosphorus fertilizer: potentials, challenges and effects on plants. *Environmental Technology and Innovation* **2020**, *19*, 100869.
59. Liu, R.; Lal, R., Synthetic apatite nanoparticles as a phosphorus fertilizer for soybean (*Glycine max*). *Scientific Reports* **2014**, *4* (1), 1-6.
60. Kottegoda, N.; Munaweera, I.; Madusanka, N.; Karunaratne, V., A green slow-release fertilizer composition based on urea-modified hydroxyapatite nanoparticles encapsulated wood. *Current Science* **2011**, 73-78.
61. Tiwari, A.; Mamedov, F.; Grieco, M.; Suorsa, M.; Jajoo, A.; Styring, S.; Tikkanen, M.; Aro, E.-M., Photodamage of iron–sulphur clusters in photosystem I induces non-photochemical energy dissipation. *Nature Plants* **2016**, *2* (4), 1-9.
62. Jeyasubramanian, K.; Thoppey, U. U. G.; Hikku, G. S.; Selvakumar, N.; Subramania, A.; Krishnamoorthy, K., Enhancement in growth rate and productivity of spinach grown in hydroponics with iron oxide nanoparticles. *RSC Advances* **2016**, *6* (19), 15451-15459.

63. Lopez, A.; Cacoub, P.; Macdougall, I. C.; Peyrin-Biroulet, L., Iron deficiency anaemia. *The Lancet* **2016**, 387 (10021), 907-916.
64. WHO *Recommendations on wheat and maize flour fortification meeting report: Interim consensus statement*; World Health Organization: 2009.
65. Meng, F.; Wei, Y.; Yang, X., Iron content and bioavailability in rice. *Journal of Trace Elements in Medicine and Biology* **2005**, 18 (4), 333-338.
66. Lucena, J. J.; Gárate, A.; Villén, M., Stability in solution and reactivity with soils and soil components of iron and zinc complexes. *Journal of Plant Nutrition and Soil Science* **2010**, 173 (6), 900-906.
67. Wang, X.; Zhang, P.; Gao, J.; Chen, X.; Yang, H., Facile synthesis and magnetic properties of Fe₃C/C nanoparticles via a sol–gel process. *Dyes and Pigments* **2015**, 112, 305-310.
68. Yadav, R. S.; Havlica, J.; Hnatko, M.; Šajgalík, P.; Alexander, C.; Palou, M.; Bartoníčková, E.; Boháč, M.; Frajkorová, F.; Masilko, J., Magnetic properties of Co_{1-x}Zn_xFe₂O₄ spinel ferrite nanoparticles synthesized by starch-assisted sol–gel autocombustion method and its ball milling. *Journal of Magnetism and Magnetic Materials* **2015**, 378, 190-199.
69. Gavrilović, T. V.; Jovanović, D. J.; Lojpur, V.; Dramićanin, M. D., Multifunctional Eu³⁺-and Er³⁺/Yb³⁺-doped GdVO₄ nanoparticles synthesized by reverse micelle method. *Scientific Reports* **2014**, 4 (1), 1-9.
70. Nikumbh, A.; Pawar, R.; Nighot, D.; Gugale, G.; Sangale, M.; Khanvilkar, M.; Nagawade, A., Structural, electrical, magnetic and dielectric properties of rare-earth substituted cobalt ferrites nanoparticles synthesized by the co-precipitation method. *Journal of Magnetism and Magnetic Materials* **2014**, 355, 201-209.
71. Safi, R.; Ghasemi, A.; Shoja-Razavi, R.; Ghasemi, E.; Sodaee, T., Rietveld structure refinement, cations distribution and magnetic features of CoFe₂O₄ nanoparticles synthesized by co-precipitation, hydrothermal, and combustion methods. *Ceramics International* **2016**, 42 (5), 6375-6382.

72. Li, H.; Yang, Z.-Y.; Liu, C.; Zeng, Y.-P.; Hao, Y.-H.; Gu, Y.; Wang, W.-D.; Li, R., PEGylated ceria nanoparticles used for radioprotection on human liver cells under γ -ray irradiation. *Free Radical Biology and Medicine* **2015**, *87*, 26-35.
73. Raut, A. V.; Jadhav, S.; Shengule, D.; Jadhav, K., Structural and magnetic characterization of 100-kGy Co 60 γ -ray-irradiated ZnFe 2 O 4 NPs by XRD, W–H plot and ESR. *Journal of Sol-Gel Science and Technology* **2016**, *79* (1), 1-11.
74. Ozel, F.; Kockar, H.; Karaagac, O., Growth of iron oxide nanoparticles by hydrothermal process: effect of reaction parameters on the nanoparticle size. *Journal of Superconductivity and Novel Magnetism* **2015**, *28* (3), 823-829.
75. Tadic, M.; Panjan, M.; Damnjanovic, V.; Milosevic, I., Magnetic properties of hematite (α -Fe₂O₃) nanoparticles prepared by hydrothermal synthesis method. *Applied Surface Science* **2014**, *320*, 183-187.
76. Rui, M.; Ma, C.; Hao, Y.; Guo, J.; Rui, Y.; Tang, X.; Zhao, Q.; Fan, X.; Zhang, Z.; Hou, T., Iron oxide nanoparticles as a potential iron fertilizer for peanut (*Arachis hypogaea*). *Frontiers in Plant Science* **2016**, *7*, 815.
77. Li, J.; Hu, J.; Xiao, L.; Wang, Y.; Wang, X., Interaction mechanisms between α -Fe₂O₃, γ -Fe₂O₃ and Fe₃O₄ nanoparticles and *Citrus maxima* seedlings. *Science of the Total Environment* **2018**, *625*, 677-685.
78. Wang, H.; Kou, X.; Pei, Z.; Xiao, J. Q.; Shan, X.; Xing, B., Physiological effects of magnetite (Fe₃O₄) nanoparticles on perennial ryegrass (*Lolium perenne* L.) and pumpkin (*Cucurbita mixta*) plants. *Nanotoxicology* **2011**, *5* (1), 30-42.
79. Li, M.; Zhang, P.; Adeel, M.; Guo, Z.; Chetwynd, A. J.; Ma, C.; Bai, T.; Hao, Y.; Rui, Y., Physiological impacts of zero valent iron, Fe₃O₄ and Fe₂O₃ nanoparticles in rice plants and their potential as Fe fertilizers. *Environmental Pollution* **2021**, *269*, 116134.
80. Robinson, N. J.; Procter, C. M.; Connolly, E. L.; Guerinot, M. L., A ferric-chelate reductase for iron uptake from soils. *Nature* **1999**, *397* (6721), 694-697.

81. Eide, D.; Broderius, M.; Fett, J.; Guerinot, M. L., A novel iron-regulated metal transporter from plants identified by functional expression in yeast. *Proceedings of the National Academy of Sciences* **1996**, *93* (11), 5624-5628.
82. Liu, Y.; Wu, T.; White, J. C.; Lin, D., A new strategy using nanoscale zero-valent iron to simultaneously promote remediation and safe crop production in contaminated soil. *Nature Nanotechnology* **2021**, *16* (2), 197-205.
83. Kobayashi, T.; Nishizawa, N. K., Iron uptake, translocation, and regulation in higher plants. *Annual Review of Plant Biology* **2012**, *63*, 131-152.
84. Curie, C.; Panaviene, Z.; Loulergue, C.; Dellaporta, S. L.; Briat, J.-F.; Walker, E. L., Maize yellow stripe1 encodes a membrane protein directly involved in Fe (III) uptake. *Nature* **2001**, *409* (6818), 346-349.
85. Sturikova, H.; Krystofova, O.; Huska, D.; Adam, V., Zinc, zinc nanoparticles and plants. *Journal of Hazardous Materials* **2018**, *349*, 101-110.
86. Palmer, C. M.; Guerinot, M. L., Facing the challenges of Cu, Fe and Zn homeostasis in plants. *Nature Chemical Biology* **2009**, *5* (5), 333.
87. Hänsch, R.; Mendel, R. R., Physiological functions of mineral micronutrients (Cu, Zn, Mn, Fe, Ni, Mo, B, Cl). *Current Opinion in Plant Biology* **2009**, *12* (3), 259-266.
88. Palmgren, M. G.; Clemens, S.; Williams, L. E.; Krämer, U.; Borg, S.; Schjørring, J. K.; Sanders, D., Zinc biofortification of cereals: problems and solutions. *Trends in Plant Science* **2008**, *13* (9), 464-473.
89. Milner, M. J.; Seamon, J.; Craft, E.; Kochian, L. V., Transport properties of members of the ZIP family in plants and their role in Zn and Mn homeostasis. *Journal of Experimental Botany* **2013**, *64* (1), 369-381.
90. Ajeesh Krishna, T.; Maharajan, T.; Victor Roch, G.; Ignacimuthu, S.; Antony Cesar, S., Structure, function, regulation and phylogenetic relationship of ZIP family transporters of plants. *Frontiers in Plant Science* **2020**, *11*, 662.

91. Hussain, D.; Haydon, M. J.; Wang, Y.; Wong, E.; Sherson, S. M.; Young, J.; Camakaris, J.; Harper, J. F.; Cobbett, C. S., P-type ATPase heavy metal transporters with roles in essential zinc homeostasis in Arabidopsis. *The Plant Cell* **2004**, *16* (5), 1327-1339.
92. Curie, C.; Cassin, G.; Couch, D.; Divol, F.; Higuchi, K.; Le Jean, M.; Misson, J.; Schikora, A.; Czernic, P.; Mari, S., Metal movement within the plant: contribution of nicotianamine and yellow stripe 1-like transporters. *Annals of Botany* **2009**, *103* (1), 1-11.
93. Zhu, J.; Li, J.; Shen, Y.; Liu, S.; Zeng, N.; Zhan, X.; White, J. C.; Gardea-Torresdey, J.; Xing, B., Mechanism of zinc oxide nanoparticle entry into wheat seedling leaves. *Environmental Science: Nano* **2020**, *7* (12), 3901-3913.
94. Zhu, H.; Gu, X.; Zuo, D.; Wang, Z.; Wang, N.; Yao, K., Microemulsion-based synthesis of porous zinc ferrite nanorods and its application in a room-temperature ethanol sensor. *Nanotechnology* **2008**, *19* (40), 405503.
95. Akhtar, M. S.; Riaz, S.; Mehmood, R. F.; Ahmad, K. S.; Alghamdi, Y.; Malik, M. A.; Naseem, S., Surfactant and template free synthesis of porous ZnS nanoparticles. *Materials Chemistry and Physics* **2017**, *189*, 28-34.
96. Ramimoghadam, D.; Hussein, M. Z. B.; Taufiq-Yap, Y. H., Hydrothermal synthesis of zinc oxide nanoparticles using rice as soft biotemplate. *Chemistry Central Journal* **2013**, *7* (1), 1-10.
97. Kim, Y.-S.; Tai, W.-P., Electrical and optical properties of Al-doped ZnO thin films by sol-gel process. *Applied Surface Science* **2007**, *253* (11), 4911-4916.
98. Bo, R.; Zhang, F.; Bu, S.; Nasiri, N.; Di Bernardo, I.; Tran-Phu, T.; Shrestha, A.; Chen, H.; Taheri, M.; Qi, S., One-step synthesis of porous transparent conductive oxides by hierarchical self-assembly of aluminum-doped ZnO nanoparticles. *ACS Applied Materials and Interfaces* **2020**, *12* (8), 9589-9599.
99. Khan, M. R.; Siddiqui, Z. A., Role of zinc oxide nanoparticles in the management of disease complex of beetroot (*Beta vulgaris* L.) caused by *Pectobacterium betavasculorum*, *Meloidogyne incognita* and *Rhizoctonia solani*. *Horticulture, Environment, and Biotechnology* **2021**, *62* (2), 225-241.

100. Semida, W. M.; Abdelkhalik, A.; Mohamed, G.; El-Mageed, A.; Taia, A.; El-Mageed, A.; Shima, A.; Rady, M. M.; Ali, E. F., Foliar application of zinc oxide nanoparticles promotes drought stress tolerance in eggplant (*Solanum melongena* L.). *Plants* **2021**, *10* (2), 421.
101. Dutta, T.; Bagchi, D.; Bera, A.; Das, S.; Adhikari, T.; Pal, S. K., Surface engineered ZnO-humic/citrate interfaces: Photoinduced charge carrier dynamics and potential application for smart and sustained delivery of zn micronutrient. *ACS Sustainable Chemistry and Engineering* **2019**, *7* (12), 10920-10930.
102. Ma, C.; White, J. C.; Dhankher, O. P.; Xing, B., Metal-based nanotoxicity and detoxification pathways in higher plants. *Environmental Science and Technology* **2015**, *49* (12), 7109-7122.
103. Torabian, S.; Zahedi, M.; Khoshgoftarmanesh, A., Effect of foliar spray of zinc oxide on some antioxidant enzymes activity of sunflower under salt stress. *Jomo Kenyatta University of Agriculture and Technology: Digital Repository* **2018**.
104. Keller, A. A.; Adeleye, A. S.; Conway, J. R.; Garner, K. L.; Zhao, L.; Cherr, G. N.; Hong, J.; Gardea-Torresdey, J. L.; Godwin, H. A.; Hanna, S., Comparative environmental fate and toxicity of copper nanomaterials. *NanoImpact* **2017**, *7*, 28-40.
105. Nair, P. M. G.; Chung, I. M., Impact of copper oxide nanoparticles exposure on *Arabidopsis thaliana* growth, root system development, root lignification, and molecular level changes. *Environmental Science and Pollution Research* **2014**, *21* (22), 12709-12722.
106. Zafar, H.; Ali, A.; Zia, M., CuO nanoparticles inhibited root growth from *Brassica nigra* seedlings but induced root from stem and leaf explants. *Applied Biochemistry and Biotechnology* **2017**, *181* (1), 365-378.
107. Xiong, T.; Dumat, C.; Dappe, V.; Vezin, H.; Schreck, E.; Shahid, M.; Pierart, A.; Sobanska, S., Copper oxide nanoparticle foliar uptake, phytotoxicity, and consequences for sustainable urban agriculture. *Environmental Science and Technology* **2017**, *51* (9), 5242-5251.
108. Da Costa, M.; Sharma, P., Effect of copper oxide nanoparticles on growth, morphology, photosynthesis, and antioxidant response in *Oryza sativa*. *Photosynthetica* **2016**, *54* (1), 110-119.

109. Ashok, A.; Kumar, A.; Bhosale, R. R.; Saleh, M. A. H.; Van den Broeke, L. J., Cellulose assisted combustion synthesis of porous Cu–Ni nanopowders. *RSC Advances* **2015**, *5* (36), 28703-28712.
110. Zhao, Q.; Zhu, L.; Lin, G.; Chen, G.; Liu, B.; Zhang, L.; Duan, T.; Lei, J., Controllable synthesis of porous Cu-BTC@ polymer composite beads for iodine capture. *ACS Applied Materials and Interfaces* **2019**, *11* (45), 42635-42645.
111. Zhang, Y.; Zhu, P.; Chen, L.; Li, G.; Zhou, F.; Lu, D. D.; Sun, R.; Zhou, F.; Wong, C.-p., Hierarchical architectures of monodisperse porous Cu microspheres: synthesis, growth mechanism, high-efficiency and recyclable catalytic performance. *Journal of Materials Chemistry A* **2014**, *2* (30), 11966-11973.
112. Jiang, J.; Lim, Y. S.; Park, S.; Kim, S.-H.; Yoon, S.; Piao, L., Hollow porous Cu particles from silica-encapsulated Cu₂O nanoparticle aggregates effectively catalyze 4-nitrophenol reduction. *Nanoscale* **2017**, *9* (11), 3873-3880.
113. O'Mara, P. B.; Wilde, P.; Benedetti, T. M.; Andronesco, C.; Cheong, S.; Gooding, J. J.; Tilley, R. D.; Schuhmann, W., Cascade reactions in nanozymes: Spatially separated active sites inside Ag-Core–Porous-Cu-shell nanoparticles for multistep carbon dioxide reduction to higher organic molecules. *Journal of the American Chemical Society* **2019**, *141* (36), 14093-14097.
114. Ravet, K.; Pilon, M., Copper and iron homeostasis in plants: the challenges of oxidative stress. *Antioxidants and Redox Signaling* **2013**, *19* (9), 919-932.
115. Sanz, A.; Pike, S.; Khan, M. A.; Carrió-Seguí, À.; Mendoza-Cózatl, D. G.; Peñarrubia, L.; Gassmann, W., Copper uptake mechanism of *Arabidopsis thaliana* high-affinity COPT transporters. *Protoplasma* **2019**, *256* (1), 161-170.
116. Ogunkunle, C. O.; Jimoh, M. A.; Asogwa, N. T.; Viswanathan, K.; Vishwakarma, V.; Fatoba, P. O., Effects of manufactured nano-copper on copper uptake, bioaccumulation and enzyme activities in cowpea grown on soil substrate. *Ecotoxicology and Environmental Safety* **2018**, *155*, 86-93.

117. Nazir, M. S.; Kassim, M. H. M.; Mohapatra, L.; Gilani, M. A.; Raza, M. R.; Majeed, K., Characteristic properties of nanoclays and characterization of nanoparticulates and nanocomposites. In *Nanoclay reinforced polymer composites*, Springer: 2016; pp 35-55.
118. Uddin, F., Clays, nanoclays, and montmorillonite minerals. *Metallurgical and Materials Transactions A* **2008**, *39* (12), 2804-2814.
119. Chen, J.; Lü, S.; Zhang, Z.; Zhao, X.; Li, X.; Ning, P.; Liu, M., Environmentally friendly fertilizers: A review of materials used and their effects on the environment. *Science of the Total Environment* **2018**, *613*, 829-839.
120. Merino, D.; Tomadoni, B.; Salcedo, M. F.; Mansilla, A. Y.; Casalongué, C. A.; Alvarez, V. A., Nanoclay as Carriers of Bioactive Molecules Applied to Agriculture. *Handbook of Nanomaterials and Nanocomposites for Energy and Environmental Applications* **2020**, 1-22.
121. Shafigh, M.; Hamidpour, M.; Abbaszadeh-Dahaji, P.; Mozafari, V.; Furrer, G., Bioavailability of Zn from layered double hydroxides: the effects of plant growth-promoting rhizobacteria (PGPR). *Applied Clay Science* **2019**, *182*, 105283.
122. Songkhum, P.; Wuttikhun, T.; Chanlek, N.; Khemthong, P.; Laohhasurayotin, K., Controlled release studies of boron and zinc from layered double hydroxides as the micronutrient hosts for agricultural application. *Applied Clay Science* **2018**, *152*, 311-322.
123. Yuan, G., An organoclay formula for the slow release of soluble compounds. *Applied Clay Science* **2014**, *100*, 84-87.
124. Mazloomi, F.; Jalali, M., Effects of vermiculite, nanoclay and zeolite on ammonium transport through saturated sandy loam soil: Column experiments and modeling approaches. *Catena* **2019**, *176*, 170-180.
125. Bhardwaj, D.; Sharma, M.; Sharma, P.; Tomar, R., Synthesis and surfactant modification of clinoptilolite and montmorillonite for the removal of nitrate and preparation of slow release nitrogen fertilizer. *Journal of Hazardous Materials* **2012**, *227*, 292-300.

126. Madusanka, N.; Sandaruwan, C.; Kottegoda, N.; Sirisena, D.; Munaweera, I.; De Alwis, A.; Karunaratne, V.; Amaratunga, G. A., Urea–hydroxyapatite-montmorillonite nanohybrid composites as slow release nitrogen compositions. *Applied Clay Science* **2017**, *150*, 303-308.
127. Said, A.; Zhang, Q.; Qu, J.; Liu, Y.; Lei, Z.; Hu, H.; Xu, Z., Mechanochemical activation of phlogopite to directly produce slow-release potassium fertilizer. *Applied Clay Science* **2018**, *165*, 77-81.
128. Verma, Y.; Datta, S.; Mandal, I. K.; Sarkar, D., Effect of phosphorus loaded organically modified nanoclay-polymer composite on release and fixation of phosphorus and its uptake by wheat (*Triticum aestivum* L.). *Journal of Pure and Applied Microbiology* **2016**, *10* (3), 2299-2306.
129. Mandal, N.; Datta, S.; Manjaiah, K.; Dwivedi, B.; Nain, L.; Kumar, R.; Aggarwal, P., Novel chitosan grafted zinc containing nanoclay polymer biocomposite (CZNCPBC): Controlled release formulation (CRF) of Zn²⁺. *Reactive and Functional Polymers* **2018**, *127*, 55-66.
130. Wei, H.; Wang, H.; Chu, H.; Li, J., Preparation and characterization of slow-release and water-retention fertilizer based on starch and halloysite. *International Journal of Biological Macromolecules* **2019**, *133*, 1210-1218.
131. Hakim, S.; Darouk, M. R. R.; Barghemadi, M.; Parvazinia, M., Fabrication of PVA/nanoclay hydrogel nanocomposites and their microstructural effect on the release behavior of a potassium phosphate fertilizer. *Journal of Polymers and the Environment* **2019**, *27* (12), 2925-2932.
132. Ganguly, S.; Das, N. C., Water uptake kinetics and control release of agrochemical fertilizers from nanoclay-assisted semi-interpenetrating sodium acrylate-based hydrogel. *Polymer-Plastics Technology and Engineering* **2017**, *56* (7), 744-761.
133. Narayanan, N.; Gupta, S.; Gajbhiye, V.; Manjaiah, K., Optimization of isotherm models for pesticide sorption on biopolymer-nanoclay composite by error analysis. *Chemosphere* **2017**, *173*, 502-511.
134. Mitter, N.; Worrall, E. A.; Robinson, K. E.; Li, P.; Jain, R. G.; Taochy, C.; Fletcher, S. J.; Carroll, B. J.; Lu, G. M.; Xu, Z. P., Clay nanosheets for topical delivery of RNAi for sustained protection against plant viruses. *Nature plants* **2017**, *3* (2), 1-10.

135. Wang, P.; Lombi, E.; Zhao, F.-J.; Kopittke, P. M., Nanotechnology: a new opportunity in plant sciences. *Trends in plant science* **2016**, *21* (8), 699-712.
136. Li, C.; Wang, P.; Lombi, E.; Cheng, M.; Tang, C.; Howard, D. L.; Menzies, N. W.; Kopittke, P. M., Absorption of foliar-applied Zn fertilizers by trichomes in soybean and tomato. *Journal of Experimental Botany* **2018**, *69* (10), 2717-2729.
137. Eichert, T.; Kurtz, A.; Steiner, U.; Goldbach, H. E., Size exclusion limits and lateral heterogeneity of the stomatal foliar uptake pathway for aqueous solutes and water-suspended nanoparticles. *Physiologia Plantarum* **2008**, *134* (1), 151-160.
138. Uzu, G.; Sobanska, S.; Sarret, G.; Munoz, M.; Dumat, C., Foliar lead uptake by lettuce exposed to atmospheric fallouts. *Environmental Science and Technology* **2010**, *44* (3), 1036-1042.
139. Avellan, A.; Yun, J.; Zhang, Y.; Spielman-Sun, E.; Unrine, J. M.; Thieme, J.; Li, J.; Lombi, E.; Bland, G.; Lowry, G. V., Nanoparticle size and coating chemistry control foliar uptake pathways, translocation, and leaf-to-rhizosphere transport in wheat. *ACS Nano* **2019**, *13* (5), 5291-5305.
140. Larue, C.; Castillo-Michel, H.; Sobanska, S.; Trcera, N.; Sorieul, S.; Cécillon, L.; Ouerdane, L.; Legros, S.; Sarret, G., Fate of pristine TiO₂ nanoparticles and aged paint-containing TiO₂ nanoparticles in lettuce crop after foliar exposure. *Journal of Hazardous Materials* **2014**, *273*, 17-26.
141. Ma, X.; Geiser-Lee, J.; Deng, Y.; Kolmakov, A., Interactions between engineered nanoparticles (ENPs) and plants: phytotoxicity, uptake and accumulation. *Science of the Total Environment* **2010**, *408* (16), 3053-3061.
142. Dietz, K.-J.; Herth, S., Plant nanotoxicology. *Trends in Plant Science* **2011**, *16* (11), 582-589.
143. Aubert, T.; Burel, A.; Esnault, M.-A.; Cordier, S.; Grasset, F.; Cabello-Hurtado, F., Root uptake and phytotoxicity of nanosized molybdenum octahedral clusters. *Journal of Hazardous Materials* **2012**, *219*, 111-118.

144. Zhai, G.; Walters, K. S.; Peate, D. W.; Alvarez, P. J.; Schnoor, J. L., Transport of gold nanoparticles through plasmodesmata and precipitation of gold ions in woody poplar. *Environmental Science and Technology Letters* **2014**, *1* (2), 146-151.
145. Lucas, W. J.; Lee, J.-Y., Plasmodesmata as a supracellular control network in plants. *Nature Reviews Molecular Cell Biology* **2004**, *5* (9), 712-726.
146. Bombo, A. B.; Pereira, A. E. r. S.; Lusa, M. G.; de Medeiros Oliveira, E.; de Oliveira, J. L.; Campos, E. V. R.; de Jesus, M. B.; Oliveira, H. C.; Fraceto, L. F.; Mayer, J. L. S., A mechanistic view of interactions of a nanoherbicide with target organism. *Journal of Agricultural and Food Chemistry* **2019**, *67* (16), 4453-4462.
147. Schwab, F.; Zhai, G.; Kern, M.; Turner, A.; Schnoor, J. L.; Wiesner, M. R., Barriers, pathways and processes for uptake, translocation and accumulation of nanomaterials in plants—Critical review. *Nanotoxicology* **2016**, *10* (3), 257-278.
148. Larue, C.; Laurette, J.; Herlin-Boime, N.; Khodja, H.; Fayard, B.; Flank, A.-M.; Brisset, F.; Carriere, M., Accumulation, translocation and impact of TiO₂ nanoparticles in wheat (*Triticum aestivum* spp.): influence of diameter and crystal phase. *Science of the Total Environment* **2012**, *431*, 197-208.
149. Spielman-Sun, E.; Lombi, E.; Donner, E.; Howard, D.; Unrine, J. M.; Lowry, G. V., Impact of surface charge on cerium oxide nanoparticle uptake and translocation by wheat (*Triticum aestivum*). *Environmental Science and Technology* **2017**, *51* (13), 7361-7368.
150. Li, J.; Tappero, R. V.; Acerbo, A. S.; Yan, H.; Chu, Y.; Lowry, G. V.; Unrine, J. M., Effect of CeO₂ nanomaterial surface functional groups on tissue and subcellular distribution of Ce in tomato (*Solanum lycopersicum*). *Environmental Science: Nano* **2019**, *6* (1), 273-285.
151. Zhu, Z.-J.; Wang, H.; Yan, B.; Zheng, H.; Jiang, Y.; Miranda, O. R.; Rotello, V. M.; Xing, B.; Vachet, R. W., Effect of surface charge on the uptake and distribution of gold nanoparticles in four plant species. *Environmental Science and Technology* **2012**, *46* (22), 12391-12398.

152. Li, H.; Ye, X.; Guo, X.; Geng, Z.; Wang, G., Effects of surface ligands on the uptake and transport of gold nanoparticles in rice and tomato. *Journal of Hazardous Materials* **2016**, *314*, 188-196.
153. Spielman-Sun, E.; Avellan, A.; Bland, G. D.; Tappero, R. V.; Acerbo, A. S.; Unrine, J. M.; Giraldo, J. P.; Lowry, G. V., Nanoparticle surface charge influences translocation and leaf distribution in vascular plants with contrasting anatomy. *Environmental Science: Nano* **2019**, *6* (8), 2508-2519.
154. Lew, T. T. S.; Wong, M. H.; Kwak, S. Y.; Sinclair, R.; Koman, V. B.; Strano, M. S., Rational design principles for the transport and subcellular distribution of nanomaterials into plant protoplasts. *Small* **2018**, *14* (44), 1802086.
155. Wong, M. H.; Misra, R. P.; Giraldo, J. P.; Kwak, S.-Y.; Son, Y.; Landry, M. P.; Swan, J. W.; Blankschtein, D.; Strano, M. S., Lipid exchange envelope penetration (LEEP) of nanoparticles for plant engineering: A universal localization mechanism. *Nano Letters* **2016**, *16* (2), 1161-1172.
156. Hu, P.; An, J.; Faulkner, M. M.; Wu, H.; Li, Z.; Tian, X.; Giraldo, J. P., Nanoparticle Charge and Size Control Foliar Delivery Efficiency to Plant Cells and Organelles. *ACS Nano* **2020**, *14* (7), 7970-7986.
157. Albanese, A.; Tang, P. S.; Chan, W. C., The effect of nanoparticle size, shape, and surface chemistry on biological systems. *Annual Review of Biomedical Engineering* **2012**, *14*, 1-16.
158. Santana, I.; Wu, H.; Hu, P.; Giraldo, J. P., Targeted delivery of nanomaterials with chemical cargoes in plants enabled by a biorecognition motif. *Nature Communications* **2020**, *11* (1), 1-12.
159. Hu, J. J.; Xiao, D.; Zhang, X. Z., Advances in peptide functionalization on mesoporous silica nanoparticles for controlled drug release. *Small* **2016**, *12* (25), 3344-3359.
160. Spielman-Sun, E.; Avellan, A.; Bland, G. D.; Clement, E. T.; Tappero, R. V.; Acerbo, A. S.; Lowry, G. V., Protein coating composition targets nanoparticles to leaf stomata and trichomes. *Nanoscale* **2020**, *12* (6), 3630-3636.

161. Baeza, A.; Colilla, M.; Vallet-Regí, M., Advances in mesoporous silica nanoparticles for targeted stimuli-responsive drug delivery. *Expert Opinion on Drug Delivery* **2015**, *12* (2), 319-337.
162. Trewyn, B. G.; Slowing, I. I.; Giri, S.; Chen, H.-T.; Lin, V. S.-Y., Synthesis and functionalization of a mesoporous silica nanoparticle based on the sol-gel process and applications in controlled release. *Accounts of Chemical Research* **2007**, *40* (9), 846-853.
163. Montalvo, D.; McLaughlin, M. J.; Degryse, F., Efficacy of hydroxyapatite nanoparticles as phosphorus fertilizer in andisols and oxisols. *Soil Science Society of America Journal* **2015**, *79* (2), 551-558.
164. Samavini, R.; Sandaruwan, C.; De Silva, M.; Priyadarshana, G.; Kottegoda, N.; Karunaratne, V., Effect of citric acid surface modification on solubility of hydroxyapatite nanoparticles. *Journal of Agricultural and Food Chemistry* **2018**, *66* (13), 3330-3337.
165. Tripathi, S.; Sonkar, S. K.; Sarkar, S., Growth stimulation of gram (*Cicer arietinum*) plant by water soluble carbon nanotubes. *Nanoscale* **2011**, *3* (3), 1176-1181.
166. Sonkar, S. K.; Roy, M.; Babar, D. G.; Sarkar, S., Water soluble carbon nano-onions from wood wool as growth promoters for gram plants. *Nanoscale* **2012**, *4* (24), 7670-7675.
167. Cao, L.; Zhou, Z.; Niu, S.; Cao, C.; Li, X.; Shan, Y.; Huang, Q., Positive-charge functionalized mesoporous silica nanoparticles as nanocarriers for controlled 2, 4-dichlorophenoxy acetic acid sodium salt release. *Journal of Agricultural and Food Chemistry* **2017**, *66* (26), 6594-6603.
168. Cao, L.; Zhang, H.; Cao, C.; Zhang, J.; Li, F.; Huang, Q., Quaternized chitosan-capped mesoporous silica nanoparticles as nanocarriers for controlled pesticide release. *Nanomaterials* **2016**, *6* (7), 126.
169. Cao, V. D.; Nguyen, P. P.; Khuong, V. Q.; Nguyen, C. K.; Nguyen, X. C.; Dang, C. H.; Tran, N. Q., Ultrafine copper nanoparticles exhibiting a powerful antifungal/killing activity against *Corticium salmonicolor*. *Bulletin of the Korean Chemical Society* **2014**, *35* (9), 2645-2648.

170. Torney, F.; Trewyn, B. G.; Lin, V. S.-Y.; Wang, K., Mesoporous silica nanoparticles deliver DNA and chemicals into plants. *Nature Nanotechnology* **2007**, *2* (5), 295-300.
171. Yang, Y.-J.; Tao, X.; Hou, Q.; Ma, Y.; Chen, X.-L.; Chen, J.-F., Mesoporous silica nanotubes coated with multilayered polyelectrolytes for pH-controlled drug release. *Acta Biomaterialia* **2010**, *6* (8), 3092-3100.
172. Liu, R.; Zhang, Y.; Zhao, X.; Agarwal, A.; Mueller, L. J.; Feng, P., pH-responsive nanogated ensemble based on gold-capped mesoporous silica through an acid-labile acetal linker. *Journal of the American Chemical Society* **2010**, *132* (5), 1500-1501.
173. Muhammad, F.; Guo, M.; Qi, W.; Sun, F.; Wang, A.; Guo, Y.; Zhu, G., pH-triggered controlled drug release from mesoporous silica nanoparticles via intracellular dissolution of ZnO nanolids. *Journal of the American Chemical Society* **2011**, *133* (23), 8778-8781.
174. Yuan, L.; Tang, Q.; Yang, D.; Zhang, J. Z.; Zhang, F.; Hu, J., Preparation of pH-responsive mesoporous silica nanoparticles and their application in controlled drug delivery. *The Journal of Physical Chemistry C* **2011**, *115* (20), 9926-9932.
175. Gao, Y.; Liang, Y.; Dong, H.; Niu, J.; Tang, J.; Yang, J.; Tang, G.; Zhou, Z.; Tang, R.; Shi, X., A Bioresponsive System Based on Mesoporous Organosilica Nanoparticles for Smart Delivery of Fungicide in Response to Pathogen Presence. *ACS Sustainable Chemistry and Engineering* **2020**, *8* (14), 5716-5723.
176. Gao, S.; Tang, G.; Hua, D.; Xiong, R.; Han, J.; Jiang, S.; Zhang, Q.; Huang, C., Stimuli-responsive bio-based polymeric systems and their applications. *Journal of Materials Chemistry B* **2019**, *7* (5), 709-729.
177. Chen, H.; Hu, J.; Zhou, H.; Zhou, X.; Xu, H., One step synthesis, characterization of F127-Mn⁺-chlorpyrifos mesoporous silica for sustained release system with pH sensitivity. *Journal of Macromolecular Science, Part A* **2019**, *56* (1), 34-41.
178. Baldi, E.; Marino, G.; Toselli, M.; Marzadori, C.; Ciavatta, C.; Tavoni, M.; Di Giosia, M.; Calvaresi, M.; Falini, G.; Zerbetto, F., Delivery systems for agriculture: Fe-EDDHA/CaCO₃ hybrid crystals as adjuvants for prevention of iron chlorosis. *Chemical Communications* **2018**, *54* (13), 1635-1638.

179. Niu, N.; He, F.; Ma, P. a.; Gai, S.; Yang, G.; Qu, F.; Wang, Y.; Xu, J.; Yang, P., Up-conversion nanoparticle assembled mesoporous silica composites: synthesis, plasmon-enhanced luminescence, and near-infrared light triggered drug release. *ACS Applied Materials and Interfaces* **2014**, *6* (5), 3250-3262.
180. Li, H.; Tan, L.-L.; Jia, P.; Li, Q.-L.; Sun, Y.-L.; Zhang, J.; Ning, Y.-Q.; Yu, J.; Yang, Y.-W., Near-infrared light-responsive supramolecular nanovalve based on mesoporous silica-coated gold nanorods. *Chemical Science* **2014**, *5* (7), 2804-2808.
181. Zhang, Z.; Wang, L.; Wang, J.; Jiang, X.; Li, X.; Hu, Z.; Ji, Y.; Wu, X.; Chen, C., Mesoporous silica-coated gold nanorods as a light-mediated multifunctional theranostic platform for cancer treatment. *Advanced Materials* **2012**, *24* (11), 1418-1423.
182. Fomina, N.; Sankaranarayanan, J.; Almutairi, A., Photochemical mechanisms of light-triggered release from nanocarriers. *Advanced Drug Delivery Reviews* **2012**, *64* (11), 1005-1020.
183. Chen, C.; Zhang, G.; Dai, Z.; Xiang, Y.; Liu, B.; Bian, P.; Zheng, K.; Wu, Z.; Cai, D., Fabrication of light-responsively controlled-release herbicide using a nanocomposite. *Chemical Engineering Journal* **2018**, *349*, 101-110.
184. Xu, Z.; Gao, Z.; Shao, X., Light-triggered release of insecticidally active spirotetramat-enol. *Chinese Chemical Letters* **2018**, *29* (11), 1648-1650.
185. Zhang, G.; Zhou, L.; Cai, D.; Wu, Z., Anion-responsive carbon nanosystem for controlling selenium fertilizer release and improving selenium utilization efficiency in vegetables. *Carbon* **2018**, *129*, 711-719.
186. Bernardo, M. P.; Guimarães, G. G.; Majaron, V. F.; Ribeiro, C., Controlled release of phosphate from layered double hydroxide structures: dynamics in soil and application as smart fertilizer. *ACS Sustainable Chemistry and Engineering* **2018**, *6* (4), 5152-5161.
187. Koo, A. N.; Rim, H. P.; Park, D. J.; Kim, J.-H.; Jeong, S. Y.; Lee, S. C., Glutathione-mediated intracellular release of anti-inflammatory N-acetyl-L-cysteine from mesoporous silica nanoparticles. *Macromolecular Research* **2013**, *21* (7), 809-814.

188. Cui, Y.; Dong, H.; Cai, X.; Wang, D.; Li, Y., Mesoporous silica nanoparticles capped with disulfide-linked PEG gatekeepers for glutathione-mediated controlled release. *ACS Applied Materials and Interfaces* **2012**, *4* (6), 3177-3183.
189. Kim, H.; Kim, S.; Park, C.; Lee, H.; Park, H. J.; Kim, C., Glutathione-induced intracellular release of guests from mesoporous silica nanocontainers with cyclodextrin gatekeepers. *Advanced Materials* **2010**, *22* (38), 4280-4283.
190. Hou, X.; Li, Y.; Pan, Y.; Jin, Y.; Xiao, H., Controlled release of agrochemicals and heavy metal ion capture dual-functional redox-responsive hydrogel for soil remediation. *Chemical Communications* **2018**, *54* (97), 13714-13717.
191. Yi, Z.; Hussain, H. I.; Feng, C.; Sun, D.; She, F.; Rookes, J. E.; Cahill, D. M.; Kong, L., Functionalized mesoporous silica nanoparticles with redox-responsive short-chain gatekeepers for agrochemical delivery. *ACS Applied Materials and Interfaces* **2015**, *7* (18), 9937-9946.
192. Kaziem, A. E.; Gao, Y.; He, S.; Li, J., Synthesis and insecticidal activity of enzyme-triggered functionalized hollow mesoporous silica for controlled release. *Journal of Agricultural and Food Chemistry* **2017**, *65* (36), 7854-7864.
193. Liang, Y.; Guo, M.; Fan, C.; Dong, H.; Ding, G.; Zhang, W.; Tang, G.; Yang, J.; Kong, D.; Cao, Y., Development of novel urease-responsive pendimethalin microcapsules using silica-IPTS-PEI as controlled release carrier materials. *ACS Sustainable Chemistry and Engineering* **2017**, *5* (6), 4802-4810.
194. Guo, M.; Zhang, W.; Ding, G.; Guo, D.; Zhu, J.; Wang, B.; Punyapitak, D.; Cao, Y., Preparation and characterization of enzyme-responsive emamectin benzoate microcapsules based on a copolymer matrix of silica-epichlorohydrin-carboxymethylcellulose. *RSC Advances* **2015**, *5* (113), 93170-93179.
195. Ye, F.; Qin, J.; Toprak, M. S.; Muhammed, M., Multifunctional core-shell nanoparticles: superparamagnetic, mesoporous, and thermosensitive. *Journal of Nanoparticle Research* **2011**, *13* (11), 6157-6167.
196. Wei, M.; Gao, Y.; Li, X.; Serpe, M. J., Stimuli-responsive polymers and their applications. *Polymer Chemistry* **2017**, *8* (1), 127-143.

197. Zhang, Y.; Chen, W.; Jing, M.; Liu, S.; Feng, J.; Wu, H.; Zhou, Y.; Zhang, X.; Ma, Z., Self-assembled mixed micelle loaded with natural pyrethrins as an intelligent nano-insecticide with a novel temperature-responsive release mode. *Chemical Engineering Journal* **2019**, *361*, 1381-1391.
198. Mattos, B. D.; Tardy, B. L.; Pezhman, M.; Kämäräinen, T.; Linder, M.; Schreiner, W. H.; Magalhães, W. L.; Rojas, O. J., Controlled biocide release from hierarchically-structured biogenic silica: surface chemistry to tune release rate and responsiveness. *Scientific Reports* **2018**, *8* (1), 1-11.
199. Sarkar, D. J.; Singh, A., Base triggered release of insecticide from bentonite reinforced citric acid crosslinked carboxymethyl cellulose hydrogel composites. *Carbohydrate Polymers* **2017**, *156*, 303-311.
200. Grillo, R.; Mattos, B. D.; Antunes, D. R.; Forini, M. M.; Monikh, F. A.; Rojas, O. J., Foliage adhesion and interactions with particulate delivery systems for plant nanobionics and intelligent agriculture. *Nano Today* **2021**, *37*, 101078.
201. Mamaeva, V.; Sahlgren, C.; Lindén, M., Mesoporous silica nanoparticles in medicine—Recent advances. *Advanced Drug Delivery Reviews* **2013**, *65* (5), 689-702.
202. Lohse, S. E.; Murphy, C. J., Applications of colloidal inorganic nanoparticles: from medicine to energy. *Journal of the American Chemical Society* **2012**, *134* (38), 15607-15620.
203. Hofmann, T.; Lowry, G. V.; Ghoshal, S.; Tufenkji, N.; Brambilla, D.; Dutcher, J. R.; Gilbertson, L. M.; Giraldo, J. P.; Kinsella, J. M.; Landry, M. P., Technology readiness and overcoming barriers to sustainably implement nanotechnology-enabled plant agriculture. *Nature Food* **2020**, *1* (7), 416-425.

Connecting Text to Chapter 3

While Chapter 2 reviewed the field of nano-enabled agriculture using inorganic porous nanoparticles as nanocarriers for agrochemicals in general, Chapter 3 presents the reasons why silica has been chosen as the nanomaterial of interest and how it can be used to encapsulate and transport azoxystrobin, a commonly used fungicide in agriculture. In this chapter, a novel protocol was developed to synthesize hollow porous silica nanoparticles (PHSN), which were further characterized in terms of particle size and surface properties using a suite of different techniques, including transmission electron microscopy, light scattering, and nitrogen sorption/desorption isotherms.

Chapter 3. Self-assembled surfactant-templated synthesis of porous hollow silica nanoparticles: mechanism of formation and feasibility of post-synthesis nanoencapsulation

3.1. Abstract

SiO₂ is bioinert and highly functionalizable, thus making it a very attractive material for nanotechnology applications such as drug delivery and nanoencapsulation of pesticides. Herein, we synthesized porous hollow SiO₂ nanoparticles (PHSN) by using cetyltrimethylammonium bromide (CTAB) and Pluronic P123 as the structure directing agents. The porosity and hollowness of the SiO₂ structure allow for the protective and high-density loading of molecules of interest inside the nanoshell. We demonstrate here that loading can be achieved post-synthesis through the pores of the PHSN. The PHSN are monodisperse with a mean diameter of 258 nm and a specific surface area of 287 m² g⁻¹. The mechanism of formation of the PHSN was investigated using 1-D and 2-D solid-state nuclear magnetic resonance (SS-NMR) and Fourier-transform infrared spectroscopy (FTIR). The data suggest that CTAB and Pluronic P123 interact forming a hydrophobic spherical hollow cage that serves as template for the hollow-porous structure. After synthesis, the surfactants were removed by calcination under 550°C and the PHSN were added to a Fe³⁺ solution followed by addition of the reductant NaBH₄ to the suspension, which led to the formation of Fe(0) NPs both on the PHSN and inside the hollow shell, as confirmed by transmission electron microscopy imaging. The imaging of the formation of Fe(0) NPs inside the hollow shell provides direct evidence of transport of solute molecules across the shell and their reactions within the PHSN, making it a versatile nanocarrier and nanoreactor.

3.2. Introduction

The development of different methods to synthesize mesoporous SiO₂ nanoparticles (MSN) has generated a lot of interest from the research community due to the promising application of MSN as a nanocarrier system. SiO₂ is an earth-abundant, bioinert compound and thus, can be safely used for many in vivo applications, particularly in medicine and agriculture.¹ In medicine for example, MSN have been tested for targeted drug delivery,² where drugs are loaded into the SiO₂ matrix and inoculated in HeLa cells – an immortal human cell line. Regli et al.³ encapsulated ibuprofen

and silicon nanocrystals inside an MSN in order to create a platform for combined drug delivery and bioimaging. The high specific surface area of MSN (greater than $1000 \text{ m}^2 \text{ g}^{-1}$), the ability to tune pore sizes and to functionalize the surface with different biomolecules enable the application of these nanoparticles for targeted binding to specific cellular sites.⁴ In agriculture, pesticides have been loaded in MSN nanocarriers and applied to plants to assess whether the pesticide in nanoformulations have either higher uptake, longevity or offer greater protection rather than pesticides applied with the traditional methods without nanocarriers.⁵ Furthermore, inorganic compounds such as silica are micronutrients for plants and have low toxicity potential, and thus, are a promising encapsulation medium for pesticides, nutrients, or other growth factors in agriculture.⁶

An alternative structure to MSN that offers many of the advantages, but also a higher internal loading volume for active ingredient molecules, is the porous hollow SiO_2 nanoparticle (PHSN). The higher internal volume can provide high local concentrations of active ingredients, and the potential for significantly higher loading per unit mass of silica, compared to MSN. Furthermore, PHSN can be used as a delivery agent that provides the slow release of active ingredient to the exterior over a more extended period. PHSN are being tested as drug delivery systems for cancer treatment for their slow release properties.⁷ The shell can also protect active ingredients from influence by certain environmental conditions. Li et al.⁸ demonstrated that the PHSN provided UV-shielding of the pesticide avermectin.

A common approach to synthesize PHSN is to grow the silica matrix around hard-template materials, such as polystyrene beads⁹ or resorcinol-formaldehyde resin nanospheres,¹⁰ which are further removed by calcination or solvent extraction to create a hollow-core nanoshell. This is a lengthy procedure and can leave contamination in the PHSN. The hard-template synthesis also requires the functionalization of the template to allow the deposition of the silica coating.¹¹ This requirement is eliminated with soft-template methods, which involves the use of one or more surfactants associated with a swelling agent – usually an oil phase. In the work of Wibowo et al.,¹² Miglyol 812, a nontoxic oil used for pharmaceutical formulations was used along with a customized polypeptide to form a positively charged nanoemulsion, which, in turn, attracted the silica precursor to the water-oil interface.

Herein, we report the synthesis protocol to produce PHSN using CTAB and Pluronic P123 only, without the use of a solid or liquid (oil) phase as template. Thus, reducing the excessive use of organic solvents and the necessity to modify hard-template structures. CTAB was selected because it is a well-known pore directing agent for the synthesis of mesoporous silica nanoparticles since the introduction of MCM-41 in 2001.¹³ CTAB self-assembles forming an ordered hexagonal mesophase micelle¹⁴ which serves as a template for a symmetrical distribution (in terms of both size and structure) of pores in the silica matrix after calcination. Pluronic P123 with its spherical micellar structure comprised of hydrophobic core (polypropylene oxide) and hydrophilic corona (polyethylene oxide)¹⁵ served as the agent causing the formation of the hollow core-template for the PHSN.

The morphology and mechanism of formation of the PHSN were studied using microscopy and spectroscopy techniques. More specifically, transmission electron microscopy (TEM) was performed to assess the PHSN shape and size, and nitrogen adsorption/desorption experiments were performed to characterize surface area and pore size distribution. Solid-state nuclear magnetic resonance (NMR) and Fourier-transform infrared spectroscopy (FTIR) analyses were performed to identify bonds and the chemical environment of different elements during the synthesis towards developing an understanding of the mechanism of formation of the PHSN.

Although, alternative micellar soft-templated synthesis has been shown with a range of different surfactants,¹⁶⁻¹⁸ they produce PHSN with very different characteristics in terms of particle size, pore size distribution and shell thickness. Herein, we used CTAB and Pluronic P123 to produce PHSN with unique characteristics to be used in diverse downstream applications, such as the encapsulation of organic compounds or other nanoparticles. In addition, we characterized in detail the mechanism of formation that dictates the structure of this PHSN. Some other studies have used solely CTAB, or solely Pluronic P123, or a combination of both to produce MSN¹⁹⁻²¹ but not PHSN. Furthermore, the previous studies did not provide evidence for whether the particles had porous shells.

Encapsulating functional biomolecules inside nanocarriers for efficient transport and uptake at biological target locations is an emerging application of nanotechnology in medicine and agriculture.^{22,23} However, although many studies²⁴⁻²⁷ report encapsulation of drugs, pesticides and biomolecules post-synthesis, they do not provide direct evidence (e.g., imaging) of the transport

of the target molecules into the hollow core of the PHSN. Slow-release rates are often cited as evidence of loading inside nanocarriers, but release rates of encapsulated compounds do not prove that the compounds were contained inside the nanoparticle core, because slow-release can occur from the compounds adsorbed on the nanoparticle pores.

We address this major knowledge gap concerning nanoencapsulation by imaging internalized compounds, post-synthesis, in the PHSN. Two different compounds ($\text{FeCl}_3 \cdot 6\text{H}_2\text{O}$ and NaBH_4), were added sequentially to the PHSN. The formation of $\text{Fe}(0)$ inside the PHSN, as shown by TEM imaging, suggests that Fe^{3+} and BH_4^- migrated to the hollow core and reacted to form $\text{Fe}(0)$ NPs. This post-synthesis encapsulation process could suggest that not only transport of mass between the interior and exterior of the nanoshell does happen, but also that reactions could take place within the PHSN. Having compounds internalized in a rigid porous structure such as a PHSN, post-synthesis, could ensure application of the nanocarriers with maximum loading and without the need for subsequent steps (e.g., calcination or acid-washing) that could otherwise damage the loaded compounds. Iron nanoparticles encapsulated in silica have promising applications in power transformers, magnetic recording heads, microwave, and magnetic sensing.²⁸

It should be noted that encapsulating compounds during synthesis, as opposed to post-synthesis, may present some drawbacks: (1) if the shell is not porous, the encapsulated material will not be released unless the nanoparticle is disassembled, and (2) if the material has its pores filled by surfactants due to the synthesis, a subsequent step to open up these pores may be required, such as calcination and acid extraction. Both calcination and acid extraction, however, may risk destroying the encapsulated materials if they do not possess heat and/or acid resistant properties.

3.3. Experimental Section

3.3.1. Materials

Tetraethyl orthosilicate ($\text{Si}(\text{OC}_2\text{H}_5)_4$, TEOS) reagent grade 98%, ammonium hydroxide solution (NH_4OH , 28.0-30.0% NH_3 basis), hexadecyltrimethylammonium bromide ($\text{C}_{19}\text{H}_{42}\text{BrN}$, CTAB), symmetric triblock copolymer Pluronic P123 and sodium borohydride (NaBH_4 , 99.99%) were purchased from Sigma-Aldrich. Deionized (DI) water ASTM type 1 was purchased from Thermo

Fisher Scientific. Ethyl alcohol (anhydrous, 100%) was purchased from Commercial Alcohols (Canada). Iron (III) chloride ($\text{FeCl}_3 \cdot 6\text{H}_2\text{O}$, 99.9%) was purchased from Acros Organics.

3.3.2. Synthesis of PHSN

In a single-neck 500 mL round-bottom flask, DI water, ethanol (33% v/v), ammonium hydroxide solution (6.7% v/v), CTAB (3.6 mM) and Pluronic P123 (0.7 mM) were added sequentially and stirred under 1000 rpm for 1 hour, until the reagents were completely dissolved. Then, TEOS (45 mM) was added dropwise at a rate of 0.75 mL/min. The solution acquired a milky color after 2 minutes and remained under magnetic stirring (1000 rpm) for 5 hours. Next, the solution was dried overnight under 80°C. In order to remove the surfactants, the PHSN dried powder was calcined at 550°C for 5 hours. Table S1 have the exact volumes and weight of each chemical used in a standard batch.

3.3.3. Characterization of PHSN

The frequency distribution of the hydrodynamic diameters of PHSN was obtained from dynamic light scattering (DLS) using Malvern Zetasizer Nano ZS (Malvern Instruments, UK). DLS analysis was conducted using PHSN suspensions in DI water with a concentration of 100 ppm. The morphology and thickness of the PHSN shell were determined by transmission electron microscopy (TEM) using a Philips model CM200 TEM at an acceleration voltage of 200 kV. For TEM analysis, 10 μL of the 100 ppm PHSN suspension placed on lacey carbon-coated grids and air-dried. The surface area and pore size distributions were determined by nitrogen adsorption/desorption experiments in a Quantachrome Autosorb-1 (Quantachrome GmbH & Co., Netherlands) using the Brenauer-Emmet-Teller (BET) and Barrett-Jyner-Halenda (BJH) approaches, respectively.

3.3.4. Understanding the synthesis mechanism of formation with SS-NMR and FTIR

Solid-State NMR experiments were performed on a Varian VNMRS with wide-bore 9.4T magnet and Varian T3 double-resonance 4 mm probe. A set of one-dimensional (1-D) and two-dimensional (2-D) NMR were performed, including 1-D single-pulse magic angle spinning (MAS) ^1H , 1-D cross-polarization (CP) MAS ^{13}C (3000 number of scans), 1-D CP-MAS ^{29}Si (512 number of scans), 2-D ^1H - ^1H exchange MAS, 2-D ^1H - ^{13}C heteronuclear correlation (HETCOR) and 2-D ^1H - ^{29}Si HETCOR. The resonance frequency for ^1H , ^{13}C and ^{29}Si were respectively 399.8, 100.5 and 79.4 MHz. The spin rates were 10 kHz. The recycle delays were 4s, except to compute the

relaxation times T_1 and $T_{1\rho}$ when it was 120 s. Total time for the 2-D experiments were 24h, 18h and 1.5 h for ^1H - ^{13}C HETCOR, ^1H - ^{29}Si HETCOR and ^1H - ^1H exchange respectively. Acquisition times were 15ms for ^{13}C , 20ms ^{29}Si , 200 ms for ^1H and 2s for ^1H - ^1H exchange. CP contact times were 1500 μs for ^{13}C and 1000 μs for ^{29}Si HETCOR. The mixing times for ^1H - ^1H exchange were 20 ms and 100 ms. The spectra were obtained for calcined PHSN and pre-calcined PHSN.

FTIR spectra for pure CTAB, Pluronic P123, PHSN pre and post-calcination were obtained with a Spectrum II (Perkin Elmer) Spectrometer with a single bounce diamond crystal. Spectra were recorded in the range from 4000 to 400 cm^{-1} at a resolution of 1 cm^{-1} . Approximately 70 mg of each sample was deposited on the diamond crystal for analysis.

3.3.5. Assessment of encapsulation in PHSN post-synthesis and calcination

To obtain direct visual proof if the void in the PHSN can contain mass that is supplied externally post-synthesis, we created iron nanoparticles in the presence of PHSN by adding $\text{FeCl}_3 \cdot 6\text{H}_2\text{O}$ and NaBH_4 . All the steps were carried out inside an anaerobic chamber containing an atmosphere of $\text{N}_2:\text{H}_2$ at a ratio of 99:1, or in sealed vials assembled inside the chamber. Firstly, $\text{FeCl}_3 \cdot 6\text{H}_2\text{O}$ (600 mg) was solubilized in a mixture of DI water (21 mL) and ethanol (9 mL) previously purged with nitrogen for 40 minutes. Secondly, 400 mg of PHSN was suspended in the FeCl_3 solution in a sealed vial was sonicated in a water bath at 37 kHz for 60 minutes (Fisherbrand 112xx Series, Thermo Fisher Scientific, operated at 100% power). The suspension was then centrifuged at 8500 rpm for 10 minutes and the supernatant was discarded. Next, the pellet was washed with degassed DI water to remove the non-internalized ferrous ions. A second solution was prepared by dissolving NaBH_4 (200 mg) in degassed DI water (6 mL). Then, 2 mL of the NaBH_4 solution was added dropwise over the FeCl_3 @PHSN pellet. The pellet was allowed to dry inside the chamber.

The PHSN with the Fe NPs were imaged and analyzed with TEM and energy-dispersive X-ray (EDX) spectrum using a Philips model CM200 TEM at an acceleration voltage of 200 kV by placing the dried powder directly on a lacey carbon-coated TEM grid.

3.4. Results and Discussions

3.4.1. PHSN Characterization

The Z-average hydrodynamic diameter measured by DLS was 258 nm (Figure 3-1a). The size distribution showed a monodisperse population of particles with a polydispersity index (PdI) of

0.187. Similar particle size distribution was obtained from TEM (Figure 3-1b) with an average diameter of 253 nm (N=100). The TEM image (Figure 3-1c) showed synthesized PHSN as spherical shells, with most of the particles having shell thickness ranging from 22 to 38 nm and the core diameter ranging from 130 to 151 nm. The size of the pores is not clear from the TEM images; therefore, nitrogen adsorption-desorption experiments were performed to identify and quantify the porosity in the SiO₂ shell. The surface area obtained from the BET method was 287 m² g⁻¹ and, as shown in Figure 3-1d, the nitrogen sorption/desorption profile exhibited characteristic type IV isotherm which is expected in the presence of cylindrical micropores.²⁹ The pore size distribution obtained from the BJH approach confirmed the presence of micropores, ranging between 1.5 and 2 nm (Figure 3-1d inset). The information about the available volume inside the shell and the pore size distribution help us understand what kind of compounds could be internalized and confined as cargo within the PHSN.

Interestingly, in this study the size of the nanoparticles did not change by varying the concentration of surfactants. However, the structure itself changed significantly when the ratio between CTAB and Pluronic P123 varied as seen in the TEM images of Figure S3-1. While the optimal ratio of CTAB:Pluronic P123 to synthesize hollow-porous silica nanoparticles was found to be 0.35:1 wt%, in cases with excess CTAB the nanoparticle no longer featured a shell but rather formed a solid-porous silica nanoparticle, similar to an MSN (Fig S3-1a). When, however, Pluronic P123 was in excess, the nanoparticle featured a larger hollow core and a much thinner SiO₂ shell (Figure S3-1b). It is interesting to note that in some studies using different surfactants, particle size varied with different surfactant concentrations but with no effect on the structure itself. For instance, in the work of Nakashima et al.³⁰ using polyacrylic acid, they obtained particles between 10 and 20 nm. In the work of Ikari et al.³¹ using hexadecyltrimethylammonium chloride (CTAC) and Pluronic F127, they obtained porous particles from 50 to 150 nm. Lastly, in the work of Lv et al.³² using CTAC and triethanolamine (TEA), they obtained porous particles between 20 and 110 nm.

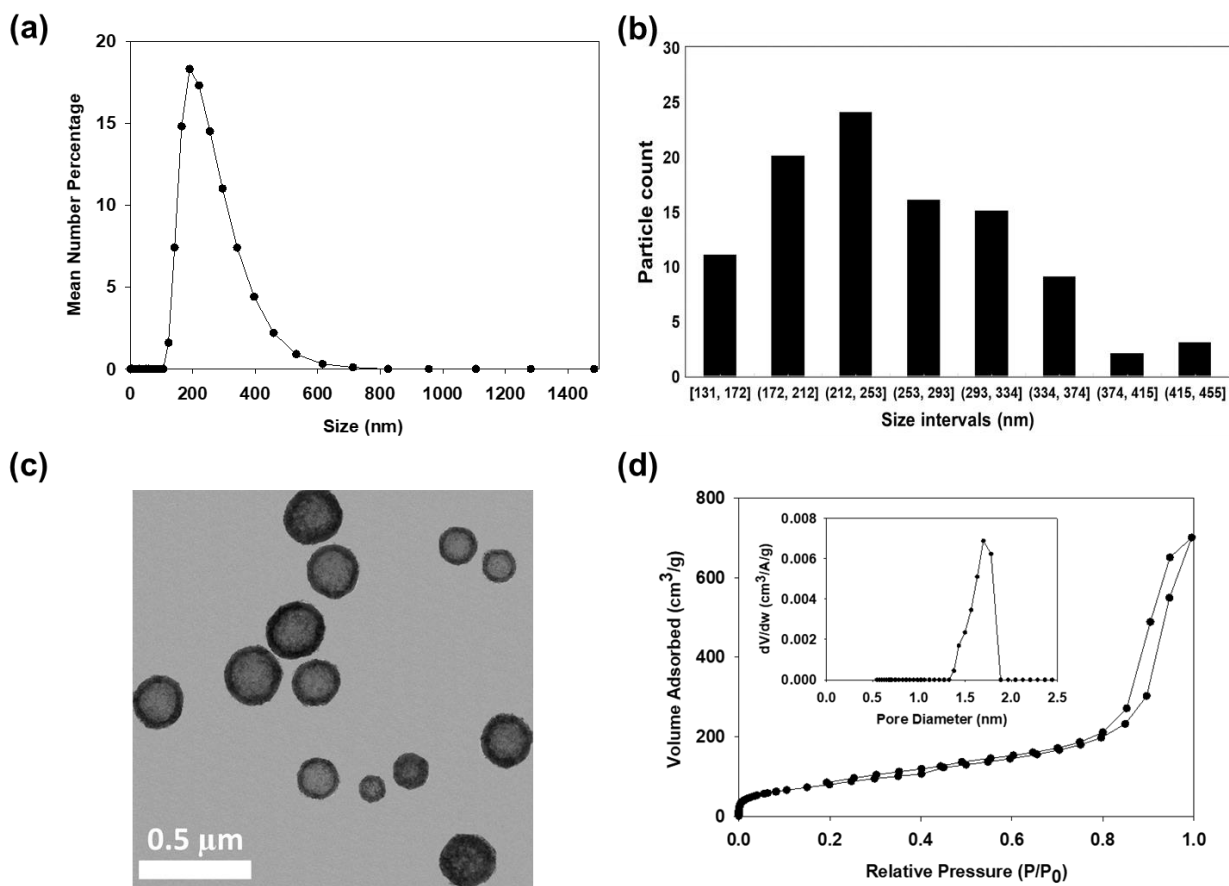


Figure 3-1. The upper images represent (a) the particle size distribution of calcined PHSN obtained from DLS and (b) the particle size distribution (N=100) of calcined PHSN from TEM. The lower figures represent (c) the TEM image of calcined PHSN, (d) the nitrogen sorption/desorption isotherm type IV profile and (d, inset) the pore size distribution of calcined PHSN obtained from BET and BJH respectively.

3.4.2. Interactions and bonds between Pluronic P123, CTAB and SiO₂ with SS-NMR spectra

1-D CP-MAS ²⁹Si (Figure 3-2a), 1-D CP-MAS ¹H (Figure 3-3a), 1-D CP-MAS ¹³C (Figure 3-3b), 2-D ¹H-²⁹Si HETCOR (Figure 3-3c), 2-D ¹H-¹³C HETCOR (Figure 3-3d) and 2-D ¹H-¹H exchange MAS (Figure 3-4) SS-NMR spectra were obtained for pre-calcined PHSN (pcal-PHSN), and 1-D CP-MAS ²⁹Si (Figure 3-2b) was obtained for calcined PHSN (PHSN). Note that both Q³ Si (≡Si-OH) and Q⁴ Si (≡Si-O-Si≡) were present in the pcal-PHSN (Figure 3-2a) and only Q⁴ Si in the PHSN (Figure 3-2b). Q⁴ Si represents Si atoms bound to O atoms, which in their turn bind to other Si atoms (Figure 3-2d). In Q³ Si, however, only three oxygen are bound to other Si atoms whereas

the fourth oxygen is associated with H (Figure 3-2c). Analysis of both the SS-NMR and FTIR spectra (discussed in the following section), suggests that Q³ Si and Q⁴ Si were present in the conjugate between a Pluronic-CTA⁺ complex and the SiO₂ precursor in the pre-calcined system. The presence of Q³ and Q⁴ Si in pcal-PHSN, and the absence of Q³ Si in PHSN suggest a shift in the chemical environment around the Si atom as a result of calcination.

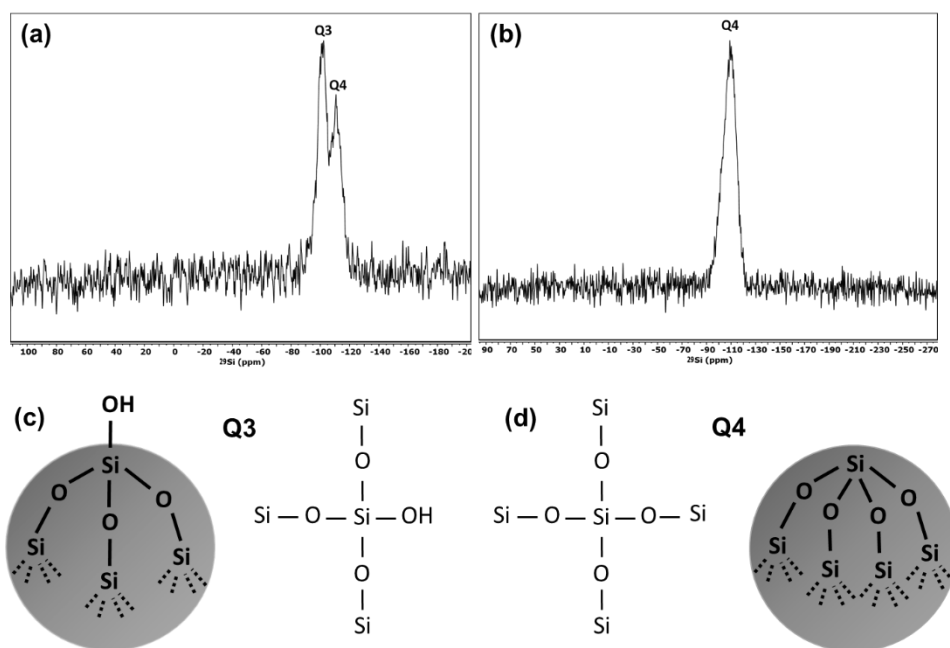


Figure 3-2. The upper images are SS-NMR spectra of (a) as-synthesized PHSN and (b) calcined PHSN. The lower images are schematic representations of (c) Q³ and (d) Q⁴ Si.

In the 1-D CP-MAS ¹H spectrum of pcal-PHSN (Figure 3-3a), we can identify the peaks for the protons in Pluronic, CTAB and Q³ Si. For Pluronic P123, the methyl (CH₃) group in the PPO block is assigned at 1.27 ppm, the methylene (CH₂) group in the PPO block is assigned at 3.82 ppm, the methine group bound to oxygen in the PPO block is assigned at 3.51 ppm and both the methylene groups bound to oxygen in the PEO block are assigned at 3.68 ppm. These observations are consistent with the work of Bae and Han.³³ The peak at 1.27 ppm and the shoulder at 1 ppm were attributed to an overlap of signals from the methylene groups of the CTAB and the methyl (CH₃) group in the PPO block.³⁴ The methyl groups of the hydrophilic head of CTAB are assigned in the same region and could explain the shoulder at 1.46 ppm. Once again, there may be an overlap between the resonance for -CH₂-N(CH₃)₃ protons of the hydrophilic head of CTAB, and the methylene and methine groups in Pluronic. This could potentially suggest that the

hydrophilic head of CTAB aligns with the less hydrophobic moieties (PEO chains) and away from the hydrophobic core of Pluronic (the PPO chain). The negatively charged hydrolyzed TEOS (SiO_2 precursor) is attracted by the positively charged Pluronic-CTAB structure – as hypothesized above – provided by the CTA^+ ions, which are located in the conjugate-water interface, whereas the PPO hydrophobic core is confined in the core. The broad peak at 5.37 ppm is assigned to the protons in Q^3 Si which is confirmed by the HETCOR ^1H - ^{29}Si spectra (Figure 3-3c). There, the resonance is observed exactly in the Q^3 Si peak and the peak at 5.37 ppm. In the CP-MAS ^{13}C (Figure 3-3b) spectrum the peaks can be assigned for the carbons in CTAB and Pluronic molecules with the support of the HETCOR ^1H - ^{13}C spectra (Figure 3-3d). The peak at 30 ppm which had the highest density of protons is assigned to the carbon in the methyl groups for both Pluronic and CTAB. The peak at 53.6 ppm is assigned to the methine group in the PPO block of Pluronic and the peak at 70.6 ppm is right in between the methylene groups in PPO and PEO blocks.

The 2-D exchange ^1H - ^1H correlation spectra indicate how neighboring protons interact and their chemical environment at mixing times of 20 ms (Figure 3-4a) and 100 ms (Figure 3-4b). As the experiment proceeds from 20 ms to 100 ms, we can observe an interaction among the protons in the Q^3 Si and protons from the hydrocarbons, suggesting they are sufficiently close. The relaxation times (T_1 and $T_{1\rho}$), shown in Table S3-2, represent one common T_1 (values ranging from 0.442 and 0.571 s with standard deviation of 9%) and multiple $T_{1\rho}$ (values ranging from 0.004 to 0.044 s with standard deviation of 55%) which suggests that the average distance between the functional groups are between 5 and 50 nm.³⁵ The spread of the proton resonance in HETCOR ^1H - ^{29}Si spectra (Figure 3-4a and 3-4b) towards the methylene groups and the presence of Q^3 Si in the PHSN could possibly suggest that the Si-O groups are sufficiently close to the methylene groups only present in the PEO chains of the Pluronic.

Overall, the SS-NMR spectra observations show: (i) A chemical shift around the Si atom (possibly caused by the interaction between the negatively charged SiO_2 colloids and the positively charged CTA^+ cations from the Pluronic- CTA^+ complex). (ii) An overlap between the methylene groups of CTAB and methyl groups in the PPO block of the Pluronic P123 (possibly indicating that the CTAB hydrophilic head and PEO chains of Pluronic in the surfactant-water interphase, whereas the PPO hydrophobic chains are confined in the core).

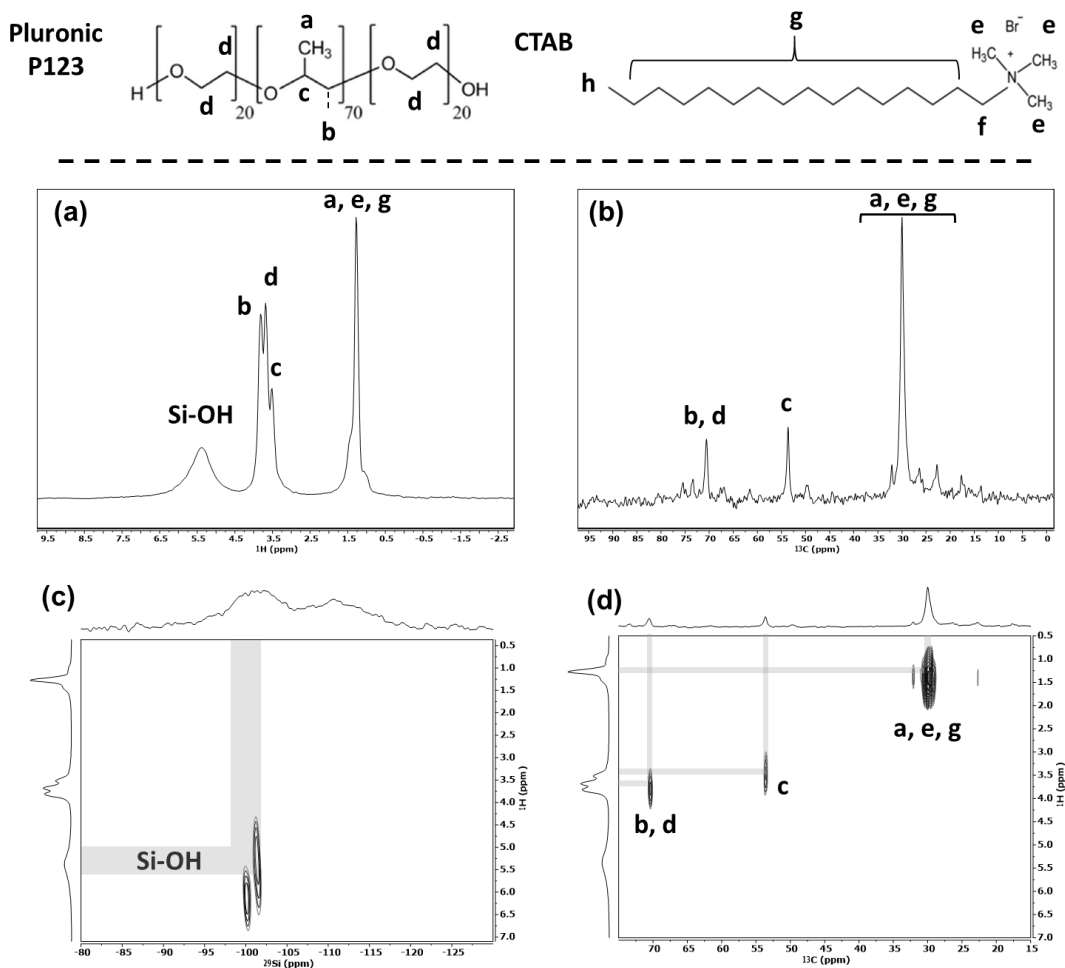


Figure 3-3. The upper image illustrates Pluronic P123 and CTAB structures with protons labeled from a to h. The lower images represent the pcal-PHSN SS-NMR spectra of (a) 1-D CP-MAS ^1H , (b) 1-D CP-MAS ^{13}C , (c) 2-D ^1H - ^{29}Si HETCOR and (d) 2-D ^1H - ^{13}C HETCOR.

These observations were only possible because SS-NMR techniques track Si, H and C atoms individually while less specific techniques, such as FTIR, is best used to define the presence or absence of functional groups. That is, although FTIR, a less specific technique, can be used complementary to support NMR observations, FTIR alone could not precisely explain what is happening with functional groups individually. Martins et al.³⁶ study showed how combining FTIR and NMR techniques permitted a comprehensive investigation of the chemical environment around silicate domains. Below, we describe the FTIR spectra and indicate how they are consistent with the observations from the SS-NMR.

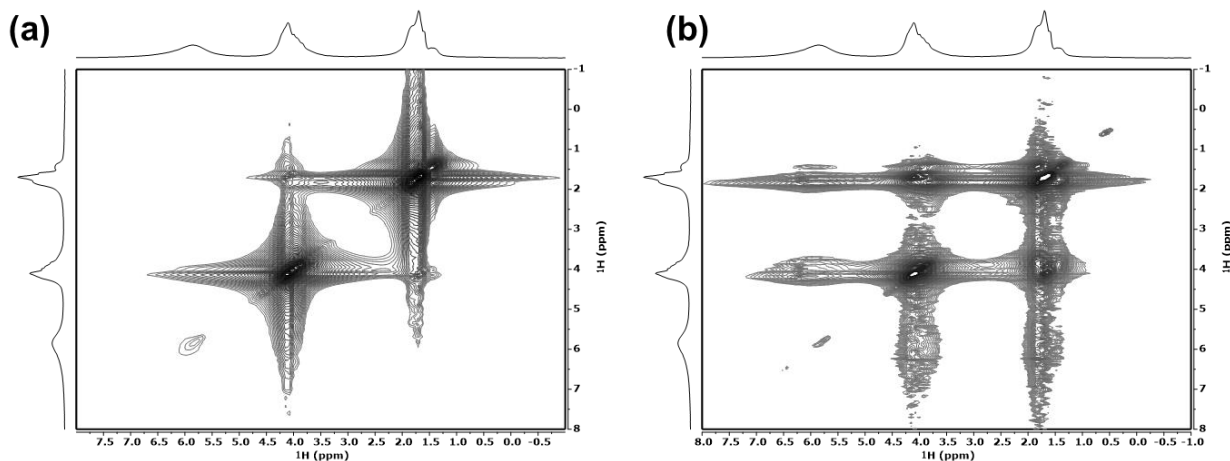


Figure 3-4. PHSN SS-NMR spectra of 2-D ^1H - ^1H exchange MAS with (a) mixing time = 20 ms and (b) mixing time = 100 ms.

3.4.3. Using FTIR to complement the information obtained with SS-NMR

FTIR spectra were obtained for pure CTAB, pure Pluronic P123, pre-calcined PHSN (pcal-PHSN) and calcined PHSN (PHSN) shown in Figure 3-5. Clear differences between the pcal-PHSN and PHSN spectra could be observed (Figure 3-5a, 3-5b and 3-6c) which could be related to the fact that the pre-calcined particle still have surfactants and residual ammonia (from the NH_4OH) associated with it from the synthesis. More specifically, these differences are noted in the $1000\text{--}900\text{ cm}^{-1}$, $1500\text{--}1300\text{ cm}^{-1}$ and $3000\text{--}2800\text{ cm}^{-1}$ regions (Figure 5a, b and c), all of which are present in the pcal-PHSN spectrum and absent in the PHSN spectrum. These bands are assigned as below.

The band at 955 cm^{-1} present in the pcal-PHSN possibly indicates the presence of Si-OH bond (Figure 3-5a). The absence of the same band in the PHSN supports the observations in the SS-NMR and possibly suggests that $\text{Q}^3\text{ Si}$ (Figure 3-2c) content is transformed into $\text{Q}^4\text{ Si}$ (Figure 3-2d) eliminating the band assigned to Si-OH bond. This could suggest a shift in the chemical environment around the Si atom after the calcination and, as discussed in the 1-D CP-MAS ^{29}Si spectra, this shift could be attributed to the interaction between the SiO_2 precursor and the CTA^+ ions of the Pluronic- CTA^+ complex.

The $3000\text{--}2800\text{ cm}^{-1}$ region shows characteristic bands for CTAB – C-H stretch of sp^3 hybridized carbon $-\text{CH}_3$ at 2855 cm^{-1} and C-H stretch of sp^3 hybridized carbon $-\text{CH}_2$ at 2925 cm^{-1} – and for Pluronic P123 – symmetric C-H stretch of $-\text{CH}_2$ broad peak from 2893 to 2865 cm^{-1}

(Figure 3-5b). Even though these characteristic bands are present in the pcal-PHSN and absent in PHSN, some of them are shifted towards high energy levels and/or are broader than the ones observed in the pure surfactants. These changes could possibly suggest that the chemical environment of these bonds is different in the pure molecules from when they are associated with the silica nanoparticles. One change is the shift of the CTAB characteristics bands from 2850 cm^{-1} (C-H stretch of $-\text{CH}_3$) and 2915 cm^{-1} (C-H stretch of $-\text{CH}_2$) towards 2855 cm^{-1} and 2925 cm^{-1} (Figure 3-5c). This shift in the energy level is consistent with the work of Poyraz et al.³⁷ and with the observations in the 1-D CP-MAS ^{29}Si (Figure 3-2a and 3-2b). In fact, they concluded that CTA^+ ions from CTAB are crucial for the surfactant- SiO_2 assembly, because the CTA^+ ions provide positive charge to the Pluronic- CTA^+ complex, thus attracting the silica precursor with large negative zeta potential at neutral and basic pH.^{37, 38} The Pluronic broad band from 2865 cm^{-1} to 2893 cm^{-1} (symmetric C-H stretch of $-\text{CH}_2$) almost disappeared (Figure 5c). Pluronic peak at 2933 cm^{-1} (asymmetric C-H stretch of $-\text{CH}_2$) also disappeared or was overlapped (Figure 5c). As intensity provides information about concentration, and the amount of CH_2 groups in 850 mg of Pluronic P123 is greater than the amount of CH_2 groups in 300 mg of CTAB, the suppression or overlapping of bands in those regions of the pcal-PHSN spectra could indicate structural changes related to the CH_2 groups in Pluronic P123. As explained above for the CTA^+ ions, these shifts in energy levels may be attributed to the formation of the Pluronic- CTA^+ complex.

Differences between pure materials and pcal-PHSN spectra can also be observed in the $1500\text{-}1300\text{ cm}^{-1}$ region (Figure 3-5b). The Pluronic peak at 1344 cm^{-1} (CH_2 wag) slightly shifted to higher energy levels. The region between $1600\text{-}1650\text{ cm}^{-1}$ is only present in pcal-PHSN due to the N-H bending³⁹ in residual ammonia in the system from the synthesis process (Figure 3-5b).

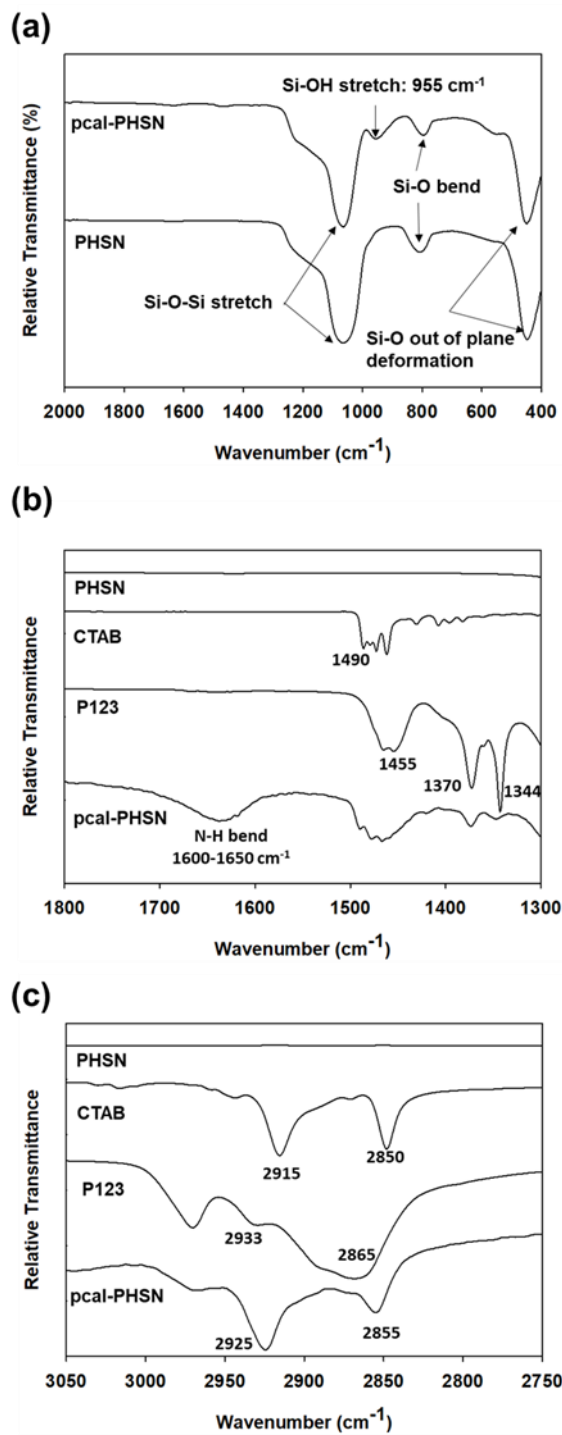


Figure 3-5. FTIR spectra of the (a) 400-200 cm⁻¹ region, (b) 1300-1800 cm⁻¹ region and (c) 2750-3050 cm⁻¹ region.

3.4.4. Mechanisms of formation and structure of PHSN

The TEM image, pore size distribution, SS-NMR spectra and FTIR spectra provide meaningful information about the shape and morphology of the PHSN as well as the chemical environment and bonds involved in the structure. Combining all this information, we could suggest the possible mechanism of formation of the PHSN (Figure 3-6). From the FTIR spectra, there are indications that Pluronic P123 formed a positively charged complex with CTA^+ ions possibly attracting/anchoring the SiO_2 from the hydrolyzed TEOS to create the SiO_2 shell. Q^4 Si (Figure 3-2d) are more hydrophobic and tend to be formed towards the core, while the more hydrophilic Q^3 Si (Figure 3-2c) are located in the interface between the surfactant complex and the aqueous phase, allowing condensation between hydrolyzed TEOS to happen and thus growing the silica shell. The observation of the proximity among the PEO chains, CTAB and the Q^3 Si is also consistent with the FTIR and SS-NMR spectra. The PEO extremities of the Pluronic P123 aligned with each other forming a hydrophobic core structure of PPO chains with outward projections comprised of PEO chains and the CTAB (Figure 3-6). The CTAB deposited parallelly to and in between the PEO chains of the Pluronic. The hydrophobic tail of CTAB was in proximity to the PPO hydrophobic region, whereas the hydrophilic head was pointed towards the PEO hydrophilic terminus. This structure is consistent with the Pluronic- CTA^+ complex model proposed by Poyraz et al.³⁷ Although Poyraz et al. demonstrated the formation of a Pluronic- CTA^+ complex, this study shows for the first time that a Pluronic- CTA^+ complex can self-assemble in a configuration that allows the SiO_2 precursor to form a spherical template for PHSN synthesis. The complexes formed by Pluronic P123 and CTAB in the study by Poyraz et al. led to formation of templates for silica nanorods. The hydrophobic core of the nanoemulsion in this study corresponds to the template onto which the SiO_2 precursor electrostatically attaches to form the PHSN shell and the CTAB long hydrocarbon chains were responsible for the meso-scaled pores in the shell. After calcination, the Pluronic P123 core and CTAB were removed from the system, making the SiO_2 nanoshell hollow and porous.

3.4.5. Internalization of $\text{FeCl}_3/\text{NaBH}_4$ and formation of iron nanoparticles inside the PHSN

The PHSN in the TEM images (Figure 3-7a to 3-7f) were filled with darker smaller circles which indicated the presence of Fe(0) nanoparticles. The existence of Fe was confirmed with EDX (Figure 3-7g), which showed peaks for Fe indicating the presence of iron species, Si and O

indicating the presence of SiO₂, the Cu and C peaks are from the lacey TEM grids which have a base of copper and are coated with carbon, and lastly, the Na peak is presumably derived from unwashed sodium from NaBH₄ that remained in the system.

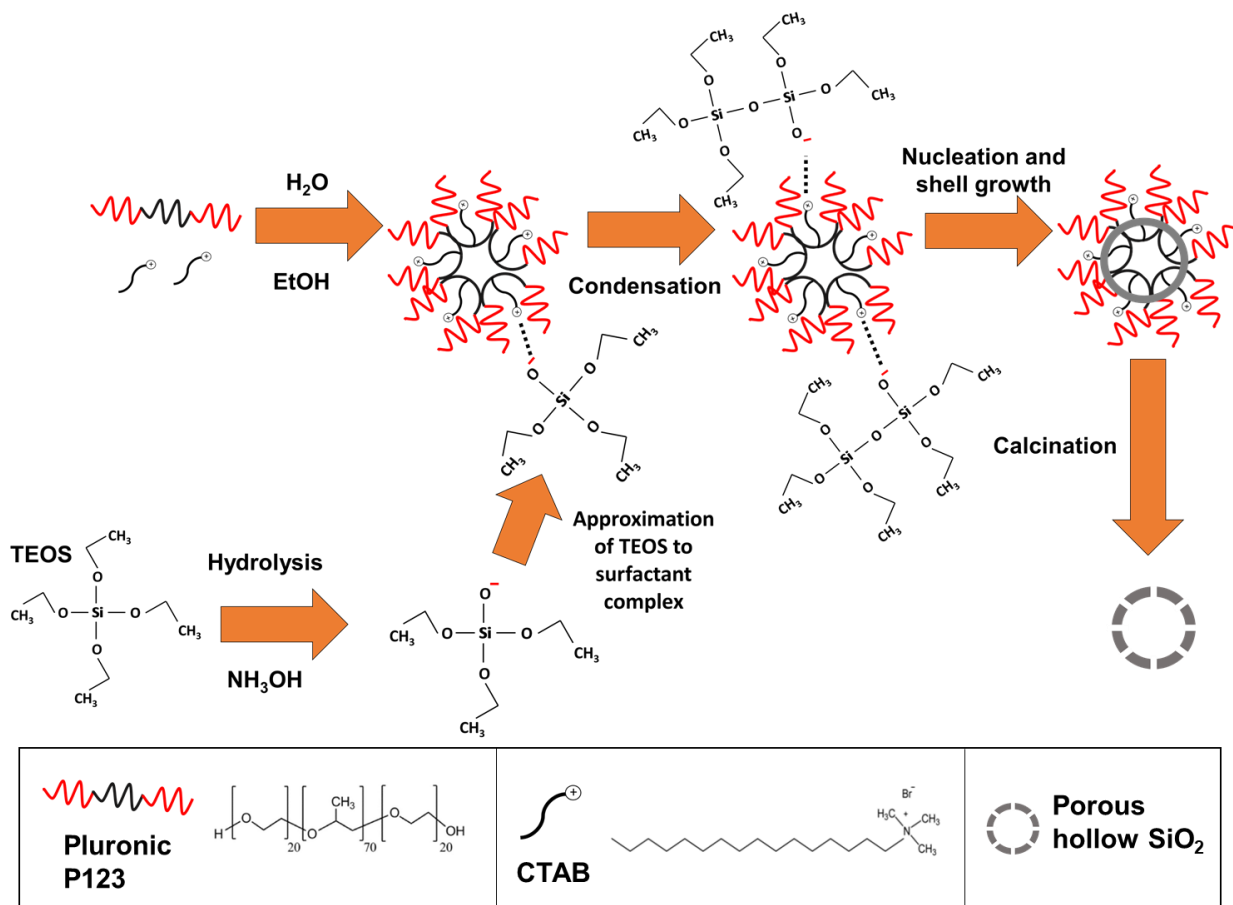


Figure 3-6. Schematic representation of the formation of CTAB-Pluronic emulsion, followed by its silanization with TEOS and calcination to make the PHSN ready for downstream applications.

Previous studies²⁴⁻²⁷ have suggested the encapsulation of organic and inorganic compounds within the PHSN post-synthesis, but whether the location and distribution of the encapsulated molecules are on or inside the hollow nanocages were not reported. In this study we demonstrate through direct observation that molecules could be internalized in the PHSN core. Because a metal such as Fe has higher contrast in TEM compared to SiO₂ it was a promising candidate for obtaining an image of an internalized mass inside the particle. In several PHSN, Fe(0) NPs were observed inside the silica shell, suggesting that the particles were formed inside the PHSN. This would not

be possible if NaBH_4 and FeCl_3 did not diffuse into the PHSN. Some $\text{Fe}(0)$ NPs were also observed attached on the PHSN, which suggests that some of the Fe^{3+} did not stay internalized in the core. The TEM images (Figure 3-7a to 3-7f) also show that only one particle is present within each shell and that can be explained by the fact that once FeCl_3 , NaBH_4 and H_2O react forming $\text{Fe}(0)$, which precipitates. The precipitated $\text{Fe}(0)$ colloids create a nucleation seed for the growth of $\text{Fe}(0)$ particles, thus the size of the iron oxide particle inside the shell is determined by the amount of reagents reacting within the shell. Figure 7b and d clearly shows differences in $\text{Fe}(0)$ particle size inside the SiO_2 shell. The transport and loading of molecules would be controlled by the size of the PHSN, the porosity of the shell, and how the molecules interact with SiO_2 .

Although TEM images are two-dimensional, we can observe consistent features in the several images, which suggests that the $\text{Fe}(0)$ was indeed in the hollow-core and not only on the exterior surface. First, the $\text{Fe}(0)$ particles were always associated with the PHSN and not once found unassociated with the PHSN, suggesting that most of Fe^{3+} was loaded on or in the particles. Secondly, we can observe that when the $\text{Fe}(0)$ particle was close to the walls of the PHSN (Figure 3-7c and 3-7e), the circular shape was flattened out in the region in contact with the shell. This was more noticeable in Figure 3-7e, where the four external $\text{Fe}(0)$ particles are flattened in the region of contact with the particle whereas the single $\text{Fe}(0)$ particle inside the shell kept its circular shape. This was also somewhat noticeable in Figure 3-7c with the iron particles presumably inside the shell having a region flattened where it contacted the silica shell. Shells can be seen around the $\text{Fe}(0)$ nanoparticles, particularly in Figures 3-7 (b, c and d), and these are typical iron oxide layers resulting from anaerobic corrosion reactions with water.⁴⁰ Based on the TEM images alone, we have not found evidence that $\text{Fe}(0)$ nanoparticles were formed inside the pores of the SiO_2 shell. It is possible that, because the pores are in the microporous range, the available space restricted the formation of a seed and the subsequent nanoparticle. Some studies have shown the formation of gold nanoparticles inside the pores of MSN, such as MCM-41.⁴¹

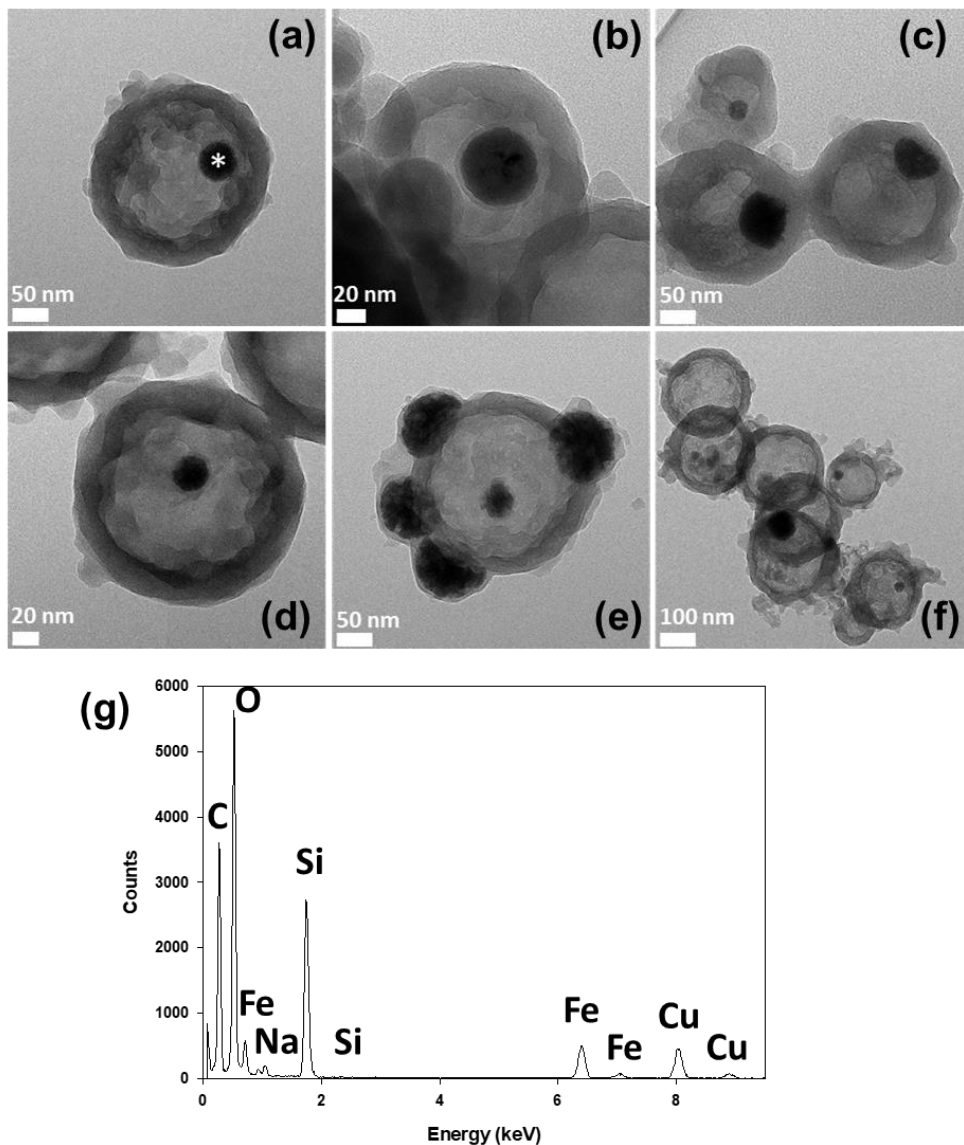


Figure 3-7. FeNP@PHSN (a-f) TEM images and (g) EDX spectrum of the marked site (*) in Figure 3-7a.

The internalization of FeCl_3 and NaBH_4 and the formation of $\text{Fe}(0)$ both inside and on the particle could be explained as follows. (i) When the calcined PHSN was immersed in the FeCl_3 solution, some of the Fe and Cl ions infiltrated the pores and filled the hollow core. (ii) After centrifugation, decanting the supernatant, and rinsing the PHSN with DI water, the Fe^{3+} could be found primarily inside the PHSN, as the non-internalized ions were washed away. However, after rinsing with DI water some of the ions inside the shell could possibly diffuse out of the PHSN or remain in the pores of PHSN. It is also possible that some Fe^{3+} was bound to silica by electrostatic

interactions or complexation.⁴²⁻⁴⁴ (iii) Later, when the sodium borohydride solution was added to the FeCl₃@PHSN pellet, Na⁺ and BH₄⁻ ions also infiltrated the pores and diffused into the Fe³⁺-filled core and reacted to form Fe(0) inside of the PHSN, or in some cases on its outer surface. This imaging is a proof of concept that molecules can be loaded either within the nanoshell or attached onto its walls. It should be noted that encapsulation of iron oxide nanoparticles within nonporous silica nanoshells have been reported by Su et al.⁴⁵ However, in that study the iron oxide particles in the core were formed through thermal treatment, from iron salts that were encapsulated in the silica shell during its synthesis, rather than the transport of dissolved iron through the silica shell.

3.5. Conclusions

The range of applications of porous nanoparticles has been increasing exponentially in different areas such as the biomedical field, and agriculture. This study demonstrates a new, more atom efficient synthesis of PHSN, which does not require a solid or non-aqueous phase as a template for synthesis. The NMR and FTIR analysis suggest that Pluronic P123 and CTA⁺ ions assembled forming a Pluronic-CTA⁺ complex. Thereafter, the positive charge provided by the CTAB hydrophilic head attracts the silica precursor and facilitates the growth of the silica shell.

Furthermore, although several studies claim to have internalized molecules within the PHSN, there was no evidence if the molecules were either indeed internalized, adsorbed in the pore surfaces or whether they were adsorbed on the external surface of the nanoshell. The internalization of FeCl₃ followed by the subsequent internalization of NaBH₄, resulted in the reduction of Fe³⁺ to Fe(0) that precipitated and started the nucleation/growth of Fe(0) NPs inside and on the shell. This experiment was a proof of concept that the shell was indeed porous-hollow and allows transport of mass through it. Understanding how molecules are internalized within nanocages can enhance nanotechnology applications in drug delivery and agricultural practices.

3.6. Supporting Information

Table S3-1. List of chemicals used for the synthesis of a standard batch of PHSN.

Chemical	Mass (mg)	Volume (mL)	Concentration in the final solution (mM)
Water	-	125	-
Ethanol	-	75	5709
NH ₄ OH	-	15	480
CTAB	300	-	3.7
Pluronic P123	850	-	0.7
TEOS	-	10	200

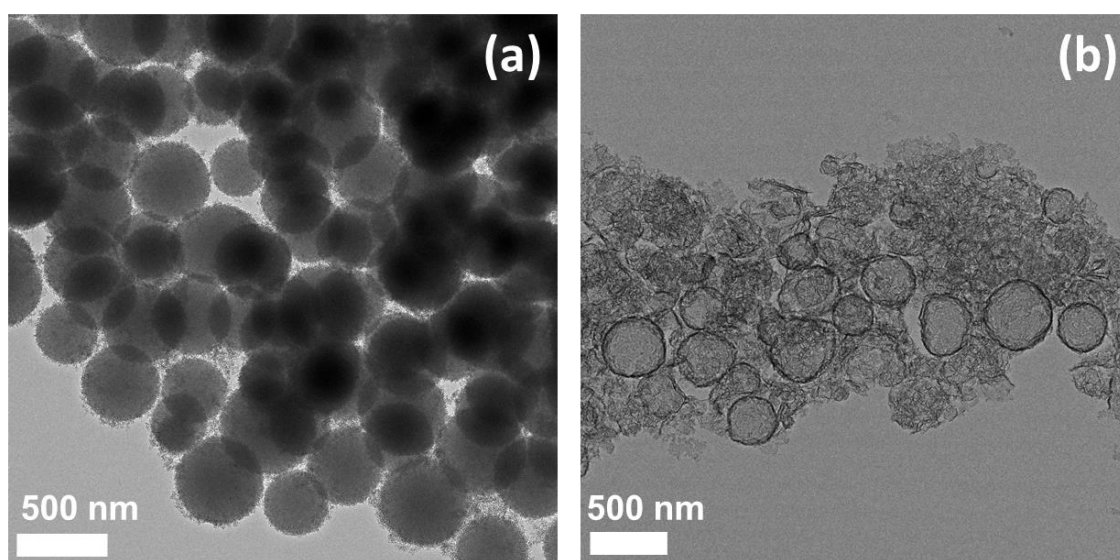


Figure S3-1. TEM image on the left (a) shows the nanoparticles synthesized with a high CTAB:Pluronic P123 ratio 0.75:1 wt% and on the right (b) nanoparticles synthesized with a low CTAB:Pluronic P123 ratio 0.1:1 wt%. When the amount of the pore-shell directing agent is exceeding (CTAB), the resulting nanoparticle that is porous without a hollow core. When the amount of core directing agent is exceeding, the resulting nanoparticle has a large hollow core and thin SiO₂ shell (Pluronic P123).

Table S3-2. Relaxation times (T_1 and $T_{1\rho}$) assigned to the peaks in the 1-D CP-MAS ^1H . The relaxation times were obtained with recycle delays of 120s. The standard deviation for both T_1 and $T_{1\rho}$ were obtained to analyze whether the differences among different peaks are representative. Note that T_1 was considered to be constant because the average was 0.51 s with a standard deviation of 0.04 s (9% of the average). Several $T_{1\rho}$ were found ranging from 0.004 to 0.044 s. According to Apperley et al.,³⁵ when T_1 is constant with multiple $T_{1\rho}$ the average domain sizes are in between 5 and 50 nm distant.

Peak (ppm)	T_1 (s)	Error (s)	$T_{1\rho}$ (s)	Error (s)
5.37	0.442	0.030	0.004	3.0E-4
3.82	0.494	0.005	0.022	0.004
1.27	0.510	0.003	0.044	0.008
1.20	0.557	0.007	0.017	0.004
1.46	0.571	0.007	0.043	0.048
3.51	0.499	0.007	0.037	0.008

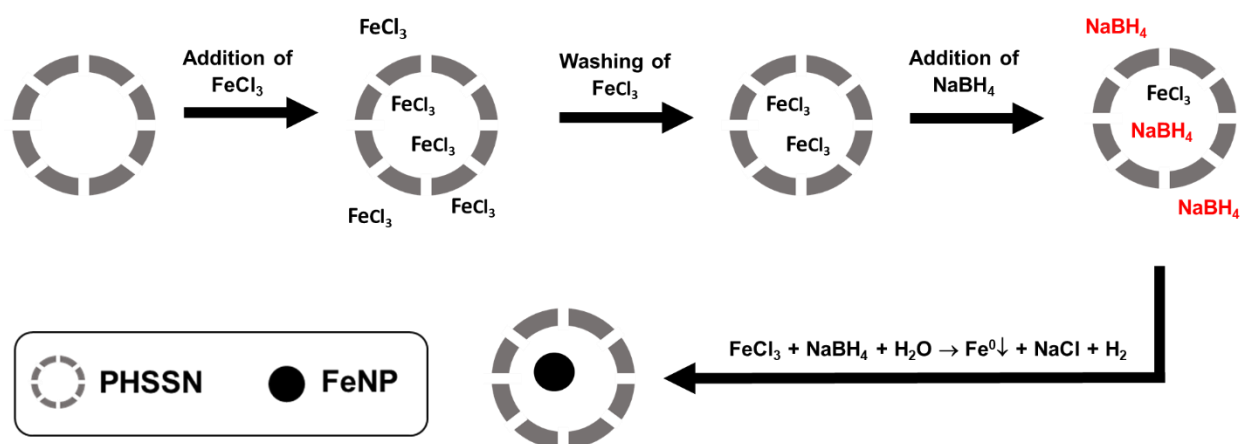


Figure S3-2. Schematic representation of the internalization of FeCl_3 and NaBH_4 in an oxygen-deprived environment and the formation of iron nanoparticles (FeNP) inside the PHSSN. First, the calcined PHSN was immersed in a concentrated FeCl_3 solution. Some of the dissolved Fe and Cl ions permeated through pores and filled the hollow-core. The suspension was centrifugated, followed by having the supernatant decanted and rinsed with DI water to remove the non-internalized ions. It was observed $\text{Fe}(0)$ formation on the PHSN shell, therefore, either some of the ions inside the shell possibly diffused out of the PHSN or some Fe^{3+} remained attached to the

surface of PHSN after rinsing with DI water. Later, NaBH₄ solution was dripped over the FeCl₃@PHSN pellet. NaBH₄ reacted to form Fe(0).

3.7. References

1. Malone-Povolny, M. J.; Schoenfisch, M. H., Extended nitric oxide-releasing polyurethanes via S-nitrosothiol-modified mesoporous silica nanoparticles. *ACS Applied Materials and Interfaces* **2019**, *11* (13), 12216-12223.
2. Nouredine, A.; Hjelvik, E. A.; Croissant, J. G.; Durfee, P. N.; Agola, J. O.; Brinker, C. J., Engineering of large-pore lipid-coated mesoporous silica nanoparticles for dual cargo delivery to cancer cells. *Journal of Sol-Gel Science and Technology* **2019**, *89* (1), 78-90.
3. Regli, S.; Kelly, J. A.; Barnes, M. A.; Andrei, C. M.; Veinot, J. G., Mesoporous silica encapsulation of silicon nanocrystals: synthesis, aqueous dispersibility and drug release. *Materials Letters* **2014**, *115*, 21-24.
4. Manzano, M.; Vallet-Regí, M., Mesoporous silica nanoparticles for drug delivery. *Advanced Functional Materials* **2020**, *30* (2), 1902634.
5. Djiwanti, S. R.; Kaushik, S., Nanopesticide: Future Application of Nanomaterials in Plant Protection. In *Plant Nanobionics*, Springer: **2019**; pp 255-298.
6. Popat, A.; Liu, J.; Hu, Q.; Kennedy, M.; Peters, B.; Lu, G. Q. M.; Qiao, S. Z., Adsorption and release of biocides with mesoporous silica nanoparticles. *Nanoscale* **2012**, *4* (3), 970-975.
7. Cheng, K.; Zhang, Y.; Li, Y.; Gao, Z.; Chen, F.; Sun, K.; An, P.; Sun, C.; Jiang, Y.; Sun, B., A novel pH-responsive hollow mesoporous silica nanoparticle (HMSN) system encapsulating doxorubicin (DOX) and glucose oxidase (GOX) for potential cancer treatment. *Journal of Materials Chemistry B* **2019**, *7* (20), 3291-3302.
8. Li, Z. Z.; Chen, J. F.; Liu, F.; Liu, A. Q.; Wang, Q.; Sun, H. Y.; Wen, L. X., Study of UV-shielding properties of novel porous hollow silica nanoparticle carriers for avermectin. *Pest Management Science* **2007**, *63* (3), 241-246.

9. Qi, G.; Wang, Y.; Estevez, L.; Switzer, A. K.; Duan, X.; Yang, X.; Giannelis, E. P., Facile and scalable synthesis of monodispersed spherical capsules with a mesoporous shell. *Chemistry of Materials* **2010**, 22 (9), 2693-2695.
10. Lu, T.; Zhu, Y.; Xu, J.; Ke, M.; Zhang, M.; Tan, C.; Fu, Z.; Qian, H., Evaluation of the toxic response induced by azoxystrobin in the non-target green alga *Chlorella pyrenoidosa*. *Environmental Pollution* **2018**, 234, 379-388.
11. Nakashima, Y., Effects of cations on the size and silica shell microstructure of hollow silica nanoparticles prepared using PAA/cation/NH₄OH template. *Colloids and Surfaces A: Physicochemical and Engineering Aspects* **2020**, 593, 124582.
12. Wibowo, D.; Zhao, C.-X.; Peters, B. C.; Middelberg, A. P., Sustained release of fipronil insecticide in vitro and in vivo from biocompatible silica nanocapsules. *Journal of Agricultural and Food Chemistry* **2014**, 62 (52), 12504-12511.
13. Vallet-Regi, M.; Ramila, A.; Del Real, R.; Pérez-Pariente, J., A new property of MCM-41: drug delivery system. *Chemistry of Materials* **2001**, 13 (2), 308-311.
14. Kresge, C.; Leonowicz, M.; Roth, W. J.; Vartuli, J.; Beck, J., Ordered mesoporous molecular sieves synthesized by a liquid-crystal template mechanism. *Nature* **1992**, 359 (6397), 710-712.
15. Luo, H.; Jiang, K.; Liang, X.; Hua, C.; Li, Y.; Liu, H., Insights into Morphological Transition of Pluronic P123 Micelles as a Function of Gallate. *Colloids and Surfaces A: Physicochemical and Engineering Aspects* **2019**, 572, 221-229.
16. Khanal, A.; Inoue, Y.; Yada, M.; Nakashima, K., Synthesis of silica hollow nanoparticles templated by polymeric micelle with core– shell– corona structure. *Journal of the American Chemical Society* **2007**, 129 (6), 1534-1535.
17. Sasidharan, M.; Zenibana, H.; Nandi, M.; Bhaumik, A.; Nakashima, K., Synthesis of mesoporous hollow silica nanospheres using polymeric micelles as template and their application as a drug-delivery carrier. *Dalton Transactions* **2013**, 42 (37), 13381-13389.

18. Zhou, X.; Cheng, X.; Feng, W.; Qiu, K.; Chen, L.; Nie, W.; Yin, Z.; Mo, X.; Wang, H.; He, C., Synthesis of hollow mesoporous silica nanoparticles with tunable shell thickness and pore size using amphiphilic block copolymers as core templates. *Dalton Transactions* **2014**, 43 (31), 11834-11842.
19. Poyraz, A. S.; Dag, O., Role of organic and inorganic additives on the assembly of CTAB-P123 and the morphology of mesoporous silica particles. *The Journal of Physical Chemistry C* **2009**, 113 (43), 18596-18607.
20. Wang, Y.; Song, H.; Zhang, H.; Liao, L.; Liu, N.; Chen, X., Direct synthesis of flat cake-type ordered mesoporous carbon in a double surfactant system of P123/CTAB. *Journal Materials Chemistry* **2011**, 21 (15), 5576-5579.
21. Yang, J.; Chen, W.; Ran, X.; Wang, W.; Fan, J.; Zhang, W.-x., Boric acid assisted formation of mesostructured silica: from hollow spheres to hierarchical assembly. *RSC Advances* **2014**, 4 (39), 20069-20076.
22. Patra, J. K.; Das, G.; Fraceto, L. F.; Campos, E. V. R.; del Pilar Rodriguez-Torres, M.; Acosta-Torres, L. S.; Diaz-Torres, L. A.; Grillo, R.; Swamy, M. K.; Sharma, S., Nano based drug delivery systems: recent developments and future prospects. *Journal of Nanobiotechnology* **2018**, 16 (1), 71.
23. de Oliveira, J. L.; Campos, E. V. R.; Bakshi, M.; Abhilash, P.; Fraceto, L. F., Application of nanotechnology for the encapsulation of botanical insecticides for sustainable agriculture: prospects and promises. *Biotechnology Advances* **2014**, 32 (8), 1550-1561.
24. Fu, Z., Direct preparation of drug-loaded mesoporous silica nanoparticles by sequential flash nanoprecipitation. *Chemical Engineering Journal* **2020**, 382, 122905.
25. Jiang, X., Aerosol fabrication of hollow mesoporous silica nanoparticles and encapsulation of L-methionine as a candidate drug cargo. *Chemical Communications* **2010**, 46 (17), 3019.
26. Liu, F., Porous hollow silica nanoparticles as controlled delivery system for water-soluble pesticide. *Materials Research Bulletin* **2006**, 41 (12), 2268.

27. Tan, S., Dynamic self-assembly synthesis and controlled release as drug vehicles of porous hollow silica nanoparticles. *Microporous and Mesoporous Materials* **2011**, *142* (2-3), 601.
28. Santra, S.; Tapeç, R.; Theodoropoulou, N.; Dobson, J.; Hebard, A.; Tan, W., Synthesis and characterization of silica-coated iron oxide nanoparticles in microemulsion: the effect of nonionic surfactants. *Langmuir* **2001**, *17* (10), 2900-2906.
29. Huh, S.; Wiench, J. W.; Yoo, J.-C.; Pruski, M.; Lin, V. S.-Y., Organic functionalization and morphology control of mesoporous silicas via a co-condensation synthesis method. *Chemistry of Materials* **2003**, *15* (22), 4247-4256.
30. Nakashima, Y.; Takai, C.; Razavi-Khosroshahi, H.; Fuji, M., Influence of the PAA concentration on PAA/NH₃ emulsion template method for synthesizing hollow silica nanoparticles. *Colloids and Surfaces A: Physicochemical and Engineering Aspects* **2018**, *546*, 301-306.
31. Ikari, K., Structural control of mesoporous silica nanoparticles in a binary surfactant system. *Langmuir* **2006**, *22* (2), 802.
32. Lv, X., Controlled synthesis of monodispersed mesoporous silica nanoparticles: Particle size tuning and formation mechanism investigation. *Microporous and Mesoporous Materials* **2016**, *225*, 238.
33. Bae, Y. K.; Han, O. H., Removal of copolymer template from SBA-15 studied by ¹H MAS NMR. *Microporous and Mesoporous Materials* **2007**, *106* (1-3), 304-307.
34. Trébosc, J.; Wiench, J. W.; Huh, S.; Lin, V. S. Y.; Pruski, M., Solid-State NMR Study of MCM-41-type Mesoporous Silica Nanoparticles. *Journal of the American Chemical Society* **2005**, *127* (9), 3057-3068.
35. Apperley, D. C.; Harris, R. K.; Hodgkinson, P., *Solid-state NMR: Basic principles and practice*. Momentum Press: **2012**.
36. Martins, G.; Berlier, G.; Coluccia, S.; Pastore, H.; Superti, G.; Gatti, G.; Marchese, L., Revisiting the nature of the acidity in chabazite-related silicoaluminophosphates: combined FTIR and ²⁹Si MAS NMR study. *The Journal of Physical Chemistry C* **2007**, *111* (1), 330-339.

37. Poyraz, A. S.; Albayrak, C.; Dag, Ö., The effect of cationic surfactant and some organic/inorganic additives on the morphology of mesostructured silica templated by pluronics. *Microporous and Mesoporous Materials* **2008**, *115* (3), 548-555.
38. Kim, K.-M.; Kim, H. M.; Lee, W.-J.; Lee, C.-W.; Kim, T.-i.; Lee, J.-K.; Jeong, J.; Paek, S.-M.; Oh, J.-M., Surface treatment of silica nanoparticles for stable and charge-controlled colloidal silica. *International Journal of Nanomedicine* **2014**, *9* (Suppl 2), 29.
39. Fleming, I.; Williams, D., Infrared and Raman Spectra. In *Spectroscopic Methods in Organic Chemistry*, Springer: **2019**; pp 85-121.
40. Cirtiu, C. M.; Raychoudhury, T.; Ghoshal, S.; Moores, A., Systematic comparison of the size, surface characteristics and colloidal stability of zero valent iron nanoparticles pre-and post-grafted with common polymers. *Colloids and Surfaces A: Physicochemical and Engineering Aspects* **2011**, *390* (1-3), 95-104.
41. Hammond-Pereira, E.; Bryant, K.; Graham, T. R.; Yang, C.; Mergelsberg, S.; Wu, D.; Saunders, S. R., Mesoporous silica-encapsulated gold core-shell nanoparticles for active solvent-free benzyl alcohol oxidation. *Reaction Chemistry and Engineering* **2020**.
42. Reardon, E., Complexing of silica by iron (III) in natural waters. *Chemical Geology* **1979**, *25* (4), 339-345.
43. Schindler, P.; Fürst, B.; Dick, R.; Wolf, P., Ligand properties of surface silanol groups. I. Surface complex formation with Fe³⁺, Cu²⁺, Cd²⁺, and Pb²⁺. *Journal of Colloid and Interface Science* **1976**, *55* (2), 469-475.
44. Pokrovski, G. S.; Schott, J.; Farges, F.; Hazemann, J.-L., Iron (III)-silica interactions in aqueous solution: Insights from X-ray absorption fine structure spectroscopy. *Geochimica et Cosmochimica Acta* **2003**, *67* (19), 3559-3573.
45. Su, Y.; Wang, Y.; Owoseni, O.; Zhang, Y.; Gamliel, D. P.; Valla, J. A.; McPherson, G. L.; John, V. T., A Bottle-around-a-Ship Method To Generate Hollow Thin-Shelled Particles Containing Encapsulated Iron Species with Application to the Environmental Decontamination of Chlorinated Compounds. *ACS Applied Materials and Interfaces* **2018**, *10* (16), 13542-13551.

Connecting Text to Chapter 4

While Chapter 3 presented a methodology to produce porous hollow silica nanoparticles (PHSN) and explored the potential to load molecules of interest within them, Chapter 4 investigates their mobility potential in the environment after the application of these nanoparticles in agricultural fields. In Chapter 4, the impact of the aforementioned characteristics on the environmental fate of these nanoparticles was investigated by assessing the transport and retention profiles of solid silica nanoparticles (SSN) and PHSN, which have significantly different structures, through model saturated porous media.

Chapter 4. Mobility of Solid and Porous Hollow SiO₂ Nanoparticles in Saturated Porous Media: Impacts of Surface and Particle Structure

4.1. Abstract

Silica nanoparticles (SiO₂ NPs) are of increasing interest in nano-enabled agriculture, particularly as nanocarriers for the targeted delivery of agrochemicals. The direct application of these in agricultural soils may lead to the release of SiO₂ NPs in the environment. Although some studies have investigated transport of solid SiO₂ NPs in porous media, there is a knowledge gap on how different SiO₂ NP structures incorporating significant porosities can affect the mobility of such particles under different conditions. Herein, we investigated the effect of pH and ionic strength (IS) on the transport of two distinct structures of SiO₂ NPs, namely solid SiO₂ NPs (SSNs) and porous hollow SiO₂ NPs (PHSNs), of comparable sizes (~200 nm). Decreasing pH and increasing ionic strength reduced the mobility of PHSNs in sand-packed columns more significantly than for SSNs. The deposition of PHSNs was approximately 3 times greater than that of SSNs when pH was 4.5 and IS 100 mM. The results are non-intuitive given that PHSNs have a lower density and the same chemical composition of SSN but can be explained by the greater surface roughness and ten-fold greater specific surface area of PHSNs, and their impacts on van der Waals and electrostatic interaction energies.

4.2. Introduction

Rapid advances in nano-enabled agriculture have been focused on making significant improvements in enhancing crop yields, mitigating energy and water footprints, and reducing unintended pollution from the use of fertilizers and pesticides.¹⁻³ The latter is achieved through precise delivery of pesticides and fertilizers using nanocarriers, which can dose these agents to plant tissues in a targeted manner and with a higher efficiency than traditional pesticide and fertilizer formulations.³⁻⁸ Porous nanosilica is a promising candidate for pesticide and fertilizer nanocarriers because SiO₂ is an earth-abundant, biocompatible material^{9, 10} that promotes plant growth, and provides resistance towards pathogens and unfavorable environmental conditions.¹⁰⁻¹² SiO₂ nanocarriers may be introduced to agricultural soils either through direct application or

through indirect releases such as discharges to soils following foliar application.¹³⁻¹⁷ It is important to investigate the mobility of silica nanocarriers to account for their subsurface transport and that of their cargo. Although several studies have investigated the transport of SSNs in geologic deposits,¹⁸⁻²¹ it is unclear how the differences in particle structure, in particular the high porosity of silica nanocarriers, fundamentally influence their mobility in porous media.

Among studies on SSN transport, Wang et al.²⁰ reported that particle size and concentration influenced the transport and retention profiles of SSNs in porous media. Small SSNs of 8 nm diameter caused higher retention and thus less mobility when compared to SSN with mean diameter of 52 nm. Moreover, that study showed that increased ionic strength reduced the overall SSN mobility in the porous medium. Zhang et al.²² reported that sorption of humic acid improved mobility of SiO₂ nanoparticles in saturated porous media because of enhanced electrostatic forces. HonetschlÄgerová et al.²³ showed that coating nanoscale zerovalent iron (nZVI) particles with a SiO₂ shell enhanced their colloidal stability and mobility in porous media compared to bare nZVI, which have high aggregation tendency and thus are very colloidally unstable.

Common parameters that influence the mobility of nano- and micro-colloids in porous media are (i) particle surface charge and coating,²³ (ii) particle size,²⁰ (iii) ionic strength,²⁴ (iv) pH,²⁵ and (v) temperature.²⁶ However, few studies have analyzed the effects of the structure of nanoparticles. Among various SiO₂ nanoparticles, most studies have investigated the transport of SSNs, most applications in agriculture focus on the use of mesoporous SiO₂, such as MCM-41,²⁷⁻³¹ and SiO₂ nanoshells, such as PHSNs,³²⁻³⁶ which are structurally different from SSNs and, therefore, may lead to different transport profiles. Given the increasing use of silica nanocarriers in agriculture, and the increased potential for release into soils, there is a critical knowledge gap on the transport behavior of silica nanocarriers in natural porous media, and whether their transport patterns differ from those of SSNs.

The objective of this study was to evaluate how the porous structure of the SiO₂ NPs influences their mobility. Two SiO₂ NPs with very distinct structure and similar size were synthesized, namely (i) SSNs which are solid spheres and (ii) PHSNs which are porous and hollow and represent nanocarriers with high porosity. The synthesis methods ensured that the particles were composed only of SiO₂. Experiments were conducted to assess the colloidal stability and mobility of these two particles in saturated, acid-washed, sand-packed columns, over a range of

pH and ionic strength (IS). Furthermore, theoretical Derjaguin-Landau-Verwey-Overbeek (DLVO) interaction energies and single collector contact efficiency calculations were performed to investigate how porosity and density differences in the two types of particles influenced colloidal stability and deposition on collector surfaces.

A fundamental understanding of the impacts of particle structure on its mobility is essential before investigation of the effects of various environmental conditions and complex particle compositions. The scope of this work allowed evaluation for the first time, of the transport profiles of two different structures of SiO₂ NPs under different solution chemistry conditions. Furthermore, it is the first experimental report of the study of the transport behavior of porous hollow nanoparticles in general. Although there have been studies with porous nanoparticles, such as in Lu et al.,³⁷ porous particles and porous hollow nanoshells are very different structurally, particularly when it comes to the density of the particle and the energy interactions of the inner and outer part of the shell with the medium, collector and other particles.

4.3. Materials and Methods

4.3.1. Porous Media

White quartz sand with 50-70 mesh particle size (Sigma-Aldrich) was used as the porous medium in this study. Scanning electron microscopy was used to confirm the sand grain morphology and size (Figure S4-1). The average grain diameter of the quartz sand was 250 μm, with diameters ranging from 210 to 297 μm. Prior to use, the sand was treated with HNO₃ (70% v/v) for 16 hours to remove metal oxides and other impurities as reported elsewhere.³⁸⁻⁴¹ The acid-washed sand was thoroughly rinsed with DI water (ASTM Type 1, Thermo Fisher) followed by three 20-minute cycles of sonication in water bath. The cloudy DI water was replaced at the end of each cycle. The electrical potential on the surface of the sand particles was quantified by measuring the zeta potential of crushed sand grains under varying conditions of pH and IS, and was negatively charged across the board (Table S4-1).

Table 4-1. Particle characterization data and calculated DLVO interaction energies by nanoparticle type, pH, IS (mM, electrolyte NaCl). Measurements of zeta potential (mV), Z-average diameter (nm), Polydispersity Index (PdI), depths of primary minima (Φ_{\min}), heights of energy barriers (Φ_{\max}) and depths of secondary wells (Φ_{\sec}) for the DLVO energy profiles. Errors denote standard deviations corresponding to measurement of 3 samples.

Experiment	Structure	pH	IS (mM)	Zeta Potential (mV)	Z-avg dia. (nm)	PdI	Particle-Particle (k _B T)			Particle-Collector (k _B T)		
							Φ_{\min}	Φ_{\max}	Φ_{\sec}	Φ_{\min}	Φ_{\max}	Φ_{\sec}
Exp 1	SSN	4.5	1	-34.6 ± 0.9	238 ± 1.9	0.14 ± 0.01	-160.4	120.2	/	-789.2	178.7	/
Exp 2	SSN	6.5	1	-52.5 ± 0.8	229 ± 5.4	0.12 ± 0.02	-4.5	255.7	/	-555.9	355.4	/
Exp 3	SSN	9.5	1	-71.3 ± 1.3	201 ± 4.9	0.05 ± 0.02	152.4	373.2	/	-289.6	495.5	/
Exp 4	SSN	9.5	10	-57.3 ± 1.1	214 ± 4.8	0.07 ± 0.03	33.2	238.0	/	-381.7	358.5	/
Exp 5	SSN	9.5	100	-37.4 ± 3.0	220 ± 3.6	0.07 ± 0.02	-132.5	82.8	-0.6	-587.9	171.2	-2.0
Exp 6	PHSN	4.5	1	-10.7 ± 0.7	240 ± 1.1	0.20 ± 0.02	-142.0	10	/	-791.3	49.1	/
Exp 7	PHSN	6.5	1	-29.2 ± 1.1	239 ± 1.8	0.19 ± 0.02	-52.6	90.4	/	-601.3	210.9	/
Exp 8	PHSN	9.5	1	-42.5 ± 2.0	221 ± 1.9	0.20 ± 0.01	47.0	173.8	/	-387.0	349.3	/
Exp 9	PHSN	9.5	10	-42.1 ± 1.5	220 ± 3.1	0.27 ± 0.03	42.3	155.8	/	-391.6	296.7	/
Exp 10	PHSN	9.5	100	-31.3 ± 0.5	239 ± 2.0	0.18 ± 0.02	-41.6	72.3	-0.3	-536.6	158.2	-1.9

4.3.2. SiO₂ Nanoparticles

SSNs were synthesized following a protocol based on the Stöber method.⁴² A solution of anhydrous ethanol (200 mL, 100%, Commercial Alcohols, Canada) and NH₄OH (15 mL, 28% NH₃ basis, Sigma-Aldrich) was stirred under 400 rpm for 30 minutes to ensure complete mixing. Then, 10 mL of tetraethyl orthosilicate (TEOS 98%, Sigma-Aldrich) was added dropwise at a rate of 1 mL/min. After 5 hours, the reaction was stopped by drying the cloudy suspension overnight at 80°C. Finally, the nanoparticles were calcined for 5h under 500°C.

PHSNs were synthesized based on a protocol previously described.³⁶ In summary, a solution of DI water (125 mL), anhydrous ethanol (75 mL), NH₄OH (7.5 mL), hexadecyltrimethylammonium bromide (CTAB, 300 mg, Sigma-Aldrich) and Pluronic P123 (850 mg, Sigma-Aldrich) was stirred under 1000 rpm for 1 hour until reagents were completely mixed. Then, 10 mL of TEOS was added dropwise at a rate of 0.75 mL/min. After 5 hours, the reaction was stopped by drying the cloudy suspension overnight at 80°C. Finally, the nanoparticles were calcined for 5h under 500°C.

The morphology of the nanoparticles was characterized by TEM (Philips, model CM200) at an acceleration voltage of 200 kV. The particle size distribution and zeta potential at different experimental conditions were characterized through DLS using Malvern Zetasizer Nano ZS (Malvern Instruments, UK). Both analyses were conducted using SSNs and PHSNs suspended in DI water with a concentration of 100 ppm. The specific surface area was determined using the BET method through nitrogen sorption/desorption experiments using a Quantachrome Autosorb-1 (Quantachrome GmbH & Co., Netherlands). FTIR spectra were obtained for both SSNs and PHSNs with a PerkinElmer Spectrum II Spectrometer with a single bounce diamond crystal. Spectra were recorded in the range from 4000 to 400 cm⁻¹ at a resolution of 1 cm⁻¹.

4.3.3. Solution Chemistry

100 ppm of SSNs and PHSNs were prepared by suspending the dried SiO₂ powder obtained from the synthesis in DI water, followed by sonication in water bath for 30 minutes. IS was adjusted in the nanoparticle suspensions and background solutions using NaCl (ACS grade, Sigma-Aldrich). The pH was adjusted dropwise with 0.1 M HCl and 0.1 M NaOH, and the counter-ions (Na⁺ and Cl⁻) were taken into account in estimating the total IS of the system. The range of pH and IS was

selected to cover different environmental conditions that the nanoparticles may encounter. While aquifers and surface water bodies are commonly found to be near neutral pH (6.5 - 7.5), slightly acidic/alkaline conditions could be occasionally achieved specific geologic conditions, at contaminated sites or in industrial wastewater.⁴³⁻⁴⁵

4.3.4. Column Experiments

A 10-cm long acrylic column (Chromaflex, Fisher) with internal diameter of 1 cm was packed with acid-washed sand using a wet packing technique described in Oliviera et al.⁴⁶ Prior to the addition of the acid-washed sand, the column was filled with DI water. Then, saturated acid-washed sand was deposited in increments of 1-cm layers while vibrating the column for 20 seconds. This procedure was repeated until the saturated acid-washed sand occupied the whole space within the 10 cm long column, yielding a porosity of 0.391 from fitting the advection dispersion equation to the tracer breakthrough curve (BTC).

At the start of each run, 3 pore volumes (PVs) of DI water were introduced to the system with the aid of a peristaltic pump at a flow rate of 1.25 mL/min, which corresponds to a Darcy velocity of $2.64 \times 10^{-4} \text{ m s}^{-1}$ within our setting. The flow rate remained constant throughout the run and for all the different conditions. 10 PVs of background solution amended with NaCl (25 mM) followed to produce the breakthrough curve (BTC) for the tracer to ensure consistency and reproducibility of the column wet packing procedure. Then, 5 PVs of particle-free electrolyte solution at desired IS and pH were injected, followed by 10 PVs of the particle suspension at 100 ppm at the respective IS and pH. Subsequently, 5 PVs of the particle-free electrolyte solution and, finally, 3 PVs of DI water were injected. Ten different experimental conditions were carried out in triplicates as detailed in Table 4-1. The SiO₂ NP concentration of 100 ppm was selected based on concentrations employed in previous column transport studies for SSNs²⁰ and concentrations relevant to foliar application of SiO₂ NPs.¹³

NaCl and particle (SSN and PHSN) concentrations exiting the column were quantified in real-time by UV-Vis spectroscopy (Agilent Technologies, Model 8453) in a quartz flow-cell (Hellma Analytics, GE, 10 mm path length, 300 μL volume) at wavelengths of 196 nm and 350 nm, respectively.

4.3.5. Interaction Energies and Collector Efficiency

The van der Waals forces and repulsive electrostatics forces for SSN and PHSN for the different experimental conditions were calculated to determine the particle-particle and particle-collector interaction energies according to the classical DLVO model (Equation 4-1) using the expressions proposed by Gregory⁴⁷ (full list of equations and theoretical considerations in Supporting Information). Interaction energies due to Born repulsion forces were not accounted for because of their negligible magnitudes.⁴⁸⁻⁵⁰ The Hamaker constant was calculated using the expressions proposed by Lipkin et al.,⁵¹ and accounted for the contributions of water core and silica shell in PHSNs. The full list of physical properties used to compute the DLVO energy profiles for SSNs and PHSNs can be found in Table S4-2. For PHSNs, the interior and exterior fluid compositions were considered to be the same, thus the van der Waals energy profile was calculated by subtracting the resulting forces generated by a particle with diameter corresponding to the inner diameter of the PHSN from the resulting forces calculated for a particle with diameter corresponding to the outer diameter of the PHSN^{52, 53} as per Equation 4-2.

$$V_{\text{tot}} = V_{\text{vdW}} + V_{\text{edl}} \quad (4-1)$$

$$V_{\text{vdW}} = V_{\text{vdW}}^{\text{out}} - V_{\text{vdW}}^{\text{in}} \quad (4-2)$$

The depths of primary minima (Φ_{min}), heights of energy barriers (Φ_{max}) and depths of secondary wells (Φ_{sec}) for the DLVO energy profiles are summarized in Table 4-1.

The single collector contact efficiency was calculated based on the empirical expressions derived from the following studies: Yao et al.,⁵⁴ Rajagopalan and Tien,⁵⁵ Tufenkji and Elimelech,⁵⁶ Ma et al.,⁵⁷ Nelson and Ginn,⁵⁸ Ma et al.,⁵⁹ and Messina and Sethi.⁶⁰ The comprehensive list of expressions used in this step is presented in Table S4-3.

4.4. Results and Discussion

4.4.1. SiO₂ NPs Characterization

The TEM images in Figure 4-1 show that while the SSN synthesized based on the Stöber method (Figure 4-1a and 4-1b) are solid with an average primary particle diameter of 184 nm, the PHSN

(Figure 4-1c and 4-1d) are hollow with an average diameter of 205 nm. Figure 4-1b and 4-1d show a more magnified TEM image of a typical SSN and PHSN. The shell thickness of the PHSNs ranged from 22 to 38 nm. An important difference in the surface characteristics of the two particle types is the significantly higher surface roughness of PHSNs created in part by the highly porous shell surface. The calculated mass of the SSNs and PHSNs were very similar. Thus, the particle number concentration of SSNs and PHSNs were very similar in all experiments.

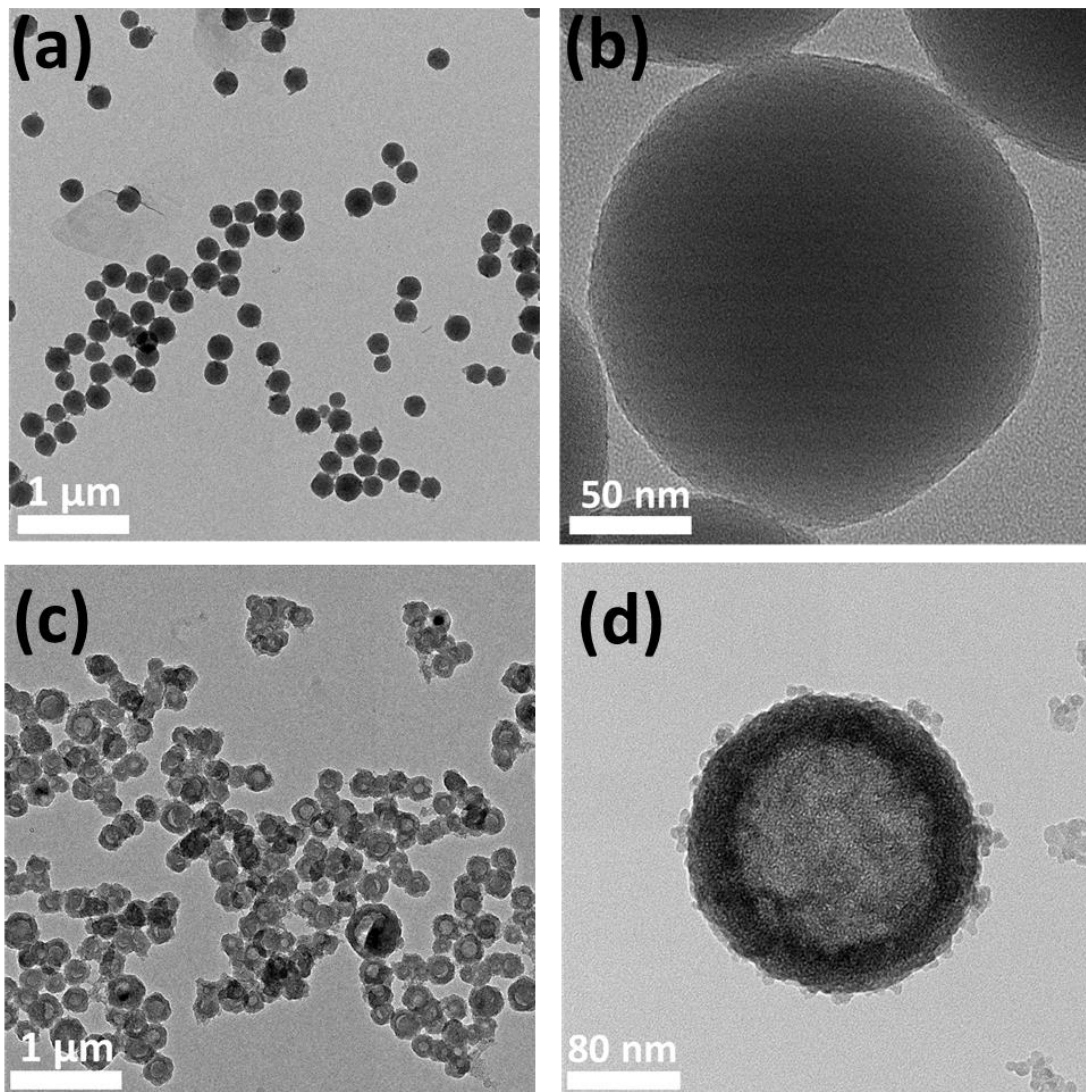


Figure 4-1. TEM images of (a and b) SSNs and (c and d) PHSNs. The images on the right exhibit more magnified images of singular (b) SSN and (d) PHSN to show the different features between both structures. Although both structures are spherically shaped, PHSNs feature a hollow core and

pores. The latter is directly responsible for the increased surface area and roughness of PHSNs when compared to SSNs.

The primary particle size distributions ($N = 100$) for SSNs and PHSNs represented in Figure S4-2a and Figure S4-2b, respectively, show that both particles have a comparable size distribution. The hydrodynamic diameter size distribution, obtained by DLS for SSNs (Figure S4-2a) is slightly narrower than for PHSNs (Figure S4-2b) as reported in Table 4-1 represented by the polydispersity index (PDI). The DLS measurements were obtained at pH 9.5 and IS 1 mM because optimal colloidal stability was obtained at these conditions. Overall, both particle populations were successfully synthesized to yield comparable size and shape, to enable direct comparison of their mobility in porous media.

The surface characteristics were investigated using BET and FTIR analyses (Figure S4-3). Although, SSNs and PHSNs have relatively similar sizes, the specific surface area of the PHSNs ($287 \pm 30 \text{ m}^2 \text{ g}^{-1}$) is approximately 10 times greater than the specific surface area of the SSNs ($29 \pm 8 \text{ m}^2 \text{ g}^{-1}$). This is due to the presence of micro-scale pores of around 2.5 nm in the PHSN surface as characterized in previous work.³⁶

The chemical composition of the SSNs and PHSNs were identical with no chemical bonds present other than those attributable to silica, as determined by FTIR analyses (Figure S4-3c). Although both populations of SiO_2 nanoparticles have the same chemical composition, the differences in their structure result in different Hamaker constants ($6.59 \times 10^{-21} \text{ J}$ for SSNs and $5.79 \times 10^{-21} \text{ J}$ for PHSNs) and zeta potentials (Table 4-1). Given the higher surface area of PHSNs, there are more counter-ions around the PHSNs compared to SSNs, resulting in a thinner solvation layer and zeta potential closer to zero.⁶¹

4.4.2. pH Effect of the Transport Behavior

The effect of pH on the transport of SSNs and PHSNs in saturated porous media was evaluated at IS 1 mM for both sets of nanoparticles. The BTCs obtained for SSNs (Figure 4-3a) show that the values for steady-state relative effluent concentration (at 9 PV) decreased as the pH also decreased, from 0.99 at pH 9.5, to 0.95 at pH 6.5 and then 0.91 at pH 4.5, suggesting that transport of SSNs is slightly hindered as the pH becomes more acidic, increasing retention of SSNs in the column. The changes in mobility of SSNs with pH are consistent with another study showing reduced

mobility of SiO₂ nanoparticles in carbonate reservoirs at acidic pH.⁶² It should be noted that the SSN hydrodynamic diameter as measured by DLS increased slightly with pH decrease from 9.5 to 4.5 (from 201 ± 4.9 nm at pH 9.5 to 238 ± 1.9 nm at pH 4.5) suggesting limited aggregation.

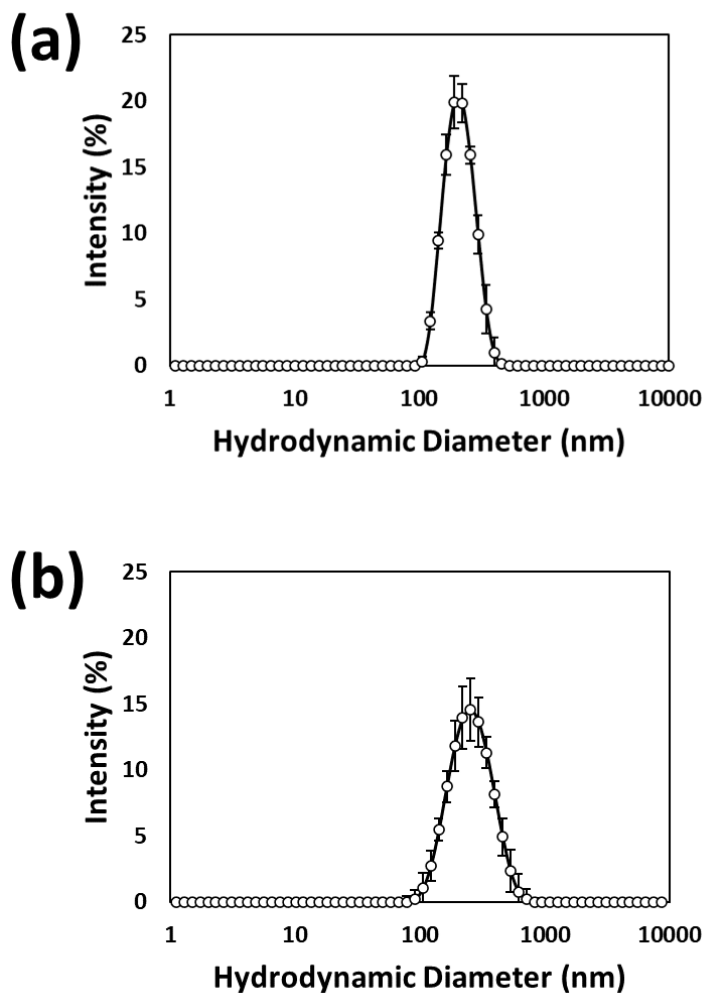


Figure 4-2. Particle size distribution at pH 9.5 and IS 1 mM of (a) SSNs and (b) PHSNs. The width of the PHSN size distribution is broader than that for SSN, indicating a higher PdI as confirmed in Table 4-1.

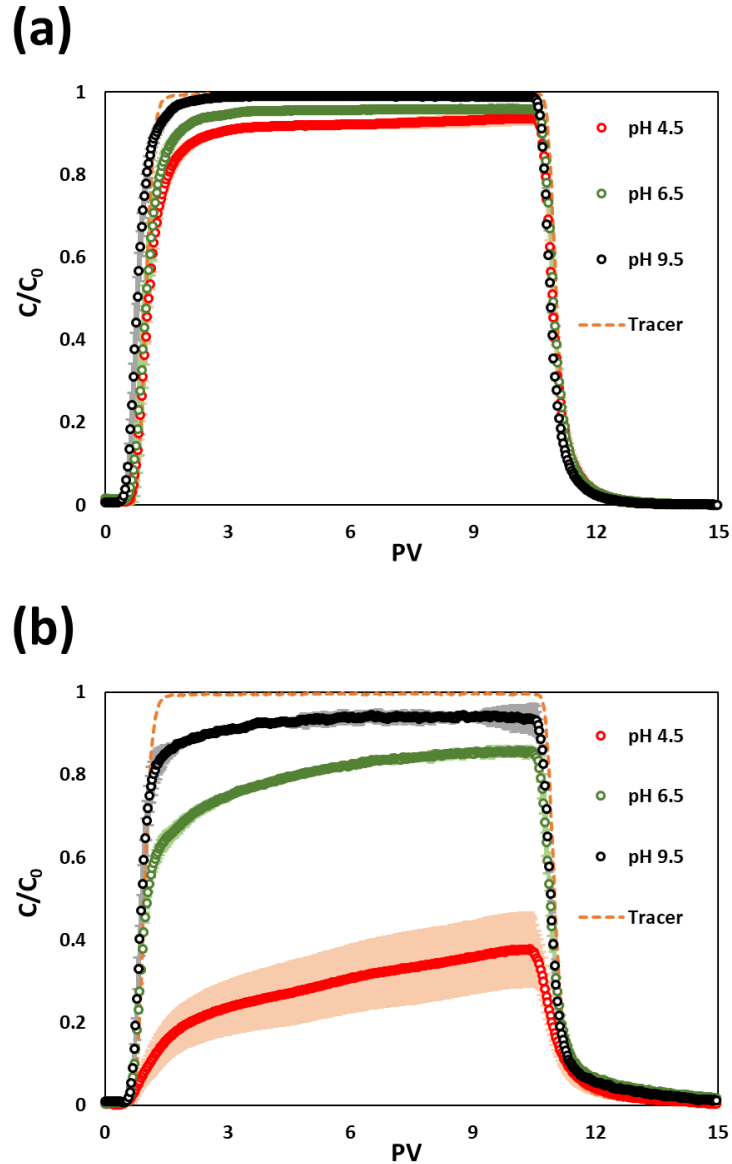


Figure 4-3 BTCs at fixed IS 1 mM and varying pH for (a) SSNs and (b) PHSNs. The shaded zones represent the standard deviation of the particle concentration run in triplicates. Wider shaded areas represent greater standard deviation among replicates. The conditions with no visible shaded areas represent runs with not relevant difference among replicates.

The DLVO energy profiles for the SSN particle-particle (Figure 4-4a) and particle-collector interactions (Figure 4-4c) at IS of 1 mM, show highly unfavorable attachment conditions. Under these conditions, the repulsion forces between SSNs and between SSNs and the sand collector surfaces resulted in elevated energy barriers and absence of secondary minima (Table 4-

1). The DLVO energy profiles for the SSN particle-collector interactions (Figure 4-4c) support the observations of low retention of SSNs from the BTC trends discussed above (Figure 4-3a). The calculated particle-particle energy barrier for SSNs at pH 4.5 was far greater than $15 k_bT$, an approximate threshold for colloidal stability, and thus do not suggest conditions favorable for SSN aggregation. However, the energy barrier was significantly lower at pH 4.5 ($120.2 k_bT$) compared to pH 9.5 ($373.2 k_bT$).

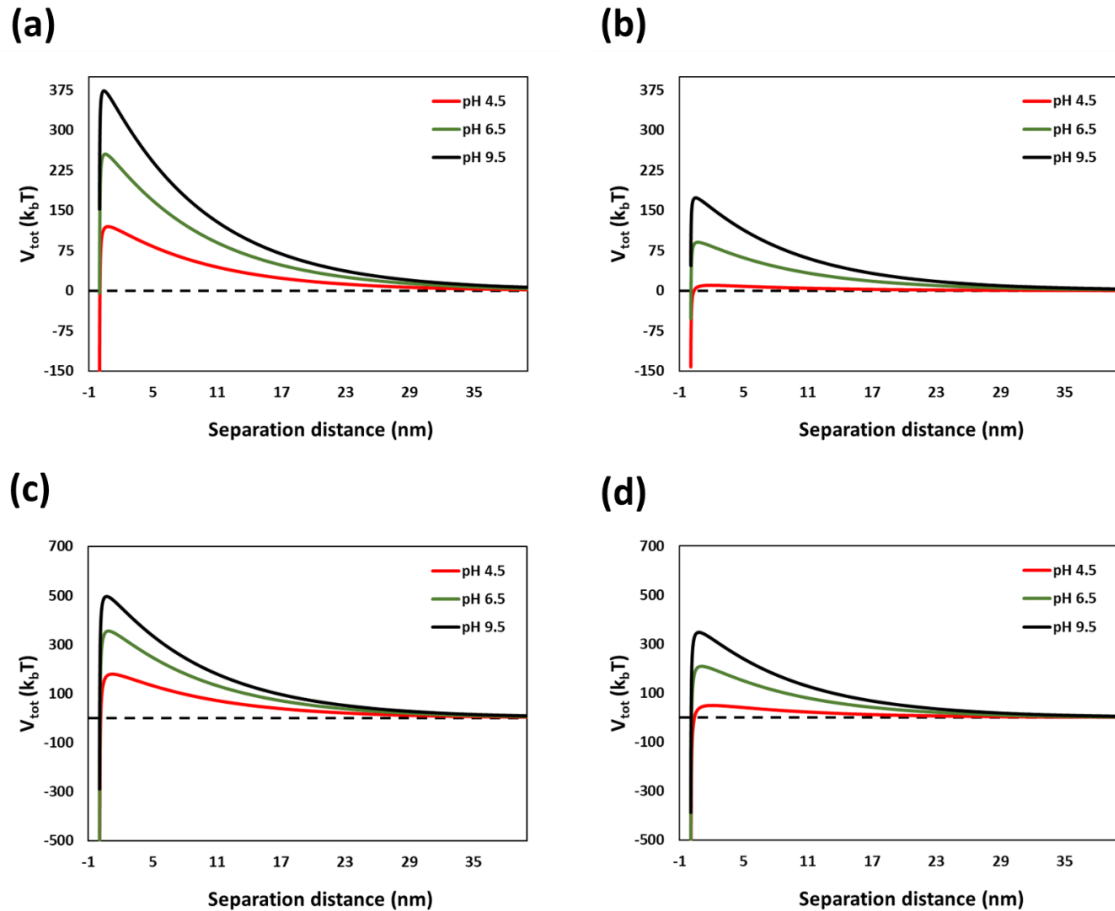


Figure 4-4. DLVO energy profiles at fixed IS 1 mM and varying pH for (a) SSN particle-particle interactions, (b) PHSN particle-particle interactions, (c) SSN particle-collector interactions, and (d) PHSN particle-collector interactions.

The values for steady-state relative effluent concentrations in the BTCs for PHSNs also decreased with decreasing pH, from 0.94 at pH 9.5 to 0.85 at pH 6.5 and then more substantially to 0.37 at pH 4.5. The extent to which the transport was hindered in PHSNs with decreasing pH

was much more significant than that in SSNs. As with SSNs, there was also a small increase in DLS-measured hydrodynamic diameters with decreasing pH (221 ± 1.9 nm at pH 9.5 to 240 ± 1.1 at pH 4.5). Although the DLVO calculations suggest that the primary maximum for particle-particle interactions of PHSNs at pH 4.5 was small at $10 k_bT$, the measured hydrodynamic diameters suggest limited aggregation, comparable to SSNs.

At pH 4.5 and IS of 1 mM, the primary energy maximum for PHSN-sand grain interactions was the lowest ($49.1 k_bT$) of the 3 pH conditions at the same IS, and thus the DLVO calculations are in qualitative agreement with the experimental observation of significantly low mobility of PHSNs at pH 4.5. However, there was no secondary minima predicted by DLVO calculations. This suggests that other parameters played a role in the transport of these nanoparticles. Straining is unlikely to be a cause for the significantly higher deposition of PHSN, given that the SSN have similar hydrodynamic diameters at corresponding pH, but had lower deposition. Furthermore, straining is not expected when the colloid diameter (d_c) to sand grain diameter (d_g) ratio (d_c/d_g) is below 0.008.⁶³ Here, the d_p/d_g ratio is approximately 0.001 for both SSN and PHSN. According to Xu et al.,⁶³ straining rates are negligibly small when $d_p/d_g < 0.008$ and, in this study, this ratio is one order of magnitude lower. There is, however, a gradual increase in C/C_0 with increasing pore volumes, suggesting some blocking or detachment of deposited PHSNs. As a first layer of deposited nanoparticles is formed, the trajectories of the subsequent nanoparticles are significantly impacted by this monolayer of deposited particles, a phenomenon previously referred to as the shadow effect.⁶⁴ The extent of the influence of the shadow effect in subsequent particle trajectory is directly related to the hydrodynamic interactions and electrostatic double layer repulsion. Therefore, as the conditions become unfavorable (lower pH and higher IS), repulsion forces decrease, thus increasing both the surface coverage of deposited nanoparticles on the sand grains and the blocking effects in the nanoparticle transport profiles.

4.4.3. IS Effect on the Transport Behavior

The effect of IS in the transport of SSNs and PHSNs in saturated porous media was evaluated at pH 9.5 and at the same SiO₂ concentration of 100 ppm as the experiments described above. The BTCs for SSNs (Figure 4-5a) showed that the values for relative effluent concentration at 9 PVs decreased as the IS increased, from 0.99 at IS 1 mM, to 0.96 at IS 10 mM and then 0.92 at IS 100 mM, which was expected and is consistent with the literature.^{20, 62} The addition of salt increases

the number of counter-ions migrating to the solvation layer of the nanoparticles, thus decreasing the Debye-length and the repulsive electrostatic forces. Although the total interaction energies calculated yielded a lowered energy barrier, a weak secondary minimum ($-2 k_bT$) was obtained only at IS of 100 mM.

The values for relative effluent concentrations at 9 PV in the BTCs for PHSN (Figure 4-5b) also decreased with increasing IS, from 0.94 at IS 1 mM to 0.88 at IS 10 mM and then 0.34 at IS 100 mM. Once again, the mobility PHSNs was much more affected by the change in IS than for SSNs. The similarity in the BTC shape with changes in pH and IS suggests that similar deposition processes are involved. As for the SSNs at pH 9.5 and IS at 100 mM, a weak secondary minimum for PHSNs was calculated from the interaction energy profiles at an IS of 100 mM.

Overall, low pH and high IS decreased the mobility of the nanoparticles in porous media. We observed similar trends between SSNs and PHSNs: (i) As pH decreased, zeta potential also decreased, which is expected because the isoelectric point of bare SiO_2 is around $\text{pH} = 2$.⁶⁵⁻⁶⁷ (ii) As IS increased, zeta potential decreased as a result of the stabilization of the excess ions in the electrical double layer of each nanoparticle by the counter-ions from the NaCl added. In both cases, a decrease in zeta potential led to a decrease in the intensity of repulsion forces between nanoparticles and between nanoparticles and sand. However, the increased retention of PHSNs compared to the SSNs, which is non-intuitive because both particles have comparable sizes (Figure 4-1) and surface chemical composition (Figure 4-2c). The DLVO interaction energies calculated are qualitatively in agreement with the mobility trends for SSNs and PHSNs, but the calculated values are not consistent in several instances. For example, if we compare the particle-collector interaction resulting energy profiles for Exp. 5 (SSNs, pH 9.5, IS 100 mM, Figure 4-6c) with Exp. 10 (PHSNs, pH 9.5, IS 100 mM, Figure 4-6d) the heights of energy barriers were comparable, and yet, the steady-state relative effluent concentrations were 0.34 and 0.96 for PHSNs and SSNs, respectively. A theoretical analysis of DLVO interaction forces between SSNs or PHSNs and collector surfaces suggested relatively small differences in the magnitude of the interaction forces,⁵³ and is in agreement with the calculations in this study. It is likely that the surface structure differences caused by the concave asperities in the PHSNs caused by the pores played an important role in the mobility of these particles.

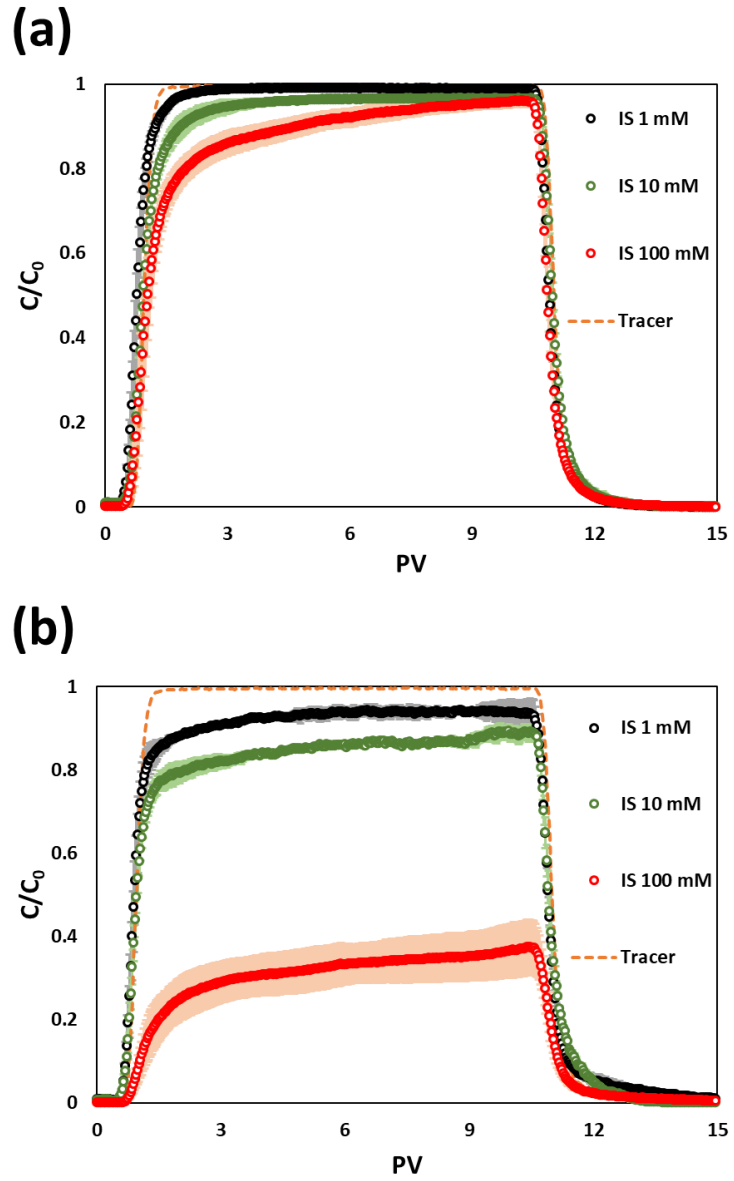


Figure 4-5. BTCs at fixed pH 9.5 and varying IS for (a) SSNs and (b) PHSNs. The shaded zones represent the standard deviation of the particle concentration run in triplicates. Wider shaded areas represent greater standard deviation among replicates. The conditions with no visible shaded areas represent runs with not relevant difference among replicates.

4.4.4. Single Collector Contact Efficiencies (η_0) and Particle-Collector Attachment Efficiencies (α_{pc})

The η_0 values as a function of particle radius (a_p) for SSNs (Figure 4-7a) and PHSNs (Figure 4-7b) were calculated based on expressions derived elsewhere.⁵⁴⁻⁵⁹ The expressions and parameters used to estimate the η_0 can be found in Table S4-3 and Table S4-4, respectively.

The average η_0 predicted for SSNs ($a_p = 92$ nm) and PHSNs ($a_p = 103$ nm) were 0.007 and 0.005, respectively. The η_0 were slightly greater for SSNs, which is contrary to observations of lower mobility of PHSNs in the column experiments. To assess the size difference effect between SSNs and PHSNs, the η_0 ratio was plotted as a function of particle size in Figure 4-7c. For any particle radius below 100 nm, SSNs and PHSNs have very similar predictions for η_0 . For any particle radius above 100 nm, the predicted η_0 for SSNs surpassed the predicted η_0 for PHSNs, indicating more chance of retention for SSNs than for PHSNs. Therefore, η_0 could not explain why contrary trends with the experimental data exist.

The α_{pc} values remained below 0.04 for all experimental conditions with SSNs, whereas they reached 0.54 and 0.59 for PHSNs at pH 4.5 and IS 1 mM, and at pH 9.5 and IS 100 mM, respectively, which were the conditions where retention was more pronounced. The α_{pc} values (Table S4-5) were calculated with Equation (4-3) below, where d_g is the sand grain diameter [L], n is the porosity of the sand-packed column, L is the column length [L], η_0 is the average single collector contact efficiency, C_0 is the initial concentration of the colloidal suspension [mol L^{-3}] and C is the concentration of the colloidal suspension exiting the column [mol L^{-3}].

$$\alpha_{pc} = -\frac{2}{3} \frac{d_g}{(1-n)L\eta_0} \ln\left(\frac{C}{C_0}\right) \quad (4-3)$$

4.4.5. Surface Roughness and the DLVO Theory

Deviations from DLVO predictions due to nanoscale physical heterogeneity have been previously reported.⁶⁸⁻⁷⁷ These deviations happen because the DLVO theory assumes that particle and collector surfaces are geometrically smooth and homogeneous, when in reality colloid may possess some degree of roughness.⁷⁰ Modeling and experimental data have demonstrated that surface roughness reduces the repulsive energy barriers, and in some cases eliminates them altogether.⁷⁰⁻

^{72, 75} For instance, Liang et al.⁷⁴ observed enhanced retention of silver nanoparticles in porous media with higher surface roughness (SR). Retention was 6.8-fold higher in relatively rough sand particles (root mean square roughness, $S_q = 524$ nm) when compared to the experimental condition using relatively smooth sand ($S_q = 93$ nm).

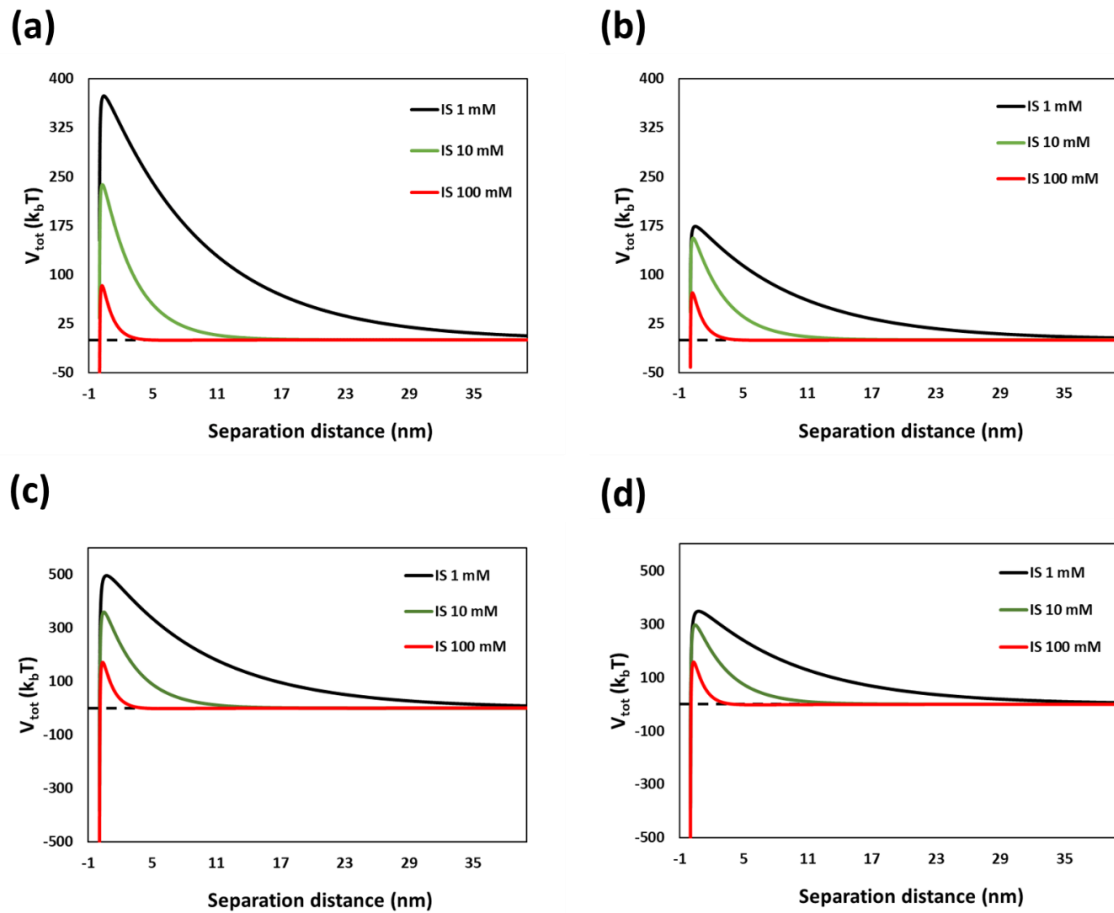


Figure 4-6. DLVO energy profiles at fixed pH 9.5 and varying IS for (a) SSN particle-particle interactions, (b) PHSN particle-particle interactions, (c) SSN particle-collector interactions, and (d) PHSN particle-collector interactions.

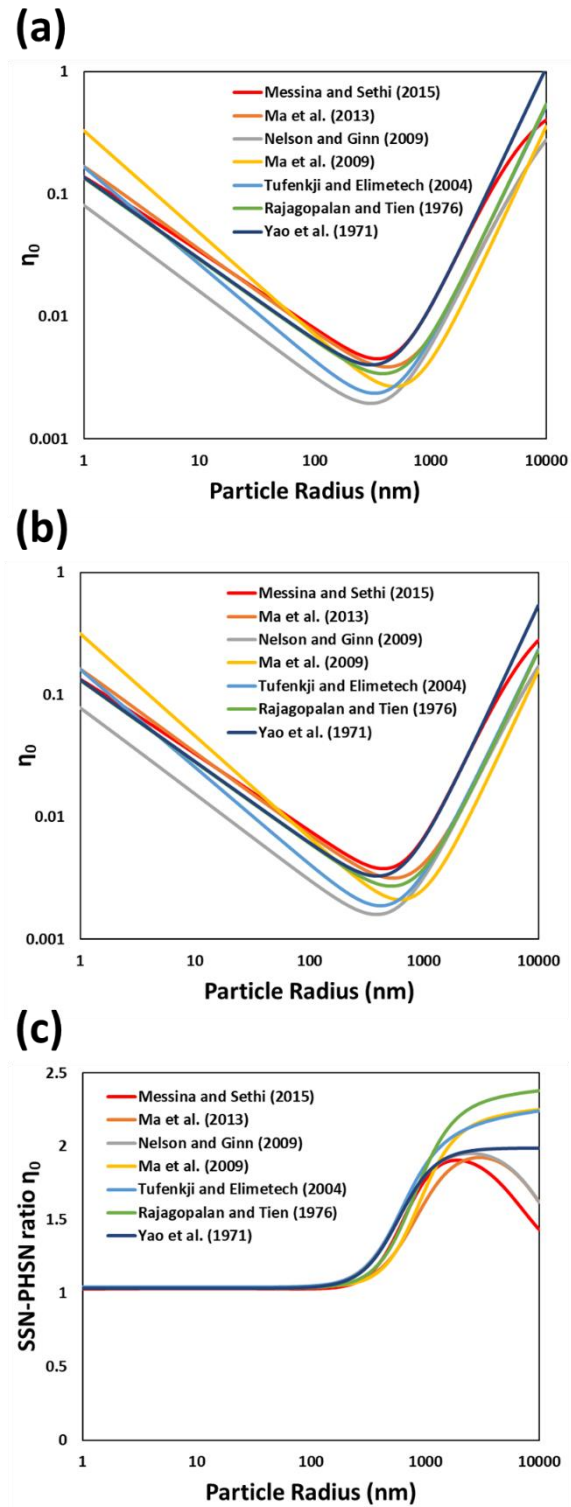


Figure 4-7. Estimates of η_0 for (a) SSNs and (b) PHSNs, and (c) the SSN-PHSN η_0 ratio.

Specifically, two phenomena are relevant: (i) the concave asperities in PHSN surface, caused by the presence of pores in the surface, result in the separation distance among particle-particle and/or particle-collector surfaces becoming larger at the pores, when compared to that of SSNs⁷² as depicted in Figure 4-8. Generally, as the separation distance increases, overall repulsive electrostatic forces generally decay faster than van der Waals interactions,⁷⁸ resulting in enhanced attraction to the collector surface. (ii) The roughness caused by the asperities on a PHSN surface alter the flow field around the particle during the column experiments, enhancing resisting adhesive torque and diminishing applied hydrodynamic torque.⁷⁹ These effects likely led to enhanced colloid immobilization on the collector in this study.

Overall, we found evidence that particle structure, particularly SR, played an important role in the transport behavior of the PHSN population when compared to that of SSN, increasing the retention of the former 3-fold. These are non-intuitive results because PHSNs have lower density, same chemical composition and similar diameter when compared to the SSNs. In this case, the interaction energies, particularly van der Waals, behave differently in a porous-hollow structure, thus causing the differences in the transport behaviors. These results explore the fundamental energy interactions in porous structures can be extrapolated to other nanomaterials with environmental significance other than SiO₂. Moreover, SSNs are used as the model particle to predict environmental fate of SiO₂-based NPs such as in Wang et al.²⁰ However, PHSNs and other mesoporous particles are being increasingly applied in agricultural fields rather than SSNs. Here we showed that the transport profile varies significantly depending on particle structure and we cannot use a one-fit-all NP model.

It is also important to note that this work has assessed the transport behavior of SiO₂ NPs in saturated sand, and thus, will differ from actual agricultural conditions. Agricultural soils are generally unsaturated, with some exceptions, such as when the soil is irrigated or during precipitation. Agricultural soil may also contain high organic matter content and other types of contaminants that could bind with the NPs and influence their mobility. These conditions, however, are not replicated in our experimental setting. Nevertheless, the use of saturated sand served as model towards a first step in assessing the fundamental differences in the transport profile of SSNs and PHSNs and how their structure plays a role in their mobility. These experiments also

replicate aquifer systems where these nanoparticles could eventually reach as it is not uncommon that residues from agricultural practices end up in groundwater.

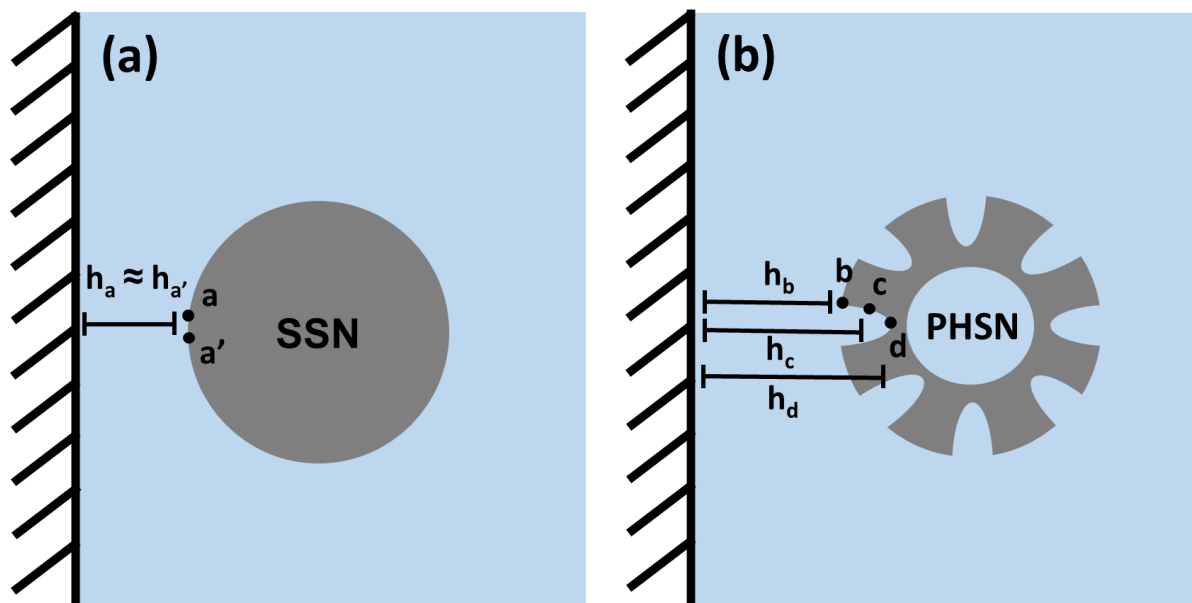


Figure 4-8. Schematic representation of the distance between sites in the SSN (a) and PHSN (b), and a hypothetical surface. For SSNs, the distance from point a to the surface, h_a , and the distance from a relatively distant point a' to the same surface, $h_{a'}$, are approximately the same. Meanwhile, in PHSNs, the distances h_b , h_c and h_d may vary significantly, even if they are at the same distance as points a and a' in scheme (a). Effectively, the overall separation distance between rough spherical surfaces and a hypothetical surface is larger than the distance between smooth spherical surfaces and a hypothetical surface.

4.5. Conclusions

Herein, we synthesized, characterized, and investigated the mobility of SSNs and PHSNs in a saturated sand-packed column in various pH and IS conditions. As expected, the zeta potential of both sets of particles approached lower absolute values as pH became more acidic and closer to the isoelectric point of SiO_2 nanoparticles. On the other hand, zeta potential approached lower absolute values as IS increased. The decrease in zeta potential indicates a decrease in the repulsive forces between nanoparticles, which in turn led to a small extent of agglomeration, and higher Pdl.

During the column experiments, deposition was enhanced by the decrease of pH and increase of IS, as acidic pH and high salinity decrease the overall colloidal stability of SiO₂ nanoparticles in suspension. The PHSNs, however, experienced a higher degree of deposition when compared to SSNs. DLVO energy profiles and single collector contact efficiency values were unable to explain why such discrepancies existed, and surface roughness likely contributed to the different extents of deposition. The surface roughness was not factored into the DLVO calculations because of the high complexity of the calculations and the many assumptions needed. The surface roughness related concave asperities of the pores lowered the repulsive energy barriers and led to more deposition.

This study elucidates how nanoparticle architecture can influence their mobility in porous media and highlights the importance of a thorough experimental analysis of the fate and transport of nanoparticles of different architecture that are likely to be discharged in the environment, such those intended for use in nano-enabled agriculture.

4.6. Supporting Information

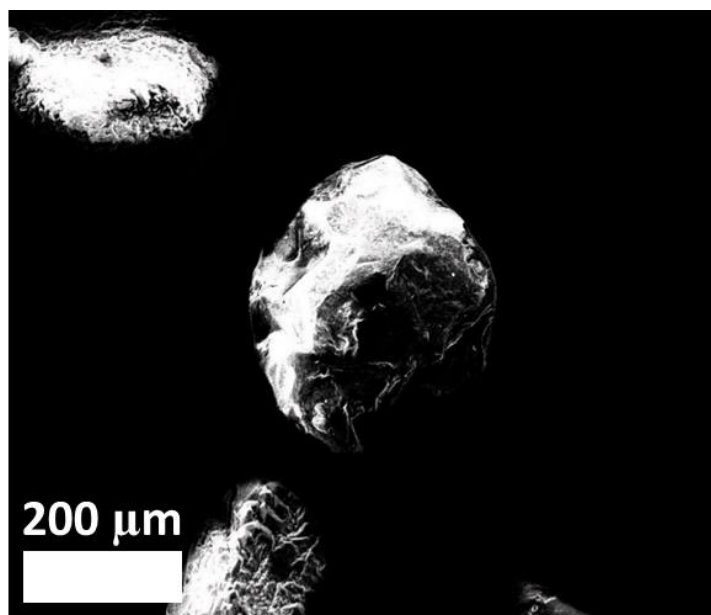


Figure S4-1. Scanning electronic microscopy (SEM) image of white quartz sand.

Table S4-1. White quartz sand zeta potential values at various conditions.

Ionic Strength (mM)	pH	Zeta potential (mV)
1	4.5	-27.4
1	6.5	-37.2
1	9.5	-45.8
10	9.5	-37.0
100	9.5	-18.7

4.6.1. Equations Used for the DLVO Energy Profile Computations

The DLVO theory predicts the interaction forces involving charged particles and surfaces immersed in electrolytes solutions. These forces govern stability and aggregation behavior in colloidal systems.^{80, 81} Classical DLVO takes into account the effects of attracting van der Waals forces and repulsive electrostatic forces, but a number of authors have introduced new expressions to include other nano-scale interactions, namely Born, steric and magnetic forces.⁴⁸⁻⁵⁰ These forces, however, are negligible for non-coated SiO₂ nanoparticles^{18, 20, 82} and thus will not be considered for the calculations. Herein we will consider the DLVO forces as the sum of van der Waals and electrostatic double layer contributions only:

$$V_{\text{tot}} = V_{\text{vdW}} + V_{\text{edl}} \quad (\text{S4-1})$$

Gregory⁴⁷ developed approximate expressions for retarded van der Waals forces for particle-particle interactions (Equation S2) and particle-collector interactions (Equation S3):

$$V_{\text{vdW}} = -\frac{H_{131}a_p}{12r\left(1 + 14\frac{r}{\lambda}\right)} \quad (\text{S4-2})$$

$$V_{\text{vdW}} = -\frac{H_{132}a_p}{6r\left(1 + 14\frac{r}{\lambda}\right)} \quad (\text{S4-3})$$

Where H_{131} [$M L^2 T^{-2}$] is the global Hamaker constant, a_p [L] is the particle radius, r [L] is the separation distance between the two surfaces and λ [L] is the characteristic wavelength of the interaction. These expressions are valid for valid for $r \ll a_p$.

Gregory⁵¹ developed an expression to estimate the global Hamaker constant:

$$H_{132} = \frac{3k_b T}{4} \left(\frac{\epsilon_{r,1} - \epsilon_{r,3}}{\epsilon_{r,1} + \epsilon_{r,3}} \right) \left(\frac{\epsilon_{r,2} - \epsilon_{r,3}}{\epsilon_{r,2} + \epsilon_{r,3}} \right) + \frac{3h\nu_e}{8\sqrt{2}} \left[\frac{(\delta_1^2 - \delta_3^2)(\delta_2^2 - \delta_3^2)}{(\delta_1^2 + \delta_3^2)(\delta_2^2 + \delta_3^2)\sqrt{(\delta_1^2 + \delta_3^2) + (\delta_2^2 + \delta_3^2)}} \right] \quad (S4-4)$$

Where k_b is the Boltzmann constant (1.38×10^{-23} J/K), T is the absolute temperature, $\epsilon_{r,i}$ the relative dielectric constant of i -th medium, h is the Planck's constant (6.626×10^{-34} J s), ν_e is the electronic absorption frequency in the UV region (3×10^{15} s⁻¹) and δ_i is the refractive index of i -th medium.

Table S4-2. Physical properties of SiO₂, water and white quartz sand at 100 nm.

Medium	Refractive Index, δ	Relative dielectric constant, ϵ
SiO ₂	1.49	3.9
White quartz sand	1.51	4.2
Water	1.33	78.5

For PHSNs, the interior and exterior fluid compositions are theoretically the same, thus the van der Waals energy profile is calculate by subtracting the resulting forces from the inner environment from the resulting forces from the outer surface of the shell^{52, 53}:

$$V_{vdW} = V_{vdW}^{out} - V_{vdW}^{in} \quad (S4-5)$$

Gregory⁸³ also derived expressions to predict electrostatic double-layer interactions between particle-particle (Equation S6) and particle-collector (Equation S7):

$$V_{\text{edl}} = 64\pi\epsilon_0\epsilon_r \frac{a_{p,1}a_{p,2}}{a_{p,1} + a_{p,2}} \left(\frac{k_b T}{zq}\right)^2 \Gamma_1\Gamma_2 e^{-\kappa r} \quad (\text{S4-6})$$

$$V_{\text{edl}} = 64\pi\epsilon_0\epsilon_r a_p \left(\frac{k_b T}{zq}\right)^2 \Gamma_1\Gamma_2 e^{-\kappa r} \quad (\text{S4-7})$$

Where ϵ_0 [$\text{I}^2 \text{t}^4 \text{M}^{-1} \text{L}^{-3}$] is the vacuum dielectric constant, $\Gamma_{1,2} = \tanh\left[\frac{zq\psi_0}{4k_b T}\right]$ is the dimensionless surface potential, z the ion valence, q [I t] is the electron charge and κ [L^{-1}] is the inverse of Debye-length. The Debye length (κ^{-1}) is calculated as per Equation S8:⁸⁴

$$\kappa^{-1} = \sqrt{\frac{\epsilon_0\epsilon_r k_b T}{q^2 n_a 2I}} \quad (\text{S4-8})$$

Where n_a [mol^{-1}] is the Avogadro number and $I = \sum z_i^2 c_i$ [mol L^{-3}] is the solution ionic strength.

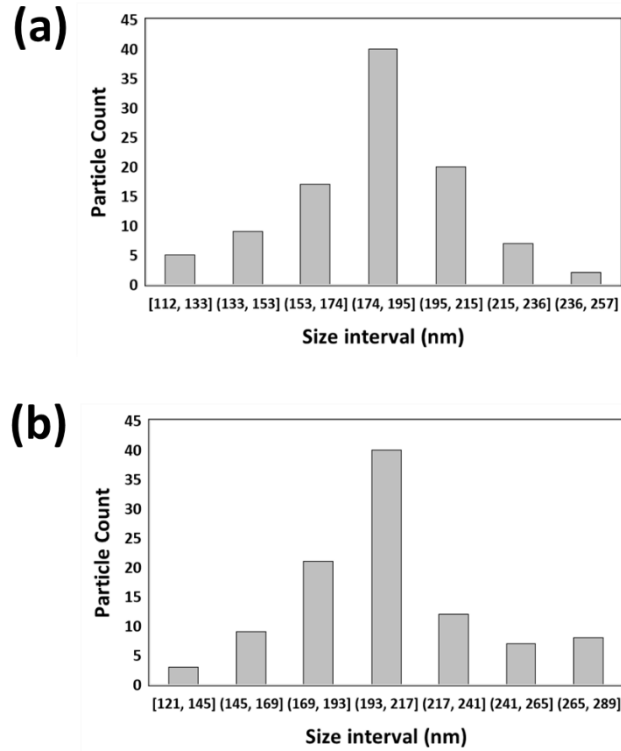


Figure S4-2. TEM size distribution ($N = 100$) of (a) SSNs and (b) PHSNs.

Table S4-3. Expressions used for the prediction of single collector contact efficiencies.

Yao et al. ⁵⁴	$\eta_0 = 4.04N_{Pe}^{-\frac{2}{3}} + N_G + \frac{3}{2}N_R^2$
Rajagopalan- Tien ⁵⁵	$\eta_0 = 4.04N_{Pe}^{-\frac{2}{3}} A_S^{0.333} + A_S N_R^{1.875} N_{LO}^{0.125} + 0.00338 A_S N_G^{1.2} N_R^{-0.4}$
Tufenkji- Elimelech ⁵⁶	$\eta_0 = 2.4 A_S^{0.333} N_{Pe}^{-0.715} N_R^{-0.081} N_{vdw}^{0.052} + 0.55 A_S N_R^{1.675} N_A^{-0.125} + 0.22 N_G^{1.11} N_R^{-0.24} N_{vdw}^{0.053}$
Ma et al. ⁵⁷	$\eta_0 = 2.3 A_S^{0.333} N_A^{0.052} N_R^{-0.08} N_{Pe}^{-0.65} + 0.55 A_S N_R^{1.8} N_A^{0.15} + 0.2 N_G^{1.11} N_R^{-0.10} N_{Pe}^{0.053} N_A^{0.053}$
Nelson- Ginn ⁵⁸	$\eta_0 = 2.4A_S^{0.333} \left(\frac{N_{Pe}}{N_{pe} + 16} \right)^{0.75} N_{Pe}^{-0.68} N_{LO}^{0.015} N_{Gi}^{0.8} + A_S N_{LO}^{0.125} N_R^{1.875} + 0.7 \left(\frac{N_{Gi}}{N_{Gi} + 0.9} \right) N_G N_R^{-0.05}$
Ma et al. ⁵⁹	$\eta_0 = \frac{8 + 4(1 - \gamma) A_S^{0.333} N_{pe}^{0.333}}{8 + 4(1 - \gamma) N_{pe}^{0.97}} N_{LO}^{0.015} N_{Gi}^{0.8} N_R^{0.028} + A_S N_R^{1.875} N_{LO}^{0.125} + 0.7 N_R^{-0.05} N_G \left(\frac{N_{Gi}}{N_{Gi} + 0.9} \right)$
Messina- Sethi ⁶⁰	$\eta_0 = \gamma^2 \left[1.5A_S N_R^{1.98} + \frac{7.56 N_{Pe}^{-1}}{2 - 2\gamma} + N_G + A_S^{0.366} N_{Pe}^{-0.634} (2.935 + 2.748 N_R^{0.374}) + 0.946 N_R^{0.655} N_{Pe}^{-0.345} \right]$

Where η_0 is the single collector contact efficiency, N_{Pe} is the Peclet number, N_G is the Gravity number, N_R is the aspect ratio, $A_S = \left[\frac{(1-\gamma^5)}{2-3\gamma+3\gamma^5-2\gamma^6} \right]$ is a porosity-dependent parameter, N_{LO} is the London-van der Waals number, N_{vdw} is the van der Waals number, N_A is the attraction number, N_{Gi} is the gravitational number, and $\gamma = \left[(1 - n)^{1/3} \right]$ is a porosity (n)-dependent parameter.

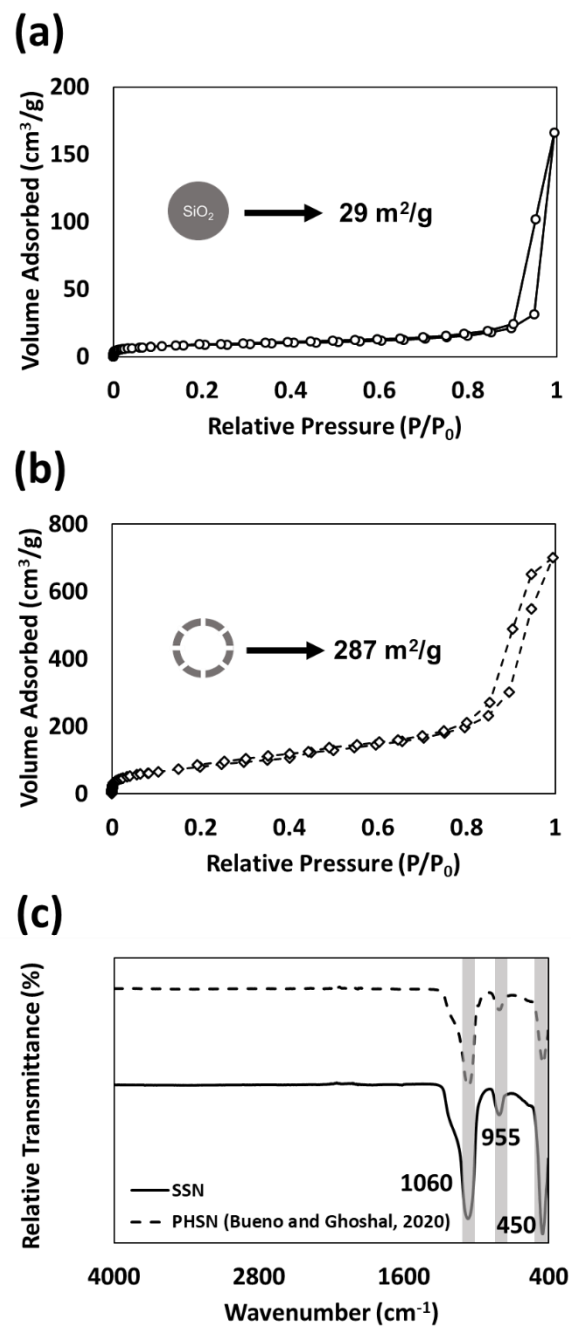


Figure S4-3. Nitrogen sorption/desorption isotherms with inset representation of the structure and specific surface area for (a) SSNs and (b) PHSNs,³⁶ and (c) FTIR spectra of the 4000-400 cm^{-1} region for SSNs and PHSN previously reported.

The FTIR spectra suggest that the surfactants (CTAB and Pluronic P123) as well as the NH₄OH used in the synthesis were successfully removed after calcination at 550°C as the only characteristic bands in the spectra belong to the bonds between silicon and oxygen atoms: (i) the band in 1060 cm⁻¹ indicates the presence of Si–OH stretch, (ii) the band in 955 cm⁻¹ indicates the presence of Si–OH bend, and (iii) the band in 450 cm⁻¹ indicates the presence of Si–O out of plane deformation.

Table S4-4. Parameters used for calculations of single collector contact efficiency.

Parameter	SSN	PHSN
Pore-water velocity (m/s)	6.78×10 ⁻⁴	6.78×10 ⁻⁴
Porous media porosity	0.391	0.391
Collector diameter (m)	2.5×10 ⁻⁴	2.5×10 ⁻⁴
Particle density (g/cm³)	2.65	1.8
Fluid density (g/cm³)	1	1
Fluid viscosity (Pa s)	1×10 ⁻³	1×10 ⁻³
Fluid temperature (K)	293	293
Global Hamaker Constant (J)	6.59×10 ⁻²¹	5.79×10 ⁻²¹

Table S4-5. Particle-Collector Attachment Efficiencies (α_{pc}) for the varying experimental conditions.

Experiment	Structure	pH	IS (mM)	α_{pc}
Exp 1	SSN	4.5	1	0.037
Exp 2	SSN	6.5	1	0.020
Exp 3	SSN	9.5	1	0.004
Exp 4	SSN	9.5	10	0.016
Exp 5	SSN	9.5	100	0.033
Exp 6	PHSN	4.5	1	0.544
Exp 7	PHSN	6.5	1	0.089
Exp 8	PHSN	9.5	1	0.034
Exp 9	PHSN	9.5	10	0.070
Exp 10	PHSN	9.5	100	0.590

4.7. References

1. Hofmann, T.; Lowry, G. V.; Ghoshal, S.; Tufenkji, N.; Brambilla, D.; Dutcher, J. R.; Gilbertson, L. M.; Giraldo, J. P.; Kinsella, J. M.; Landry, M. P., Technology readiness and

overcoming barriers to sustainably implement nanotechnology-enabled plant agriculture. *Nature Food* **2020**, *1* (7), 416-425.

2. Kah, M.; Tufenkji, N.; White, J. C., Nano-enabled strategies to enhance crop nutrition and protection. *Nature Nanotechnology* **2019**, *14* (6), 532-540.

3. Lowry, G. V.; Avellan, A.; Gilbertson, L. M., Opportunities and challenges for nanotechnology in the agri-tech revolution. *Nature Nanotechnology* **2019**, *14* (6), 517-522.

4. Ditta, A., How helpful is nanotechnology in agriculture? *Advances in Natural Sciences: Nanoscience and Nanotechnology* **2012**, *3* (3), 033002.

5. Kopittke, P. M.; Lombi, E.; Wang, P.; Schjoerring, J. K.; Husted, S., Nanomaterials as fertilizers for improving plant mineral nutrition and environmental outcomes. *Environmental Science: Nano* **2019**, *6* (12), 3513-3524.

6. Camara, M. C.; Campos, E. V. R.; Monteiro, R. A.; Santo Pereira, A. d. E.; de Freitas Proença, P. L.; Fraceto, L. F., Development of stimuli-responsive nano-based pesticides: emerging opportunities for agriculture. *Journal of Nanobiotechnology* **2019**, *17* (1), 1-19.

7. de Oliveira, J. L.; Campos, E. V. R.; Bakshi, M.; Abhilash, P.; Fraceto, L. F., Application of nanotechnology for the encapsulation of botanical insecticides for sustainable agriculture: prospects and promises. *Biotechnology Advances* **2014**, *32* (8), 1550-1561.

8. Grillo, R.; Abhilash, P. C.; Fraceto, L. F., Nanotechnology applied to bio-encapsulation of pesticides. *Journal of Nanoscience and Nanotechnology* **2016**, *16* (1), 1231-1234.

9. Epstein, E., The anomaly of silicon in plant biology. *Proceedings of the National Academy of Sciences* **1994**, *91* (1), 11-17.

10. Luyckx, M.; Hausman, J.-F.; Lutts, S.; Guerriero, G., Silicon and plants: current knowledge and technological perspectives. *Frontiers in Plant Science* **2017**, *8*, 411.

11. El-Shetehy, M.; Moradi, A.; Maceroni, M.; Reinhardt, D.; Petri-Fink, A.; Rothen-Rutishauser, B.; Mauch, F.; Schwab, F., Silica nanoparticles enhance disease resistance in Arabidopsis plants. *Nature Nanotechnology* **2020**, 1-10.

12. Abdel-Haliem, M. E.; Hegazy, H. S.; Hassan, N. S.; Naguib, D. M., Effect of silica ions and nano silica on rice plants under salinity stress. *Ecological Engineering* **2017**, *99*, 282-289.
13. Attia, E. A.; Elhawat, N., Combined foliar and soil application of silica nanoparticles enhances the growth, flowering period and flower characteristics of marigold (*Tagetes erecta* L.). *Scientia Horticulturae* **2021**, *282*, 110015.
14. Zhao, P.; Yuan, W.; Xu, C.; Li, F.; Cao, L.; Huang, Q., Enhancement of spirotetramat transfer in cucumber plant using mesoporous silica nanoparticles as carriers. *Journal of Agricultural and Food Chemistry* **2018**, *66* (44), 11592-11600.
15. Cui, J.; Li, Y.; Jin, Q.; Li, F., Silica nanoparticles inhibit arsenic uptake into rice suspension cells via improving pectin synthesis and the mechanical force of the cell wall. *Environmental Science: Nano* **2020**, *7* (1), 162-171.
16. Tian, L.; Shen, J.; Sun, G.; Wang, B.; Ji, R.; Zhao, L., Foliar Application of SiO₂ Nanoparticles Alters Soil Metabolite Profiles and Microbial Community Composition in the Pakchoi (*Brassica chinensis* L.) Rhizosphere Grown in Contaminated Mine Soil. *Environmental Science and Technology* **2020**, *54* (20), 13137-13146.
17. Fatemi, H.; Pour, B. E.; Rizwan, M., Foliar application of silicon nanoparticles affected the growth, vitamin C, flavonoid, and antioxidant enzyme activities of coriander (*Coriandrum sativum* L.) plants grown in lead (Pb)-spiked soil. *Environmental Science and Pollution Research* **2021**, *28* (2), 1417-1425.
18. Kim, I.; Taghavy, A.; DiCarlo, D.; Huh, C., Aggregation of silica nanoparticles and its impact on particle mobility under high-salinity conditions. *Journal of Petroleum Science and Engineering* **2015**, *133*, 376-383.
19. Al-Anssari, S.; Nwideo, L.; Ali, M.; Sangwai, J. S.; Wang, S.; Barifcani, A.; Iglauer, S. In *Retention of silica nanoparticles in limestone porous media*, SPE/IATMI Asia Pacific Oil & Gas Conference and Exhibition, Society of Petroleum Engineers: **2017**.
20. Wang, C.; Bobba, A. D.; Attinti, R.; Shen, C.; Lazouskaya, V.; Wang, L.-P.; Jin, Y., Retention and transport of silica nanoparticles in saturated porous media: effect of concentration and particle size. *Environmental Science and Technology* **2012**, *46* (13), 7151-7158.

21. Qin, Y.; Wen, Z.; Zhang, W.; Chai, J.; Liu, D.; Wu, S., Different roles of silica nanoparticles played in virus transport in saturated and unsaturated porous media. *Environmental Pollution* **2020**, *259*, 113861.
22. Zhang, M.; Li, D.; Ye, Z.; Wang, S.; Xu, N.; Wang, F.; Liu, S.; Chen, J.; Gu, H., Effect of humic acid on the sedimentation and transport of nanoparticles silica in water-saturated porous media. *Journal of Soils and Sediments* **2020**, *20* (2), 911-920.
23. HonetschlÄgerová, L.; Janouškovcová, P.; Kubal, M., Enhanced transport of Si-coated nanoscale zero-valent iron particles in porous media. *Environmental Technology* **2016**, *37* (12), 1530-1538.
24. Li, J.; Bhattacharjee, S.; Ghoshal, S., The effects of viscosity of carboxymethyl cellulose on aggregation and transport of nanoscale zerovalent iron. *Colloids and Surfaces A: Physicochemical and Engineering Aspects* **2015**, *481*, 451-459.
25. Chen, J.; Ji, Q.; Zheng, P.; Chen, T.; Wang, C.; Mahmood, Q., Flootation and control of granular sludge in a high-rate anammox reactor. *Water Research* **2010**, *44* (11), 3321-3328.
26. Ishii, S.; Bell, J.; Marshall, F., Phytotoxic risk assessment of ambient air pollution on agricultural crops in Selangor State, Malaysia. *Environmental Pollution* **2007**, *150* (2), 267-279.
27. Torney, F.; Trewyn, B. G.; Lin, V. S.-Y.; Wang, K., Mesoporous silica nanoparticles deliver DNA and chemicals into plants. *Nature Nanotechnology* **2007**, *2* (5), 295-300.
28. Abdelrahman, T. M.; Qin, X.; Li, D.; Senosy, I. A.; Mmby, M.; Wan, H.; Li, J.; He, S., Pectinase-responsive carriers based on mesoporous silica nanoparticles for improving the translocation and fungicidal activity of prochloraz in rice plants. *Chemical Engineering Journal* **2021**, *404*, 126440.
29. Plohl, O.; Gyergyek, S.; Zemljíč, L. F., Mesoporous silica nanoparticles modified with N-rich polymer as a potentially environmentally-friendly delivery system for pesticides. *Microporous and Mesoporous Materials* **2021**, *310*, 110663.

30. Xu, Y.; Xu, C.; Huang, Q.; Cao, L.; Teng, F.; Zhao, P.; Jia, M., Size Effect of Mesoporous Silica Nanoparticles on Pesticide Loading, Release, and Delivery in Cucumber Plants. *Applied Sciences* **2021**, *11* (2), 575.
31. Gao, X.; Kundu, A.; Bueno, V.; Rahim, A. A.; Ghoshal, S., Uptake and Translocation of Mesoporous SiO₂-Coated ZnO Nanoparticles to Solanum lycopersicum Following Foliar Application. *Environmental Science and Technology* **2021**.
32. Feng, J.; Chen, W.; Shen, Y.; Chen, Q.; Yang, J.; Zhang, M.; Yang, W.; Yuan, S., Fabrication of abamectin-loaded mesoporous silica nanoparticles by emulsion-solvent evaporation to improve photolysis stability and extend insecticidal activity. *Nanotechnology* **2020**, *31* (34), 345705.
33. Liu, F.; Wen, L.-X.; Li, Z.-Z.; Yu, W.; Sun, H.-Y.; Chen, J.-F., Porous hollow silica nanoparticles as controlled delivery system for water-soluble pesticide. *Materials Research Bulletin* **2006**, *41* (12), 2268-2275.
34. Li, Z.-Z.; Xu, S.-A.; Wen, L.-X.; Liu, F.; Liu, A.-Q.; Wang, Q.; Sun, H.-Y.; Yu, W.; Chen, J.-F., Controlled release of avermectin from porous hollow silica nanoparticles: Influence of shell thickness on loading efficiency, UV-shielding property and release. *Journal of Controlled Release* **2006**, *111* (1-2), 81-88.
35. Wen, L. X.; Li, Z. Z.; Zou, H. K.; Liu, A. Q.; Chen, J. F., Controlled release of avermectin from porous hollow silica nanoparticles. *Pest Management Science* **2005**, *61* (6), 583-590.
36. Bueno, V.; Ghoshal, S., Self-Assembled Surfactant-Templated Synthesis of Porous Hollow Silica Nanoparticles: Mechanism of Formation and Feasibility of Post-Synthesis Nanoencapsulation. *Langmuir* **2020**, *36* (48), 14633-14643.
37. Lu, H.; Dong, J.; Xi, B.; Cai, P.; Xia, T.; Zhang, M., Transport and retention of porous silicon-coated zero-valent iron in saturated porous media. *Environmental Pollution* **2021**, *276*, 116700.
38. Torkzaban, S.; Wan, J.; Tokunaga, T. K.; Bradford, S. A., Impacts of bridging complexation on the transport of surface-modified nanoparticles in saturated sand. *Journal of Contaminant Hydrology* **2012**, *136*, 86-95.

39. Raychoudhury, T.; Tufenkji, N.; Ghoshal, S., Aggregation and deposition kinetics of carboxymethyl cellulose-modified zero-valent iron nanoparticles in porous media. *Water Research* **2012**, *46* (6), 1735-1744.
40. Raychoudhury, T.; Tufenkji, N.; Ghoshal, S., Straining of polyelectrolyte-stabilized nanoscale zero valent iron particles during transport through granular porous media. *Water Research* **2014**, *50*, 80-89.
41. Tosco, T.; Bosch, J.; Meckenstock, R. U.; Sethi, R., Transport of ferrihydrite nanoparticles in saturated porous media: role of ionic strength and flow rate. *Environmental Science and Technology* **2012**, *46* (7), 4008-4015.
42. Stöber, W.; Fink, A.; Bohn, E., Controlled growth of monodisperse silica spheres in the micron size range. *Journal of Colloid and Interface Science* **1968**, *26* (1), 62-69.
43. Schaffer, M.; Boxberger, N.; Börnick, H.; Licha, T.; Worch, E., Sorption influenced transport of ionizable pharmaceuticals onto a natural sandy aquifer sediment at different pH. *Chemosphere* **2012**, *87* (5), 513-520.
44. Lara, P.; Morett, E.; Juárez, K., Acetate biostimulation as an effective treatment for cleaning up alkaline soil highly contaminated with Cr (VI). *Environmental Science and Pollution Research* **2017**, *24* (33), 25513-25521.
45. Luo, W.; Kelly, S. D.; Kemner, K. M.; Watson, D.; Zhou, J.; Jardine, P. M.; Gu, B., Sequestering uranium and technetium through co-precipitation with aluminum in a contaminated acidic environment. *Environmental Science and Technology* **2009**, *43* (19), 7516-7522.
46. Oliviera, I.; Demond, A.; Salehzadeh, A., Packing of sands for the production of homogeneous porous media. *Soil Science Society of America Journal* **1996**, *60* (1), 49-53.
47. Gregory, J., Approximate expressions for retarded van der Waals interaction. *Journal of Colloid and Interface Science* **1981**, *83* (1), 138-145.
48. De Vicente, J.; Delgado, A.; Plaza, R.; Durán, J.; González-Caballero, F., Stability of cobalt ferrite colloidal particles. Effect of pH and applied magnetic fields. *Langmuir* **2000**, *16* (21), 7954-7961.

49. Ruckenstein, E.; Prieve, D. C., Adsorption and desorption of particles and their chromatographic separation. *American Institute of Chemical Engineers Journal* **1976**, *22* (2), 276-283.
50. Phenrat, T.; Liu, Y.; Tilton, R. D.; Lowry, G. V., Adsorbed polyelectrolyte coatings decrease Fe₀ nanoparticle reactivity with TCE in water: conceptual model and mechanisms. *Environmental Science and Technology* **2009**, *43* (5), 1507-1514.
51. Lipkin, D. M.; Israelachvili, J. N.; Clarke, D. R., Estimating the metal-ceramic van der Waals adhesion energy. *Philosophical Magazine A* **1997**, *76* (4), 715-728.
52. Shen, C.; Bradford, S. A.; Flury, M.; Huang, Y.; Wang, Z.; Li, B., DLVO interaction energies for hollow particles: The filling matters. *Langmuir* **2018**, *34* (43), 12764-12775.
53. Shen, C.; Bradford, S.; Wang, Z.; Huang, Y.; Zhang, Y.; Li, B., DLVO interaction energies between hollow spherical particles and collector surfaces. *Langmuir* **2017**, *33* (40), 10455-10467.
54. Yao, K.-M.; Habibian, M. T.; O'Melia, C. R., Water and waste water filtration. Concepts and applications. *Environmental Science and Technology* **1971**, *5* (11), 1105-1112.
55. Rajagopalan, R.; Tien, C., Trajectory analysis of deep-bed filtration with the sphere-in-cell porous media model. *American Institute of Chemical Engineers Journal* **1976**, *22* (3), 523-533.
56. Tufenkji, N.; Elimelech, M., Correlation equation for predicting single-collector efficiency in physicochemical filtration in saturated porous media. *Environmental Science and Technology* **2004**, *38* (2), 529-536.
57. Ma, H.; Pedel, J.; Fife, P.; Johnson, W. P., Hemispheres-in-cell geometry to predict colloid deposition in porous media. *Environmental Science and Technology* **2009**, *43* (22), 8573-8579.
58. Nelson, K. E.; Ginn, T. R., New collector efficiency equation for colloid filtration in both natural and engineered flow conditions. *Water Resources Research* **2011**, *47* (5).
59. Ma, H.; Hradisky, M.; Johnson, W. P., Extending applicability of correlation equations to predict colloidal retention in porous media at low fluid velocity. *Environmental Science and Technology* **2013**, *47* (5), 2272-2278.

60. Messina, F.; Marchisio, D. L.; Sethi, R., An extended and total flux normalized correlation equation for predicting single-collector efficiency. *Journal of Colloid and Interface Science* **2015**, *446*, 185-193.
61. Suttiponparnit, K.; Jiang, J.; Sahu, M.; Suvachittanont, S.; Charinpanitkul, T.; Biswas, P., Role of surface area, primary particle size, and crystal phase on titanium dioxide nanoparticle dispersion properties. *Nanoscale Research Letters* **2011**, *6* (1), 27.
62. Liu, Q.; Sun, Z.; Santamarina, J. C., Transport and adsorption of silica nanoparticles in carbonate reservoirs: A sand column study. *Energy Fuels* **2019**, *33* (5), 4009-4016.
63. Xu, S.; Gao, B.; Saiers, J. E., Straining of colloidal particles in saturated porous media. *Water Resources Research* **2006**, *42* (12).
64. Ko, C.-H.; Elimelech, M., The “shadow effect” in colloid transport and deposition dynamics in granular porous media: measurements and mechanisms. *Environmental Science and Technology* **2000**, *34* (17), 3681-3689.
65. Lazaro, A.; Vilanova, N.; Barreto Torres, L. D.; Resoort, G.; Voets, I. K.; Brouwers, H., Synthesis, polymerization, and assembly of nanosilica particles below the isoelectric point. *Langmuir* **2017**, *33* (51), 14618-14626.
66. Iler, K. R., The chemistry of silica. *Solubility, Polymerization, Colloid and Surface Properties And Biochemistry of Silica* **1979**.
67. Bergna, H. E.; Roberts, W. O., *Colloidal silica: fundamentals and applications*. CRC Press: **2005**; Vol. 131.
68. Rabinovich, Y. I.; Adler, J. J.; Ata, A.; Singh, R. K.; Moudgil, B. M., Adhesion between nanoscale rough surfaces: I. Role of asperity geometry. *Journal of Colloid and Interface Science* **2000**, *232* (1), 10-16.
69. Katainen, J.; Paajanen, M.; Ahtola, E.; Pore, V.; Lahtinen, J., Adhesion as an interplay between particle size and surface roughness. *Journal of Colloid and Interface Science* **2006**, *304* (2), 524-529.

70. Suresh, L.; Walz, J. Y., Effect of surface roughness on the interaction energy between a colloidal sphere and a flat plate. *Journal of Colloid and Interface Science* **1996**, *183* (1), 199-213.
71. Hoek, E. M.; Bhattacharjee, S.; Elimelech, M., Effect of membrane surface roughness on colloid– membrane DLVO interactions. *Langmuir* **2003**, *19* (11), 4836-4847.
72. Hoek, E. M.; Agarwal, G. K., Extended DLVO interactions between spherical particles and rough surfaces. *Journal of Colloid and Interface Science* **2006**, *298* (1), 50-58.
73. Shen, C.; Jin, Y.; Zhuang, J.; Li, T.; Xing, B., Role and importance of surface heterogeneities in transport of particles in saturated porous media. *Critical Reviews in Environmental Science and Technology* **2020**, *50* (3), 244-329.
74. Liang, Y.; Zhou, J.; Dong, Y.; Klumpp, E.; Šimůnek, J.; Bradford, S. A., Evidence for the critical role of nanoscale surface roughness on the retention and release of silver nanoparticles in porous media. *Environmental Pollution* **2020**, *258*, 113803.
75. Bhattacharjee, S.; Ko, C.-H.; Elimelech, M., DLVO interaction between rough surfaces. *Langmuir* **1998**, *14* (12), 3365-3375.
76. Bradford, S. A.; Torkzaban, S., Colloid interaction energies for physically and chemically heterogeneous porous media. *Langmuir* **2013**, *29* (11), 3668-3676.
77. Jin, C.; Zhao, W.; Normani, S. D.; Zhao, P.; Emelko, M. B., Synergies of media surface roughness and ionic strength on particle deposition during filtration. *Water Research* **2017**, *114*, 286-295.
78. Hahn, M. W.; O'Melia, C. R., Deposition and reentrainment of Brownian particles in porous media under unfavorable chemical conditions: Some concepts and applications. *Environmental Science and Technology* **2004**, *38* (1), 210-220.
79. Bradford, S. A.; Torkzaban, S.; Shapiro, A., A theoretical analysis of colloid attachment and straining in chemically heterogeneous porous media. *Langmuir* **2013**, *29* (23), 6944-6952.
80. Verwey, E. J. W.; Overbeek, J. T. G., Theory of the stability of lyophobic colloids. *Journal of Colloid and Interface Science* **1955**, *10* (2), 224-225.

81. Derjaguin, B.; Landau, L., Theory of the stability of strongly charged lyophobic sols and of the adhesion of strongly charged particles in solutions of electrolytes. *Progress in Surface Science* **1993**, *43* (1-4), 30-59.
82. Chen, Z. H.; Kim, C.; Zeng, X.-b.; Hwang, S. H.; Jang, J.; Ungar, G., Characterizing size and porosity of hollow nanoparticles: SAXS, SANS, TEM, DLS, and adsorption isotherms compared. *Langmuir* **2012**, *28* (43), 15350-15361.
83. Gregory, J., Interaction of unequal double layers at constant charge. *Journal of Colloid and Interface Science* **1975**, *51* (1), 44-51.
84. Dunphy Guzman, K. A.; Finnegan, M. P.; Banfield, J. F., Influence of surface potential on aggregation and transport of titania nanoparticles. *Environmental Science and Technology* **2006**, *40* (24), 7688-7693.

Connecting Text to Chapter 5

Chapter 5 continues to explore the environmental fate of porous hollow silica nanoparticles (PHSN) started in Chapter 4, where the mobility of PHSN was evaluated in model subsurface porous media. Chapter 5 investigates whether PHSN-encapsulated pesticides have an impact on plant and soil health and how these compare with non-encapsulated pesticide applications. In this chapter, several factors were assessed to gauge how plants and soil microbial community responded to different treatments involving nanoencapsulated azoxystrobin, non-encapsulated azoxystrobin, and nanocarrier alone. The factors assessed included overall pesticide uptake by plants, plant growth development, and soil microbial community shifts. Chapters 4 and 5 combined provide an overview of the environmental fate of nanoformulations after application and how they interact with living organisms and soils.

Chapter 5. Impacts of Porous Silica-Nanoencapsulated Pesticide Applied on Soils on Plant Growth and Soil Microbial Community

5.1. Abstract

Porous silica (SiO_2) nanocarriers have the potential to improve agricultural crop productivity. However, the impacts of nanoencapsulated pesticides on soil health and plant growth, and how they compare with conventional pesticide have not been systematically elucidated. In this study, we investigated how applying azoxystrobin nanoencapsulated in porous hollow SiO_2 nanocarriers to agricultural soil impacted the soil microbial community and plant development, using *Solanum lycopersicum* grown in the laboratory in soil microcosms. The data showed that plant growth was heavily inhibited by the non-encapsulated pesticide treatment compared to that with encapsulated pesticide yielding 3.85-fold less biomass, while soil microbial community experienced few to no changes regardless of the treatment. There was a 2.7-fold higher azoxystrobin uptake per unit dry plant biomass after 10 days of exposure for the non-encapsulated pesticide treatment when compared to that of nanoencapsulated pesticide, but only 1.5-fold increase in absolute uptake. After 20 days of exposure, however, the absolute uptake and uptake per unit of dry biomass were 3-fold and 10-fold higher, respectively, for the nanopesticide treatment. The differences in uptake can be attributed to phytotoxicity caused by the high the bioavailability of the non-encapsulated pesticide. The nanocarrier promoted slow release of the pesticide over days, which prevented phytotoxicity, and allowed healthy plant growth.

5.2. Environmental Significance

Nanoencapsulated pesticides are viewed as a promising technology to improve pesticide utilization rates in agriculture. It is, however, unclear whether these nanoformulations are indeed more effective than the conventional pesticide formulations. In this work, we reported higher uptake and longer exposure of azoxystrobin in the nanoencapsulated form compared to those of the non-encapsulated form. This indicates that nanoencapsulated pesticides can be more efficient in delivering the active ingredient and could potentially reduce application times. Furthermore, the nanocarrier did not seem to affect soil and plant health. In fact, it mitigated the toxic effect of the

pesticide towards plant growth. Overall, the deployment of nanocarriers in agriculture shows potential to increase efficiency while not creating negative implications to the environment.

5.3. Introduction

There is growing interest in exploring the development and use of nanomaterials of various composition and forms for efficient delivery of pesticides, nutrients or other growth factors to crop plants, towards increasing crop yields and reducing agrochemical wastage and environmental contamination.¹⁻⁵ Nanocarriers are a class of nanomaterials that can facilitate targeted delivery and controlled release of pesticides and fertilizers in plants.⁶ There is significant interest in using nanocarriers both for foliar or root applications. Although application of nanoformulations on leaves, rather than directly on soils, can better reduce fertilizer and pesticide wastage and avoid soil contamination,²⁻⁴ soil drenching with nanomaterial dispersions could be necessary to condition agricultural soils before the addition of seeds, to minimize pests and to provide optimal plant growth conditions.⁷⁻¹⁴ Nanocarriers may provide advantages over conventional formulations by aiding the dispersion of hydrophobic chemicals, providing controlled release of the active ingredient, and prevent their abiotic or abiotic degradation in soil.

SiO₂ NPs designed as porous structures have been recently suggested as promising nanocarrier for pesticides. SiO₂ is an earth-abundant material, it is a potentially safe material to be used in agriculture.¹⁵⁻¹⁷ Enhanced uptake of silicon increased plant resistance to pathogens and abiotic stress.^{16, 18-21} Furthermore, SiO₂ NPs have been shown to enhance growth, protein content and photosynthesis of lupin,²² and protect wheat against UV-B stress,²³ chromium- and arsenic-induced oxidative stress,^{24, 25} and improve its germination,²⁶ root growth and chlorophyll content.²⁷ Tian et al.²⁸ reported that continuous application of SiO₂ NPs increased activity of enzymes associated with carbon and nitrogen cycling in soil. A few studies have shown that encapsulating pesticides within SiO₂ NPs could increase pesticide translocation and fungicidal activity, provide controlled and targeted delivery properties, and promote physical protection against premature degradation.²⁹⁻³⁵ For instance, Xu et al.³⁵ reported that encapsulating pyraoxystrobin within a carbon nanotube-mesoporous silica nanoparticle (MSN) composite and introducing it in growth medium, enhanced the upward translocation of the fungicide 3.5-fold in cucumber seedlings in hydroponic systems. Abdelrahman et al.²⁹ developed a stimuli-responsive MSN to control the

delivery of prochloraz to rice plants. Pectin was functionalized into the MSNs surface to cover the pores, acting as a gatekeeper compound, and when pectinase was added to the system, pectin was hydrolyzed, thus releasing prochloraz. The authors claimed to have enhanced pesticide translocation and fungal activity over a prolonged period when compared to conventional prochloraz formulations.

Herein, we encapsulated azoxystrobin within porous hollow SiO₂ NPs (PHSNs) and examined its impacts on plant growth in soil systems as well the soil microbial population, and how they compare with non-encapsulated azoxystrobin applications following soil application. PHSNs are particularly promising nanocarriers because they allow for the high-density loading of molecules. Unlike MSNs, PHSNs have larger pore volume than MSN due to a void core, where one of the same or several different molecules can be encapsulated. Bueno and Ghoshal (2020)³⁶ demonstrated that solutes can be transported across the porous shell of the PHSN. Azoxystrobin was selected because it is a commonly used fungicide for crop agriculture worldwide, is highly efficient,³⁷ has broad spectrum coverage and is a systemic pesticide. Studies have reported phytotoxicity of azoxystrobin to apple and grape cultivars³⁸⁻⁴⁰ as well as to soil microbiota other than targeted pathogenic microorganisms.⁴¹ Therefore, an ideal nanocarrier for azoxystrobin would mitigate its toxicity towards crops and vital soil microbiota by providing controlled release of the azoxystrobin. Assessing adverse effects of PHSN and the encapsulated azoxystrobin on soil microbiota is important to verify because they regulate nutrient cycling and carry out other important functions for plant growth. Major shifts in key soil microbial communities other than in the targeted pathogenic microorganisms can affect the soil health and the ability to cultivate crops.

In this work, we demonstrated the slower release of nanoencapsulated azoxystrobin from PHSN compared to the dissolution rate of the non-encapsulated azoxystrobin. We hypothesized that the nanoencapsulated form of azoxystrobin will have different uptake extents and distributions compared to the non-encapsulated form, and thus different impacts on plant health.

5.4. Experimental Section

5.4.1. Materials

Tetraethyl orthosilicate (TEOS, reagent grade 98%), ammonium hydroxide solution (NH₄OH, 28.0-30.0% NH₃ basis), hexadecyltrimethylammonium bromide (CTAB) and Pluronic P123 were

purchased from Sigma-Aldrich. Deionized (DI) water ASTM type 1, Invitrogen UltraPure DNase-, RNase-free DI water, HPLC grade solvents (water, acetonitrile and methanol), formic acid, ammonium acetate, anhydrous magnesium sulphate (MgSO_4), dimethyl sulfoxide, and sodium acetate were purchased from Thermo Fisher Scientific. Primary and secondary amine (PSA) salt was purchased from Agilent. Anhydrous ethanol (100%) was purchased from Commercial Alcohols (Canada). *Solanum lycopersicum* seeds (Heirloom, Beefsteak Bush) were purchased from McKenzie Seeds (Canada). iTaq Universal SYBR Green Supermix was purchased from BioRad. Bovine serum albumin was purchased from New England BioLabs. Azoxystrobin ($\text{C}_{22}\text{H}_{17}\text{N}_3\text{O}_5$, CAS Registry Number 131860-33-8, $\log K_{ow}$ 3.7) was provided by Vive Crop Protection Inc (Canada) in powder form. Deuterated internal standard (D_4 -azoxystrobin) was purchased from Toronto Research Chemicals (Canada).

Soil was collected from an agricultural site at the Macdonald campus of McGill University. The soil was characterized by A&L Canada Laboratories (Ontario, Canada) and the soil properties are shown in Table S5-1.

5.4.2. SiO_2 NPs Synthesis

Porous hollow SiO_2 NPs (PHSN) were synthesized as reported in our previous work.³⁶ Briefly, in a round-bottom flask, 300 mg of CTAB and 850 mg of Pluronic were added to a mixture containing 75 mL of anhydrous ethanol and 125 mL of DI water. The surfactants self-assembled forming the hollow core for the SiO_2 NP. Then, 15 mL of NH_4OH is added to alkalize the medium and accelerate the hydrolysis of the silica precursor, TEOS, which was added dropwise at a rate of 0.75 mL/min for 13.33 min. The reaction was allowed to proceed for 5 hours under vigorous magnetic stirring. The suspension was dried overnight under 80 °C and calcined under 550°C for 5 h to remove any trace of surfactants and ammonia by-products. Detailed characterization data for PHSN has been reported in our prior studies and found to be approximately 253 nm in diameter,³⁶ with a porous shell of thickness ranging from 22 to 38 nm,³⁶ micro-scaled pores in the order of 1.5 nm,³⁶ a specific surface area of 287 $\text{m}^2 \text{g}^{-1}$,³⁶ and surface zeta potential -29.2 ± 1.1 mV at pH 6.5 and ionic strength 1 mM (NaCl).⁴²

5.4.3. Azoxystrobin loading and release rates

0.1 mg/mL of azoxystrobin was solubilized in a mixture containing DI water (80%) and methanol (20%). Without methanol, most of the azoxystrobin added at this concentration would remain in its solid phase due to its low aqueous solubility (6 µg/mL). Furthermore, when solubilized, the solute (azoxystrobin) is able to infiltrate the pores and reach the hollow core of the PHSN.³⁶ These experiments were performed in Nalgene Teflon tubes to avoid azoxystrobin sorption onto the container's walls. This ratio was determined by measuring the dissolved azoxystrobin in mixtures of varying water-methanol ratios, to identify low methanol doses that provide sufficient solubilization of azoxystrobin. Then, PHSN were added to the system at a concentration of 0.67 mg/mL. The tubes were stirred at 200 rpm. Solution aliquots were collected at specific time intervals, diluted in acetonitrile, and analyzed using an Agilent 1260 Infinity II HPLC system equipped with UV detector (at 255 nm characteristic wavelength), using acetonitrile and water (80:20 v/v) as the mobile phase. At the 8th day, the PHSN were separated from the solution through centrifugation under 5500 rpm for 15 min. The final azoxystrobin concentration in the solution and loaded in the PHSN were quantified in the HPLC-UV to account for the mass balance. The loaded azoxystrobin was extracted from the PHSN through successive acetonitrile extractions until no further azoxystrobin could be extracted.

The release time profile of the nanoencapsulated azoxystrobin was obtained by dispersing the azoxystrobin-loaded PHSN in a mixture of DI water-methanol (80:20 v/v). Due to azoxystrobin's low aqueous solubility as previously discussed, the release profile would be limited by the dissolution rate. The addition of methanol eliminates the solubility limitation and allows the investigation of the release profile of the pesticide in the PHSN hollow core and porous shell and as well from the solid phase non-encapsulated azoxystrobin. Aliquots were collected at different time intervals and analyzed in HPLC-UV. The dissolution profile for pure azoxystrobin was obtained to compare the release profiles of the pure compound and the loaded compound.

5.4.4. Plant growth conditions and soil amendment

The *Solanum lycopersicum* seeds were sterilized in a 1.5% sodium hypochlorite solution for 15 min and then rinsed thoroughly with DI water. The seeds were covered in slightly wet tissue paper placed inside Petri dishes and allowed to germinate for 10 days in total darkness. Seedlings at the same growth stage were carefully picked and transplanted to soil. Each pot contained

approximately 61.6 g of dry soil and the humidity was kept at 70% of the water holding capacity at 1/3 bar. Four different treatments were analyzed to assess the impact of nanoencapsulated pesticides (i) Azo@PHSN: For the encapsulated pesticide, the soil was homogeneously amended with a suspension containing 5 mg of SiO₂ NPs and 0.75 mg of azoxystrobin in 7.5 mL of an 80:20 water-methanol mixture. (ii) Azo: For the non-encapsulated pesticide formulation, the soil was amended with 0.75 mg of azoxystrobin in 7.5 mL of an 80:20 water-methanol mixture (v/v). (iii) PHSN: A control with only SiO₂ NPs amendment was prepared by suspending 5 mg of SiO₂ NPs in a 7.5 mL 80:20 water-methanol mixture. (iv) Lastly, a control amendment was prepared by homogenizing a 7.5 mL 80:20 water-methanol mixture in soil to assess the impact of the water-methanol mixture would have itself in the plant growth and soil microbial community. It is important to note that the soil was amended with more than the recommended amount of azoxystrobin established by the EPA,⁴³ Health Canada⁴⁴ and commercial suppliers, which is around 0.2 ppm for *Solanum lycopersicum*. This was done to ensure observable effects of the pesticide and quantitatively assess if the SiO₂ nanocarrier was able to mitigate the pesticide toxicity/inhibitory effects. The pots were placed randomly and equidistant in an incubator with controlled conditions for 20 days: relative humidity at 70 ± 5%, a light/dark cycle of 16:8 h using a 36 W LED grow light system (IPower) with wavelengths at 430, 465, 630 and 660 nm to maximize chlorophyll activity, and constant temperature of 21 ± 1 °C.

5.4.5. Plant health data

The plants ($N = 3$) were harvested at days 10 and 20. The plant health was assessed by quantifying five observable characteristics and traits of the plants, including dry biomass (mg), root length (cm), shoot length (cm), number of leaflets, and length of the longest leaflet (cm). Statistical analysis (ANOVA one-way followed by Tukey's test, $p < 0.05$) was performed to identify significant statistical differences among the phenotypic traits assessed.

5.4.6. Azoxystrobin uptake measurements in plants

The plants were thoroughly rinsed with DI water and dried overnight at 110°C. Then the dried biomass was homogenized followed by pesticide extraction using a modified version of the QuEChERS (quick, easy, cheap, effective, rugged, and safe) method.⁴⁵ In summary, a mixture containing 4 mL of acetonitrile in 1% acetic acid, 0.8 g of MgSO₄, and 0.2 g of sodium acetate were added to each 0.2 g of homogenized biomass ($N = 3$) for each treatment. The mixture was

vortexed for 15 min, followed by centrifugation at $2240 \times g$ for 5 min under 20°C and recovery of the supernatant. Then, 1 mL of the supernatant was transferred to centrifuge tubes containing 50 mg of PSA and 150 mg of MgSO_4 , which were further vortexed for 1 min, followed by another step of centrifugation at $2240 \times g$ for 5 min under 20°C . Finally, the supernatant was passed through a $0.22 \mu\text{m}$ polytetrafluoroethylene (PTFE) filter before proceeding to the measurements. Azoxystrobin quantification from the extract solution was performed in an Agilent 1290 Infinity II liquid chromatograph (LC) coupled to a quadrupole time-of-flight mass spectrometer (QToF-MS) (Agilent) operating in positive electrospray ionization mode. The method validation for the recovery rates in homogenized plant biomass was assessed in the Table S5-2. Azoxystrobin was extracted and measured from soil based on a protocol described previously.⁴⁶ 1 g of soil dried in room temperature was shook with 2 mL of acetonitrile for 1 h under 20 rpm on a vertical shaker, followed by centrifugation ($1882 \times g$ for 5 min) and filtration ($0.22 \mu\text{m}$ PTFE filter) steps before LC analysis.

5.4.7. DNA extraction and sequencing

Bulk soil ($N = 3$) and soil loosely attached to roots ($N = 3$) were collected at days 10 and 20. The genomic DNA was extracted from approximately 250 mg of dry soil using a DNeasy PowerSoil Pro kit (Qiagen). The extracted DNA concentration was quantified using the PicoGreen method⁴⁷,⁴⁸ (Invitrogen Quant-iT PicoGreen dsDNA Assay Kit, Thermo Fisher) to make sure it was within the range required by Genome Québec (Canada). The V4 region of the 16S rRNA gene in archaea and bacteria was amplified using the primers 515F (5'-GTGCCAGCMGCCGCGGTAA-3') and 806R (5'-GGACTACHVGGGTWTCTAAT-3'). The ITS1 region of the ITS rRNA gene in fungi was amplified using the primers ITS1F (5'-CTTGGTCATTTAGAGGAAGTAA-3') and 58A2R (5'-CTGCGTTCTTCATCGAT-3'). The amplified sequences were sequenced on Illumina MiSeq using the PE250 protocol.

5.4.8. Sequencing analysis

The sequence reads were processed using QIIME2 (version 2019.4) pipeline.⁴⁹ The processing included (i) pairing forward and reverse sequence reads, (ii) demultiplexing sequences by linking the barcode information with the corresponding samples, (iii) denoising the amplicon sequence data with DADA2 pipeline⁵⁰ and truncating at position 240 where quality started to drop significantly. Taxonomic ranks were assigned to the 16S rRNA processed sequences using Naïve

Bayes Taxonomic Classifier⁵¹ trained with the Greengenes database.⁵² Taxonomic ranks were assigned to the ITS rRNA processed sequences fitting a classifier for the UNITE database⁵³ and training it with a fungal ITS mock community published in Taylor et al.⁵⁴ Alpha (α) diversity metrics (Faith phylogenetic diversity (PD)⁵⁵ and Pielou's evenness indices⁵⁶), and beta (β) diversity metrics (weighted UniFrac⁵⁷) for the Principal Coordinate Analysis (PCoA) were performed through the q2-diversity pipeline.

5.4.9. Quantitative polymerase chain reaction (qPCR)

To determine bacterial and fungal load in each treatment, relative qPCR quantifications of the 16S rRNA and 18S rRNA genes for bacteria and fungi, respectively, were undertaken. It was performed using the universal primers, Ba519F and Ba907R, for bacteria community and, Fung5F and FF390R, for fungi community, as previously reported by Lueders et al.^{58,59} A standard curve was established using 10-fold dilutions of soil genomic DNA (gDNA) ($10^0 - 10^{-4}$). The relative concentrations in each treatment were quantified using triplicate samples per treatment, and technical duplicates for each sample. The percentage change as compared to day 0 control for each treatment was then calculated by dividing values by the average for day 0 controls. Each 20 μ L reaction contained 10 μ L of iTaq Universal SYBR Green Supermix, 500 nM of each primer, 0.2 μ g/ μ L bovine serum albumin, 5% dimethyl sulfoxide, and 1 μ L of the serial dilutions of the standard soil gDNA, or 100-fold dilution of unknown gDNA for bacteria and 20-fold dilutions for fungi. The reaction was run on a CFX connect real-time PCR detection system (BioRad). The thermal cycling protocol for bacteria was as follows: denaturation at 95°C for 3 minutes followed by 40 cycles of amplification (10 s at 95 °C, 30 s at 50 °C, 60 s at 72 °C). For fungi, the denaturation step took place at 95°C for 3 minutes followed by 40 cycles of amplification (20s at 95°C, 30s at 50°C, 90s at 72°C). The specificity of each reaction was verified after each run through a melting curve analysis between 65°C and 95°C, the efficiency of the reaction was calculated to be above 90% for both, and the purity of reagents was verified by running no template controls.

5.5. Results and discussion

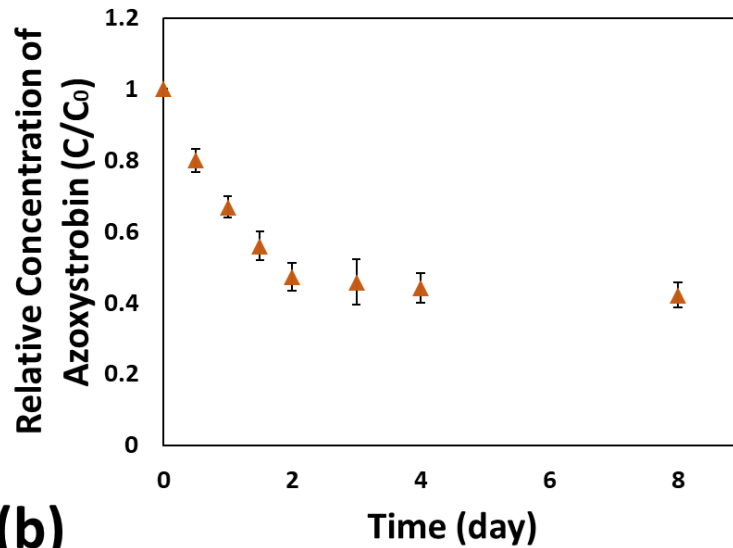
5.5.1. PHSN encapsulation provides controlled release properties

The decrease in the concentration of azoxystrobin over time in the particle-free solution phase outside the particles indicates the loading of the fungicide within the PHSN (Figure 5-1a). These

results suggest that sorption is also taking place, because the entrapment of azoxystrobin in the void space of the pores and hollow core would not lower concentration in the bulk solution. We compared the loading rates of PHSN with solid SiO₂ NPs with similar sizes (~ 200 – 250 nm) as shown in Figure S5-1, which suggests that surface area plays a dominant role in the loading capacity of the nanocarrier. While SSNs (specific surface area: 29 m² g⁻¹) did not sorb a significant amount of the pesticide, PHSN (specific surface area: 287 m² g⁻¹) were loaded with azoxystrobin 14-fold higher than that of SSN after 8 days of contact in solution. Control experiments confirmed that close to no azoxystrobin adsorbed was onto the Teflon tube's walls. Therefore, all the decrease in the concentration of azoxystrobin can be attributed to its encapsulation within the nanocarrier. The mass balance of azoxystrobin at the end of the experiment in day 14 was satisfactory, with 66.9 ± 1.4% of the initial azoxystrobin mass was extracted from the PHSNs, and 42.2 ± 3.4% of remained in solution, accounting for approximately of 107.8% of the initial azoxystrobin in the system. Most of the loading of azoxystrobin within PHSNs took place in the first 2 days, and the solution phase azoxystrobin concentrations plateaued after day 3, as shown in the loading profile in Figure 5-1a.

Following the loading, the PHSN suspension was centrifuged to separate the PHSNs from the solution, and the pellets were introduced in a release medium similar to the loading medium (20% v/v methanol solution), to compare the release profile of nanoencapsulated azoxystrobin and the non-encapsulated fungicide. Figure 5-1b shows that non-encapsulated and nanoencapsulated azoxystrobin had considerably distinct release profiles in the release medium. All the non-encapsulated azoxystrobin was dissolved after few hours, whereas the nanoencapsulated azoxystrobin followed a controlled, prolonged release that extended over days. In fact, only 43.5 ± 5.8% of azoxystrobin was released after 240 hours. Due to the high loading of azoxystrobin, excessive dosing of PHSN is not required, making the process cost-effective.

(a)



(b)

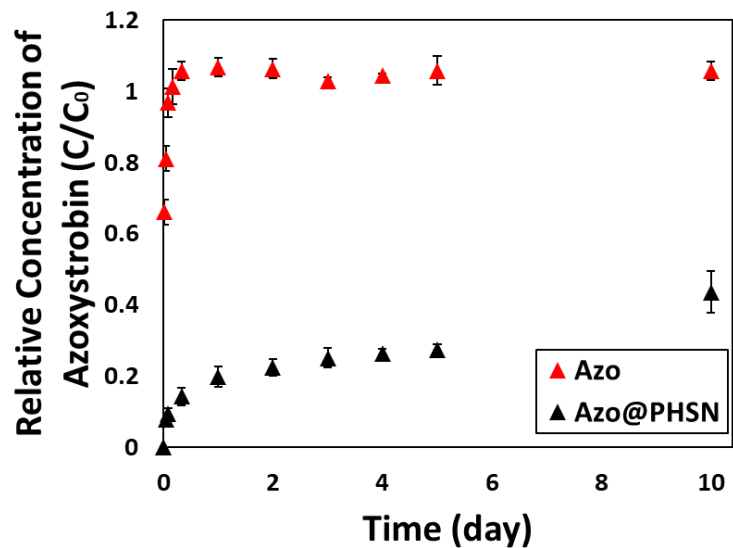


Figure 5-1. (a) Relative concentration (C/C_0) of azoxystrobin in solution (20% v/v methanol) phase over time and (b) Concentration of azoxystrobin over time in solution (20% v/v methanol) released from pure (Azo) and encapsulated azoxystrobin (Azo@PHSN).

5.5.2. Azoxystrobin uptake profiles differed significantly among the treatments

Although the same amount of azoxystrobin (0.75 mg) was added in the Azo and Azo@PHSN treatments, the azoxystrobin uptake varied significantly among them. Figure 5-2a shows that the

concentration of azoxystrobin per unit mass of the plant dry weight (dw) for the non-encapsulated treatment (Azo) at 12.77 ± 0.68 mg/kg dw at day 10 was more than double the nanoencapsulated treatment (Azo@PHSN). In terms of azoxystrobin mass uptake (Figure 5-2b), there was no significant difference in the uptake between Azo and Azo@PHSN treatments on day 10, and thus the changes in concentration were primarily related to the change in plant biomass (Figures 5-2c and 3a). At day 20, the azoxystrobin concentration in the plants with the Azo treatment decreased to 0.89 ± 0.11 mg/kg dw, which is partly attributable to an increase in the biomass, and partly due to a decrease in the mass of azoxystrobin present in the plants (Figures 5-2d and 5-3a). The latter suggests that the plants were able to metabolize and/or excrete the fungicide through guttation droplets from leaves and through roots exudates.⁶⁰ Evidence of azoxystrobin metabolism inside the plants with both Azo and Azo@PHSN was confirmed by identifying peaks for suspected azoxystrobin metabolites by LC-MS. This indicates that the nanoencapsulated azoxystrobin was bioavailable to the plant tissues. The list of suspected metabolites found in plants for different treatments and time points is presented in Table S5-3. On the other hand, the concentration of azoxystrobin in plants for the nanoencapsulated treatment (Azo@PHSN) did not differ by much from day 10 to day 20, decreasing from 4.72 ± 0.14 to 2.65 ± 0.13 mg/kg dw, respectively. However, for that treatment, azoxystrobin mass uptake increased 3.4-fold between days 10 and 20 and was accompanied by significant increases in biomass growth (Figures 5-2c, 5-2d and 5-3a), which resulted in relatively constant azoxystrobin concentrations in the plant, suggesting the sustained uptake of pesticide over time during an active growth period.

The azoxystrobin plant uptake efficiency (ratio of pesticide mass uptake to dosed) was 1% for the Azo treatment) to 5% for the Azo@PHSN treatment over the 20-day experiment, indicating that nanoencapsulation leads to more efficient pesticide uptake. Xu et al.³⁵ reported comparable uptake efficiencies for another kind of strobilurin pesticide, the pyraoxystrobin. The non-encapsulated form yielded 1.5% while the MSN-encapsulated form yielded 3.5% of uptake after 10 days. This trend suggests that SiO₂-based nanocarriers enhance pesticide uptake when compared to the non-encapsulated counterparts. Plant-free soil microcosms dosed with the azoxystrobin showed that the concentration of azoxystrobin in soil did not decrease after 20 days, indicating that biodegradation is not playing a role in the differences of uptake in this work. Si uptake in plants was not monitored because of the limitations to identify what fraction constitutes

the Si from the engineered NPs and that from naturally occurring SiO₂ in the environment. Moreover, the amount of Si added to the system is significantly below the background level of Si in soil, and plants can accumulate Si in the form of SiO₂ that could potentially lead to the biosynthesis of SiO₂ NPs.⁶¹

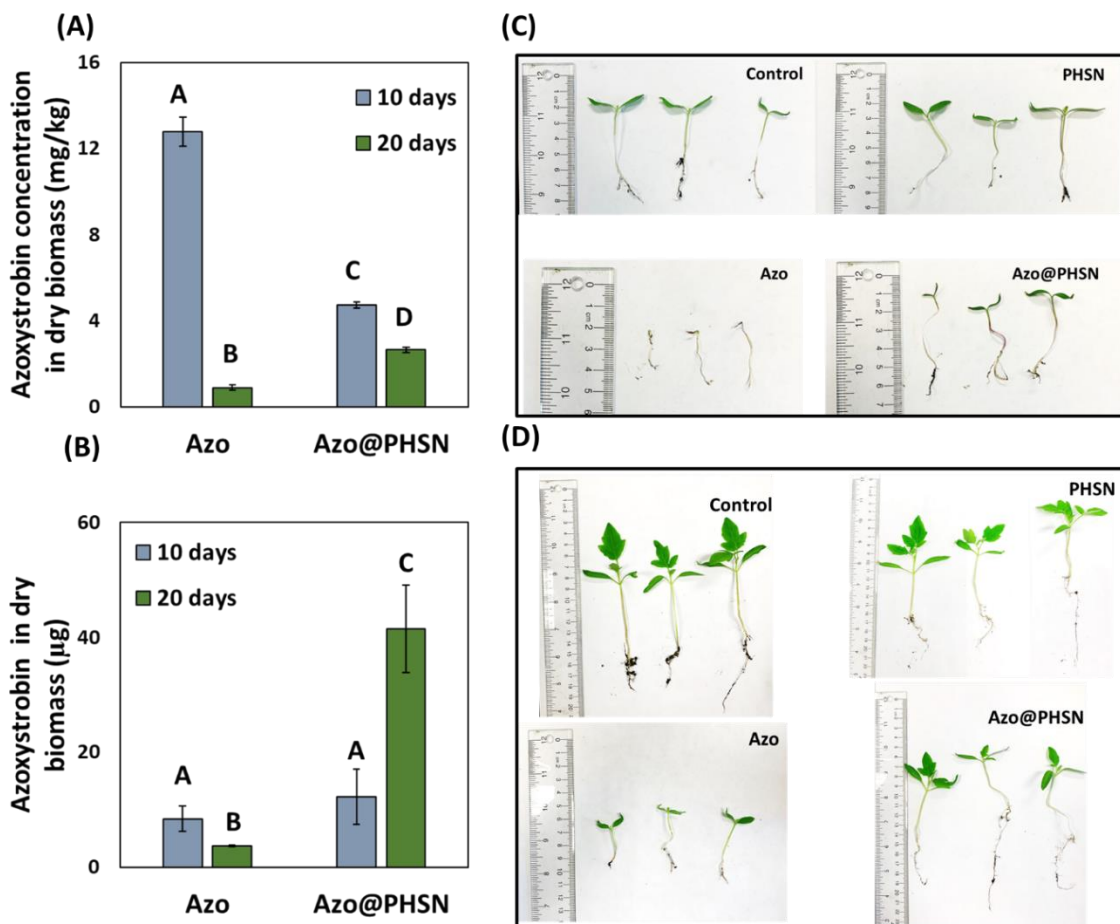


Figure 5-2. (A) Azoxystrobin concentration per unit of dry plant biomass at days 10 and 20 for Azo and Azo@PHSN treatments. The dry biomass was derived from plants after thorough rinse of the roots. (B) Azoxystrobin absolute uptake at days 10 and 20. Different letters (A, B, C and D) indicate significant statistical differences among samples (ANOVA one-way test followed by Tukey's test, $p < 0.05$ threshold). (B) Photos of the plants harvested at day 10. (C) Photos of the plants harvested at day 20.

5.5.3. Azoxystrobin when loaded in a SiO₂ porous nanocarrier minimized its inhibitory effects on plants

The plant health was quantified by monitoring five measurable indicators in the plants harvested in days 10 (Figure 5-2b) and 20 (Figure 5-2c). These observable traits included the plant biomass (dry wt), the number of leaflets, and the length of the roots, shoot and longest leaflet. The quantitative measure for each trait, separated by treatments, is shown in Figure 5-3. ANOVA one-way analysis followed by Tukey's test were performed to identify significant statistical differences among the treatments and the error bars represent the standard deviation for each treatment ($N = 3$).

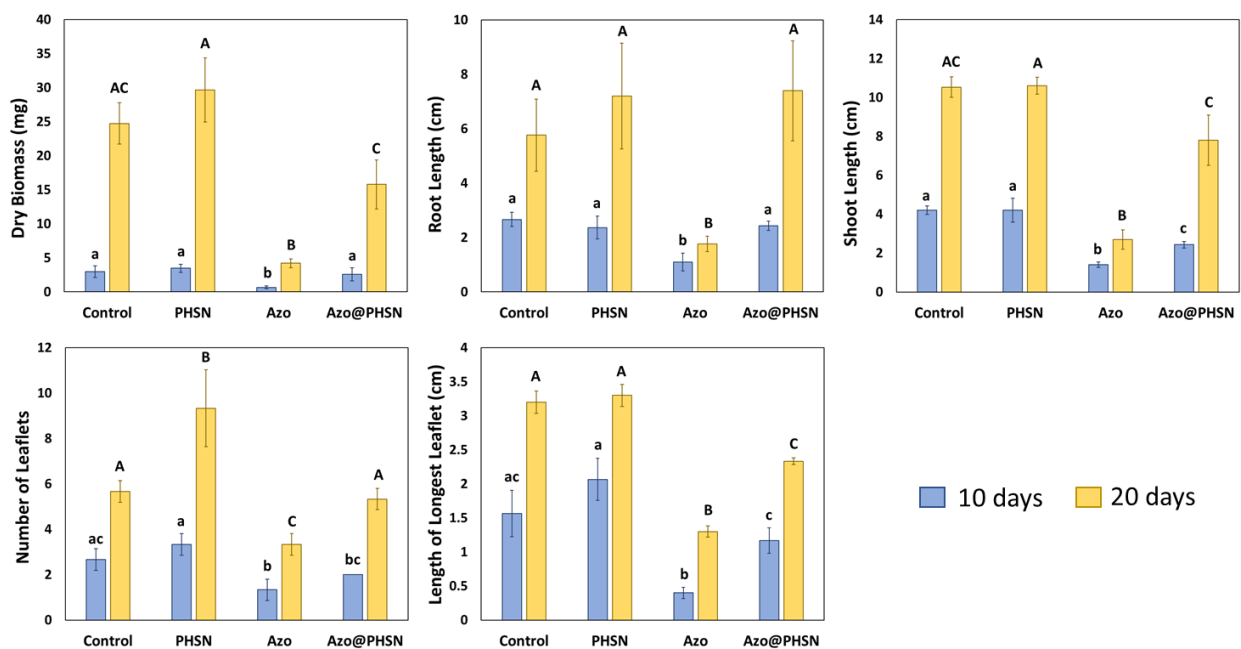


Figure 5-3. The measures of five phenotypic traits (dry mass, root length, shoot length, number of leaflets and length of the longest leaflet) as indicators of the impacts of each treatment in the plant growth. Different letters (*a*, *b* and *c* for samples at day 10, *A*, *B* and *C* for samples at day 20) indicate significant statistical differences among samples (ANOVA one-way test followed by Tukey's test, $p < 0.05$ threshold).

The dry biomass at day 10 varied little among control, nanoparticle only (PHSN), and encapsulated azoxystrobin (Azo@PHSN) treatments. However, the treatment with non-encapsulated pesticide (Azo) yielded 4.4-fold, 5.2-fold, and 3.8-fold less biomass than control,

PHSN and Azo@PHSN treatments, respectively. It is evident that at the concentration applied, azoxystrobin caused inhibitory effects on the plant growth. However, the Azo@PHSN treatment resulted in biomass yield somewhat in between the PHSN and Azo treatments, with no statistical difference compared to control ($p > 0.05$). The same trends in the pesticide concentration and biomass yield were observed at day 20. This suggests that the non-encapsulated azoxystrobin is somehow inhibiting plant growth and the PHSN might be limiting the negative effects of high levels of pesticide exposure to a certain extent by releasing it over time, thus mitigating its toxicity. Azoxystrobin has been shown to cause toxicity towards some varieties of cultivars.^{38-40, 62, 63}

Similarly, the length of the roots at day 10 and 20 was similar among the control, PHSN and Azo@PHSN treatments, leading to no significant statistical difference among the three treatments ($p > 0.05$). The Azo treatment yielded the smallest root length. The Azo treatment led again to the least root development.

There was no significant difference in the shoot length between control and PHSN treatments at days 10 and 20 of harvesting. The shoot development was somewhat impacted at day 10 for both azoxystrobin treatments (Azo and Azo@PHSN), but at day 20 the shoot development was evident for the Azo@PHSN. The Azo treatment continued to inhibit the plant development in a greater extent than the other treatments.

To some extent, the results for the other two observable indicators (number of leaflets and length of the longest leaflet) follow similar trends as the previous three observable traits: (i) Azo@PHSN overall showed little difference to control and PHSN, except for dry mass and length of the longest leaf, for which the treatment yielded lower values. (ii) Azo treatment always yielded the indicators with the lowest values, which suggests that azoxystrobin caused inhibitory effects on the plant development. (iii) PHSN treatment in all cases yielded similar results when compared to control, with the exception to the number of leaflets indicator where PHSN treatment yielded significantly more leaflets than control ($p < 0.05$).

Overall, the growth of *Solanum lycopersicum* was negatively impacted by the pesticide-dosed treatments. While the treatment with non-encapsulated azoxystrobin yielded the lowest amount of biomass and highest growth inhibition, the treatment with nanoencapsulated azoxystrobin was placed somewhat in between the treatment with azoxystrobin and controls with

respect to those parameters. The treatment with the nanoencapsulated azoxystrobin yielded less growth inhibition because the release profile of azoxystrobin in a porous nanocarrier was controlled and slowly released the AI for days, while the treatment with non-encapsulated azoxystrobin resulted in an immediate dissolution. The uptake per unit of dry biomass profiles in Figure 5-3 suggest that azoxystrobin was rapidly available in the Azo treatment and decreasing rapidly from then on, while the nanoencapsulated treatment released the pesticide in a controlled manner over time, which helped minimize the phytotoxic effects observed with the Azo treatment.

5.5.4. Nanopesticides had limited impact on the soil microbial community structures

Between 95 to 99% of the pesticide applied remained in the soil after nanoencapsulated and non-encapsulated pesticide treatments over the 20-day experiment. Therefore, the effect of the remaining azoxystrobin on the soil microbiota should also be investigated to grasp the full impact of applying nanoencapsulated pesticides and how that compare with non-encapsulated pesticide or no pesticide at all.

There are conflicting results about the azoxystrobin impacts on the microbial community in the literature. While some studies reported azoxystrobin reduced microbial diversity by inhibiting the growth of a number of bacteria and fungi in soil,⁶⁴⁻⁶⁶ particularly its target pathogens, Deuteromycetes, Ascomycetes, Basidiomycetes and Oomycetes,³⁷ others have suggested that the fungicide had little to no significant effect on soil microbial communities.⁶⁷⁻⁶⁹ Such contrasting conclusions are likely attributed to differences in the soil properties, fungicide doses and application methods used in each study.

The level of richness and diversity in the soil microbiota is a key indicator to assess the health of the soil because the microbial communities work symbiotically to maintain its fertility, productivity and sustainability.⁷⁰ A diverse consortium of soil bacteria drives nitrogen and carbon cycling ensuring proper nutrient distribution,⁷¹ suppression of (a)biotic stresses due to pathogens,⁷² drought, high salinity and metabolization of pesticides.⁷³ Fungi are normally responsible for nutrient translocation and metabolization of biomolecules, enhancing nutrient availability to other microorganisms.⁷⁴ Therefore, any disruption or deregulation in the soil microbiota may have serious consequences to the whole ecosystem. Figure 5-4 and Figure 5-5 show the taxonomic abundance of fungi at class level and bacteria and archaea at phylum level, respectively.

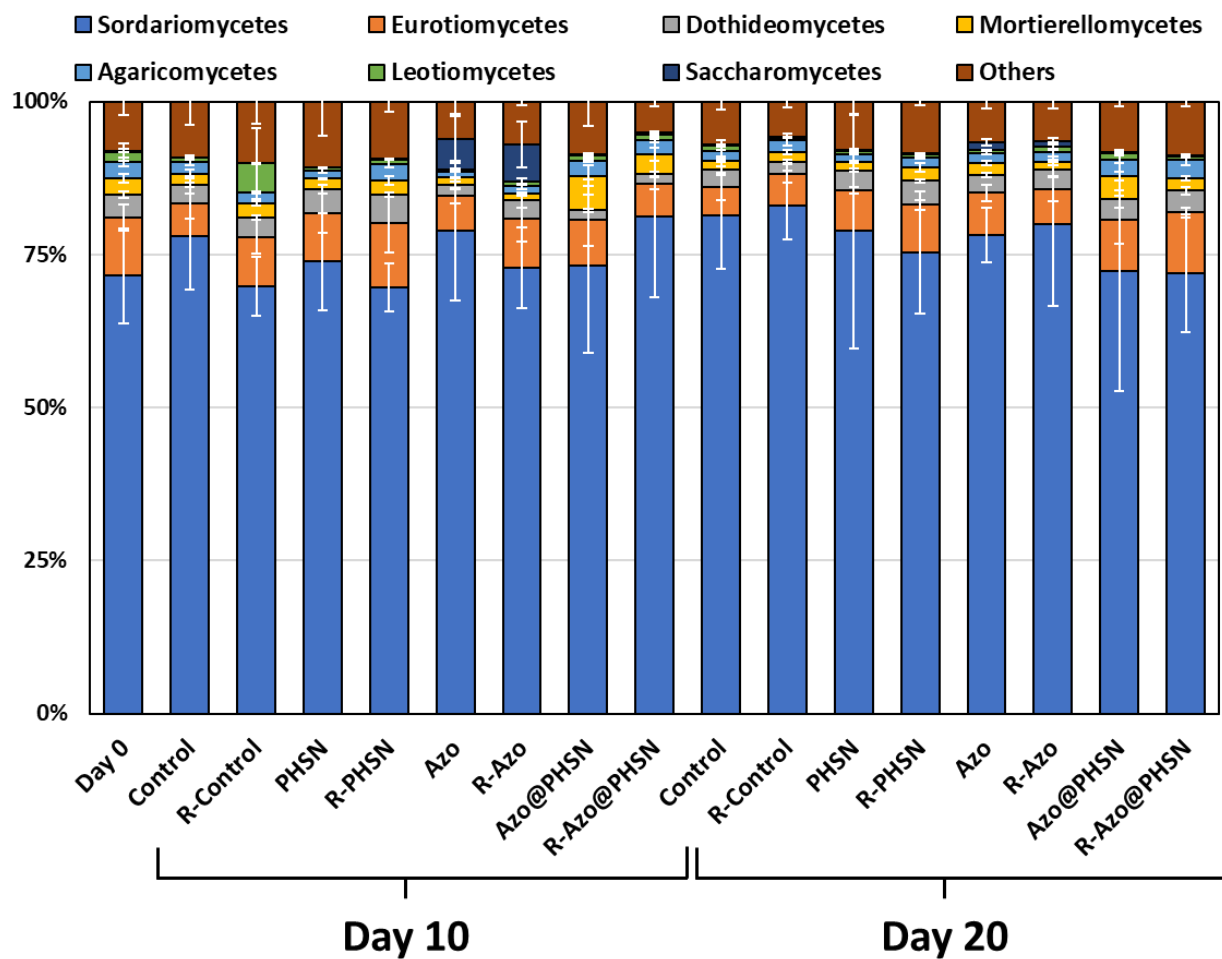


Figure 5-4. Relative taxonomic abundance of fungi communities at a class level. The communities obtained from loosely attached soil to the roots have the prefix *R-* in front of the treatment ID. The communities obtained from bulk soil have no prefix in front of the treatment ID.

With few exceptions, there was no significant effect on the fungi community coming from any of the treatments in terms of relative abundance, for both bulk soil and the soil loosely attached to the roots. The soils treated with azoxystrobin saw a significant increase ($p < 0.05$) in *Saccharomycetes* of 44-fold at day 10 and of 15-fold at day 20 when compared to the soils without pesticide dosing (control and PHSN treatments). The increase of 5 to 6% in relative abundance of *Saccharomycetes* was accompanied by an evenly decrease of all the other classes between 1 and 2%. *Saccharomycetes* play an important role in mineralization processes and nutrient cycling in soil.⁷⁵ In both cases, it is noticeable that when differences occurred, they tended to be more

significant at day 10 than at day 20. This suggests that the soil microbiota acclimated to the pesticides over time. Nonetheless, the small differences in taxonomic relative abundance suggest that microbial community changes are not the driver for the differences in plant growth reported above.

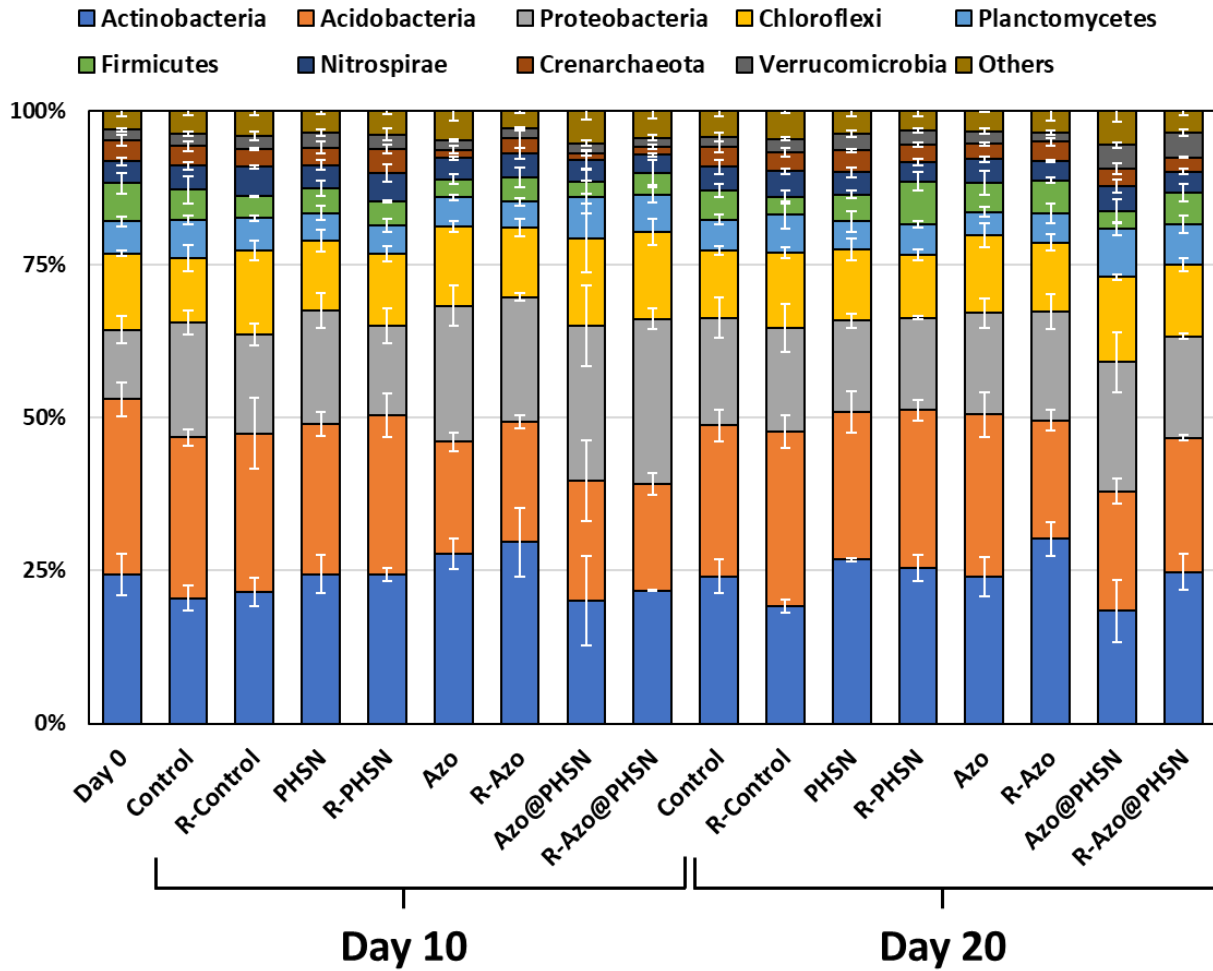


Figure 5-5. Relative taxonomic abundance of bacterial and archaea communities at a phylum level. The communities obtained from loosely attached soil to the roots have the prefix *R-* in front of the treatment ID. The communities obtained from bulk soil have no prefix in front of the treatment ID.

Similarly, with few exceptions, there was no significant effect on the bacterial community composition for any of the treatments, for both bulk soil and the soil loosely attached to the roots. The soils treated with azoxystrobin (Azo and Azo@PHSN treatments) experienced higher relative

abundance of *Proteobacteria* on day 10 (+ 6.7%), but relatively no difference at day 20 when compared to the soils without pesticide dosing (control and PHSN treatments). Among key functions in the soil, *Proteobacteria* are generally associated with cycling of nitrogen, sulphur and carbon.⁷⁶ On the other hand, the soils treated with azoxystrobin (both as Azo and Azo@PHSN) experienced lower relative abundance of *Acidobacteria* at days 10 (- 6.9%) and 20 (- 4.0%). *Acidobacteria* is very sensitive to change in soil physicochemical properties,⁷⁷ thus the addition of pesticides likely negatively disrupted this phylum.

The PCoA for the bacterial and archaea communities (Figure 5-6a) revealed that there are two parameters affecting the β -diversity – the measurement of the change in diversity of species from one system to another – of these communities: (1) time, and to a smaller extent (2) different treatments. There are two distinct clusters based on time periods, one that includes the triplicates from day 0, most treatments from days 10 and 20 located mostly in the border between *Q1* and *Q4*, and the other cluster includes the treatments with azoxystrobin which are primarily in *Q2* and *Q3*. Furthermore, the pesticide treatments at day 10 are further away from the initial soil stage (at day 0) than the same treatments at day 20. Therefore, the pesticide-dosed treatments had a more significant impact on the β -diversity of community compared to other treatments. This effect, however, was more significant in the first 10 days, and the microbial community in the soils tended to bounce back to their initial stage as the day progressed until day 20. Similarly, the PCoA for the fungi communities (Figure 5-6b) revealed that pesticide-dosed treatments and time also influenced the β -diversity of these communities. Although the different treatment triplicates are more spread out in the fungi communities PCoA, the pesticide-dosed treatments located mostly in *Q2* and *Q3* are still the furthest away from the initial stage triplicates at day 0 in *Q4*, and as time progressed to day 20, the triplicates tended to bounce back to the initial stage. This is another instance where the data suggests that the soil microbiota acclimated to azoxystrobin. While relative abundance did not change considerably among samples (Figures 5-4 and 5-5), β -diversity shifts are more evident (Figure 5-6), suggesting that although the pesticide treatments (Azo and Azo@PHSN) did not affect the relative abundance, they seemed to have an effect in the overall richness and evenness of the samples when compared to the ones treated without pesticides (control and PHSN).

Further α -diversity – the measurement of the change in diversity within one sample – analyses were performed to investigate whether there are statistically significant differences

among treatments and can be found in Supporting Information (Figure S5-4). Overall, the analysis in α -diversity analysis indicated that there were few differences among treatments, mostly associated with treatments dosed with pesticides. Lo⁷⁸ reported that soils with high organic matter content enhance sorption of hydrophobic agrochemicals, such as azoxystrobin, making them unavailable to microorganisms. Thus, hydrophobic pesticides may have minimal effects on microbial community in soils with abundant organic matter. These results suggest that the toxic effect of azoxystrobin may be a direct effect on the plant, rather than an effect on the soil microbiota which then would affect the plant growth.

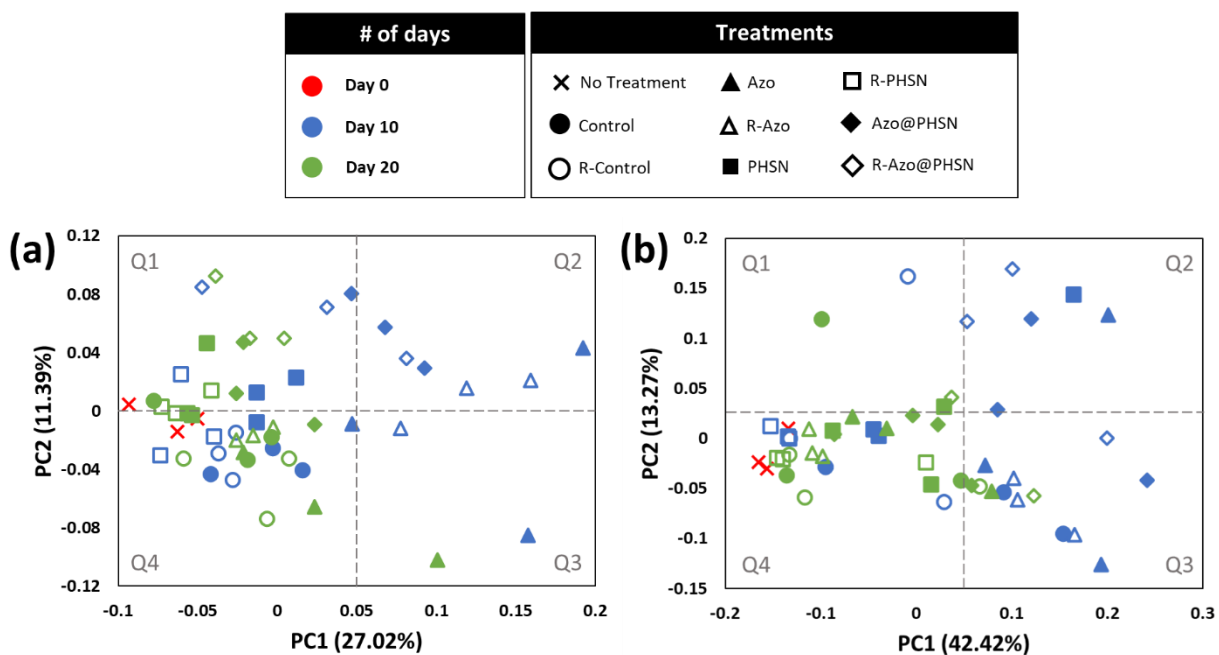


Figure 5-6. PCoAs for (a) bacterial and archaea communities and (b) fungi community. The communities obtained from loosely attached soil to the roots have the prefix *R*- in front of the treatment ID. The communities obtained from bulk soil have no prefix in front of the treatment ID.

The qPCR data for bacterial and archaea communities (Figure S5-2) and fungi communities (Figure S5-3) confirmed the trends observed with the relative abundance and diversity analyses. The bacterial and archaea community changes (Figure S5-2) do not vary significantly compared with control at day 0 or the control systems at day 10 and 20 to the extent

to explain why such abrupt inhibition in plant growth was observed during Azo and Azo@PHSN treatments. The fungi community data (Figure S5-3) showed that Azo@PHSN was the only instance where the community numbers decreased when compared to day 0, particularly at day 10 for bulk soil and soil loosely attached to the root's microbial communities. The continuous supply of the pesticide over a longer period of time promoted by the encapsulated formulation likely was responsible to decrease the overall fungi community numbers, while a one-dose non-encapsulated pesticide formulation was not able to maintain the biocide effects for the same period of time.

5.6. Conclusions

In this study, the pesticide encapsulation promoted the slow, controlled release of the AI over days, whereas the non-encapsulated formulation of pesticide experienced a rapid dissolution within hours. This controlled release mitigated the impacts of the pesticide in the plant health. Plants in soils which were treated with non-encapsulated azoxystrobin yielded less biomass than those treated with nanoencapsulated azoxystrobin. In terms of soil microbiota, all treatments led to relatively minor changes in the soil microbial communities. It is unlikely that these shifts influenced the plant growth, because key bacterial and fungi communities responsible for soil health, were not heavily impacted.

Overall, the use of nanocarriers to encapsulate and transport AIs did not seem to negatively impact the plant health and soil microbial community, rather it helped mitigate the phytotoxicity by slowly releasing the pesticide over time. The nano-encapsulated azoxystrobin was bioavailable in the plants as evidenced by generation of its metabolic products. The relatively small mass of PHSN added in soil (5 mg per 61.6 g soil) led to a five-fold increase in azoxystrobin uptake, with almost no phytotoxicity. In our prior study, we also found that the PHSN have limited mobility in subsurface granular media, due to their high surface roughness. These are particularly promising results for pesticide application of silica nanocarriers and imply that fewer pesticide applications may be necessary with the use of nanocarriers. However, these results need to be verified with different soil types and crops.

5.7. Supporting Information

Table S5-1. List of the soil properties.

Analysis	Result
pH	7.0
C _{om} (%)	4.1
P (ppm)	152
K (ppm)	357
Mg (ppm)	291
Al (ppm)	759
Na (ppm)	14
CEC (meq/100 g)	16.9
Water Holding Capacity at 1/3 bar (%) ^a	22.9
Water Holding Capacity at 15 bars (%) ^a	13.26
Available Water Capacity (%) ^a	9.69
Sand (%)	31
Silt (%)	34
Clay (%)	35

Note: C_{om}: organic matter concentration, P: phosphate, K: potassium, Mg: magnesium, Al: aluminum, Na: sodium, CEC: cation exchange capacity, ^a USDA no. 42 method.

5.7.1. Matrix Effects on the Azoxystrobin Detection

To validate the azoxystrobin measurements from the biomass extract, recovery validation was determined by spiking control plant biomass after homogenization with azoxystrobin in different concentration ranges. The low-range and high-range concentration comprised in spiking azoxystrobin in homogenized biomass to a final concentration of 10 ppb and 500 ppb, respectively. The recoveries ($N = 3$) for the low range (RL) and high range (RH) can be found in Table S5-2.

Table S5-2. Azoxystrobin recoveries in homogenized biomass for low- and high-range concentrations.

Range	Sample ID	Recovery (%)	Average (%)	Standard Deviation (%)
Low	RL1	102	105	2.5
	RL2	108		
	RL3	106		
High	RH1	107	107	1.0
	RH2	106		
	RH3	108		

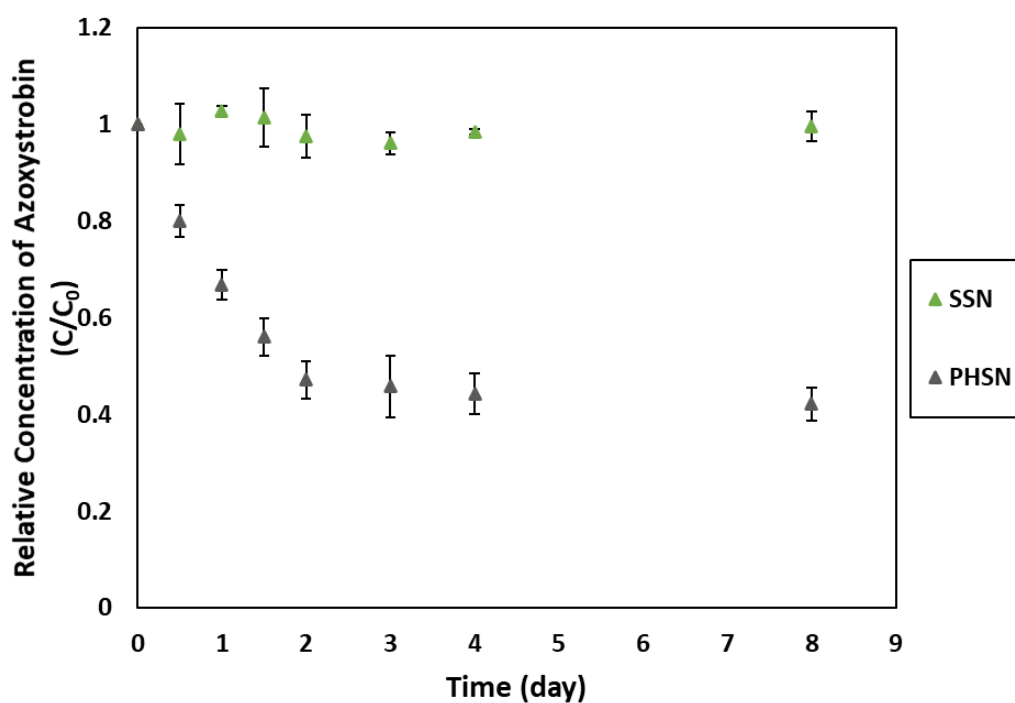


Figure S5-1. Relative concentration (C/C_0) of azoxystrobin in solution (20% v/v methanol) phase over time using solid SiO_2 NPs (SSN) and porous hollow SiO_2 NPs (PHSN) as nanocarriers.

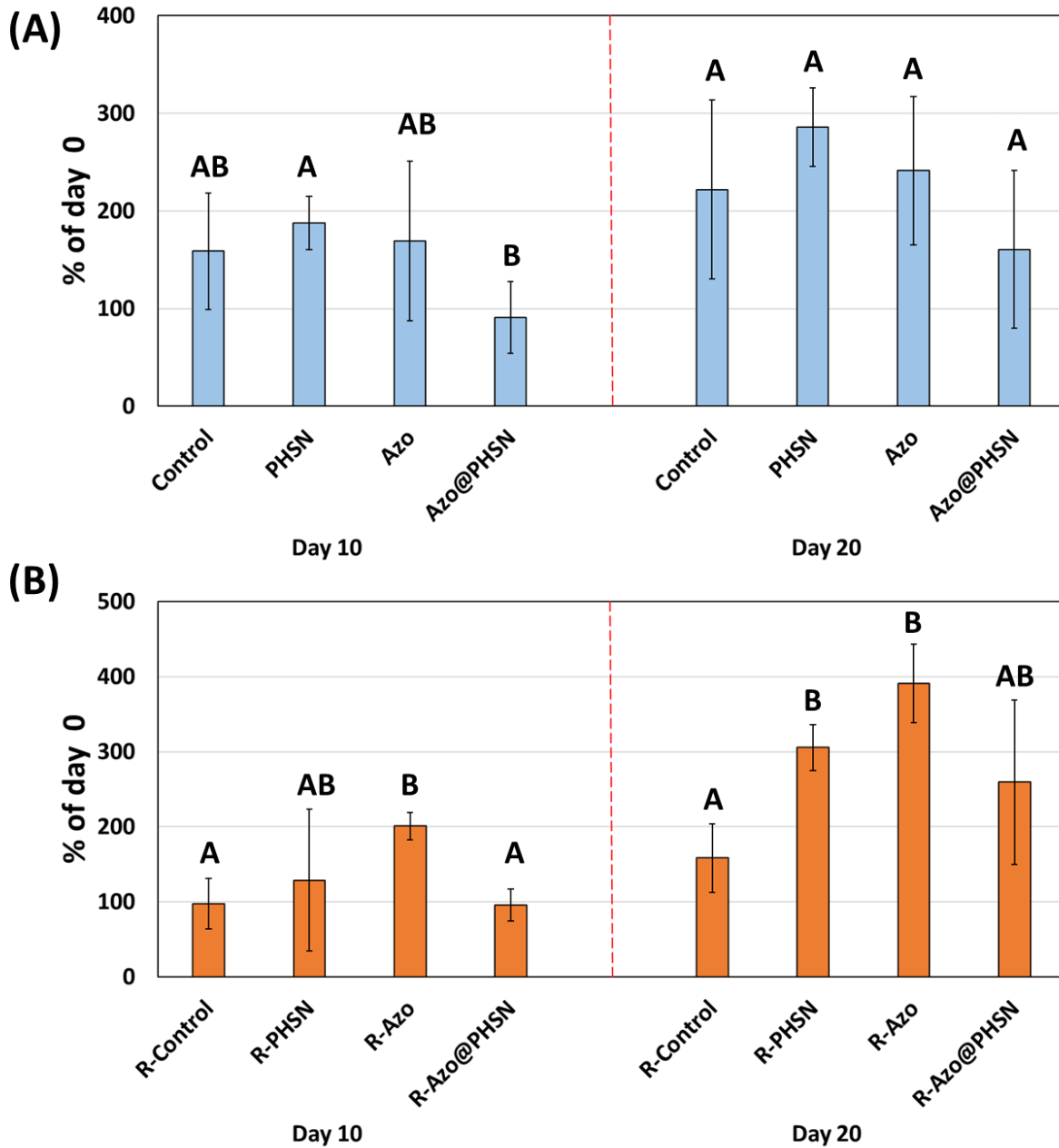


Figure S5-2. Percentage of day 0 soil microbial community following qPCR targeting the gene 16S rRNA for total bacterial and archaea communities using (A) bulk soil and (B) soil loosely attached to the roots. Different letters (*A* and *B*) indicate significant statistical differences among samples (ANOVA one-way test followed by Tukey's test, $p < 0.05$ threshold).

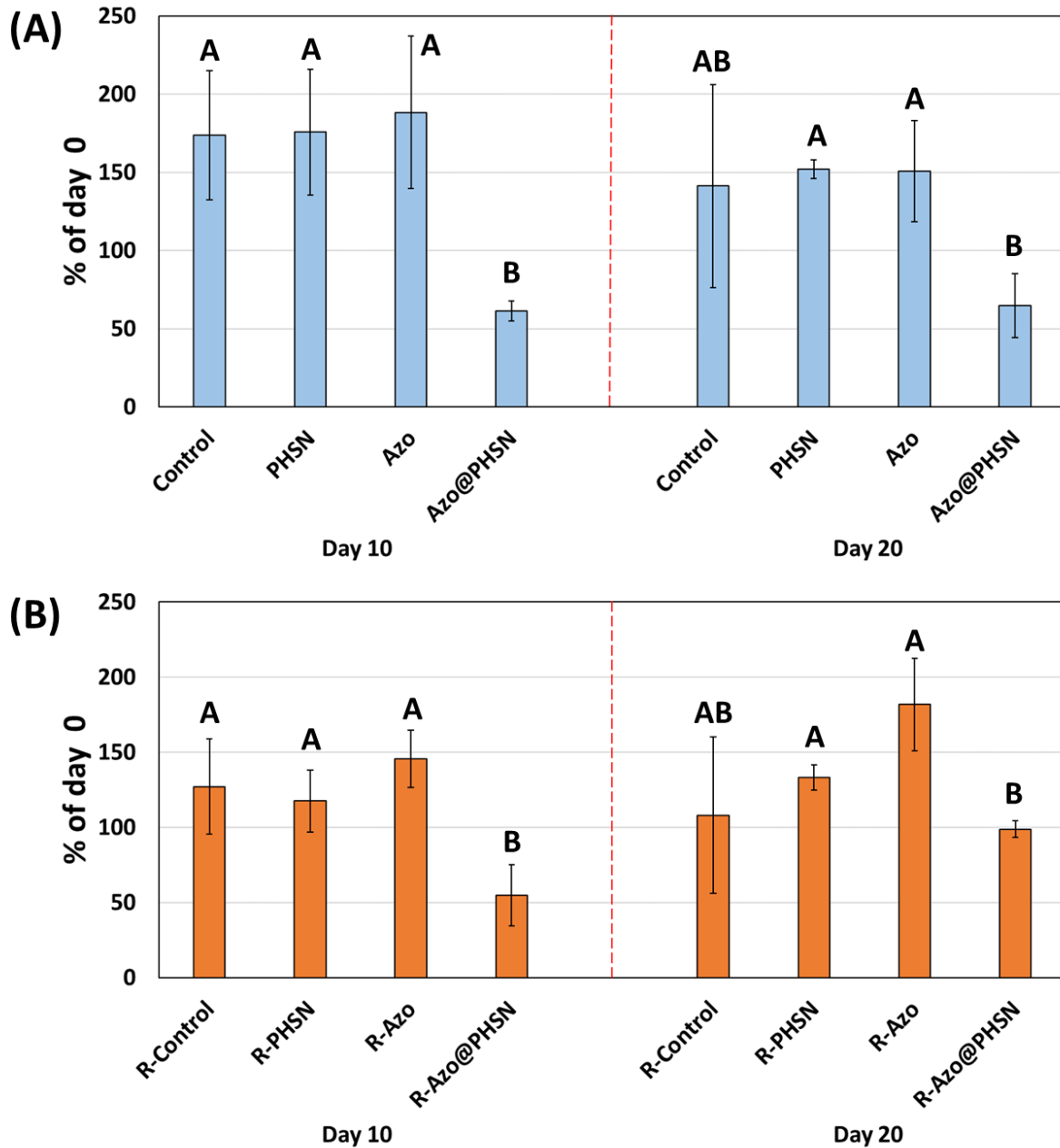


Figure S5-3. Percentage of day 0 soil microbial community following qPCR targeting the gene 18S rRNA for total fungi communities using (A) bulk soil and (B) soil loosely attached to the roots. Different letters (*A* and *B*) indicate significant statistical differences among samples (ANOVA one-way test followed by Tukey's test, $p < 0.05$ threshold).

5.7.2. Pielou's evenness index (J') and Faith's Phylogenetic Diversity (PD)

The Pielou's evenness index (J')⁵⁶ is the numerical representation that quantifies how equal the microbial communities are in the sample. In other words, it is the mathematical measurement of the biodiversity in the sample. At day 10, there was no significant statistical difference among the bacterial communities for all treatments, based on the J' (Figure S5-4a). The variance was analyzed through Kruskal-Wallis pairwise testing and no p-value was below the $p < 0.05$ threshold. Similarly, at day 20 there was no significant statistical difference among the bacterial communities (Figure S5-4b). The p-values of the pairwise comparison between control and Azo treatments, and control and Azo@PHSN treatments had the lowest p-values overall, 0.15 and 0.20, respectively. Faith's phylogenetic diversity (PD) is another way to measure biodiversity mathematically⁵⁵. It, however, revealed the same conclusions as for the J' : no statistical difference could be determined among the bacterial communities with different treatments at days 10 (Figure S5-4c) and 20 (Figure S5-4d).

For fungi communities, at 10 days, three pairwise Kruskal-Wallis combinations of the J' indicated significant statistical difference, (1) day zero and Azo treatments, (2) day zero and PHSN treatments, and (3) day zero and Azo@PHSN treatments (Figure S5-4e), indicating that except for the day zero and control, all other treatments showed significant differences in the biodiversity when compared to the initial stage. After 20 days, however, the variance analysis of the J' indicated that only two combinations were statistically different, day zero and Azo@PHSN treatments, and control and Azo@PHSN treatments (Figure S5-4f), suggesting that the soil microbial community biodiversity differences tended to diminish as the days progressed. Faith's PD showed a different trend from the J' at day 10, where there were statistical changes only between Azo treatment and other three treatments: control, PHSN and Azo@PHSN (Figure S5-4g). At day 20, Faith's PD variance analysis showed representative differences in biodiversity between Azo and Azo@PHSN treatments, control and Azo@PHSN treatments (Figure S5-4h).

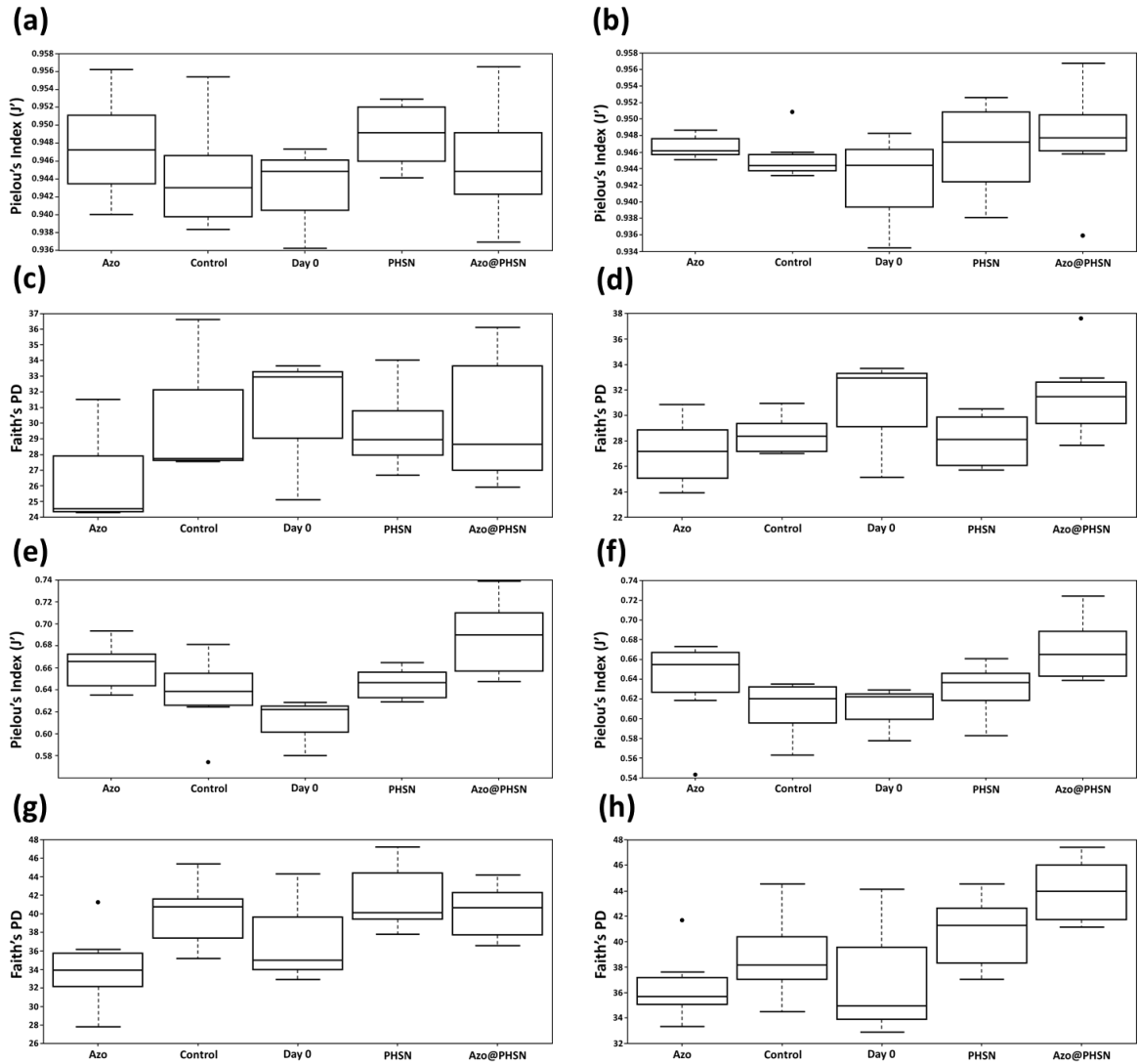
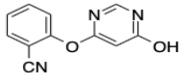
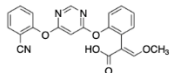
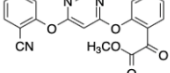
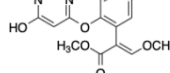
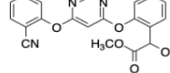


Figure S5-4. α -diversity boxplots representing (a) Pielou's evenness index for samples at day 10, (b) Pielou's evenness index for samples at day 20, (c) Faith's PD for samples at day 10, and (d) Faith's PD for samples at day 20 for the bacterial and archaea communities. α -diversity boxplots representing (e) Pielou's evenness index for samples at day 10, (f) Pielou's evenness index for samples at day 20, (g) Faith's PD for samples at day 10, and (h) Faith's PD for samples at day 20 for the fungi communities. The black dots above and below the error bars in some instances indicate outliers.

Table S5-3. List of suspected metabolites derived from azoxystrobin in tomato plants for different treatments and data points. The peaks were categorized by low, medium and high based on the comparison among them and do not have quantification purposes.

Suspected metabolites of azoxystrobin in <i>Solanum lycopersicum</i>							
Structure							
Formula	C ₁₁ H ₇ N ₃ O ₂	C ₂₁ H ₁₅ N ₃ O ₅	C ₇ H ₅ NO	C ₂₀ H ₁₃ N ₃ O ₅	C ₁₅ H ₁₄ N ₂ O ₅	C ₂₀ H ₁₅ N ₃ O ₅	
Ion m/z ratio	214.06166	390.10902	120.04494	376.09337	303.09813	378.10902	
Treatment	Replicate	Peak Intensity					
Azo [Day 10]	1	Low	Low	Not detected	Not detected	Low	Low
	2	Low	Low	Not detected	Not detected	Low	Low
	3	Low	Low	Not detected	Not detected	Low	Low
Azo [Day 20]	1	Low	Low	Not detected	Low	Low	Low
	2	Low	Low	Not detected	Low	Low	Low
	3	Low	Low	Not detected	Low	Low	Low
Azo@PHSN [Day 10]	1	Medium	Medium	Not detected	Low	Low	Medium
	2	Medium	Medium	Not detected	Low	Low	Medium
	3	Medium	Medium	Not detected	Low	Low	Medium
Azo@PHSN [Day 20]	1	High	High	Low	High	High	High
	2	High	High	Low	High	High	High
	3	High	High	Low	High	High	High

5.8. References

1. Kah, M.; Kookana, R. S.; Gogos, A.; Bucheli, T. D., A critical evaluation of nanopesticides and nanofertilizers against their conventional analogues. *Nature Nanotechnology* **2018**, *13* (8), 677-684.
2. Kah, M.; Tufenkji, N.; White, J. C., Nano-enabled strategies to enhance crop nutrition and protection. *Nature Nanotechnology* **2019**, *14* (6), 532-540.
3. Lowry, G. V.; Avellan, A.; Gilbertson, L. M., Opportunities and challenges for nanotechnology in the agri-tech revolution. *Nature Nanotechnology* **2019**, *14* (6), 517-522.
4. Hofmann, T.; Lowry, G. V.; Ghoshal, S.; Tufenkji, N.; Brambilla, D.; Dutcher, J. R.; Gilbertson, L. M.; Giraldo, J. P.; Kinsella, J. M.; Landry, M. P., Technology readiness and overcoming barriers to sustainably implement nanotechnology-enabled plant agriculture. *Nature Food* **2020**, *1* (7), 416-425.
5. Rodrigues, S. M.; Demokritou, P.; Dokoozlian, N.; Hendren, C. O.; Karn, B.; Mauter, M. S.; Sadik, O. A.; Safarpour, M.; Unrine, J. M.; Viers, J., Nanotechnology for sustainable food production: promising opportunities and scientific challenges. *Environmental Science: Nano* **2017**, *4* (4), 767-781.
6. Patra, J. K.; Das, G.; Fraceto, L. F.; Campos, E. V. R.; del Pilar Rodriguez-Torres, M.; Acosta-Torres, L. S.; Diaz-Torres, L. A.; Grillo, R.; Swamy, M. K.; Sharma, S., Nano based drug delivery systems: recent developments and future prospects. *Journal of Nanobiotechnology* **2018**, *16* (1), 1-33.
7. Elmer, W. H.; White, J. C., The use of metallic oxide nanoparticles to enhance growth of tomatoes and eggplants in disease infested soil or soilless medium. *Environmental Science: Nano* **2016**, *3* (5), 1072-1079.
8. Pereira, A. E.; Grillo, R.; Mello, N. F.; Rosa, A. H.; Fraceto, L. F., Application of poly (epsilon-caprolactone) nanoparticles containing atrazine herbicide as an alternative technique to control weeds and reduce damage to the environment. *Journal of Hazardous Materials* **2014**, *268*, 207-215.

9. Tarafdar, J.; Raliya, R.; Mahawar, H.; Rathore, I., Development of zinc nanofertilizer to enhance crop production in pearl millet (*Pennisetum americanum*). *Agricultural Research* **2014**, *3* (3), 257-262.
10. Raliya, R.; Tarafdar, J. C., ZnO nanoparticle biosynthesis and its effect on phosphorous-mobilizing enzyme secretion and gum contents in Clusterbean (*Cyamopsis tetragonoloba* L.). *Agricultural Research* **2013**, *2* (1), 48-57.
11. Prasad, T.; Sudhakar, P.; Sreenivasulu, Y.; Latha, P.; Munaswamy, V.; Reddy, K. R.; Sreeprasad, T.; Sajanalal, P.; Pradeep, T., Effect of nanoscale zinc oxide particles on the germination, growth and yield of peanut. *Journal of Plant Nutrition* **2012**, *35* (6), 905-927.
12. Alidoust, D.; Isoda, A., Effect of $\gamma\text{Fe}_2\text{O}_3$ nanoparticles on photosynthetic characteristic of soybean (*Glycine max* (L.) Merr.): foliar spray versus soil amendment. *Acta Physiologiae Plantarum* **2013**, *35* (12), 3365-3375.
13. Linglan, M.; Chao, L.; Chunxiang, Q.; Sitao, Y.; Jie, L.; Fengqing, G.; Fashui, H., Rubisco activase mRNA expression in spinach: modulation by nanoanatase treatment. *Biological Trace Element Research* **2008**, *122* (2), 168-178.
14. Servin, A.; Elmer, W.; Mukherjee, A.; De la Torre-Roche, R.; Hamdi, H.; White, J. C.; Bindraban, P.; Dimkpa, C., A review of the use of engineered nanomaterials to suppress plant disease and enhance crop yield. *Journal of Nanoparticle Research* **2015**, *17* (2), 1-21.
15. El-Shetehy, M.; Moradi, A.; Maceroni, M.; Reinhardt, D.; Petri-Fink, A.; Rothen-Rutishauser, B.; Mauch, F.; Schwab, F., Silica nanoparticles enhance disease resistance in *Arabidopsis* plants. *Nature Nanotechnology* **2020**, 1-10.
16. Luyckx, M.; Hausman, J.-F.; Lutts, S.; Guerriero, G., Silicon and plants: current knowledge and technological perspectives. *Frontiers in Plant Science* **2017**, *8*, 411.
17. Abdel-Haliem, M. E.; Hegazy, H. S.; Hassan, N. S.; Naguib, D. M., Effect of silica ions and nano silica on rice plants under salinity stress. *Ecological Engineering* **2017**, *99*, 282-289.
18. Azeem, M.; Iqbal, N.; Kausar, S.; Javed, M. T.; Akram, M. S.; Sajid, M. A., Efficacy of silicon priming and fertigation to modulate seedling's vigor and ion homeostasis of wheat

(*Triticum aestivum* L.) under saline environment. *Environmental Science and Pollution Research* **2015**, 22 (18), 14367-14371.

19. Coskun, D.; Britto, D. T.; Huynh, W. Q.; Kronzucker, H. J., The role of silicon in higher plants under salinity and drought stress. *Frontiers in Plant Science* **2016**, 7, 1072.

20. Schurt, D. A.; Cruz, M. F.; Nascimento, K. J.; Filippi, M. C.; Rodrigues, F. A., Silicon potentiates the activities of defense enzymes in the leaf sheaths of rice plants infected by *Rhizoctonia solani*. *Tropical Plant Pathology* **2014**, 39 (6), 457-463.

21. Ning, D.; Song, A.; Fan, F.; Li, Z.; Liang, Y., Effects of slag-based silicon fertilizer on rice growth and brown-spot resistance. *PLoS One* **2014**, 9 (7), e102681.

22. Sun, D.; Hussain, H. I.; Yi, Z.; Rookes, J. E.; Kong, L.; Cahill, D. M., Mesoporous silica nanoparticles enhance seedling growth and photosynthesis in wheat and lupin. *Chemosphere* **2016**, 152, 81-91.

23. Tripathi, D. K.; Singh, S.; Singh, V. P.; Prasad, S. M.; Dubey, N. K.; Chauhan, D. K., Silicon nanoparticles more effectively alleviated UV-B stress than silicon in wheat (*Triticum aestivum*) seedlings. *Plant Physiology and Biochemistry* **2017**, 110, 70-81.

24. Tripathi, D. K.; Singh, V. P.; Prasad, S. M.; Chauhan, D. K.; Dubey, N. K., Silicon nanoparticles (SiNp) alleviate chromium (VI) phytotoxicity in *Pisum sativum* (L.) seedlings. *Plant Physiology and Biochemistry* **2015**, 96, 189-198.

25. Cui, J.; Li, Y.; Jin, Q.; Li, F., Silica nanoparticles inhibit arsenic uptake into rice suspension cells via improving pectin synthesis and the mechanical force of the cell wall. *Environmental Science: Nano* **2020**, 7 (1), 162-171.

26. Siddiqui, M. H.; Al-Whaibi, M. H., Role of nano-SiO₂ in germination of tomato (*Lycopersicon esculentum* seeds Mill.). *Saudi Journal Of Biological Sciences* **2014**, 21 (1), 13-17.

27. Bao-Shan, L.; Chun-hui, L.; Li-jun, F.; Shu-chun, Q.; Min, Y., Effect of TMS (nanostructured silicon dioxide) on growth of Changbai larch seedlings. *Journal of Forestry Research* **2004**, 15 (2), 138-140.

28. Tian, L.; Shen, J.; Sun, G.; Wang, B.; Ji, R.; Zhao, L., Foliar Application of SiO₂ Nanoparticles Alters Soil Metabolite Profiles and Microbial Community Composition in the Pakchoi (*Brassica chinensis* L.) Rhizosphere Grown in Contaminated Mine Soil. *Environmental Science and Technology* **2020**, *54* (20), 13137-13146.
29. Abdelrahman, T. M.; Qin, X.; Li, D.; Senosy, I. A.; Mmby, M.; Wan, H.; Li, J.; He, S., Pectinase-responsive carriers based on mesoporous silica nanoparticles for improving the translocation and fungicidal activity of prochloraz in rice plants. *Chemical Engineering Journal* **2021**, *404*, 126440.
30. Plohl, O.; Gyergyek, S.; Zemljič, L. F., Mesoporous silica nanoparticles modified with N-rich polymer as a potentially environmentally-friendly delivery system for pesticides. *Microporous and Mesoporous Materials* **2021**, *310*, 110663.
31. Feng, J.; Chen, W.; Shen, Y.; Chen, Q.; Yang, J.; Zhang, M.; Yang, W.; Yuan, S., Fabrication of abamectin-loaded mesoporous silica nanoparticles by emulsion-solvent evaporation to improve photolysis stability and extend insecticidal activity. *Nanotechnology* **2020**, *31* (34), 345705.
32. Liu, F.; Wen, L.-X.; Li, Z.-Z.; Yu, W.; Sun, H.-Y.; Chen, J.-F., Porous hollow silica nanoparticles as controlled delivery system for water-soluble pesticide. *Materials Research Bulletin* **2006**, *41* (12), 2268-2275.
33. Li, Z.-Z.; Xu, S.-A.; Wen, L.-X.; Liu, F.; Liu, A.-Q.; Wang, Q.; Sun, H.-Y.; Yu, W.; Chen, J.-F., Controlled release of avermectin from porous hollow silica nanoparticles: Influence of shell thickness on loading efficiency, UV-shielding property and release. *Journal of Controlled Release* **2006**, *111* (1-2), 81-88.
34. Wen, L. X.; Li, Z. Z.; Zou, H. K.; Liu, A. Q.; Chen, J. F., Controlled release of avermectin from porous hollow silica nanoparticles. *Pest Management Science* **2005**, *61* (6), 583-590.
35. Xu, Y.; Xu, C.; Huang, Q.; Cao, L.; Teng, F.; Zhao, P.; Jia, M., Size Effect of Mesoporous Silica Nanoparticles on Pesticide Loading, Release, and Delivery in Cucumber Plants. *Applied Sciences* **2021**, *11* (2), 575.

36. Bueno, V.; Ghoshal, S., Self-Assembled Surfactant-Templated Synthesis of Porous Hollow Silica Nanoparticles: Mechanism of Formation and Feasibility of Post-Synthesis Nanoencapsulation. *Langmuir* **2020**, *36* (48), 14633-14643.
37. Bartlett, D. W.; Clough, J. M.; Godwin, J. R.; Hall, A. A.; Hamer, M.; Parr-Dobrzanski, B., The strobilurin fungicides. *Pest Management Science* **2002**, *58* (7), 649-662.
38. Bazuin, J., Azoxystrobin found to be phytotoxic to certain varieties of apples. *USEPA Pesticide Program Update* **1999**, *21*.
39. Lalancette, N.; Cowgill, W.; Compton, J.; Foster, K. In *Sensitivity of apple cultivars to azoxystrobin fungicide*, Proc. of the 76th Cumberland Shenandoah Fruit Workers Conference. November, **2000**; pp 16-17.
40. Landers, A., Drift reduction in the vineyards of New York and Pennsylvania. *Aspects of Applied Biology* **2000**, (57), 67-73.
41. Jin, L.; Chen, C.; Wang, J.; CHEN, Y.; ZHOU, M.-g., Activity of azoxystrobin and SHAM of four plant pathogens. *Scientia Agricultura Sinica* **2007**, *10*.
42. Bueno, V.; Bosi, A.; Tosco, T.; Ghoshal, S., Mobility of Solid and Porous Hollow SiO₂ Nanoparticles in Saturated Porous Media: Impacts of Surface and Particle Structure. *Journal of Colloid and Interface Science* **2022**, *606*, 480-490.
43. United States Environmental Protection Agency Pesticide Fact Sheet: Azoxystrobin. https://www3.epa.gov/pesticides/chem_search/reg_actions/registration/fs_PC-128810_07-Feb-97.pdf (accessed 7 March 2021).
44. Health Canada Proposed Maximum Residue Limit PMRL2020-48, Azoxystrobin. <https://www.canada.ca/en/health-canada/services/consumer-product-safety/pesticides-pest-management/public/consultations/proposed-maximum-residue-limit/2020/azoxystrobin-various/document.html> (accessed 29 September 2021).
45. Lehotay, S., AOAC official method 2007.01 pesticide residues in foods by acetonitrile extraction and partitioning with Magnesium Sulfate. *Journal of AOAC International* **2007**, *90* (2), 485-520.

46. Kah, M.; Weniger, A.-K.; Hofmann, T., Impacts of (Nano) formulations on the Fate of an Insecticide in Soil and Consequences for Environmental Exposure Assessment. *Environmental Science and Technology* **2016**, *50* (20), 10960-10967.
47. Singer, V. L.; Jones, L. J.; Yue, S. T.; Haugland, R. P., Characterization of PicoGreen reagent and development of a fluorescence-based solution assay for double-stranded DNA quantitation. *Analytical Biochemistry* **1997**, *249* (2), 228-238.
48. Ahn, S. J.; Costa, J.; Rettig Emanuel, J., PicoGreen quantitation of DNA: effective evaluation of samples pre-or post-PCR. *Nucleic acids research* **1996**, *24* (13), 2623-2625.
49. Bolyen, E.; Rideout, J. R.; Dillon, M. R.; Bokulich, N. A.; Abnet, C.; Al-Ghalith, G. A.; Alexander, H.; Alm, E. J.; Arumugam, M.; Asnicar, F. *QIIME 2: Reproducible, interactive, scalable, and extensible microbiome data science*; 2167-9843; PeerJ Preprints: **2018**.
50. Callahan, B. J.; McMurdie, P. J.; Rosen, M. J.; Han, A. W.; Johnson, A. J. A.; Holmes, S. P., DADA2: high-resolution sample inference from Illumina amplicon data. *Nature methods* **2016**, *13* (7), 581-583.
51. Wang, Q.; Garrity, G. M.; Tiedje, J. M.; Cole, J. R., Naive Bayesian classifier for rapid assignment of rRNA sequences into the new bacterial taxonomy. *Applied and Environmental Microbiology* **2007**, *73* (16), 5261-5267.
52. McDonald, D.; Price, M. N.; Goodrich, J.; Nawrocki, E. P.; DeSantis, T. Z.; Probst, A.; Andersen, G. L.; Knight, R.; Hugenholtz, P., An improved Greengenes taxonomy with explicit ranks for ecological and evolutionary analyses of bacteria and archaea. *The ISME Journal* **2012**, *6* (3), 610-618.
53. Kõljalg, U.; Nilsson, R. H.; Abarenkov, K.; Tedersoo, L.; Taylor, A. F.; Bahram, M.; Bates, S. T.; Bruns, T. D.; Bengtsson-Palme, J.; Callaghan, T. M., Towards a unified paradigm for sequence-based identification of fungi. Wiley Online Library: **2013**.
54. Taylor, D. L.; Walters, W. A.; Lennon, N. J.; Bochicchio, J.; Krohn, A.; Caporaso, J. G.; Pennanen, T., Accurate estimation of fungal diversity and abundance through improved lineage-specific primers optimized for Illumina amplicon sequencing. *Applied and Environmental Microbiology* **2016**, *82* (24), 7217-7226.

55. Faith, D. P., Conservation evaluation and phylogenetic diversity. *Biological Conservation* **1992**, *61* (1), 1-10.
56. Pielou, E. C., The measurement of diversity in different types of biological collections. *Journal of Theoretical Biology* **1966**, *13*, 131-144.
57. Lozupone, C. A.; Knight, R., Global patterns in bacterial diversity. *Proceedings of the National Academy of Sciences* **2007**, *104* (27), 11436-11440.
58. Lueders, T.; Manefield, M.; Friedrich, M. W., Enhanced sensitivity of DNA- and rRNA-based stable isotope probing by fractionation and quantitative analysis of isopycnic centrifugation gradients. *Environmental Microbiology* **2004**, *6* (1), 73-78.
59. Lueders, T.; Wagner, B.; Claus, P.; Friedrich, M. W., Stable isotope probing of rRNA and DNA reveals a dynamic methylotroph community and trophic interactions with fungi and protozoa in oxic rice field soil. *Environmental Microbiology* **2004**, *6* (1), 60-72.
60. Edwards, C., Factors that affect the persistence of pesticides in plants and soils. *Pesticide Chemistry-3* **1975**, 39-56.
61. Bansal, V.; Ahmad, A.; Sastry, M., Fungus-mediated biotransformation of amorphous silica in rice husk to nanocrystalline silica. *Journal of the American Chemical Society* **2006**, *128* (43), 14059-14066.
62. LANGE, J. H., A study of apple trees exposed to the fungicide azoxystrobin and mixture interactions with surfactants. *International Journal of Environmental Studies* **2004**, *61* (2), 173-187.
63. Godwin, J.; Anthony, V.; Clough, J.; Godfrey, C. R., ICIA5504: A novel, broad spectrum, systemic beta-methoxyacrylate fungicide. **1992**.
64. Baćmaga, M.; Wyszowska, J.; Kucharski, J., Bioaugmentation of soil contaminated with azoxystrobin. *Water, Air, & Soil Pollution* **2017**, *228* (1), 1-9.
65. Wang, X.; Lu, Z.; Miller, H.; Liu, J.; Hou, Z.; Liang, S.; Zhao, X.; Zhang, H.; Borch, T., Fungicide azoxystrobin induced changes on the soil microbiome. *Applied Soil Ecology* **2020**, *145*, 103343.

66. Baćmaga, M.; Kucharski, J.; Wyszowska, J., Microbial and enzymatic activity of soil contaminated with azoxystrobin. *Environmental Monitoring and Assessment* **2015**, *187* (10), 1-15.
67. Adetutu, E.; Ball, A.; Osborn, A., Azoxystrobin and soil interactions: degradation and impact on soil bacterial and fungal communities. *Journal of Applied Microbiology* **2008**, *105* (6), 1777-1790.
68. Bending, G. D.; Rodríguez-Cruz, M. S.; Lincoln, S. D., Fungicide impacts on microbial communities in soils with contrasting management histories. *Chemosphere* **2007**, *69* (1), 82-88.
69. Wang, F.; Li, X.; Zhu, L.; Du, Z.; Zhang, C.; Wang, J.; Wang, J.; Lv, D., Responses of Soil Microorganisms and Enzymatic Activities to Azoxystrobin in Cambisol. *Polish Journal of Environmental Studies* **2018**, *27* (6).
70. Kennedy, A. C.; Stubbs, T. L., Soil microbial communities as indicators of soil health. *Annals of Arid Zone* **2006**.
71. Albrecht, S.; Okon, Y.; Lonquist, J.; Burris, R., Nitrogen Fixation by Corn-Azospirillum Associations in a Temperate Climate 1. *Crop Science* **1981**, *21* (2), 301-306.
72. Bruehl, G. W., *Soilborne Plant Pathogens*. Macmillan publishing company: **1987**.
73. Schroll, R.; Becher, H. H.; Dörfler, U.; Gayler, S.; Grundmann, S.; Hartmann, H. P.; Ruoss, J., Quantifying the effect of soil moisture on the aerobic microbial mineralization of selected pesticides in different soils. *Environmental Science and Technology* **2006**, *40* (10), 3305-3312.
74. Henriksen, T.; Breland, T., Nitrogen availability effects on carbon mineralization, fungal and bacterial growth, and enzyme activities during decomposition of wheat straw in soil. *Soil Biology and Biochemistry* **1999**, *31* (8), 1121-1134.
75. Botha, A., The importance and ecology of yeasts in soil. *Soil Biology and Biochemistry* **2011**, *43* (1), 1-8.
76. Spain, A. M.; Krumholz, L. R.; Elshahed, M. S., Abundance, composition, diversity and novelty of soil Proteobacteria. *The ISME Journal* **2009**, *3* (8), 992-1000.

77. Mhete, M.; Eze, P. N.; Rahube, T. O.; Akinyemi, F. O., Soil properties influence bacterial abundance and diversity under different land-use regimes in semi-arid environments. *Scientific African* **2020**, *7*, e00246.
78. Lo, C.-C., Effect of pesticides on soil microbial community. *Journal of Environmental Science and Health Part B* **2010**, *45* (5), 348-359.

Connecting Text to Chapter 6

Previous chapters described the synthesis, pesticide encapsulation, and environmental fate of porous hollow silica nanoparticles (PHSN) formulations. In its turn, Chapter 6 explores the uptake and translocation of PHSN-encapsulated azoxystrobin following foliar application in tomato plants. Environmental fate analysis (Chapters 4 and 5) was performed before application analysis (Chapter 6) because if a promising product ends up becoming an emergent contaminant, it is not even worth pursuing the product deployment and production in larger scale, seen that companies are now aiming to create sustainable products with clean design. Therefore, after assessing the environmental implications of nanoformulation with azoxystrobin and PHSN, this chapter investigates what happens to this nanoformulation after its applications, including the internalization profiles and how it is transported within the plant. Tracking silica nanoparticles is particularly challenging, but it was possible here using a suite of advanced analytical techniques, including single particle inductively coupled plasma–mass spectrometry and inductively coupled plasma optical emission spectroscopy.

Chapter 6. Uptake and Translocation of a Silica Nanocarrier and an Encapsulated Organic Pesticide Following Foliar Application in Tomato Plants

6.1. Abstract

Pesticide losses are estimated to reach up to 99%, which poses a sustainability challenge to agriculture. Pesticide nanoencapsulation and its foliar application are a promising approach for improving the efficiency of pesticide application. Here, we investigated the uptake and translocation of azoxystrobin encapsulated within porous hollow silica nanoparticles (PHSNs) of mean diameter 253 ± 73 nm, following foliar application on tomato plants. The PHSNs enabled slow release of loaded azoxystrobin over several days. Azoxystrobin was quantified in five different plant parts, yielding 8.7 ± 1.3 μg of the pesticide distributed to other plant tissues after 4 days following 20 μg nanoencapsulated pesticide application on a single leaflet of each plant. In parallel, the uptake and translocation of the PHSNs (as total Si and particulate SiO_2) in the plant was characterized. The nanoencapsulated pesticide was taken up and distributed slower than the non-encapsulated pesticide, and the uptake rate and translocation patterns for PHSN and pesticide were different. Moreover, the data indicate knowledge gaps in the translocation mechanisms of nanoparticles in plants because PHSNs were translocated throughout the plant, although they are much larger than known size exclusion limits (up to ~ 50 nm) inside plant tissues.

6.2. Introduction

The agriculture industry must innovate to meet the increasing global food demand that is expected to increase 1.5-fold in the next 40 years, without increasing its environmental footprint.¹ Based on current practices, this increasing pressure to produce more food will lead to the increase of the use of pesticides by almost 5 times.² Traditional pesticide application practices, which involve application to soil or spraying over crops, are inefficient and it is estimated that up to 99% of pesticides are lost to the environment and not taken up in the plant.^{3,4} These inefficiencies require addition of more pesticides than necessary, resulting in higher costs, and adverse environmental impacts from increased contamination of agricultural land, groundwater, and surface water bodies.⁵⁻⁷ The use of nanocarriers loaded with pesticides in precision foliar application can enable

efficient pesticide uptake by the plant and their controlled release in the plant over time. This provides an opportunity to tackle some of these shortcomings, by decreasing the loss of pesticides and the environmental contamination that follows, and by potentially reducing the number of application cycles required to grow crops.

Recent advances in the synthesis of SiO₂ NPs of different structures have made them promising candidates for nanoencapsulation of molecules of interest, such as pesticides^{8,9}. Bueno and Ghoshal¹⁰ developed a protocol to synthesize porous hollow SiO₂ NPs (PHSNs) and demonstrated the feasibility of encapsulating solutes and smaller nanoparticles within the porous SiO₂ shell. PHSNs possess a hollow core that allows the high-density loading of molecules of interest within its core and shell. Porous nanocarriers can act as slow-release frameworks, which allow pesticides to be continuously released at a slow rate, reducing the need for multiple applications.^{11,12} Moreover, previous studies have demonstrated that Si-based NPs dosed in plants induced tolerance towards biotic and abiotic stresses, such as disease, drought, and salinity imbalance.¹³⁻¹⁶ Furthermore, Si is an earth-abundant element and exhibit low toxicity towards living organisms.¹⁷

Despite the promising potential of nano-enabled agriculture, research in the field is still underexplored. Little is known about how plants internalize and transport NPs following foliar application, which hinders our capability to design optimal nanocarriers to transport the needed molecules of interest and deliver them to the desired plant parts, at a pace that is not too fast such that it could lead to potential toxicity, but not too slow such that it would provide insufficient protection against pests.

Based on the state-of-the-art knowledge, it is known that there are several pathways for foliar entry, including cuticle and trichome pores, stomata, foliar wounds, hydathodes and lenticels.¹⁸ While stomata, hydathodes and lenticels size exclusion limits (SELs) are in the micron-scale, cuticular pore SELs often fall within 0.1 to 10 nm.¹⁸ NPs with 100 nm diameter have been reported to traverse the cuticle region upon momentary disruption in the waxy cuticular layer.¹⁹ After foliar entry, NPs must overcome several internal barriers before reaching the vascular system (xylem and phloem), where the NPs can finally be translocated within plants. Two important routes to cross the epidermis and mesophyll (palisade and spongy) are the apoplastic and symplastic pathways. The former is the pathway between cells with SELs between 5 and 20 nm through which

molecules diffuse freely²⁰⁻²² and the latter is the pathway to transport low-density molecules through an interconnected network of protoplasts with SELs ranging from 3 to 50 nm.^{23, 24} Theoretically, we should not expect particles larger than the SELs to be able to be taken up and translocate within plants, but some studies have shown the uptake and translocation of larger NPs.^{19, 25, 26}

Knowledge gaps in the mechanisms of uptake and transport of NPs within plants exist because tracking NP mobility *in planta* is hindered by limitations in detection and quantification of non-metal NPs, with common analytical techniques. To date, only a few studies have tracked translocation *in planta* of NPs (mainly metallic), such as TiO₂,^{27, 28} ZnO,^{25, 28} Au,²⁶ CeO₂²⁹ and Pt.³⁰ Gao et al.²⁵ showed translocation of mesoporous SiO₂-coated ZnO NPs following foliar application, by characterizing the total Zn and the relative concentrations of the NPs in different plant parts using single particle mode inductively coupled plasma mass spectrometry (spICP-MS). However, the total Si uptake was not quantified. To understand the uptake and translocation in plants of different constituents in composite NPs such as nanoencapsulated pesticides, the distribution of all constituents needs to be characterized in the different plant parts. The encapsulated pesticide could either be released from the nanocarrier at the site of application on the plant, or the nanocarrier can be taken up and translocated with the encapsulated pesticide. As well, the nanocarrier may be partly or entirely dissolved or disintegrated in the plant.

In this study, we assessed the uptake and translocation of azoxystrobin encapsulated within PHSNs. Azoxystrobin is applied to soils to remove fungal pests from the soil prior to sowing,³¹ and to leaves to actively combat fungal infections in the plant.³² The application of azoxystrobin in fields and greenhouses for tomato cultivars has been reported by means of dips, soil drenches and foliar sprays.³³ In this study, the nanoformulation was applied directly on a selected leaflet. The pesticide quantification in different plant parts was conducted using liquid chromatograph (LC) coupled to a quadrupole time-of-flight mass spectrometer (QToF-MS). Quantifying Si uptake in plant parts is challenging because SiO₂ is not easily solubilized using conventional acid-based methodologies to allow elemental analysis. Currently, common protocols to digest SiO₂ involve the use of hydrofluoric acid (HF), which is extremely toxic, and corrosive to instruments and glassware.^{34, 35} Furthermore, the quantification of digested Si alone is not direct evidence of NP translocation because Si may be dissolved and translocated as silicic acid in plants. Therefore,

appropriate techniques must be used to quantify total Si as well as identify whether the Si is in the particulate form as SiO₂ nanoparticles. To circumvent the use of HF, we used a modified version of the HF-free protocol to dissolve SiO₂ NPs developed by Bossert et al.³⁶ to determine the total Si in plant tissues. We combined the results with those obtained from spICP-MS to evaluate the fraction of Si was solubilized or in the particulate form (as NP). This distinction between solubilized and particulate form is important because a recent study showed that solid SiO₂ NPs can be solubilized within watermelon plants (*Citrullus lanatus*), thus Si can be found in both forms after uptake and translocation.³⁷ In that study, evidence of dissolution of particulate SiO₂ was obtained from transmission electronic microscopy (TEM) after incubation of the nanoparticles in simulated xylem sap. It is important to note that in that study, the SiO₂ NP dissolution in the plant tissue was not verified and concentrations of NP in the plant tissues were not determined.

To the best of our knowledge, this is the first study to quantify the uptake and translocation of an organic compound encapsulated within an inorganic nanocarrier, as well as the inorganic nanocarrier. The model plant used in this study was tomato (*Solanum lycopersicum*), an important cash crop worldwide (\$8.5 billion market³⁸), and its protection from numerous pests is a priority.³⁹

40

6.3. Experimental Section

6.3.1. Chemicals

Chemicals used and their sources are stated in the Supporting Information.

6.3.2. Nanocarrier synthesis

The PHSNs were synthesized following a previously reported protocol.¹⁰ Briefly, 300 mg of CTAB, 850 mg of Pluronic P123 and 15 mL of NH₄OH (30% v/v) were added sequentially to an aqueous solution containing ethanol (37.5% v/v). The reagents were allowed to mix until total dissolution. Then, the SiO₂ precursor, TEOS, was added dropwise at 0.0125 mL/s for 800 s. Following the TEOS addition, the reaction was allowed to proceed for 5 hours under vigorous mixing. Finally, the suspension was dried overnight at 80°C and the resulting powder was calcined at 550°C for 5 h to remove the remaining surfactants and ammonia. These NPs were fully characterized in a previous work^{10, 41} and their key parameters are summarized in Table S6-1.

6.3.3. Azoxystrobin nanoencapsulation

The encapsulation of azoxystrobin within the nanocarriers was achieved by suspending the PHSNs (0.67 mg/mL) in an methanol-water mixture (20% v/v methanol) containing azoxystrobin (0.1 mg/mL) as previously reported.⁴² The water-methanol ratio in the solution was optimized to fully solubilize the pesticide while keeping conditions favorable for the azoxystrobin to be loaded within the nanocarriers, by infiltrating the porous shell and filling the hollow core and more importantly by sorption on the surface of the nanoporous shell. Then, aliquots of the suspension were analyzed periodically using an Agilent 1260 Infinity II HPLC system equipped with UV detector and quantified at 255 nm, the characteristic wavelength.

6.3.4. Seed germination and hydroponic system

Solanum lycopersicum seeds (McKenzie Seeds, Canada) were sterilized in a 1.5% sodium hypochlorite solution for 30 min and then rinsed thoroughly with DI water. The seeds were covered in slightly wet tissue paper placed inside Petri dishes and allowed to germinate for 14 days in total darkness. Seedlings at the same growth stage were carefully picked and transplanted to hydroponic pots containing 25% Hoagland medium. The pots were illuminated with a 36 W LED grow light system (IPower) with wavelengths at 430, 465, 630 and 660 nm to maximize chlorophyll activity under a 16h-8h day-night cycle routine. Air was continuously supplied over the course of the experiment with the aid of a porous stone that sparged air bubbles. The plants were grown in ambient temperature (23 ± 2 °C) and the Hoagland solution was replaced every 3 days for each treatment to maintain sufficient amount of nutrients in the media. After 14 days of growth, the azoxystrobin-PHSN formulation prepared previously was applied directly on a selected leaflet. The total volume applied totaled 200 μ L applied dropwise at increments of 10 μ L. The final dosing contained 133 μ g of PHSNs and 20 μ g of azoxystrobin. Two other treatments were prepared for comparison: (i) A treatment with no PHSN to compare the uptake of solubilized azoxystrobin with that of encapsulated pesticide, in this treatment, 200 μ L of an aqueous methanol solution (20% v/v) containing 20 μ g of solubilized azoxystrobin was applied on the leaflet surface; (ii) A treatment without PHSN and azoxystrobin as control, where 200 μ L of a methanol solution (20% v/v) was applied directly on the selected leaflet. The treatments with the azoxystrobin-PHSN formulation and solubilized azoxystrobin will henceforth be referred to as Azo@PHSN and Azo, respectively.

Half the plants were grown for 2 days and the others for 4 days. Upon harvesting, the plants were separated in 5 parts: (i) dosed leaflet, which represents the leaflet where the formulation was applied, (ii) mature leaflets, which represent the leaflets grown before the leaf that was dosed, (iii) young leaflets, which represent the leaflets grown after the leaflet that was dosed, (iv) stem, and (v) roots. Each treatment was prepared in triplicates ($N = 3$). Because the harvesting at day 2 and day 4 and the pesticide/SiO₂ measurements are sacrificial, three sets of triplicates was prepared for each day for all treatments.

6.3.5. Azoxystrobin uptake quantification

Each one of the 5 plant parts was dried overnight at 110 °C on aluminum weighing dishes, and the respective dry masses (mg) were measured. The dried plant parts were then transferred to a falcon tube for the pesticide extraction and quantification using a modified version of the QuEChERS (quick, easy, cheap, effective, rugged, and safe) method.⁴³ The detailed pesticide extraction procedure is described in the Supporting Information. Then, the extract was filtered through a 0.22 µm polytetrafluoroethylene (PTFE) filter and analyzed for azoxystrobin in an Agilent 1290 Infinity II LC coupled to a QToF-MS (Agilent) operating in positive electrospray ionization mode. The concentration of azoxystrobin in the medium was analyzed through direct injection in LC-QToF-MS.

6.3.6. Total Si uptake quantification

Each plant part was digested using a modified 3-step method reported elsewhere.^{25, 36} First, the biomass was digested with a solution combining HNO₃ and H₂O₂ at high temperatures. The biomass from each plant part was submerged in a solution containing 2.15 mL HNO₃ (70% v/v) and 2.85 mL DI water at 95 °C for 2 h, then 1.5 mL of H₂O₂ (30% v/v) was added to the tube and allowed to react at 95 °C for 2 h to complete the biomass digestion. Second, the digestate was subjected to a modified version of the HF-free method to dissolve SiO₂ NPs: 2.5 mL of KOH (4 M) was added to every 1 mL of digestate to increase the pH to 13.6, then the SiO₂ digestion was allowed to proceed overnight. Finally, H₂SO₄ (2.25 M) was added to the digestate dropwise until the pH decreased from 13.6 to 1.3 and, only then, the samples were analyzed for Si in the ICP-OES. Dissolved Si(OH)₄ was subjected to the same modified 3-step digestion protocol described previously and used for calibration. The concentration of Si in the medium was analyzed following the 3-step digestion protocol without further dilution.

6.3.7. spICP-MS measurements of PHSN uptake

Each plant part was subjected to enzymatic digestion to facilitate extraction of the PHSNs by breaking down some of the organic matter, based on a protocol suggested by Dan et al.⁴⁴ In summary, the biomass was homogenized using an IKA T10 Basic S1 Disperser in 8 mL of citrate buffer (pH 5.6), which according to the manufacturer is within the optimum pH range for Macerozyme R-10, a macerating enzyme for plant tissues. Then, 2 mL of the enzymatic solution (50 mg/mL) was added to the system and incubated at 37 °C for 24 h. After incubation, the samples were allowed to settle for 1 h and the supernatant was diluted 100 times prior to the analysis using a PerkinElmer NexION 300x ICP-MS in single particle mode. Particle size distribution and particle concentration in the samples were measured simultaneously in each analysis. An integration dwell time of 100 μ s with sampling time of 100 s was used to measure the samples. Ultra-uniform gold NPs of size 55 nm (nanoComposix) at a concentration of 10^5 particles/mL were used for determination of spICP-MS transport efficiency (7.5 to 8.5%), both in DI water and the enzyme-digested plant matrix. The calibration of Si was performed using Single-Element (Si) and Multi-Element (Mo, Sb, Si, Sn and Ti) ICP and ICP-MS Certified Reference Standards (VWR). The concentration of PHSN in the medium was analyzed following the enzymatic digestion protocol. Leaflets, stem, and roots from control plants were spiked with PHSNs for method validation.

6.4. Results and Discussion

6.4.1. Azoxystrobin loading in PHSN

The TEM image in Figure 6-1a shows the hollow core inside the porous silica shell of the spherical PHSN and are in agreement with the PHSN characterization performed in our previous studies.^{10, 41, 42} Figure 6-1b (●) indicates the loading profile of azoxystrobin over time in the PHSNs in a methanol solution (20% v/v). The suspension containing the PHSNs and dissolved azoxystrobin was stirred at 130 rpm for 8 days, at which time the pesticide mass transfer from the solution to the PHSNs plateaued, yielding 0.50 ± 0.01 mg of azoxystrobin loaded into the PHSNs, accounting for $66.9 \pm 1.4\%$ of the initial pesticide in solution. The release time profile shown in Figure 6-1b (●) demonstrates that the PHSN enabled the slow release of the azoxystrobin over time as reported in our prior study⁴², releasing $43.5 \pm 5.8\%$ of azoxystrobin over 10 days into a fresh methanol

solution. In comparison, the non-encapsulated solid phase azoxystrobin completely dissolved in the methanol solution after 3 hours.⁴²

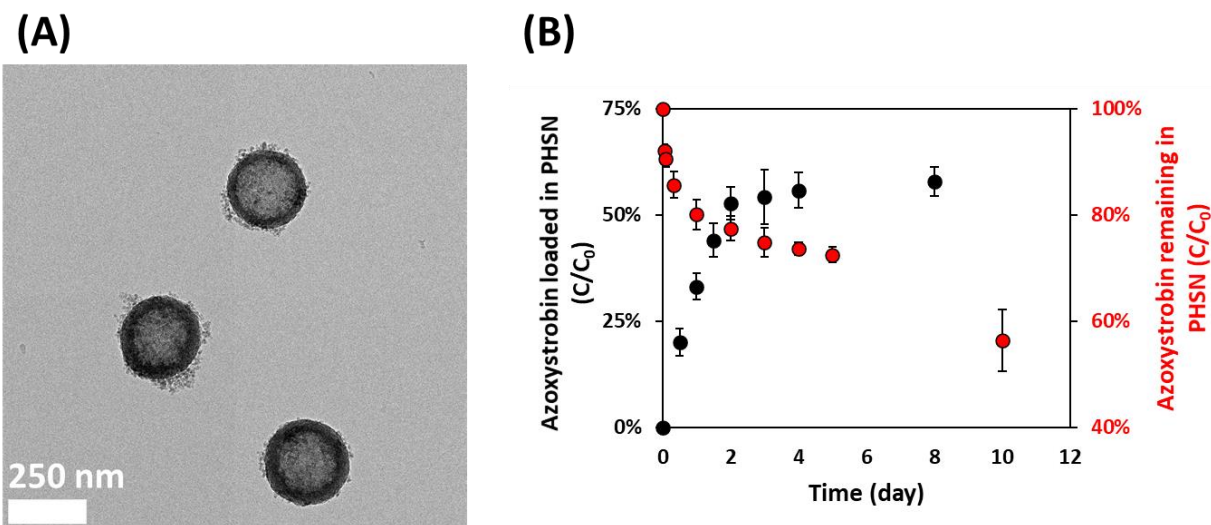


Figure 6-1. Characterization of (A) particle size and shape using TEM and (B) azoxystrobin loading and release profiles within the PHSN based on the data of a previous work.⁴² The black data points (●) represent the amount of azoxystrobin being loaded in the PHSN over time after introducing the nanocarriers in a methanolic solution of azoxystrobin. The red data points (●) represent the amount of azoxystrobin remaining in the PHSNs over time after separating the azoxystrobin-loaded PHSN and introducing them into an aqueous release medium containing methanol (20% v/v).

6.4.2. Uptake and translocation of azoxystrobin in different plant parts

Figure 6-2a shows the amounts of azoxystrobin in five different plant parts (dosed leaflet, mature leaflets, young leaflets, stem, and roots), towards characterization of the pesticide translocation, and how they differ among treatments and harvesting periods. The data suggest that 4 days after dosing, azoxystrobin was found in each one of the five plant parts with abundance as follows: Stem > Young leaflets > Mature Leaflets > Roots (ANOVA one-way test followed by Tukey's test, $p < 0.05$), for both the Azo and Azo@PHSN treatments. The distribution of azoxystrobin throughout the plant was expected because azoxystrobin is a well-known systemic fungicide. That is, once internalized, azoxystrobin is readily translocated to every part of the plant and makes the infiltrated plant tissue toxic to fungi.^{45, 46} In fact, azoxystrobin has been reported to have elevated uptake in leaflets, enhanced xylem-systemic movement and translaminar movement (leaf penetration), and

increased translocation to areas of new growth.⁴⁷ While the xylem transport is unidirectional (upwards), phloem transport is bidirectional and is determined by the nutritional requirements of the plants.⁴⁸ Furthermore, xylem-phloem exchanges may also occur through symplastic and apoplastic transport.⁴⁹ Because the pesticide has elevated xylem-systemic activity, its upward translocation is favored, not surprisingly to areas of new growth, which in our case corresponds to the young leaflets and the stem that connects them to the mature part of the plant.

Figure 6-2b shows the concentration of azoxystrobin in each plant part normalized by the total amount of azoxystrobin quantified for each treatment. It is evident that azoxystrobin uptake and translocation was faster for the non-encapsulated azoxystrobin treatment. At day 2 after dosing, 35% of the azoxystrobin was measured in different plant parts other than the dosed leaflet for the Azo treatment whereas only 21% of the azoxystrobin translocated for the Azo@PHSN treatment. The same trend follows at day 4 after dosing, where 58% of the azoxystrobin was translocated for the Azo treatment compared to only 42% for the Azo@PHSN treatment.

The targeted amount of azoxystrobin was 20 µg/plant and the amount of azoxystrobin recovered based on this target was $108 \pm 6\%$, $98 \pm 3\%$, $95 \pm 7\%$, and $103 \pm 8\%$ for the Azo treatment at day 2, Azo@PHSN treatment at day 2, Azo treatment at day 4, and Azo@PHSN treatment at day 4, respectively. No azoxystrobin was detected in the control plants. The detection limit of azoxystrobin using LC-QToF-MS was 0.28 ng per g of dried plant tissue, and significantly lower than the concentrations of azoxystrobin in the plant parts.

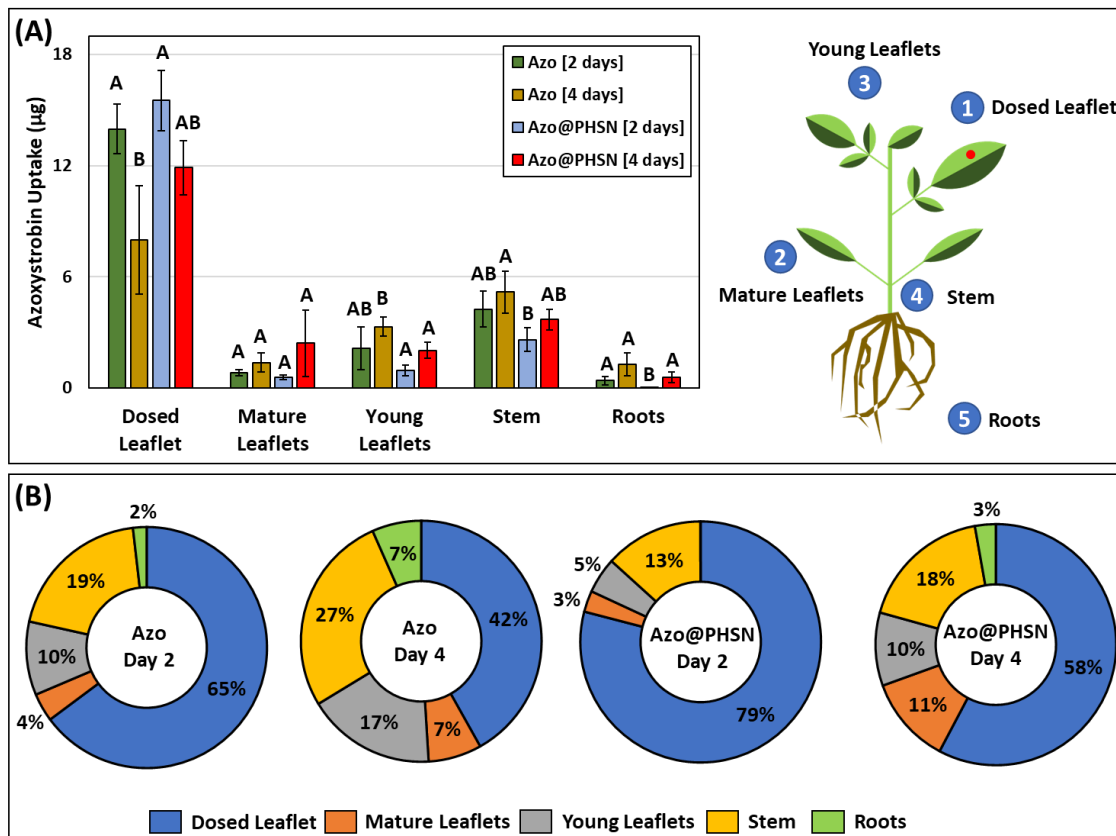


Figure 6-2. Azoxystrobin distribution in different plant parts 2 and 4 days after dosing with Azo and Azo@PHSN treatments. (A) Mass of azoxystrobin in different plant parts. Error bars represent the standard deviation of the samples ($N = 3$). Different letters (A and B) indicate significant statistical differences among samples, while same letters indicate no significant statistical differences among samples (ANOVA one-way test followed by Tukey's test, $p < 0.05$). (B) Mass of azoxystrobin in different plant parts normalized by the total amount of azoxystrobin.

6.4.3. Uptake and translocation of Si in different plant parts

The data in Figure 6-3 suggests that at day 2 after dosing, Si was distributed in the entire plant, except for the mature leaflets in the Azo@PHSN treatment. At day 4, however, some Si was measured in the mature leaflets, suggesting a slower translocation of Si to the mature leaflets, compared to that for azoxystrobin. The Si in the plant tissues may be present as silicic acid derived from digestion of the PHSN in the plant,³⁷ or as PHSNs, and the speciation is discussed in the following section.

There was a statistically significant decrease in the amount of Si on the dosed leaflet, from $48.6 \pm 1.6 \mu\text{g}$ at day 2 to $35.3 \pm 1.0 \mu\text{g}$ at day 4, suggesting that the PHSNs were continuously taken up and translocated over the course of the experiment. At the same time, there were statistically significant increases in the concentration of Si in the mature leaflets, young leaflets, and roots, but no significant difference was observed in the concentration of Si in the stem. The distribution profile for Si was slightly different than that of azoxystrobin: Stem > Roots > Young leaflets > Mature leaflets. While the mechanisms of internalization and translocation for pesticides are more established, those of NPs and their constituents are yet to be comprehensively established.

The data in Figure 6-3b show the concentration of Si in each plant part normalized by the total amount of Si. It is evident that Si is being internalized over time and distributed in the whole plant. At day 2, 12% of Si dosed was measured in different plant parts other than the dosed leaflet, while at day 4, the translocated Si reached 31%. Little to no Si reached the mature leaflets. It is known that the plant has mechanisms to distribute internalized nutrients preferably to areas of new growth, frequently associated with foliar senescence,⁵⁰ taking Si to the root tips, stem, and younger leaflets, while older parts of the plant, that are already well-established, receive less nutrients over time.

The targeted amount of Si was $62 \mu\text{g/plant}$, incorporated in the $133 \mu\text{g/plant}$ of PHSN as SiO_2 , applied on a leaflet. The amount of Si recovered based on this target yielded $89 \pm 1\%$ and $82 \pm 1\%$ Azo@PHSN treatment at day 2 and Azo@PHSN treatment at day 4, respectively. Smaller recoveries for Si were expected compared to those of azoxystrobin due to the difficulty of digesting SiO_2 NPs, and further measurement challenges associated with the complex sample matrix of digested plant biomass and the background interferences contributed by additional elements introduced in the 3-step digestion method. Similar yields were obtained in the original method developed by Bossert et al.³⁶ No Si or nanoparticulate SiO_2 was measured in the control plants. The detection limit of total Si in ICP-OES was approximately $9 \mu\text{g/g}$ of dried plant tissue. The measured concentrations of Si were significantly higher than the instrument detection limit, but only slightly higher for those measured in the young leaflets at day 2 and mature leaflets at day 4.

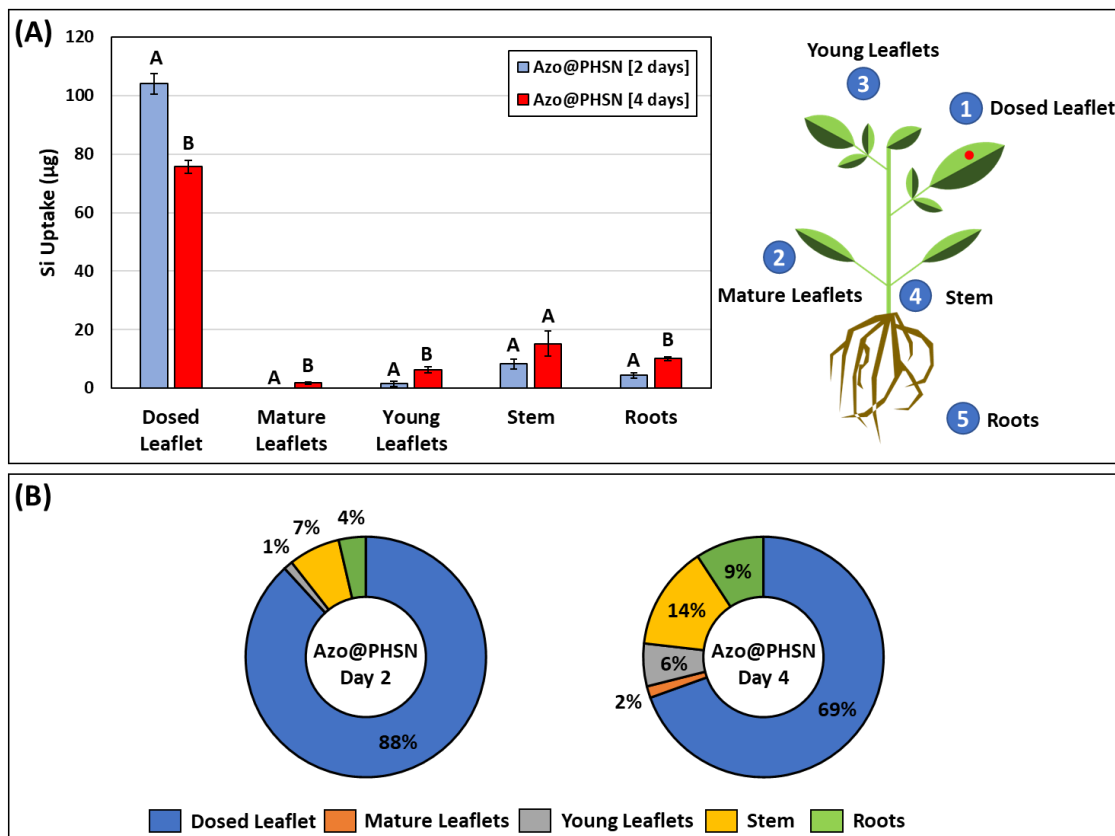


Figure 6-3. Si distribution in different plant parts 2 and 4 days after dosing Azo@PHSN treatment. (A) Mass of Si in different plant parts. Error bars represent the standard deviation of the samples ($N = 3$). Different letters (*A* and *B*) indicate significant statistical differences among samples, while same letters indicate no significant statistical differences among samples (ANOVA one-way test followed by Tukey's test, $p < 0.05$). (B) Mass of Si in different plant parts normalized by the total amount of Si measured by ICP-OES.

6.4.4. Characterization of particulate SiO₂ uptake and translocation in different plant parts

Figure 6-4 demonstrates that PHSNs were found in all plant parts except for the mature leaflets, in both harvesting periods (2 and 4 days after foliar application). The distribution of PHSNs found in different parts of the plant are in agreement with the data obtained for total Si content: Stem > Roots > Young leaflets > Mature leaflets inferred from Figure 6-3. Figure 6-4 conveys the relative abundance of PHSNs in different plant parts and shows the concentration in the supernatant in the enzyme digestate of each plant part. Those are not the true PHSN concentrations because some PHSN remained in the residual solid biomass in the digestate, which was not analyzed in the ICP-MS due to the presence of large biomass particles which could clog its aspirator and nebulizer.

Important information about transformations of PHSN within *Solanum lycopersicum* can be inferred from the data in Figures 6-3 and 6-4. The total Si measurements in Figure 6-3 indicated that while no Si was found in the mature leaflets at day 2, some Si was measured in the mature leaflets at day 4. No PHSN signal was identified in mature leaflets on day 2 and day 4 with the spICP-MS measurements. The size and mass detection limits for SiO₂ with spICP-MS were 133 nm and 0.5 µg per g of dried plant tissue, respectively. It is possible that SiO₂ NPs were present in the mature leaflets at levels below the spICP-MS detection limit after 2 and 4 days. However, because the total Si content quantified using ICP-OES in the mature leaflets at day 4 exceeded the mass detection limit value of spICP-MS, these data suggest that Si in the mature leaflets at day 4 was predominantly present as solubilized Si, Si(OH)₄. Furthermore, some aggregation took place after 4 days in/on the dosed leaflet as shown in Figure 6-4. It is possible that aggregation took place because the NPs interacted with cuticular biomolecules on the leaflet surface, with other biomolecules inside the leaflet.

Figure 6-4 presents direct evidence that NPs of 253 nm diameter not only were taken up by the leaflet but also translocated to the stem, roots, and young leaflets. The PHSNs were small enough to pass through the stomata openings, which range from 10 to 100 µm depending on the plant and species.^{20, 51} In *Solanum lycopersicum*, stomata can be found in both the abaxial and adaxial surfaces, although they are more abundant in the former.⁵² Furthermore, one could not rule out the chance of uptake of NPs through trichomes, which are greatly abundant in *Solanum lycopersicum*⁵³, and foliar wounds, which could have occurred naturally or induced by the presence of PHSNs, azoxystrobin, methanol or a combination of these in the suspension. However, the data on translocation following uptake in the dosed leaflet is non-intuitive, based on reported SELs for apoplastic and symplastic transport.^{20-24, 54} Nonetheless, previous studies have suggested that NPs with negative surface charge exceeding -30 mV, which is within the range of ζ-potential for our PHSN, as reported in Table S6-1, are more likely to be internalized through the leaflets and roots, while NPs with surface charge approaching neutral are unable to cross the cellular lipid bilayer.^{55, 56} Moreover, Hu et al.⁵⁷ suggested that smaller NPs require a greater absolute surface charge to be internalized and distributed within the plant compared to larger NPs. According to previous studies,⁵⁸⁻⁶⁰ negatively charged NPs also have enhanced translocation to aerial parts. A few studies have also shown NPs of 50 nm,²⁶ 70 nm²⁵ and 150 nm¹⁹ in diameter being taken up and translocated

within plants, which suggests that there are translocation mechanisms and pathways that can overcome the recognized SELs.

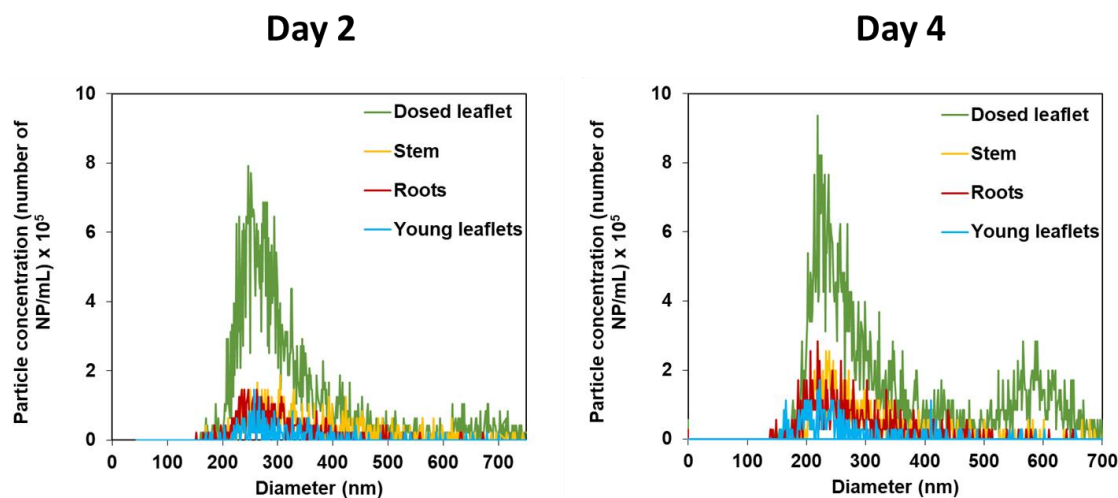


Figure 6-4. PHSN size distribution in different plant parts at different harvesting periods measured by spICP-MS. No PHSN signal was measured in mature leaflets at days 2 and 4 of harvesting. These experiments were performed in triplicates ($N = 3$).

6.4.5. Uptake and Translocation Mechanisms of Azoxystrobin and SiO₂

The measurements of azoxystrobin, total Si and particulate SiO₂, suggest that both the pesticide as well as the nanocarrier were taken up and distributed to different plant parts over the course of the experiments. The mass of azoxystrobin and Si translocated in the whole plant from the dosed leaflet (derived from a summation of the amounts taken up in the different plant parts except the mature leaflet) is shown in Figure S6-1. While there is no statistical difference ($p > 0.05$) in the translocated amount of pesticide for the non-encapsulated azoxystrobin at days 2 and 4, there is considerably more pesticide translocation ($p < 0.05$) for the encapsulated pesticide treatment at day 4 when compared to day 2 (Figure S6-1a). It could be attributed, at least in part, to the slower uptake and distribution of particles (Azo@PHSN) compared to solubilized molecules (Azo). From Figure 6-2a, the azoxystrobin uptake between days 2 and 4, was more significant for the Azo treatment than for the Azo@PHSN treatment. This suggests that the azoxystrobin uptake in the dosed leaflet was hindered when encapsulated in the PHSN. Figure 6-3a shows that there was Si (likely as PHSN) uptake between days 2 and 4. Figure S6-1b shows that the translocated Si increased from $6.5 \pm 1.2 \mu\text{g}$ at day 2 to $15.5 \pm 1.6 \mu\text{g}$ at day 4. This gradual uptake of Si contributed

to differences in uptake and translocation of azoxystrobin. While non-encapsulated azoxystrobin enters the plant without any hindrance, the uptake of the encapsulated pesticide depends on the uptake of the whole nanoformulation. Figure S6-2 and Figure S6-3 show images of the dosed leaflets upon harvesting at days 2 and 4, respectively, where some PHSN powder is visible on the leaflet surface, but no residues were visible for the non-encapsulated azoxystrobin. The slower uptake and translocation of azoxystrobin encapsulated in the PHSNs, may be beneficial in providing protection to fungal pests in the plant over a longer time. Neither azoxystrobin nor Si (in the particulate form as SiO_2 or in the dissolved form as Si(OH)_4) were found in the growth medium after 2 and 4 days, suggesting that excretion through roots exudates did not take place within the period considered, although pesticide root excretion is a possible pathway reported in a previous study.⁶¹ Neither treatment had visible beneficial or inhibitory effects in the growth of the tomato plants, and the biomass associated with different plant parts was comparable as shown in Figure S6-4 and Figure S6-5.

Table 6-1 summarizes the Si to azoxystrobin ratio found in the different plant parts and harvesting periods, when compared to the original formulation of Azo@PHSN. Apart from the ratio in the dosed leaflet, which is comparable to the original (dosing) formulation, the ratios in the other plant parts varied significantly. This indicates that azoxystrobin dissociated from the PHSN and translocated separately, because the rate of translocation is different between azoxystrobin and Si. This is evident when we compare the amount of azoxystrobin measured in the roots and mature leaflets. At day 2, while azoxystrobin was detected in the roots for the Azo treatment, none was found for the Azo@PHSN treatment. However, after 4 days, azoxystrobin was found in the roots for both treatments. Conversely, Si was detected in the roots both on days 2 and 4 (Figure 6-3) and as particulate SiO_2 (Figure 6-4). For the mature leaflets, azoxystrobin was quantified at days 2 and 4 for both treatments, whereas no Si was quantified at day 2 for the Azo@PHSN treatment. Moreover, the measurement of Si at day 4 was not associated with a significant increase in azoxystrobin, which would have been expected if Si in the particulate form was carrying the pesticide.

The slower overall uptake and translocation of azoxystrobin when encapsulated within PHSN as compared to its non-encapsulated form is different compared to a previous study where ZnO NPs were encapsulated within a porous SiO_2 shell and applied on tomato leaflets.²⁵ In that

study, we reported a 5-fold increase of Zn uptake when encapsulated compared to the non-encapsulated ZnO. Translocation was also greatly enhanced with encapsulation leading to significantly higher ZnO content quantified in young leaflets and stem. Thus, ZnO NPs, which are significantly greater in size than azoxystrobin molecules, had their uptake and translocation enhanced while those of azoxystrobin were reduced. A possible explanation is that while ZnO NPs are not inherently easily taken up and distributed by plants, there are natural pathways for Si uptake, thus making the SiO₂ shell enhance the ZnO NP uptake and translocation.²⁵ On the other hand, azoxystrobin was identified to have the optimal capacity to be internalized and distributed throughout the plant (systemic features) among hundreds of its homologs developed during its discovery.⁴⁷ This suggests that the size and physiochemical properties of the encapsulated compound play an important role in how it is taken up and distributed inside the same plant.

Table 6-1. Si to azoxystrobin ratio in different systems.

System	Harvest Day	Si to azoxystrobin ratio^{a, b}
Original formulation	-	3.10:1
Dosed leaflet	2	3.92 ± 0.10 : 1 ± 0.10
	4	3.71 ± 0.08 : 1 ± 0.12
Mature leaflets	2	- ^c
	4	0.42 ± 0.02 : 1 ± 0.75
Young leaflets	2	0.89 ± 0.03 : 1 ± 0.31
	4	1.80 ± 0.04 : 1 ± 0.21
Stem	2	1.84 ± 0.05 : 1 ± 0.25
	4	2.42 ± 0.17 : 1 ± 0.15
Roots	2	- ^d
	4	10.17 ± 0.03 : 1 ± 0.49

^a The ratio was adjusted to account for the recovery of Si and azoxystrobin.

^b The standard deviation was normalized by the quantified values of Si and azoxystrobin.

^c No Si (or below the detection limit) was measured in the mature leaflets at day 2.

^d No azoxystrobin (or below the detection limit) was quantified in the roots at day 2.

6.5. Environmental Implications

Our results show that PHSNs at least 5-fold greater than apoplastic and symplastic SEL thresholds were translocated, suggesting that there are unknown mechanisms that facilitate translocation of

these nanocarriers. SiO₂ NP and azoxystrobin translocation profiles varied significantly, which depends on the intrinsic characteristics of each compound and how the plant uses them. The overall trends were that (i) the amount of the pesticide in the dosed leaflet decreased with time in both treatments, indicating the uptake into the leaflets, and (ii) the uptake and translocation of the encapsulated pesticide (Azo@PHSN treatment) occurred at a more controlled rate than for the free pesticide (Azo treatment). Overall, this work provides a better understanding of the mechanisms for uptake and nanoencapsulated pesticides, in tomato plants. It also points to the need for more studies to investigate the mechanistic pathways that plants use to internalize and distribute NPs. Furthermore, it is important to note that additional studies are necessary to assess the efficiency of foliar application of pesticides encapsulated in inorganic nanocarriers in protecting the crops from fungal infections and its impacts on crop yields. The data from this study can facilitate the design of efficient formulations and optimized nanocarriers for controlled release of pesticides, prior to application in actual field studies, which are expensive and time-consuming.

6.6. Supporting Information

6.6.1. List of Chemicals

Tetraethyl orthosilicate (TEOS, reagent grade 98%), ammonium hydroxide solution (NH₄OH, 28.0-30.0% NH₃ basis), hexadecyltrimethylammonium bromide (CTAB), Pluronic P123, Macerozyme R-10 (Pectinase from *Rhizopus* sp.), sodium citrate dihydrate (≥ 99%), citric acid (ACS reagent, ≥ 99.5%), sulfuric acid (95-98% H₂SO₄, ACS grade), potassium hydroxide (≥ 90% KOH, reagent grade, flakes), silicic acid (Si(OH)₄, 80 mesh, powder) and Hoagland's No. 2 basal salt mixture were purchased from Sigma-Aldrich. Deionized (DI) water ASTM type 1, methanol (HPLC grade), acetonitrile (HPLC grade), nitric acid (67-70% HNO₃, TraceMetal grade), anhydrous magnesium sulphate (MgSO₄), and sodium acetate were purchased from Thermo Fisher Scientific. Primary and secondary amine (PSA) salts were purchased from Agilent Technologies. Single-Element (Si) and Multi-Element (Mo, Sb, Si, Sn and Ti) ICP and ICP-MS Certified Reference Standards were purchased from VWR. Anhydrous ethanol (100%) was purchased from Commercial Alcohols (Canada). Azoxystrobin was provided by Vive Crop Protection Inc (Canada) in powder form. *Solanum lycopersicum* seeds (Heirloom, Beefsteak Bush) were purchased from McKenzie Seeds (Canada).

6.6.2. Pesticide Extraction

Firstly, the dried biomass was fully homogenized using an IKA T10 Basic S1 Disperser. Then, 4 mL of acetonitrile in 1% acetic acid, 0.8 g of MgSO₄, and 0.2 g of sodium acetate were added to every 0.2 g of homogenized sample, which was further vortexed for 15 min. This step was followed by the centrifugation at 2240 × g for 5 min under 20 °C and recovery of the supernatant. Then, 1 mL of the supernatant was transferred to centrifuge tubes containing 50 mg of PSA and 150 mg of MgSO₄, which were further vortexed for 1 min, followed by another step of centrifugation at 2240 × g for 5 min under 20 °C.

Table S6-1. Key parameters obtained from PHSN characterization.

Parameter	Value
Average diameter (nm)	253 ± 73 ¹⁰
Shell thickness range (nm)	22 – 38 ^{10, 41}
Pore size range (nm)	1.5 – 2.0 ¹⁰
Specific surface area (m² g⁻¹)	287 ¹⁰
Zeta potential, ζ (mV) at pH 6.5 and ionic strength of 1 mM	- 29.2 ± 1.1 ⁴¹

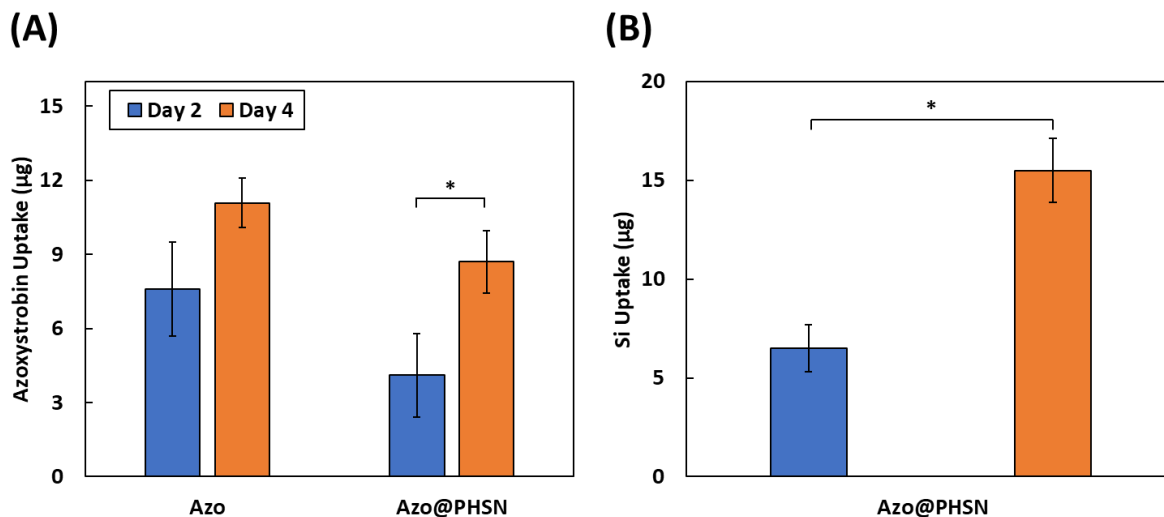


Figure S6-1. Total amount of (A) azoxystrobin and (B) Si that were translocated to different plant parts measured in LC-QToF-MS and ICP-OES, respectively. These values excluded the amount of azoxystrobin and SiO₂ measured in the dosed leaflet because some amounts may remain non-internalized on the surface of the leaflet. Error bars represent the standard deviation of the replicates ($N = 3$). Asterisk symbol (*) indicates significant statistical differences among samples with $p < 0.05$ (ANOVA one-way test followed by Tukey's test).

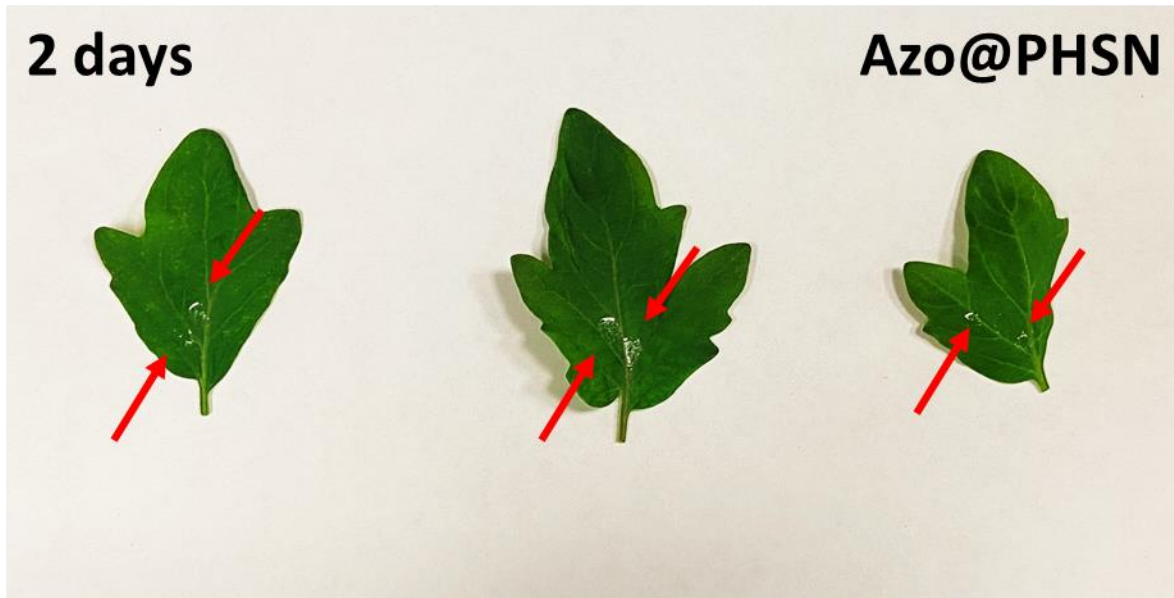


Figure S6-2. Images of the dosed leaflet ($N = 3$) upon harvesting at day 2 for the Azo@PHSN treatment (top) and Azo treatment (bottom). The red arrows indicate the PHSN powder residue remaining on the surface of the leaflet. No leaflet burn or other adverse effects were observed for either treatment.

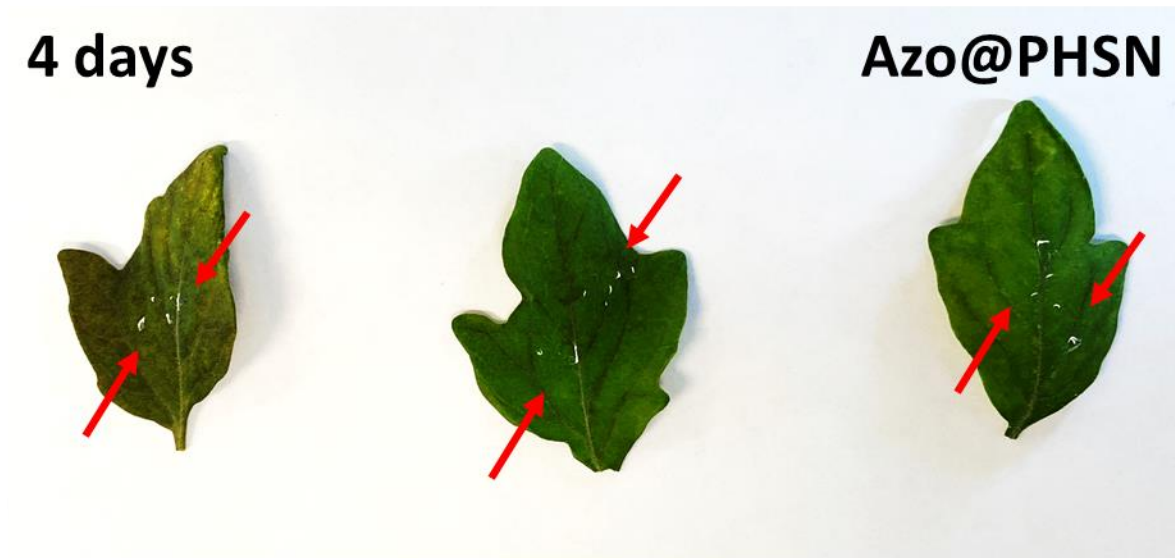


Figure S6-3. Images of the dosed leaflet ($N = 3$) upon harvesting at day 4 for the Azo@PHSN treatment (top) and Azo treatment (bottom). The red arrows indicate the PHSN powder residue remaining on the surface of the leaflet. No leaflet burn or other adverse effects were observed for either treatment.

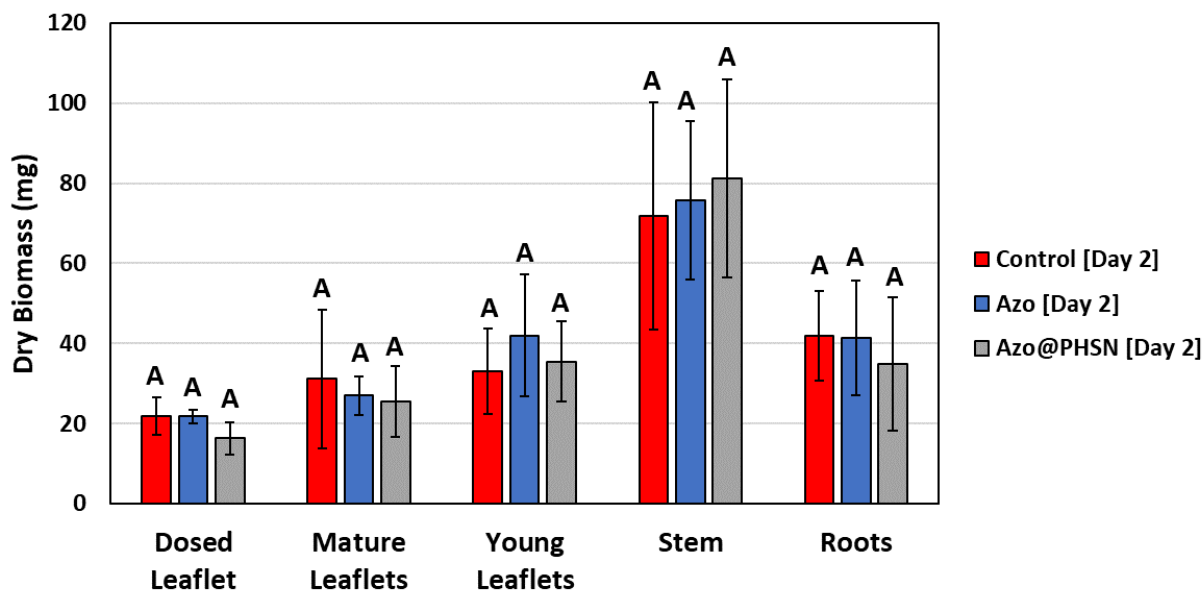


Figure S6-4. Dry biomass (mg) of different plant parts in different treatments upon harvesting at day 2. The error bars correspond to the standard deviation of the triplicates. The letter *A* above the error bars indicate that there were no statistical differences among treatments (ANOVA one-way test followed by Tukey's test, $p < 0.05$ threshold).

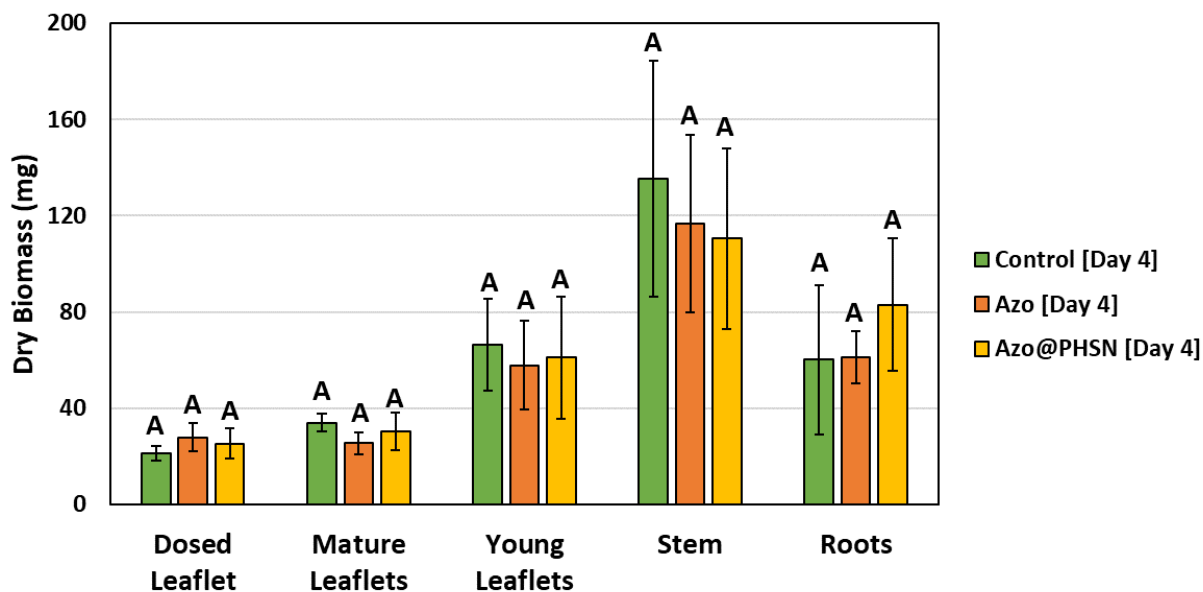


Figure S6-5. Dry biomass (mg) of different plant parts in different treatments upon harvesting at day 4. The error bars correspond to the standard deviation of the triplicates. The letter *A* above the

error bars indicate that there were no statistical differences among treatments (ANOVA one-way test followed by Tukey's test, $p < 0.05$ threshold).

6.7. References

1. Avellan, A.; Yun, J.; Morais, B. P.; Clement, E. T.; Rodrigues, S. M.; Lowry, G. V., Critical Review: Role of Inorganic Nanoparticle Properties on Their Foliar Uptake and in Planta Translocation. *Environmental Science and Technology* **2021**.
2. Tilman, D.; Fargione, J.; Wolff, B.; D'antonio, C.; Dobson, A.; Howarth, R.; Schindler, D.; Schlesinger, W. H.; Simberloff, D.; Swackhamer, D., Forecasting agriculturally driven global environmental change. *Science* **2001**, 292 (5515), 281-284.
3. Pimentel, D.; Burgess, M., Small amounts of pesticides reaching target insects. Springer: 2012.
4. Pimentel, D., Amounts of pesticides reaching target pests: environmental impacts and ethics. *Journal of Agricultural and Environmental Ethics* **1995**, 8 (1), 17-29.
5. Prasad, M. N. V., *Agrochemicals detection, treatment and remediation*. Butterworth-Heinemann: 2020.
6. Manyi-Loh, C.; Mamphweli, S.; Meyer, E.; Okoh, A., Antibiotic use in agriculture and its consequential resistance in environmental sources: potential public health implications. *Molecules* **2018**, 23 (4), 795.
7. Kumar, S.; Meena, R. S.; Jhariya, M. K., *Resources use efficiency in agriculture*. Springer: 2020.
8. Liu, F.; Wen, L.-X.; Li, Z.-Z.; Yu, W.; Sun, H.-Y.; Chen, J.-F., Porous hollow silica nanoparticles as controlled delivery system for water-soluble pesticide. *Materials Research Bulletin* **2006**, 41 (12), 2268-2275.
9. Zhao, X.; Cui, H.; Wang, Y.; Sun, C.; Cui, B.; Zeng, Z., Development strategies and prospects of nano-based smart pesticide formulation. *Journal of Agricultural and Food Chemistry* **2017**, 66 (26), 6504-6512.

10. Bueno, V.; Ghoshal, S., Self-Assembled Surfactant-Templated Synthesis of Porous Hollow Silica Nanoparticles: Mechanism of Formation and Feasibility of Post-Synthesis Nanoencapsulation. *Langmuir* **2020**, *36* (48), 14633-14643.
11. Chen, J.; Wang, W.; Xu, Y.; Zhang, X., Slow-release formulation of a new biological pesticide, pyoluteorin, with mesoporous silica. *Journal of Agricultural and Food Chemistry* **2011**, *59* (1), 307-311.
12. Chen, H.; Chen, L.; Shen, Z.; Zhou, H.; Hao, L.; Xu, H.; Zhou, X., Synthesis of mesoporous silica post-loaded by methyl eugenol as an environment-friendly slow-release bio pesticide. *Scientific Reports* **2020**, *10* (1), 1-12.
13. Zellner, W.; Lawrence, D., Silicon as a biostimulant in agriculture. *Burleigh Dodds Series in Agricultural Sciences* **2020**, *1*, 1-38.
14. Ashkavand, P.; Tabari, M.; Zarafshar, M.; Tomášková, I.; Struve, D., Effect of SiO₂ nanoparticles on drought resistance in hawthorn seedlings. *Lešne Prace Badawcze* **2015**, *76* (4).
15. Abdel-Halim, M. E.; Hegazy, H. S.; Hassan, N. S.; Naguib, D. M., Effect of silica ions and nano silica on rice plants under salinity stress. *Ecological Engineering* **2017**, *99*, 282-289.
16. Tripathi, D. K.; Singh, S.; Singh, V. P.; Prasad, S. M.; Dubey, N. K.; Chauhan, D. K., Silicon nanoparticles more effectively alleviated UV-B stress than silicon in wheat (*Triticum aestivum*) seedlings. *Plant Physiology and Biochemistry* **2017**, *110*, 70-81.
17. Malone-Povolny, M. J.; Schoenfisch, M. H., Extended nitric oxide-releasing polyurethanes via S-nitrosothiol-modified mesoporous silica nanoparticles. *ACS Applied Materials and Interfaces* **2019**, *11* (13), 12216-12223.
18. Wang, P.; Lombi, E.; Zhao, F.-J.; Kopittke, P. M., Nanotechnology: a new opportunity in plant sciences. *Trends in Plant Science* **2016**, *21* (8), 699-712.
19. Larue, C.; Castillo-Michel, H.; Sobanska, S.; Trcera, N.; Sorieul, S.; Cécillon, L.; Ouerdane, L.; Legros, S.; Sarret, G., Fate of pristine TiO₂ nanoparticles and aged paint-containing TiO₂ nanoparticles in lettuce crop after foliar exposure. *Journal of Hazardous Materials* **2014**, *273*, 17-26.

20. Eichert, T.; Kurtz, A.; Steiner, U.; Goldbach, H. E., Size exclusion limits and lateral heterogeneity of the stomatal foliar uptake pathway for aqueous solutes and water-suspended nanoparticles. *Physiologia Plantarum* **2008**, *134* (1), 151-160.
21. Ma, X.; Geiser-Lee, J.; Deng, Y.; Kolmakov, A., Interactions between engineered nanoparticles (ENPs) and plants: phytotoxicity, uptake and accumulation. *Science of the Total Environment* **2010**, *408* (16), 3053-3061.
22. Dietz, K.-J.; Herth, S., Plant nanotoxicology. *Trends in Plant Science* **2011**, *16* (11), 582-589.
23. Zhai, G.; Walters, K. S.; Peate, D. W.; Alvarez, P. J.; Schnoor, J. L., Transport of gold nanoparticles through plasmodesmata and precipitation of gold ions in woody poplar. *Environmental Science and Technology Letters* **2014**, *1* (2), 146-151.
24. Lucas, W. J.; Lee, J.-Y., Plasmodesmata as a supracellular control network in plants. *Nature Reviews Molecular Cell Biology* **2004**, *5* (9), 712-726.
25. Gao, X.; Kundu, A.; Bueno, V.; Rahim, A. A.; Ghoshal, S., Uptake and Translocation of Mesoporous SiO₂-Coated ZnO Nanoparticles to *Solanum lycopersicum* Following Foliar Application. *Environmental Science and Technology* **2021**.
26. Avellan, A.; Yun, J.; Zhang, Y.; Spielman-Sun, E.; Unrine, J. M.; Thieme, J.; Li, J.; Lombi, E.; Bland, G.; Lowry, G. V., Nanoparticle size and coating chemistry control foliar uptake pathways, translocation, and leaf-to-rhizosphere transport in wheat. *ACS Nano* **2019**, *13* (5), 5291-5305.
27. Larue, C.; Laurette, J.; Herlin-Boime, N.; Khodja, H.; Fayard, B.; Flank, A.-M.; Brisset, F.; Carriere, M., Accumulation, translocation and impact of TiO₂ nanoparticles in wheat (*Triticum aestivum* spp.): influence of diameter and crystal phase. *Science of the Total Environment* **2012**, *431*, 197-208.
28. Raliya, R.; Nair, R.; Chavalmane, S.; Wang, W.-N.; Biswas, P., Mechanistic evaluation of translocation and physiological impact of titanium dioxide and zinc oxide nanoparticles on the tomato (*Solanum lycopersicum* L.) plant. *Metallomics* **2015**, *7* (12), 1584-1594.

29. Hong, J.; Peralta-Videa, J. R.; Rico, C.; Sahi, S.; Viveros, M. N.; Bartonjo, J.; Zhao, L.; Gardea-Torresdey, J. L., Evidence of translocation and physiological impacts of foliar applied CeO₂ nanoparticles on cucumber (*Cucumis sativus*) plants. *Environmental Science and Technology* **2014**, *48* (8), 4376-4385.
30. Kranjc, E.; Mazej, D.; Regvar, M.; Drobne, D.; Remškar, M., Foliar surface free energy affects platinum nanoparticle adhesion, uptake, and translocation from leaves to roots in arugula and escarole. *Environmental Science: Nano* **2018**, *5* (2), 520-532.
31. Gullino, M. L.; Minuto, A.; Gilardi, G.; Garibaldi, A., Efficacy of azoxystrobin and other strobilurins against *Fusarium* wilts of carnation, cyclamen and Paris daisy. *Crop Protection* **2002**, *21* (1), 57-61.
32. Cochran, K.; Steger, A. J.; Holland, R.; Rupe, J. C., Effects of Soybean Cultivar, Foliar Application of Azoxystrobin, and Year on Seed Vigor and Microflora Under Delayed Harvest Conditions. *Plant Disease* **2021**, PDIS-04-20-0843-RE.
33. Bubici, G.; Amenduni, M.; Colella, C.; D'amico, M.; Cirulli, M., Efficacy of acibenzolar-S-methyl and two strobilurins, azoxystrobin and trifloxystrobin, for the control of corky root of tomato and verticillium wilt of eggplant. *Crop Protection* **2006**, *25* (8), 814-820.
34. Wang, X.; Zhang, Y.; Ni, L.; You, C.; Ye, C.; Jiang, R.; Liu, L.; Liu, J.; Han, C., A review of treatment strategies for hydrofluoric acid burns: current status and future prospects. *Burns* **2014**, *40* (8), 1447-1457.
35. Kirkpatrick, J.; Enion, D.; Burd, D., Hydrofluoric acid burns: a review. *Burns* **1995**, *21* (7), 483-493.
36. Bossert, D.; Urban, D. A.; Maceroni, M.; Ackermann-Hirschi, L.; Haeni, L.; Yajan, P.; Spuch-Calvar, M.; Rothen-Rutishauser, B.; Rodriguez-Lorenzo, L.; Petri-Fink, A., A hydrofluoric acid-free method to dissolve and quantify silica nanoparticles in aqueous and solid matrices. *Scientific Reports* **2019**, *9* (1), 1-12.
37. Kang, H.; Elmer, W.; Shen, Y.; Zuverza-Mena, N.; Ma, C.; Botella, P.; White, J. C.; Haynes, C. L., Silica Nanoparticle Dissolution Rate Controls the Suppression of *Fusarium* Wilt of Watermelon (*Citrullus lanatus*). *Environmental Science and Technology* **2021**.

38. Capobianco-Uriarte, M. d. l. M.; Aparicio, J.; De Pablo-Valenciano, J.; Casado-Belmonte, M. d. P., The European tomato market. An approach by export competitiveness maps. *PloS One* **2021**, *16* (5), e0250867.
39. Rajametov, S. N.; Lee, K.; Jeong, H.-B.; Cho, M.-C.; Nam, C.-W.; Yang, E.-Y., Physiological Traits of Thirty-Five Tomato Accessions in Response to Low Temperature. *Agriculture* **2021**, *11* (8), 792.
40. Paret, M. L.; Vallad, G. E.; Averett, D. R.; Jones, J. B.; Olson, S. M., Photocatalysis: effect of light-activated nanoscale formulations of TiO₂ on *Xanthomonas perforans* and control of bacterial spot of tomato. *Phytopathology* **2013**, *103* (3), 228-236.
41. Bueno, V.; Bosi, A.; Tosco, T.; Ghoshal, S., Mobility of Solid and Porous Hollow SiO₂ Nanoparticles in Saturated Porous Media: Impacts of Surface and Particle Structure. *Journal of Colloid and Interface Science* **2022**, *606*, 480-490.
42. Bueno, V.; Wang, P.; Harrison, O.; Bayen, S.; Ghoshal, S., Impacts of Porous Silica-Nanoencapsulated Pesticide Applied to Soil on Plant Growth and Soil Microbial Community. *ChemRxiv* **2021**. DOI: 10.33774/chemrxiv-2021-rt454
43. Lehotay, S. J., Determination of pesticide residues in foods by acetonitrile extraction and partitioning with magnesium sulfate: collaborative study. *Journal of AOAC International* **2007**, *90* (2), 485-520.
44. Dan, Y.; Zhang, W.; Xue, R.; Ma, X.; Stephan, C.; Shi, H., Characterization of gold nanoparticle uptake by tomato plants using enzymatic extraction followed by single-particle inductively coupled plasma–mass spectrometry analysis. *Environmental Science and Technology* **2015**, *49* (5), 3007-3014.
45. Liu, P.; Wang, H.; Zhou, Y.; Meng, Q.; Si, N.; Hao, J. J.; Liu, X., Evaluation of fungicides enestroburin and SYP1620 on their inhibitory activities to fungi and oomycetes and systemic translocation in plants. *Pesticide Biochemistry and Physiology* **2014**, *112*, 19-25.
46. Crowdy, S.; Wain, R., Aryloxyaliphatic acids as systemic fungicides. *Nature* **1950**, *165* (4206), 937-938.

47. Bartlett, D. W.; Clough, J. M.; Godwin, J. R.; Hall, A. A.; Hamer, M.; Parr-Dobrzanski, B., The strobilurin fungicides. *Pest Management Science* **2002**, *58* (7), 649-662.
48. White, P. J., Long-distance transport in the xylem and phloem. In *Marschner's mineral nutrition of higher plants*, Elsevier: 2012; pp 49-70.
49. VAN BEL, A. J. E., Xylem-phloem exchange via the rays: the undervalued route of transport. *Journal of Experimental Botany* **1990**, *41* (6), 631-644.
50. Maillard, A.; Diquélou, S.; Billard, V.; Laîné, P.; Garnica, M.; Prudent, M.; Garcia-Mina, J.-M.; Yvin, J.-C.; Ourry, A., Leaf mineral nutrient remobilization during leaf senescence and modulation by nutrient deficiency. *Frontiers in Plant Science* **2015**, *6*, 317.
51. Uzu, G.; Sobanska, S.; Sarret, G.; Munoz, M.; Dumat, C., Foliar lead uptake by lettuce exposed to atmospheric fallouts. *Environmental Science and Technology* **2010**, *44* (3), 1036-1042.
52. Galmes, J.; Ochogavía, J. M.; Gago, J.; Roldán, E. J.; Cifre, J.; Conesa, M. À., Leaf responses to drought stress in Mediterranean accessions of *Solanum lycopersicum*: anatomical adaptations in relation to gas exchange parameters. *Plant, Cell & Environment* **2013**, *36* (5), 920-935.
53. Bergau, N.; Bennewitz, S.; Syrowatka, F.; Hause, G.; Tissier, A., The development of type VI glandular trichomes in the cultivated tomato *Solanum lycopersicum* and a related wild species *S. habrochaites*. *BMC Plant Biology* **2015**, *15* (1), 1-15.
54. Aubert, T.; Burel, A.; Esnault, M.-A.; Cordier, S.; Grasset, F.; Cabello-Hurtado, F., Root uptake and phytotoxicity of nanosized molybdenum octahedral clusters. *Journal of Hazardous Materials* **2012**, *219*, 111-118.
55. Lew, T. T. S.; Wong, M. H.; Kwak, S. Y.; Sinclair, R.; Koman, V. B.; Strano, M. S., Rational design principles for the transport and subcellular distribution of nanomaterials into plant protoplasts. *Small* **2018**, *14* (44), 1802086.
56. Wong, M. H.; Misra, R. P.; Giraldo, J. P.; Kwak, S.-Y.; Son, Y.; Landry, M. P.; Swan, J. W.; Blankschtein, D.; Strano, M. S., Lipid exchange envelope penetration (LEEP) of

nanoparticles for plant engineering: A universal localization mechanism. *Nano Letters* **2016**, *16* (2), 1161-1172.

57. Hu, P.; An, J.; Faulkner, M. M.; Wu, H.; Li, Z.; Tian, X.; Giraldo, J. P., Nanoparticle Charge and Size Control Foliar Delivery Efficiency to Plant Cells and Organelles. *ACS Nano* **2020**, *14* (7), 7970-7986.

58. Zhu, Z.-J.; Wang, H.; Yan, B.; Zheng, H.; Jiang, Y.; Miranda, O. R.; Rotello, V. M.; Xing, B.; Vachet, R. W., Effect of surface charge on the uptake and distribution of gold nanoparticles in four plant species. *Environmental Science and Technology* **2012**, *46* (22), 12391-12398.

59. Li, H.; Ye, X.; Guo, X.; Geng, Z.; Wang, G., Effects of surface ligands on the uptake and transport of gold nanoparticles in rice and tomato. *Journal of Hazardous Materials* **2016**, *314*, 188-196.

60. Spielman-Sun, E.; Avellan, A.; Bland, G. D.; Tappero, R. V.; Acerbo, A. S.; Unrine, J. M.; Giraldo, J. P.; Lowry, G. V., Nanoparticle surface charge influences translocation and leaf distribution in vascular plants with contrasting anatomy. *Environmental Science: Nano* **2019**, *6* (8), 2508-2519.

61. Edwards, C., Factors that affect the persistence of pesticides in plants and soils. *Pesticide Chemistry-3* **1975**, 39-56.

Chapter 7. Conclusions, Implications and Future Work

7.1. Conclusions

Significant increase in food demand due to population growth is inevitable. This will increase the pressure on crop productivity and agricultural practices to make them more efficient and sustainable. Among some innovative technologies, nano-enabled agriculture provides a promising framework for solving some of the current shortcomings in agriculture, such as providing a carrier (nanoparticles) to encapsulate and transport active ingredients (AI), control their release over an extended period, increase their apparent solubility particularly for poorly soluble organic pesticides, increase pesticide bioavailability and uptake in plants, among others.

This thesis explored the use of porous hollow silica nanoparticles (PHSN) to promote enhancements in the application process of azoxystrobin, a top-selling broad-spectrum fungicide. The work included the synthesis, characterization, application, and environmental fate analysis of the nanoformulation. Some of the major findings and conclusions are described in detail below:

- 1) Development of a new method to synthesize PHSNs through soft templating, which involved the use of two surfactants that self-assembled forming the template for the hollow cavity and pores on the silica shell. The mechanism of formation was meticulously investigated to understand how each compound plays a role in the final PHSN structure using a suite of techniques, including transmission electron microscopy, dynamic light scattering, nitrogen sorption assays, Fourier-transform infrared spectroscopy, energy-dispersive X-ray, and solid-state nuclear magnetic resonance techniques as shown in **Chapter 3**.
- 2) Demonstration of proof of encapsulation of ferrous ions that further reacted with a reducing agent forming iron nanoparticles within the PHSN as shown in **Chapter 3**. This was the first imaging demonstration of the encapsulation of compounds within a nanoparticle. Later, in **Chapter 5** and **Chapter 6**, azoxystrobin was loaded into the PHSNs in sufficient amount to be used in agricultural settings. The loading took place through diffusion of the solubilized pesticide from the bulk solution to the hollow cavity and through sorption and deposition onto the silica surface. These results demonstrated that the PHSN were indeed porous and hollow, that different types of compounds of varying

sizes and physicochemical properties (ions, nanoparticles, and organic molecules) could be encapsulated within the silica shell, and that PHSNs could act as a versatile nanocarrier and nanoreactor.

- 3) Demonstration that particle structure and particle surface properties play an important role in the transport profile of different nanoparticles as shown in **Chapter 4**. Due to the increased specific surface area, porosity, and varying zeta potential of PHSNs, they move through saturated porous media differently from solid spherical silica nanoparticles. All these three factors combined cause deviations from the standard Derjaguin-Landau-Verwey-Overbeek (DLVO) theory, thus not being captured by modeling. After several runs in varying experimental conditions of pH and ionic strength, it is evident that PHSNs took longer to move through the 10-cm sand-packed column across the board because of their enhanced interactions with the collector (sand particles) and other nanoparticles, causing them to be more retained in the column when compared to solid silica nanoparticles (SSN). The shadow effect firstly introduced in a previous study is likely one of the phenomena explaining why PHSN and SSN transport profile through saturated porous media varied so significantly.
- 4) Demonstration that the PHSNs promoted slow release of azoxystrobin releasing 43.5% of the encapsulated pesticide in 10 days, while non-encapsulated azoxystrobin fully solubilized in the medium after 3 hours as shown in **Chapter 5**. This allows an extended exposure of azoxystrobin over time rather than a one-time exposure.
- 5) Investigation of the effects of nanoencapsulated azoxystrobin on plant growth and soil microbial communities and how these compare with non-encapsulated azoxystrobin formulations as shown in **Chapter 5**. Overall, the encapsulation within PHSN mitigated the toxicity caused by azoxystrobin in the plant development. Plants treated with the nanoencapsulated formulation were less impacted than the ones treated with non-encapsulated pesticide when compared to controls in terms of plant biomass, lengths of root, shoot and longest leaf, and number of leaves. Both nanoencapsulated and non-encapsulated pesticide treatments impacted the soil microbial community to some extent. However, these shifts in soil microbial community did not affect key microbes responsible for important activities to keep the soil functional, such as nutrient cycling. The soil microbial community bounced back at the end of the experiment, presenting results closer

to the controls, suggesting that the soil acclimated to the formulations after 20 days. The shifts observed in the communities were not able to explain why the plant growth was so much impacted in the treatments with pesticides (nanoencapsulated and non-encapsulated) in the first place, leaving the toxicity of azoxystrobin as the main factor contributing to the inhibition in the plant growth.

- 6) Investigation of the uptake and translocation profiles of nanoencapsulated azoxystrobin in tomato plants grown hydroponically as shown in **Chapter 6**. Both the PHSN and the pesticide were quantified in different plant tissues (dosed leaf, mature leaves, young leaves, stem, and roots) after 2 and 4 days. The distribution profile between the silica nanoparticles and azoxystrobin varied, suggesting that they have different translocation mechanisms for distribution within the plant. The results are interesting because large particles in the range of 200 nm diameter were taken up and distributed throughout the plant, even though the size exclusion limits (SEL) discussed in the literature pointed out that particles over 50 nm could not be internalized following foliar application, let alone be distributed to different plant parts.

7.2. Implications

The results obtained from this work have direct implications in advancing the knowledge on the field. The specific implications of each one of the previous stated conclusions are detailed below:

- 1) The development of a novel soft-template method using a combination of two surfactants to synthesize PHSNs mitigates the shortcomings of other synthesis methods. In hard-template methods, the hard template must be functionalized to allow the anchorage of the silica shell precursor to the hard template, which could be polystyrene beads and resorcinol-formaldehyde. Furthermore, the hard template must be removed post-synthesis through calcination or acid wash. For other previously published soft template methods, one or more surfactants are used in combination with a swelling agent, usually an oil phase, to create a nano-emulsion. In some cases, the functionalization of the surface of these nano-emulsions are also required to attract the silica precursor to the oil-water interface. Here, I decreased the steps necessary for the synthesis to occur. No functionalization is necessary because the positively charged CTAB forming a self-assembly structure with Pluronic P123 is responsible for attracting and anchoring the silica precursor onto the template.

Moreover, no oil phase is necessary as swelling agent because the complex CTA⁺-Pluronic P123 has the right size to template PHSNs of approximately 200 nm in diameter. In summary, the method developed in this thesis minimizes the complexity of previously described synthesis method, which increases the chances of a successful and reproducible synthesis. It is important to note that the protocol was optimized to produce SiO₂ nanoparticles with diameter, pore size and shape capable of carrying organic pesticides. Hence, particles with different characteristics may be tuned to accommodate different application needs.

- 2) A major knowledge gap in the field of AI nanoencapsulation was that no imaging for proof of encapsulation was not available. Encapsulation/loading of AI to a nanocarrier was claimed successful when the nanocarrier was able to release the AI over extended periods of time that differed significantly from the non-encapsulated compound. Here, I showed image confirmation that Fe ions were internalized and further reacted with a reducing agent to form Fe nanoparticles inside the PHSN. The TEM images and EDX show proof that the nanocarrier was indeed porous and hollow, and that one can encapsulate different compounds within nanocarriers. The same approach can be replicated to prove that other structures are porous and hollow. It is important to note that the encapsulation experiments were performed with inorganic ions and organic pesticide, hence encapsulation feasibility and profile may vary depending on the molecule size, polarity and hydrophobicity.
- 3) Demonstrating that particles with different architectural and surface properties have significantly different transport profiles in saturated porous media stresses the fact that one cannot predict the environmental fate of different nanocarriers based on simplistic modeling using a spherical solid nanoparticle. Nowadays, most studies use pristine, spherical nanoparticles to evaluate the potential environmental implications of the deployment of nanotechnology in agriculture. However, as demonstrated in this thesis, nanoparticle transport profiles may vary differ and deviate from standard DLVO theory. It is important to note that the column experiments were performed with clean, acid-washed sand. Hence, the transport profiles may differ in heterogeneous soil columns. A major limitation in tracking SiO₂ in soils, however, is that soils are naturally rich in SiO₂-based compounds, rendering it challenging to identify what fraction corresponds to naturally-

occurring SiO₂ and what fraction corresponds to the engineered nanoparticles added to the system.

- 4) As the PHSNs promoted the slow release of the AI over an extended period of time, they can be used to carry high-density concentration of an AI in a compacted space. In agriculture, for instance, one will be able to reduce the number of pesticide applications in a single harvest. Instead of applying these agrochemicals several times to ensure that the crops are protected against pests throughout the season, one may simply adjust the concentration of these agrochemicals to a single application of the nanoformulation. Then, the slow release promoted by the PHSNs will ensure that enough AI is available throughout the crop season. It is important to note that the release experiments were performed in a model release medium containing deionized water and methanol at an 80:20 ratio (v/v). Hence, release profiles may vary in unsaturated agricultural soil and complex aqueous systems.
- 5) The results in **Chapter 5** are important for two reasons: (i) they show that not only the nanoparticles did not have an adverse effect on the plants and soil microbial community, but they helped mitigate the toxic effects of the pesticides towards the plants, and (ii) thus they demonstrated that, based on the experiments performed in this thesis, deploying nanotechnology in agriculture have beneficial outcomes to the crops. A major knowledge gap in the field was to make sure that the nanocarriers would not have important negative effects on the plant and soil health, which would render nano-enabled agriculture unfeasible and generate another class of emerging environmental contaminants. It is important to note that the soil microbial community was not affected in the agricultural soil used in this work. However, these results may vary in soils with considerably lower organic matter content.
- 6) The results in **Chapter 6** shed light on the uptake and translocation mechanisms in plants. It was believed that nanoparticles with diameter over 50 nm were too large to be internalized and distributed inside plants, due to the SELs. Here, however, particles as large as 250 nm were internalized following foliar application and distributed throughout the plants, from shoot to root. These results challenge current understanding on how these nanoparticles are internalized and transported within plants. It is important to note that

these studies were performed with tomato plants (*Solanum lycopersicum*). Hence, uptake patterns may be different in other plants or with particles of different diameters and shapes.

7.3. Future work

This thesis covered the synthesis, characterization, application, and environmental fate of PHSN-encapsulated azoxystrobin. There are, however, some topics outside the scope of this thesis that could further advance the knowledge in the field. For example, one could vary the experimental conditions of the PHSN synthesis method developed here to explore whether the particle size, pore size and cavity size can be tuned. Having PHSN of different diameter and pore size distribution could help understand what conditions are important to optimize loading and delivery of AI, and plant uptake and translocation.

Stimuli-responsive nanocarriers have been gaining increasing interest lately. It involves functionalizing the surface of nanocarriers to modulate the release of AI based on a response to a stimulus, which includes change of pH, temperature, light, redox balance, among others. This could ensure that the AI is only released under certain conditions depending on the needs of the application. Surface functionalization could also enhance the transport by targeting the delivery site, which could be a plant organelle or tissue. All these sophisticated ideas are only possible because of the work done in this thesis and in similar works previously published that explored the fundamentals of using nanoparticles as carriers for AI in agriculture. Ultimately, it is important to make sure whether these novel nanoformulations are advantageous when compared to the traditional applications in practice nowadays.